

UNIVERSITY OF RIJEKA
FACULTY OF ENGINEERING

Marko Perčić

**CHARACTERIZATION OF
PARAMETERS INFLUENCING
FRICTION IN THE NANOMETRIC
DOMAIN**

DOCTORAL THESIS

Rijeka, 2020.

UNIVERSITY OF RIJEKA
FACULTY OF ENGINEERING

Marko Perčić

**CHARACTERIZATION OF
PARAMETERS INFLUENCING
FRICTION IN THE NANOMETRIC
DOMAIN**

DOCTORAL THESIS

Thesis Supervisor: Prof. D. Sc. Saša Zelenika

Thesis Co-supervisor: Prof. D. Sc. Igor Mezić

Rijeka, 2020.

Thesis Supervisor: Prof. D. Sc. Saša Zelenika, University of Rijeka, Croatia, Faculty of Engineering

Thesis Co-supervisor: Prof. D. Sc. Igor Mezić, University of California, Santa Barbara, CA, USA

This doctoral thesis was discussed on _____ at the University of Rijeka, Croatia, Faculty of Engineering in front of the following Evaluation Committee:

1. Assist. Prof. D. Sc. Ervin Kamenar, University of Rijeka, Faculty of Engineering, Croatia
2. Assist. Prof. D. Sc. Goran Gregov, University of Rijeka, Faculty of Engineering, Croatia
3. Prof. D. Sc. Željko Domazet, University of Split, Faculty of Electrical Engineering, Mechanical Engineering and Naval Architecture, Croatia

Dedicated to my family.

“L'essentiel est invisible pour les yeux.”
Antoine de Saint-Exupéry: *“Le Petit Prince”*

Acknowledgements

The multidisciplinary research topic presented in this thesis is the result of thorough physical experiments and numerical modelling conducted by the author, many of which would not be possible without the support of helpful individuals, each in their field. First, I would like to thank my thesis supervisor Prof. Saša Zelenika and co-supervisor Prof. Igor Mezić for their helpful comments and discussions during the work on the thesis.

The experimental measurements were conducted on the premises of the Centre for Micro- and Nanosciences and Technologies (NANORI) and the Department of Physics, both at the University of Rijeka, Croatia. Sample synthesis with Atomic Layer Deposition (ALD), and analyses via X-ray Photoelectron Spectroscopy (XPS) and Secondary Ion Mass Spectrometry (SIMS) would not be possible without the precious help of Assist. Prof. Robert Peter and Assist. Prof. Iva Šarić. At the same institution, imaging of microcantilever sensors and various structures via Field-Emission Scanning Electron Microscope (FE-SEM) was done with great help from Assist. Prof. Ivana Jelovica Badovinac. Furthermore, the synthesis of samples by employing Pulsed Laser Deposition (PLD) was conducted at the Institute of Physics in Zagreb, Croatia, with great help of Assist. Prof. Nikša Krstulović.

The ideas implemented in the numerical part of the research were stimulated with useful advices and discussions with Prof. Senka Mačešić, Assist. Prof. Stefan Ivić, and Aleksandr Andrejčuk of AIMdyn, Inc.

Great support during the long hours of working on this research came from my dear friends and colleagues from the Department of Mechanical Engineering Design, the NANORI and the whole Faculty of Engineering, who I also thank. But the biggest “thank you” for all their unconditional support and encouragement goes to my family to whom I dedicate my thesis.

The work described in the thesis is, in turn, enabled by using the equipment funded via the ERDF project RC.2.2.06-0001 “*Research Infrastructure for Campus- based Laboratories at the University of Rijeka – RISK*”, as well as via the support of the University of Rijeka grants uniri-tehnic-18-32 “*Advanced mechatronics devices for smart technological solutions*” and 17.10.2.1.02 “*Measuring, modelling and compensating friction in high-precision devices: From macro- to nanometric scale*”. The work was partially supported also by the Croatian Science Foundation project IP-11-2013-2753 “*Laser Cold Plasma Interaction and Diagnostics*”. The GoSumD software is provided by AIMdyn, Inc.

Abstract

Friction and wear are recognized as one of the most puzzling problems, not only in many engineering and manufacturing applications, but also in a fundamental scientific sense. In fact, friction is a nonlinear stochastic effect with a distinct time, position and temperature variability. While frictional phenomena on the macro- and meso-scales can be considered well described, and their characteristic features can be simulated via suitable models, as well as generally efficiently compensated by using proper control typologies, the study of friction, the parameters that influence its value and the respective models in the nanometric domain are still in an early stage, due to various experimental and modelling complexities.

The research performed in the framework of the doctoral thesis provides a scientific contribution to the study of dry (unlubricated) friction by characterising the parameters influencing its value at the nanometric scale, and especially the dependence of friction on material properties, loading conditions, the velocity of motion, as well as temperature. The characterisation of the dependence of friction on the listed parameters is based on experimental measurements performed by employing a Scanning Probe Microscope (SPM). Due to the number and variety of the monitored influences, the number and type of measurements is determined by a state-of-the-art Design of Experiment (DoE) methodology by employing Voronoi tessellations. To obtain predictive models linking the process variables to the value of nanometric friction, the obtained measurement results are then validated numerically via a thorough comparative analysis of state-of-the-art machine learning methods. Despite the marked complexity of the analysed phenomena and the inherent dispersion of the measurements, the developed symbolic regression models, show, depending on the type of the sample, an excellent prediction accuracy between 72 and 91%.

Keywords: nanometric friction, atomic force microscopy, nanotribology of thin films, experimental measurements, friction modelling

Prošireni sažetak

Trenje i trošenje su jedan od najizazovnijih problema u mnogih inženjerskim i proizvodnim primjenama. Doista, trenje je nelinearna stohastička pojava s izraženom vremenskom, prostornom i temperaturnom varijabilnošću. Dok je trenje u makro- i mezodomeni dobro objašnjeno te je njegove učinke, primjerenim modelima, moguće modelirati i, primjerenim sustavima regulacije, najčešće i uspješno kompenzirati, u nanometarskom području je proučavanje trenja, parametara koji utječu na trenje, te nalaženje odgovarajućeg modela tih pojava još u zametku.

Karakterizacijom utjecajnih parametara u nanometarskom području, a posebice ovisnosti trenja o svojstvima materijala, opterećenju, brzini relativnog gibanja te temperaturi tribološkog para, istraživanje provedeno u sklopu doktorske disertacije daje znanstveni doprinos izučavanju trenja klizanja bez podmazivanja. Eksperimentalno su analizirani tanki filmovi pet različitih materijala: aluminijevog oksida (Al_2O_3), aluminijska, molibden disulfida (MoS_2), titanijevog dioksida (TiO_2) te martenzitnog nehrđajućeg čelika (X39CrMo17-1). Doista, zbog povoljnih svojstava otpornosti na trošenje i njihove tvrdoće, prevlake od Al_2O_3 i TiO_2 su često korišteni materijali za primjene u mikro- i nanoelektromehaničkim sustavima (M(N)EMS) kao i, općenito, u preciznim konstrukcijama. Ti su uzorci sintetizirani u obliku tankog filma metodom taloženja atomskih slojeva (*Atomic Layer Deposition* – ALD) na silicijev (Si) supstrat. Ostali proučavani uzorci su odabrani za istraživanje zbog njihove široke primjene u općem strojarstvu te u preciznim konstrukcijama. Zbog povoljnih kliznih svojstava sulfida, MoS_2 se, tako, često koristi kao kruto mazivo. Čisti Al je jedan od najčešće korištenih materijala za lake i precizne konstrukcije, dok je martenzitni nehrđajući čelik X39CrMo17-1 odabran kao predstavnik visokokvalitetne grupe čelika za strojne elemente. Ovi uzorci su sintetizirani metodom taloženja pulsirajućim laserom (*Pulsed Laser Deposition* – PLD), što je omogućilo i da se prvi puta postigne sintetiziranje tankog filma visokolegiriranog čelika.

Eksperimentalno mjerenje pretražnim mikroskopom atomskih sila u modalitetu rada mjerenja poprečne sile (*Lateral Force Microscopy* – LFM) vršeno je na svim uzorcima strukturiranim načinom u eksperimentalnim točkama definiranim trima promjenjivim tehnološkim parametrima: normalnom silom $F_N = 10 \dots 150$ nN, brzinom klizanja $v = 5 \dots 500$ nm/s i temperaturom $\vartheta = 20 \dots 80$ °C. Pedeset mjernih točaka je pritom definirano Voronoi teselacijskom *Design of Experiment* (DoE) metodom podjele domene mjerenja u granicama promjene navedenih utjecajnih parametara, te je mjerenje u svakoj točki ponovljeno pet puta,

pa je tako u analizi ukupno izvršeno 1,250 mjerenja. Eksperimentalna metodologija je u tom kontekstu strukturirana na način da u kalibracijskom postupku uzima u obzir i promjenjive učinke adhezije ali i vodeći računa o potrebi kompenzacije temperaturnih rastezanja. Razvijenom metodologijom je po prvi puta uopće postignuto mjerenje trenja na nanometarskoj razini s tri promjenjive veličine.

Dobiveni rezultati mjerenja omogućavaju ne samo uvid u ponašanje pojedinog analiziranog materijala u danim promjenjivim uvjetima, već i određivanje korelacijskih funkcija koje povezuju parametre procesa s vrijednošću sile trenja na nanometarskoj razini. Temeljita komparativna analiza primjene različitih naprednih metoda strojnog učenja na mjerne podatke je omogućila određivanje korelacijskih funkcija, odnosno prediktivnog modela trenja. Usprkos kompleksnosti analiziranih fizikalnih pojava te značajnom rasipanju mjernih rezultata, provedena je analiza omogućila da se, ovisno o uzorku, primjenom razvijenog matematičkog modela metodom simboličke regresije, dobije točnost predviđanja sile trenja, u odnosu na radne parametre, na razini od 72 do 91%. Takva izvanredna točnost predikcije omogućava ne samo uvid u funkcijsku ovisnost trenja na nanometarskoj razini o promatranim varijablama, nego i stvara preduvjete za proširenje postojećih modela trenja, čime bi se njihova praktična primjenjivost proširila i na nanometarsku razinu.

Ključne riječi: trenje u nanometarskom području, mikroskopija atomskih sila, nanotribologija tankih filmova, eksperimentalna mjerenja, modeliranje trenja

Table of Contents

Acknowledgements	xi
Abstract	xiii
Prošireni sažetak	xv
1. Introduction	1
1.1. Scientific Motivation.....	1
1.2. Aims of the Work.....	2
1.3. Contributions of the Thesis	2
1.4. Organization of the Thesis	4
2. State-of-the-Art	7
2.1. Nanotribology and M(N)EMS	11
2.2. State-of-the-Art in Experimental Nanotribology	13
3. Experimental Measurements of Nanoscale Friction	17
3.1. Used Experimental Apparatus and Methodology	18
3.2. Sampling of the Experimental Design Space	18
3.3. Synthesis of the Thin-film Samples	20
3.3.1. <i>Atomic Layer Deposition (ALD)</i>	21
3.3.2. <i>Pulsed Laser Deposition (PLD)</i>	22
3.4. Characterization of the Samples.....	23
3.4.1. <i>X-Ray Photoelectron Spectroscopy</i>	23
3.4.2. <i>Secondary Ion Mass Spectrometry</i>	24
3.5. Experimental Measurement of the Nanoscale Friction Force	26
3.5.1. <i>Calibration of the Probes</i>	27
3.5.2. <i>Measurement of the Adhesion Forces</i>	32
3.5.3. <i>Temperature Effects on the Variability of the Normal Force</i>	36
3.6. Tip Wear and its Influence on Adhesion.....	37
4. Results of Experimental Measurements and their First-order Analysis	41
5. Development of a Predictive Model of Nanoscale Friction	49
5.1. Test Dataset – Experimental Measurements	51
5.2. Data Preparation	57

5.3.	Data Normality	59
5.4.	Metrics – Model Selection Criteria	62
5.5.	k-fold Cross-validation.....	64
5.6.	Machine Learning Regression Methods.....	66
5.6.1.	<i>Multilayer Perceptron</i>	67
5.6.2.	<i>Random Decision Trees and Forests</i>	68
5.6.3.	<i>Support Vector Regression</i>	69
5.7.	Comparison of Machine Learning Models.....	70
5.7.1.	<i>1D Considerations</i>	70
5.7.2.	<i>2D Considerations</i>	76
5.8.	Genetic Programming – Symbolic Regression	83
5.8.1.	<i>Grammatical Evolution GP</i>	85
5.8.2.	<i>Offspring Selection GP</i>	85
5.8.3.	<i>Age-Layered Population Structure GP</i>	86
5.8.4.	<i>Multi-gene GP</i>	86
5.9.	Comparison of Symbolic Regression Models	87
6.	Results and Discussion	91
7.	Conclusions and Outlook	105
	List of References	109
	List of Symbols	125
	Latinic symbols.....	125
	Greek symbols	127
	List of Abbreviations	129
	List of Figures	131
	List of Tables	137
	Appendices	139
	Appendix A CVT-based Measurement points	141
	Appendix B CVT-based F_f and F_A Measurements	143
	Appendix C MC-based Measurement Points.....	171
	Appendix D MC-based F_f and F_A Measurements.....	173
	Curriculum Vitae et Studiorum	185

1. Introduction

This part of the thesis provides general introductory information about the presented research. The introductory part is conceived as a brief overview of general scientific motivation, aims and contributions of the conducted research presented in this thesis, and, an outline of the thesis organization.

1.1. Scientific Motivation

Tribology is the scientific discipline that studies friction, wear and lubrication. It is of major practical importance for mechanical engineering applications, especially in the designing stage, as well as for securing an efficient and reliable working life of various parts, assemblies and systems. In fact, since most of practical engineering devices are assemblies with several parts in contact and relative motion, friction is inevitable. To create the conditions for designing components and systems with minimal power dissipation and degradation, great attention was dedicated so far to the study of the physical and chemical origins of friction [130], [138]. Despite the large number of tribology studies on the macroscopic scale, a clear understanding of the physical fundamentals of friction does not yet exist [14], [153]. The main reason for this lack of insight is the difficulty in observing the interactions that occur deep in the contact regions between the two bodies. The macroscopic contact of two smooth solid surfaces is, in fact, composed of a large number of contacts between microasperities existing on both surfaces in contact [25], [26]. Friction phenomena is, in reality, based on atomic interactions between the two surfaces in contact, as well as microscopic elastic and plastic deformations, which define the morphology and distribution of stress in these contacts. This is the main reason why it is important to gain a better insight into the mechanisms of friction and contribute to the research especially in the micro- and nanodomains [133], [145]. Research of frictional phenomena in these domains is, thus, not only of paramount importance for obtaining physical insights into the studied complex phenomenon and the very origin of friction, but also a steppingstone to the development of novel models and techniques for practical applications.

The wide applicability of tribological research, at all scales, is a big motivation for thorough studies in this area. Applications range from nanometric and atomic scales, pertaining particularly to micro- and nanoelectromechanical devices, implemented nowadays all around us, e.g., in medical applications, scientific and other instruments in all spheres of human

endeavours, to large-scale engineering marvels, and even space exploration. All these areas confirm that friction is an omnipresent phenomenon. Also, achieving the goal of more efficient, precise and reliable engineering designs is simply “a must” in attaining modern, sustainable and ever more environmentally friendly future devices and structures [67], [68].

1.2. Aims of the Work

Based on the outlined motivation, the goal of this thesis is to contribute to the basic understanding of the friction phenomena at the nanometric scale by applying state-of-the-art experimental and mathematical methods. The study of nanotribological phenomena is hence performed by experimental methods, i.e., via thorough experimental analyses of a chosen set of samples by atomic force microscopy. The main objective of the experimental study is to collect data on the friction force while varying multiple influencing parameters, i.e., the conditions affecting the tribological behaviour of individual samples and a silicon tip of the scanning probe microscope. The considered variable parameters are those that influence the most the physical process of friction, i.e., normal force F_N , sliding velocity v , and temperature ϑ . The studied materials are, in turn, of practical importance for applications such as M(N)EMS systems and precision mechanical engineering: aluminium oxide (alumina) (Al_2O_3), aluminium (Al), molybdenum disulphide (MoS_2), titanium dioxide (TiO_2), and martensitic stainless steel (X39CrMo17-1). To determine the optimal configuration of experimental measurements while performing complex and time-consuming experiments involving several variable influencing parameters imposed on different samples, the Design of Experiments (DoE) methodology is applied, allowing to reduce the required number of individual measurements while providing enough data for the subsequent modelling and insight into the observed phenomena. The final and most important goal is to obtain the simplest and most precise form of correlation function(s), i.e., functions that link the value of the friction force with the considered variable influencing parameters for each of the tested materials. Furthermore, the discovery of the underlying mathematical form describing this complex physical phenomenon will also provide novel and state-of-the-art fundamental insights into the tribological behaviour at the nanometric scales with multidimensional influential parameters.

1.3. Contributions of the Thesis

The research presented in the doctoral thesis constitutes an effort to give a scientific contribution to the fundamental studies of friction. The contribution of the work consists in

clarifying and quantifying the impact of the main influencing parameters on the frictional force in the nanometric range. Resolving this problem involves the analysis and synthesis of previous theoretical findings and experimental results thus allowing the identification and development of novel experimental and mathematical approaches. The main hypothesis of the performed research, based on extensive experimental study while observing the influence of variable parameters and materials, as well as via a thorough and detailed mathematical analysis of the obtained results, is that it is possible to attain accurate functional correlations allowing to completely characterise the value of the frictional force in the nanometric domain with multidimensional variable parameters.

The experimental part of the research involves studying the selected thin-film samples: Al₂O₃, Al, MoS₂, TiO₂ and X39CrMo17-1. In this framework, the Al₂O₃ and TiO₂ samples, which are often used as standard materials for coating of various M(N)EMS structures and have thoroughly studied optical and electronic (semi-conductive) properties, are produced via Atomic Layer Deposition (ALD). On the other hand, Al, MoS₂ and X39CrMo17-1 are materials which are broadly used in general engineering applications as structural materials (aluminium and steel) or as a solid lubricant (MoS₂) and have been synthesized by using Pulsed Layer Deposition (PLD). The synthesis of a stainless-steel thin-film sample is not described so far in the accessible literature, so that its obtainment presents by itself a novel contribution of the thesis. This type of sample allows also a future comparison of the herein obtained data with data relative to the behaviour of the bulk material of the same chemical composition and structure in micro- or macrotribological regimes, creating the preconditions for further studies of scale-effects and the eventual development of multi-scale models.

The friction force on all samples is assessed experimentally by using the Atomic Force Microscope (AFM) in Lateral Force Microscopy (LFM – known also as the FFM – Friction Force Microscopy) mode. To minimise the number of needed measurements, the experiments performed on the analysed samples are then configured by applying a novel Design of Experiment (DoE) methodology. In fact, a preliminary study of the possibility to use for this purpose conventional DoE methods such as Box-Behnken, Taguchi, or various factorial designs, allowed establishing that all of them allow describing only the low-order trends of frictional variability with respect to the influencing parameters taken into account, and generally would not provide a detailed insight into the studied phenomena. The sampling of the experimental design space is, thus, obtained by using the Centroidal Voronoi Tessellation (CVT) technique. Since up to date this sampling method was not applied to nanotribological measurements, this, alongside the developed elaborated experimental methodology for the

concurrent characterization of the studied influencing parameters on friction in the nanometric domain, presents again a novel contribution of the thesis. Due to the complex and time-consuming nature of the used experimental technique, the number of points selected for the main experimental part for each of the used sample materials is then 50, with 5 repetitions for each measurement point, resulting in a total number of 1,250 measurements.

A novel approach to modelling the data collected via the resulting well-structured experiments, is, however, needed. A thorough comparative analysis of state-of-the art Machine Learning (ML) methods, namely the so-called black-box algorithms (support vector machine, random forest, multilayer perceptron, etc.) on one hand, and the function-generating (white-box) modelling methods (various types of Symbolic Regression (SR) based on Genetic Programming (GP)) on the other is hence performed on the obtained experimental datasets, providing the basis for testing the predictive performance these methods. A novel predictive model of nanoscale friction is thus proposed, allowing to obtain predictive function(s) of the dependence of the value of the friction force in the nanometric domain each of the considered sample materials in the multidimensional space defined by the considered ranges of influencing parameters. These functional correlations provide a very important and valuable scientific contribution for further research in the field of friction and the development and validation of novel theoretical and practical models. The performed research contributes, thus, successfully to a more complete and far profounder understanding of tribological phenomena on the nanometric scale.

Thus, a complex phenomenon, such as friction at the nanoscale, comprising of multiple and concurrently interacting parameters with complex synergistic effects, is for the first time successfully studied by employing complex novel experimental methodologies, in the framework of a newly-developed systematic approach for multidimensional experimental analysis based on applied state-of-the-art machine learning and artificial intelligence methods.

1.4. Organization of the Thesis

The doctoral thesis is organized in structured sections covering each of the main parts of the research. In Chapter 1 the main scientific motivation and objectives of the research are underlined, especially stressing the contributions given to the considered research field. The state-of-the-art in experimental nanotribology is presented in Chapter 2 where brief historical notes and introductory basics of tribology are given as well. Chapter 3 of the work describes in detail the developed experimental methodology for measuring the nanoscale friction force,

including the measurements of the adhesive forces. A detailed report about the used Design of Experiments, the synthesis of the analysed samples, the characterisation of the samples, and the description of the salient features of the measurement methodology using the AFM are provided in this part of the work as well. Important insights into the original contributions to the experimental research in this field, in terms of measurements with multiple variable parameters as well as of the introduced correction terms of the calibration factors, compensating for the temperature variability of the adhesive forces, are thoroughly described. The obtained experimental data are systematically analysed in Chapter 4, thus providing the basis for the development of a predictive model of nanoscale friction. Numerical methodologies used for data mining, implemented by employing various state-of-the-art machine learning methods, are comparatively analysed in terms of their predictive performances on separately measured testing datasets. Based on such a sound scientific foundation for the selection of the best performing method, a predictive model is finally chosen and scrutinized in Chapter 5 of the thesis. The hence obtained results and the respective critical discussion are given in this section of the work as well. The wide-ranging conclusive remarks and a foresight of the possible future research directions are presented in the conclusions of the thesis in Chapter 6.

2. State-of-the-Art

Friction is an omnipresent phenomenon in all natural and man-made processes involving contacts between two bodies in relative motion. The resulting force, which opposes the movement of the two bodies in contact, is the friction force that, in fact, is a reaction force to externally imposed force conditions. Part of the energy used to generate movement of the bodies in contact is transferred to the frictional phenomena and dissipated through heat generation, elastic and plastic deformation of contact surfaces and other manifestations [14].

The studies of interactions between two surfaces in contact date back to ancient times, i.e., to ever-since humanity started evolving enough to take advantages of man-made devices and primitive systems to aid them in everyday life. The study of friction closely follows the technical aspects of human development. Ever since the earliest civilizations, from the Stone Age, through Egyptian, Roman, and Greek periods, but also in the far-east and South American civilizations, there are evidences that lubrication and friction phenomena were empirically studied and applied to processes [48]. The insight in frictional phenomena through ages, from the rubbing of two pieces of wood for producing fire, the invention of the wheel, or lubricating sliding ways for huge stone blocks in Egypt, was very limited, until renaissance flourished, and a new generation of thinkers started systematically studying the physical phenomena surrounding us. In this period the great master Leonardo Da Vinci studied such phenomena as well, and he is considered as the first individual who studied friction systematically [48], [73].

In more recent times, the importance of friction on economy and energy consumption was emphasized particularly in 1966 in the famous report by H. P. Jost [81] for the British government, where the term tribology was introduced and it was concluded and emphasised that friction and wear have a significant cost on UK economy. More than 50 years later, the importance of acknowledging the effects of friction is increasingly present in modern technologies [68]. The growing concerns over energy consumption and environmental sustainability requires nowadays new ideas and multidisciplinary approaches to overcoming the still not fully grasped nature of friction. Contemporary reports [68], [186] emphasize, thus, the impact of friction and wear on energy consumption, economic expenditure, and CO₂ emissions present on the global scale, with estimates that ~23% (119 EJ) of world's total energy consumption originates from tribological contacts. In this total, 20% (103 EJ) is used to overcome friction, and 3% (16 EJ) to remanufacture worn parts and spare equipment due to wear and wear-related failures [68], [186]. Taking advantage of the new tribology technologies

(surfaces, materials, and lubrication technologies) for friction reduction and wear protection in mechanical systems, have, therefore, the potential to produce enormous energy savings [68], [186].

Regarding the development of corresponding friction models, especially important is the work of the French physicist Guillaume Amontons, that postulated the “laws” of friction - stating that the friction force is proportional to normal load and independent of the contact area [48], [174], as well as, afterwards, the work of Charles Augustin de Coulomb that added the rule that friction is independent of sliding velocity [48], [174], thus providing first modern contributions to the scientific treatise on friction. These conclusions are based on empirical observations and, even though often called laws, there is no fundamental principle that forbids a system to exhibit friction properties that do not obey them. In any case, these observations can be summarized by the equation [48], [174]:

$$\mu = \frac{dF_f}{dF_N} \quad (2.1)$$

where μ represents the dimensionless friction coefficient corresponding to the ratio of the friction force F_f and the applied normal force F_N .

Further developments of science, and industry-based society in general, led to a publication by Richard Stribeck, a German scientist and engineer, who defined a curve that relates friction with viscosity, speed and load [48], [174]. A modern-age breakthrough in tribology during the 1950s was then given by Philip Bowden and David Tabor [27], with their physical explanations of the laws of friction, where they determined that the true area of contact is a small percentage of the apparent contact area, and that true contact is formed by the asperities on the surfaces of the bodies in relative motion [62]. As the applied normal force increases, more asperities come into contact, while the average area of each asperity also increases. Generally, in tribological terms, any mechanical system with technical surfaces in contact and in relative motion can be seen as a tribo-system with rough surfaces that comprise the real contact area A_R given, as shown in Figure 2.1 that presents the basis for all modern research in tribology, by the contacting asperities.

The resulting conditions of the tribo-system are defined by numerous characteristics including the materials in contact, their mechanical properties, operational parameters such as velocity, lubrication and roughness, as well as the interaction parameters comprising the interaction potential and atomic-scale interactions in the asperities themselves [61], [62], [80]. The multiple concurrent effects that influence the interactions in a single asperity contact are

the cause of the significant difficulties in modelling frictional phenomena. At present, one is thus limited to observing and mathematically describing the single asperity contact depending on the scale of interest, whereas the different dominant mechanisms can include plastic deformation of the involved materials at high contact pressures, elastic-plastic regimes, and fully elastic deformation, but also the lubrication conditions, the properties of the used lubricant(s), third-body interaction, wear-induced particles and cold welding, or even nanoscale effects of adsorbed water layers' meniscus and the nanoscale physical properties of the surfaces in contact.

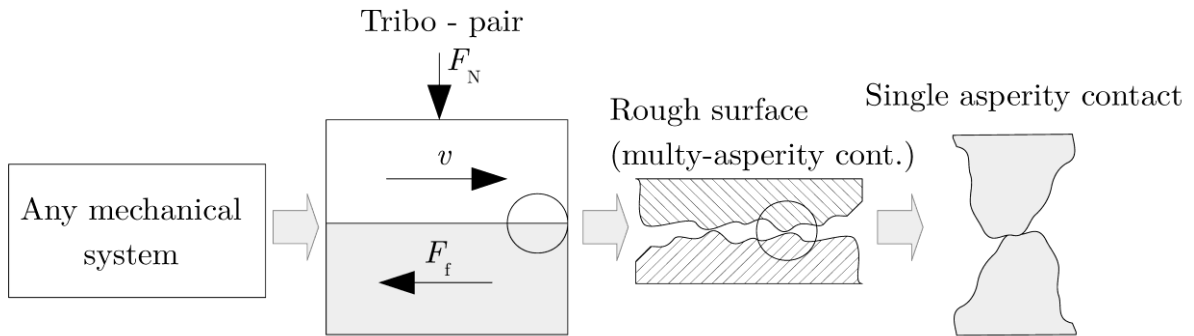


Figure 2.1 Friction between two surfaces is governed by the behaviour in a single asperity contact.

The development of contact mechanics models describing single asperity contacts have allowed showing that the latter are indeed the main source of the macro-scale frictional behaviour. In synthesis, single asperity models originate from Hertz's solution relating to the elastic contact between a sphere and a planar surface and between two spheres, where equations for the determination of the contact radius and the indentation depth were derived, but, adhesion and surface forces in the contact region are neglected [77]. Since adhesive effects play an important role at the single asperity contacts' scales, an extension of the Hertz model was elaborated by Johnson, Kendall and Roberts [80], resulting in the well-known JKR theory. The basic contribution of this model is the inclusion of the adhesive effect within the contact zone, while the adhesive interaction outside the contact zone are neglected. The JKR method considers the surface energy of adhesion of both involved surfaces, resulting in a real area of contact A_R larger than that defined by the Hertz model [77], [134]:

$$A_R = \left(\frac{3}{4} \frac{\pi R^*}{E^*} \left[F_N + 3\pi R^* \lambda + \sqrt{6\pi R^* \lambda F_N + 3\pi R^* \lambda^2} \right] \right)^{\frac{2}{3}} \quad (2.2)$$

where λ is the effective surface energy of adhesion of the involved surfaces, R^* is the effective

contact radius, and E^* the effective Young's modulus. The two last quantities are defined as [77], [134]:

$$R^* = \frac{R_1 R_2}{R_1 + R_2} \quad (2.3)$$

$$\frac{1}{E^*} = \frac{1 - \nu_1^2}{E_1} + \frac{1 - \nu_2^2}{E_2} \quad (2.4)$$

where R_i are the radii of the spheres in contact, E_i are the respective Young's moduli while ν_i are the corresponding Poisson ratios of the two bodies. From these relations, and considering the effects of adhesion, the JKR model predicts the force needed to remove the bodies from contact, i.e., the pull-out force, defined as [77], [134]:

$$F_P^{JKR} = -\frac{3}{2} \pi \lambda R^* \quad (2.5)$$

By expanding the Hertz theory with adhesive effects, the JKR theory enables, thus, to explain the formation of contacts during the unloading cycle, i.e., the occurrence of the negative normal force.

An alternative thermodynamic approach based still on Hertz theory, was, in turn, used by Derjaguin, Muller and Toporov (DMT) [46], where the attractive adhesive force is added to the normal load so as to obtain the corrected indentation depth and contact area. Due to a finite effect of adhesion when the applied load is zero, the DMT model leads to a so-called sub-linear dependence of the friction force on the exerted normal load, which is an observation of non-vanishing friction at below-zero normal load due to further existence of adhesive forces in the contact even though the applied load is zero, thus the resulting sphere-plane model pull-out force can thus be expressed as [46]:

$$F_P^{DMT} = -2\pi \lambda R^* \quad (2.6)$$

The DMT model was experimentally proven first by Enachescu et al. [51] on a hydrogen-terminated diamond (111)/tungsten carbide mono-asperity interface using an ultra-high vacuum atomic force microscope (UHV-AFM). By measuring the local conductance in contact as a function of the applied load, it was hence shown that, for the considered extremely hard single asperity contact, the load dependence is perfectly described by the DMT continuum mechanics model. Since the DMT model takes into account the surface forces outside of the contact, but not the deformations due to these forces, it is suited well when dealing with rigid contacts and low surface energies, while the JKR model is more appropriate for more compliant contacts and higher surface energies [162].

2.1. Nanotribology and M(N)EMS

In the above section, a brief basis of fundamental tribological terms was given, providing insight into the imperative importance of single-asperity contact behaviour. In fact, the study of single asperity interactions is an important link between the macro- and the nano world. The impact of surface forces is clearly noticeable in friction and adhesion with micro- and nanocontacts. In particular, the adhesion force between two objects can originate from a combination of different contributions such as the van der Waals forces, the electrostatic force, chemical and hydrogen bonding forces, capillary forces, and others [34], [80]. The interaction between two surfaces in contact is therefore a complex phenomenon induced by a great variety of interactions that must hence be considered.

Friction cannot be studied without considering wear as well. Friction, wear and adhesion are, in fact, intimately related and, to understand what happens at the macroscopic level, the non-equilibrium processes occurring at the molecular level must be considered [32], [34].

Novel experimental techniques such as the Atomic Force Microscope (AFM) or the Scanning Probe Microscope (SPM), which is used in this work and will be comprehensively elaborated below, allow looking down to the atomic scale and provide means to approximate closely the conditions of the single asperity contact [23], [60], [72]. Other methods for researching the same complex phenomena can be based on computational simulations on the atomic level, i.e., on Molecular Dynamics (MD) simulations of atomistic behaviour that have shown that, depending on the atomic-level geometry of the contact, deviations from a continuum approach can occur [55], [135]. In addition to the general shape or the nanoscale roughness of the contacting bodies, the relative arrangement of atoms at the interface can have thus a strong impact on nanoscale friction and area-load relations [13], [109], [134].

Friction and adhesion are also a widely recognised cause of failure of micro- and nano-electromechanical devices (MEMS and NEMS), comprising relative motion of the constituting elements, inferring an even greater importance of their study [15], [17], [26], [156]. In fact, miniaturisation implies a growth of the surface-to-volume ratio, thus inducing a scale-dependent increase of the importance of friction and adhesion and their prevalence over volumetric forces. Tribological phenomena have slowed the development of micro- and nanoelectromechanical systems (M(N)EMS), limiting in some instances their commercial application to those systems that do not include contacting sliding interfaces [17]. As a result of large surface forces, M(N)EMS components tend even to stick together. This “stiction” behaviour poses an engineering problem both for the device itself and its design process.

Despite many important advances, failure is thus, unfortunately, unavoidable for most MEMS devices (e.g., gears, locks, shutters, optical switches, etc.) that incorporate sliding interfaces [15], [58], [156]. What is more, in ambient conditions, due to the condensation of humidity, the surface might be covered by a thin layer of water. The adsorbed water molecules influence then the contact between the two solids, modifying their adhesion and friction. From a general point of view, the wetting phenomenon corresponds to the equilibrium between a solid phase on which are deposited atoms or molecules of a liquid phase, and the whole is surrounded by atoms or molecules of a gaseous phase. The molecules of water arrange themselves in the gaps and small cavities between the surface asperities. They form capillaries that bind the neighbouring surfaces. For constant environmental conditions, the size of the capillary depends on the geometry and chemistry of the surfaces [8], [11], [34].

All these phenomena are taken into account in nanotribology where, when compared to conventional tribology and microtribology with notable surface wear and dominating bulk material properties, light load conditions and nanoscale surface properties and interactions dominate the resulting tribological phenomena. Nanoscale tribology studies are thus critical for micro- and nanostructure analyses but, by enabling an in-depth insight into the fundamental contact behaviour, they also provide an invaluable bridge between science and engineering [17], [134].

Devices characterised by micro- and nanopositioning precision are often required in precision engineering as well as in micro- and nanosystems' technologies. The accuracy of these devices is again often limited by frictional effects with their stochastic nonlinear characteristics [14], [111]. In modern applications of precision machines and positioning devices, it was then experimentally proven several times that the generalized approximation models of friction show satisfactory performances for control purposes which has been often proven experimentally [5], [82], [83]. These models, such as the Generalized Maxwell-Slip (GMS), the Lu-Gre and others [5], [7], [131], [132], are based on generalization and system identification but they do not provide sufficiently good results when true nanometric positioning is aimed at [47], [63], [150]. While frictional phenomena on the macro- and meso-scales are well described and their effects can be simulated via suitable models [5], [82], [131], [132], [176], [182], as well as generally efficiently compensated by employing proper control techniques [83], [99], [111], [182], the available friction models do not consider true nanometric motion or scaling phenomena related to friction.

The conventional models provide, hence, often insufficient precision for micron- or submicron-size devices, where the mechanisms influencing friction are different from that

dominating macroscale friction. Nanotribology is hence once more an essential ingredient in establishing the basic understanding, not only in the fundamental tribological sense, but also relative to interfacial phenomena in MEMS and NEMS devices, computer storage devices and other ultra-high precision applications [17], [58].

2.2. State-of-the-Art in Experimental Nanotribology

Experimental research of friction at the nano- and atomic levels is carried out mainly in the last three decades or so, upon the development of new experimental techniques, such as the Scanning Tunneling Microscope (STM) by Nobel prize winners G. Binnig and H. Rohrer [24], [25]. These breakthroughs started a scientific revolution in the field, and soon afterwards the AFM was developed by the same team [23]. The experimental and theoretical studies of friction on the atomic scale received therefore a significant impetus.

Among the first published studies of the characteristics of friction at the atomic level between the sharp tip of tungsten and a graphite substrate, conducted by using AFM, is that published by Mate et al. in 1987 [109]. Very low forces ($<10^{-4}$ N) are used in this experiment, and the average coefficient of friction is found to be 0.012. This experiment allowed also showing the stick-slip effect at the atomic level, with a period equal to the lattice constants of graphite. After this early work, many researchers headed in the direction of analysing friction at the atomic level. Akamine et al. 1990 used hence an AFM device to measure, at the normal force level of the order of 10^{-7} N, the characteristic stick-slip effect of gold on mineral silicate (mica), and reported on the resulting characteristic saw-tooth dependence of force vs. displacement [3]. By using an AFM, Ruan and Bushan in 1994 employed a Si_3N_4 tip to investigate the influence of surface roughness on the tribological properties of graphite and concluded that the coefficient of friction varies with different surface roughness of the analysed substrates. The measured friction coefficient was in this case found to be 0.01 for the RMS (Root Mean Square) roughness of 10 nm, and 0.03 for the RMS roughness of 140 nm. This result was explained by the loss of orientation of the substrate with large surface roughness [142]. Fujisawa et al. in 1993 explored the stick-slip behaviour at the atomic level between mica and Si_3N_4 . They used different directions of scanning to investigate the influence of lattice orientation to vertical and lateral forces, and observed the characteristic vertical force in the shape of a square wave, as well as the characteristic lateral forces as a saw-toothed wave during the movement in the stick-slip regime [54]. Using AFM, Tambe and Bushan in 2004 studied the effect of the scale, i.e., the size of the sample on the tribological characteristics, and

concluded that the friction coefficient decreased by reducing the observed scale. The friction coefficient of Si (111) in a macroscale experiment, with a normal force of 1 N, was 0.6, while the friction coefficient reported for the nanoscale experiment, with normal forces in the range of 1-15 μN , was reduced by almost 10 times to the value of 0.05. This drastic change in the coefficient of friction was explained to be the consequence of different mechanisms of friction at the various considered scales, as well as of the different conditions of contact between the two materials (the adhesion effects) [156]. The influence of the sliding speed on the tribological properties of the materials at the nanoscale was investigated by Tambe and Bushan in 2005 [157]. Their study was performed on a variety of materials involving lubrication such as monocrystalline Si (100) with a layer of oxide, polymers PDMS (poly(dimethylsiloxane)) and PMMA (poly- (methylmethacrylate)) coated with a DLC (Diamond-Like Carbon), with a layer of various lubricants such as PFPE (perfluoropolyether) based Z-DOL and Z-15 (commercial lubricants), and a monolayer hexadecanethiol (HDT) which are used in practice as lubricants for magnetic disks. For pure Si the frictional force was reduced from 20 nN to 15 nN, while in the case of Si with a Z-15 coating, the friction force was reduced from 5 to 3 nN, while, due to the formation of a meniscus of condensed water molecules, a corresponding increase in sliding velocity from 5 to 1000 $\mu\text{m/s}$ was also induced. Bushan and Sundararajan (1998) studied the effects of relative humidity and the radius of the tip of the probe on the nanotribological behaviour of the sample. The primary purpose of changing the apex radius of the tip in the experiments, was to change the contact surface. Their results showed that the friction coefficient increased with higher humidity and larger contact surfaces [20]. By using a micro-tribotester and an AFM, Sung et al. (2003) carried out an investigation of the effects of the contact angle between the tip and the surface on the friction coefficient, and concluded that the tribological characteristics of the materials at the nanoscale are highly dependent on the structure of the surface, on topology and on the geometry of the contact [155].

Complex effects involved in nanoscale contacts comprise, therefore, effects of scale, adhesion, wear, normal load, surface roughness and sliding velocity or the properties of the involved materials – that all form the tribological system. It is often necessary to study also the effects of temperature, humidity, and even the history of the contact at the observed surface, and the instruments needed to perform this research are today readily commercially available with all the accompanying computer equipment and associated control and experimental set-up peripherals.

To further understand the phenomenon of friction and adhesion at the nanoscale level, many influential scientific groups around the world are thus performing a vast number of

measurements. Effects analysed in more recent studies in the field are concentrated on frictional behaviour of 2D materials such as single-layer graphene (SLG). Chu et al. studied hence the effect of confined water between nanolayers of SLG, and reported variations of the friction force and varying positive and negative velocity dependences [40]. Milne et al. reported, in turn, that the adhesive forces in vacuum conditions are dependent on the sliding history between the analysed asperities [116]. Newer studies indicate, moreover, a very intricate, often nonlinear, dependence of friction in the micro- and nanoscales on velocity and temperature but even on the normal loads [14].

From this comprehensive but necessarily brief overview given in this chapter, it can be concluded that the current state of nanoscale friction research is still relatively limited to studies of the influence of a single variable parameter on the friction force, and that these often report conflicting conclusions. Proposed models resulting from the experimental findings are even more rare, and mostly limited to micro- and macroscale experiments [152]. It is therefore clear that this field of research will greatly benefit from the work reported in this thesis where a structured, multi-variable, experimental analysis of different materials, and a novel predictive mathematical model allowing to specifically characterize the main variables' effects on nanoscale friction, are proposed. In the next section of the work an exhaustive description of the main constituents of such an innovative and powerful tool will hence be given.

3. Experimental Measurements of Nanoscale Friction

Based on a thorough study of the current state-of-the-art related to the experimental methodology applicable to nanotribological studies given in Chapter 2 of this work, a structured transdisciplinary method for the experimental determination of the value of the friction force in the nanometric domain on thin film samples is developed and presented in this part of the thesis¹. As described in Chapter 2, a clear need for the extension of SPM experimental studies to the concurrent validation of the influence of multiple variable parameters on nanoscale friction is evident [107], [163]. The dependence of nanoscale friction on multiple process parameters on these scales, comprising normal forces, sliding velocities and temperature, is thus studied here experimentally via the Atomic Force Microscope (AFM) in the Lateral Force Microscopy (LFM) mode, which is described below. The procedure used to characterise the stiffness of the used probes, and especially the influence of adhesion on the obtained results, is thoroughly described. The developed measurement methodology, based on elaborated design of experiments algorithms, is successfully implemented to concurrently characterise the dependence of nanoscale friction in the multidimensional space defined by the considered process parameters. This allows establishing a novel methodology extending the current state-of-the-art of nanotribological studies, since it allows not only gathering experimental data, but doing it systematically and concurrently for several influencing variables at once, and including important effects in the calibration procedures and wear effect anticipation. This, in turn, creates the basis for determining generalizing correlations of the value of nanoscale friction in any multidimensional experimental space that will be demonstrated in Chapters 4 and 5 of this thesis. All these creates the preconditions to eventually extend the available macro- and mesoscale friction models to a true multiscale model that will considerably improve the design, modelling and production of MEMS devices, but also of all precision positioning systems aimed at micro- and nanometric accuracy and precision.

¹ Part of the work described in this chapter was published recently by the author of the thesis and his collaborators in a peer-reviewed scientific paper [128], which was produced and published as part of the obligations foreseen in the curriculum of the doctoral study of the Faculty of Engineering of the University of Rijeka, Croatia, and hence this chapter is based, partly directly derived and cited from this work.

3.1. Used Experimental Apparatus and Methodology

The measurements of the values of the friction force on a careful selection of thin film samples are performed in this work by using the Bruker Dimension Icon SPM [160] available at the Centre for Micro- and Nanosciences and Technologies (NANORI) of the University of Rijeka, Croatia [159], while they are controlled by using the respective NanoScope hardware and software (Figure 3.1).

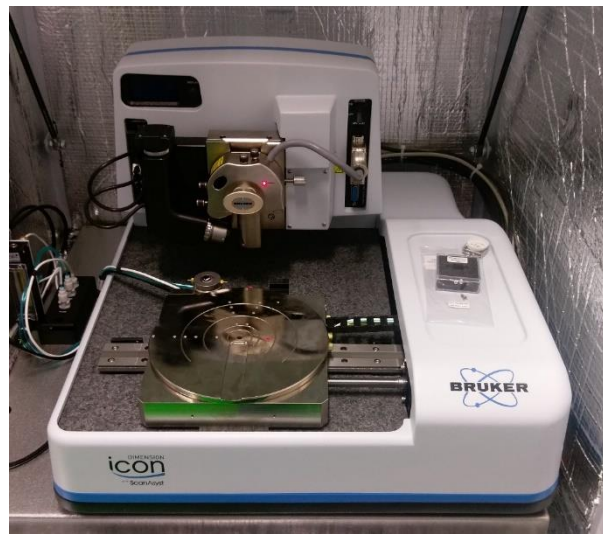


Figure 3.1 Bruker Dimension Icon Scanning Probe Microscope at the NANORI lab [160].

3.2. Sampling of the Experimental Design Space

The distribution of measurement points in the considered experimental space is determined in this work by using a structured design of experiments (DoE) approach. Standard DoE methods such as (full) factorial design, split-plot design, linear regression, Monte Carlo, Taguchi, Box-Behnken and others [43], [66], [110], [152] are, however, poorly suited to obtain a detailed insight into the studied multidimensional stochastic phenomenon. In fact, these approaches are commonly aimed at conventional industrial practises where results are generally limited to the values of the control variables inducing local extrema of the dependent variable [66]. Since recent studies indicate, in turn, marked advantages in terms of the space filling properties of an approach where DoE is conducted by using centroidal Voronoi tessellation (CVT) sampling [4], [50], [53], [84], [140], which is efficiently implemented in the commercially available GoSumD software [2], CVT is used in this work to determine the sample points in the considered multidimensional process parameters space [128], [129]. In fact, the parameters influencing nanoscale friction concurrently considered in this work, and

their respective value ranges, are:

- ※ normal force $F_N = 10 \text{ nN} \dots 150 \text{ nN}$,
- ※ sliding velocity $v = 5 \text{ nm/s} \dots 500 \text{ nm/s}$, and
- ※ temperature $\vartheta = 20 \text{ }^\circ\text{C} \dots 80 \text{ }^\circ\text{C}$.

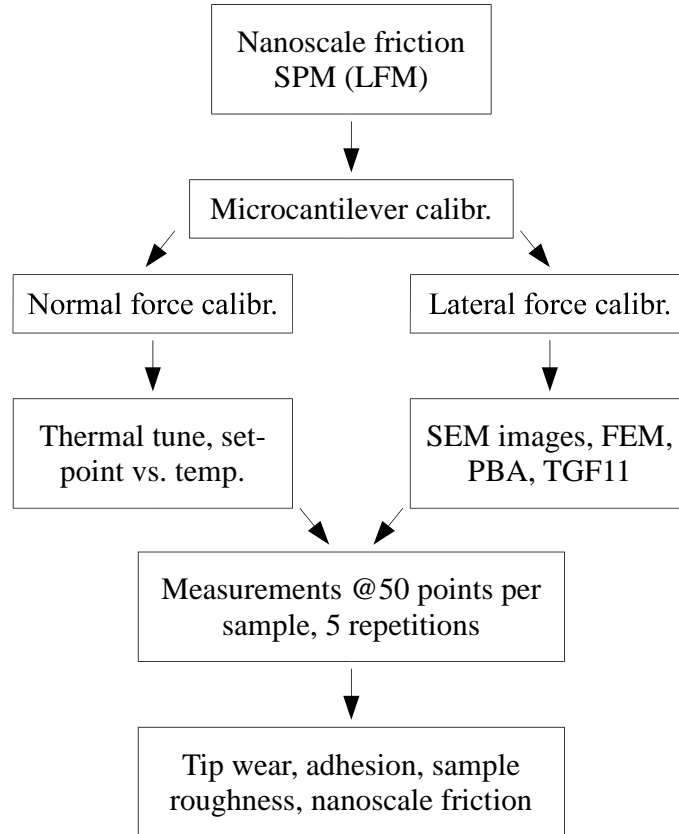


Figure 3.2 Proposed experimental methodology for obtaining concurrently the dependence of nanoscale friction on several influencing parameters by using LFM [128].

Given then a set of desired points (“generators”) and a distance function from each generator to its mass centroid, Voronoi tessellations are subdivisions of the experimental space. The variation of the influencing parameters is therefore defined via a discrete uniform distribution, i.e., a distribution where a finite number n of homogeneously spaced values has the same probability to be observed [2], [4], [50], [84], [140]. The integer parameters of the distribution can thus be specified as:

$$n = b - a + 1 \quad (3.1)$$

where a and b are the lower and upper bounds of the values of the considered influencing parameter. The distribution of sample points is thus generated by a discrete probability distribution k attained by using a probability mass function $f(k)$ defined in equation (3.2). On

the other hand, the cumulative distribution function $F(k)$, given by equation (3.3), is used to specify the placement of multivariate random variables (i.e., the points in the considered multi-dimensional influencing parameters' space) [50]:

$$f(k) = \begin{cases} 1/n & \text{if } a \leq k \leq b \\ 0 & \text{otherwise} \end{cases} \quad (3.2)$$

$$F(k) = \begin{cases} 0 & \text{if } k < a \\ \frac{[k] - a + 1}{n} & \text{if } a \leq k < b \\ 1 & \text{if } k > b \end{cases} \quad (3.3)$$

Given a density function, the centre of mass of each subset making up the Voronoi tessellation can thus be determined. Since, however, generally the locations of the generators do not coincide with the centres of mass of the data subsets, distinct Voronoi tessellations called CVTs are used to assure the convergence of these locations [128], [129] and determine finally the 50 measurement points aimed at in the considered multidimensional experimental space defined by the range of variation of the process parameters: F_N , ν and \mathcal{G} . The thus obtained values of these influencing parameters in the required 50 sampling points are reported in Appendix A at the end of the thesis [128].

3.3. Synthesis of the Thin-film Samples

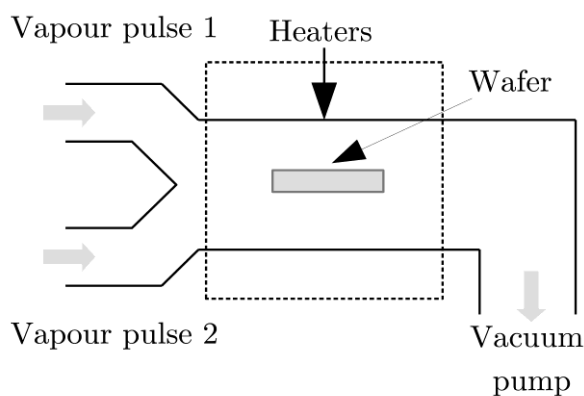
The experimentally analysed samples in this work are carefully selected to be representative of specific characteristic features of vastly used thin-films and comprise: aluminium oxide (alumina or Al_2O_3), titanium dioxide (TiO_2), molybdenum disulphide (MoS_2), aluminium (Al) and X39CrMo17-1 stainless steel (denoted further on, for brevity, as SS). In fact, Al_2O_3 has not only good mechanical properties (especially hardness and strength), for which it is broadly used in MEMS technology (e.g., in packaging of MEMS devices), as well as in integrated circuit (IC) technology, but it is also used in thin film form for coatings in implants, for insulating applications, and when wear is to be minimised. On the other hand, TiO_2 is broadly used in MEMS technology for optical elements such as filters and mirrors, or as a biocompatible coating in implants (e.g., dental ones). MoS_2 is a typical sample of a material with good lubricating properties, although it is also used in nanotechnology for its electrical properties. Aluminium, next to being the most widely used non-ferrous metal, is used as thin film for electrical contacts and interconnectors, for reflective surfaces (as e.g., in the Texas Instruments'

Digital Light Processor (DLP) device) or in micromechanical components. Finally, SS is chosen as the most widely used general-purpose engineering material.

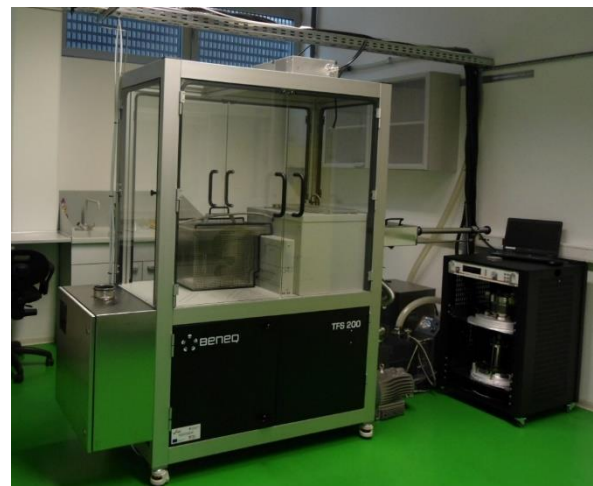
3.3.1. Atomic Layer Deposition (ALD)

Atomic Layer Deposition (ALD – principally shown in Figure 3.3a) is a vapour phase technique (i.e., a variant of the chemical vapour deposition (CVD) techniques) enabling the deposition of thin films of a wide range of materials, such as metal oxides and noble metals, depending on the used precursor. The method relies on sequential, self-limiting chemical reactions of precursor species. It is most often used in industrial and research applications for coating M(N)EMS and various micrometre-sized structures [17]. All samples obtained in the frame of this work are deposited on a silicon (Si) wafer.

The Al_2O_3 and TiO_2 samples used in this work are hence synthesized in the thermal mode on a Beneq TFS 200 ALD device (Figure 3.3b) [160] at the NANORI facilities of the University of Rijeka, Croatia [159]. The employed precursors are, respectively, trimethylaluminium ($\text{Al}(\text{CH}_3)_3$) and titanium-tetrachloride (TiCl_4) in combination with water vapour (H_2O), while high-purity nitrogen (purity 6.0) is used as the purging gas. The deposition of Al_2O_3 is carried out at 200 °C with the following ALD cycle: a 180 ms $\text{Al}(\text{CH}_3)_3$ pulse is followed by a 1 s purge, then a 180 ms H_2O pulse and, again, a 1 s purge. For the TiO_2 deposition at 150 °C, the pulsing times for TiCl_4 and H_2O are, respectively, 250 ms and 180 ms, followed by purging cycles of, respectively, 3 and 2 s [128], [129].



(a)



(b)

Figure 3.3 Scheme of the ALD process (a) and the used Beneq ALD device (b) [128].

3.3.2. Pulsed Laser Deposition (PLD)

Pulsed Laser Deposition (PLD), shown principally in Figure 3.4a, and depicted in the photograph of the herein factually used device at the Institute of Physics in Zagreb, Croatia, in Figure 3.4b, is a physical vapour deposition (PVD) technique where high power laser pulses in a vacuum chamber are used to melt, vaporize and ionize the surface of the target material. This ablation produces a plasma plume that rapidly expands away from the target, while the ablated material is collected on the substrate surface (silicon wafer). To control the deposition process, the Optical Emission Spectroscopy (OES) method is used for *in situ* characterization of the obtained plasma, which allows obtaining plasma properties, and is thus used to optimize the pulsed laser characteristics for obtaining the desired atomic structure of the deposited thin film. The technique is widely used for the production of a wide range of superconductive and insulating circuit components, as well as for biocompatible and medical applications. Its main advantage with respect to the ALD method is that PLD enables the stoichiometric transfer of material from the target to the substrates' surface, allowing a precise chemical composition of the used target material to be deposited in the form of a thin film [112], [170].

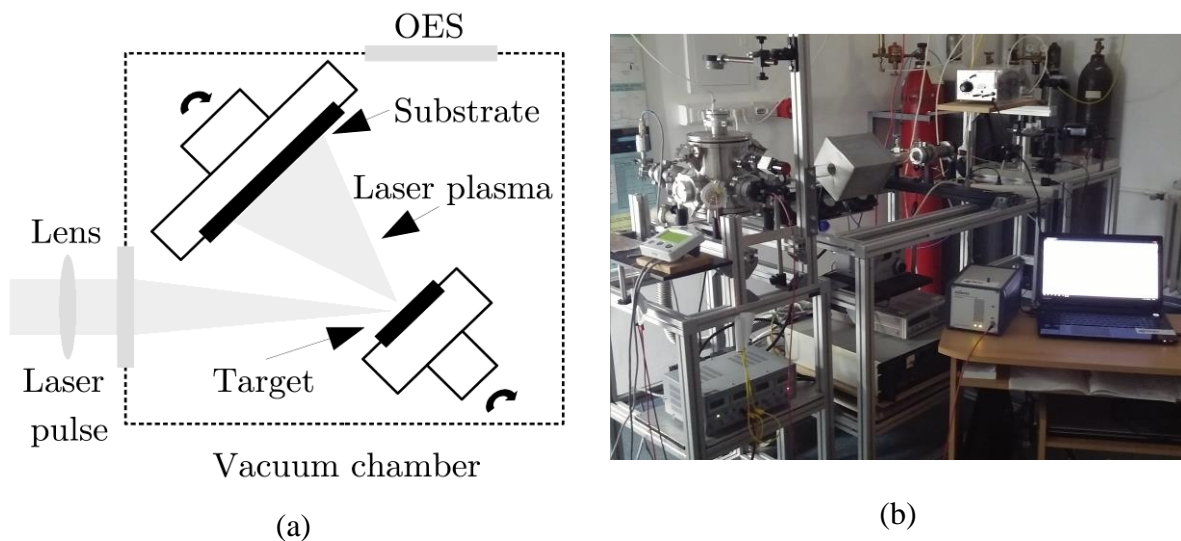


Figure 3.4 Scheme of the PLD process (a) and the factual PLD set-up used in the work (b) [128].

This property of the PLD method is used in this work to synthesize in the form of a thin film the martensitic SS X39CrMo17-1 characterised by a complex chemical composition. Other samples obtained by using PLD are the 99.99% pure Al, and the 99.9% pure MoS₂ obtained from Testbourne Ltd, UK. The Nd:YAG laser parameters employed in the thus used PLD process at the Institute of Physics in Zagreb, Croatia [187], are: wavelength 1064 nm, pulse

duration 4 ns at a 5 Hz repetition rate and with a pulse energy of 340 mJ. Laser pulses are focused then on the target that is parallel to the Si substrate and inclined by 45° with respect to the impinging laser beam, yielding a fluence of 18 J/cm². 5,000 laser pulses are finally used to obtain the desired film thickness of several tens of nanometres. The distance between the target, which is rotated to avoid drilling and increase films' homogeneity, and the substrate, is 3 cm. Both the target holder and the substrate are kept on a floating potential at room temperature in a high vacuum (< 10⁻³ mbar) environment [128], [129].

3.4. Characterization of the Samples

In order to determine their properties, namely the thickness, surface morphology, and composition, the obtained samples are thoroughly characterized before the LFM measurements by using X-Ray Photoelectron Spectroscopy and Secondary Ion Mass Spectrometry.

3.4.1. X-Ray Photoelectron Spectroscopy

X-ray photoelectron spectroscopy (XPS) is a widely used method for the characterization of surfaces, which provides valuable quantitative and chemical state information. The analysis is accomplished in this frame by exciting the surface of the sample with mono-energetic x-rays causing photoelectrons to be emitted from it. The energy of the emitted photoelectrons is then measured by an electron energy analyser. The chemical state, elemental identity, and the quantity of the detected element can be determined from the binding energy and intensity of the resulting photoelectron peak. The obtained spectra allow thus confirming the elemental characteristics of the synthesized films [128].

The analyses in the frame of this work are done on a SPECS XPS device [172], depicted on Figure 3.5, available once more at the NANORI premises of the University of Rijeka, Croatia [159].

The XPS spectra are hence measured via the spectrometer of the XPS device, which is equipped with a hemispherical energy analyser PHOIBOS 100 MCD-5 and a monochromatized source of Al K α X-rays of up to 1486.74 eV. The typical XPS vacuum level during the performed analyses is in the 10⁻⁹ mbar range. The obtained photoemission spectra, whose background is subtracted, are finally fitted with sets of Gaussian–Lorentzian functions [71], [118]. The measurements allow thus establishing that indeed the sample films are of high purity, but also that on their surface a thin (few atomic monolayers) oxide film is formed. The latter is characterised by a spectral contribution induced by O-H or O-C bonds; there is also a tendency

towards the formation of surface hydroxide OH groups [126].



Figure 3.5 Used Specs X-ray Photoelectron Spectroscopy (XPS) equipped with a hemispherical energy analyser PHOIBOS 100 MCD-5 [159].

3.4.2. Secondary Ion Mass Spectrometry

The Secondary Ion Mass Spectroscopy (SIMS) method is based on using an internally generated beam of ions focused on the surface of the sample to generate, via sputtering, secondary ions. By analysing the generated secondary ions with a mass spectrometer, information about the elemental, isotopic and molecular composition of the upper layers of the analysed sample are hence obtained. The results of the analyses provide information about the elemental composition (down to the ppb level) in dependence also from the depth from the surface, thus enabling the determination of the obtained films' thicknesses [102], [128].

The used Hiden SIMS device [160], available again at the NANORI premises of the University of Rijeka, Croatia [159], is equipped with two ion guns, a quadrupole mass analyser and a residual gas analyser (RGA), allowing thus in-depth profiles to be obtained by using 3 keV Ar^+ primary ion beams impinging at 45° , while collecting the resulting positive secondary ions.

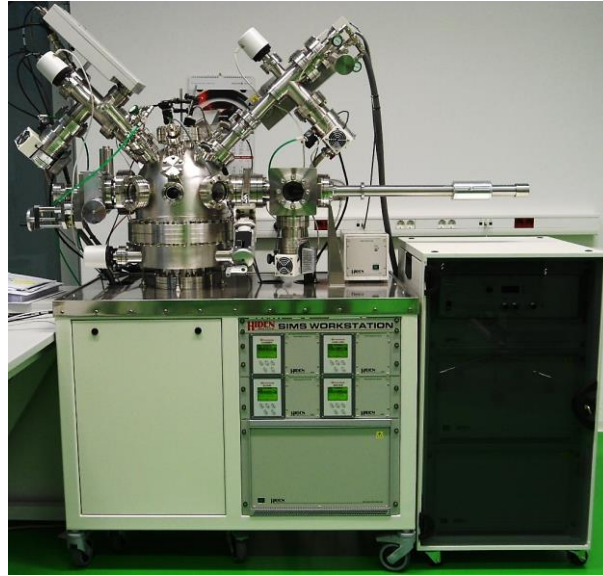


Figure 3.6 Used Hidden Secondary Ion Mass Spectrometer (SIMS) at the NANORI [159].

The depth scale of the SIMS craters is, in turn, determined by employing the Dektak XT stylus surface profilometer [160].

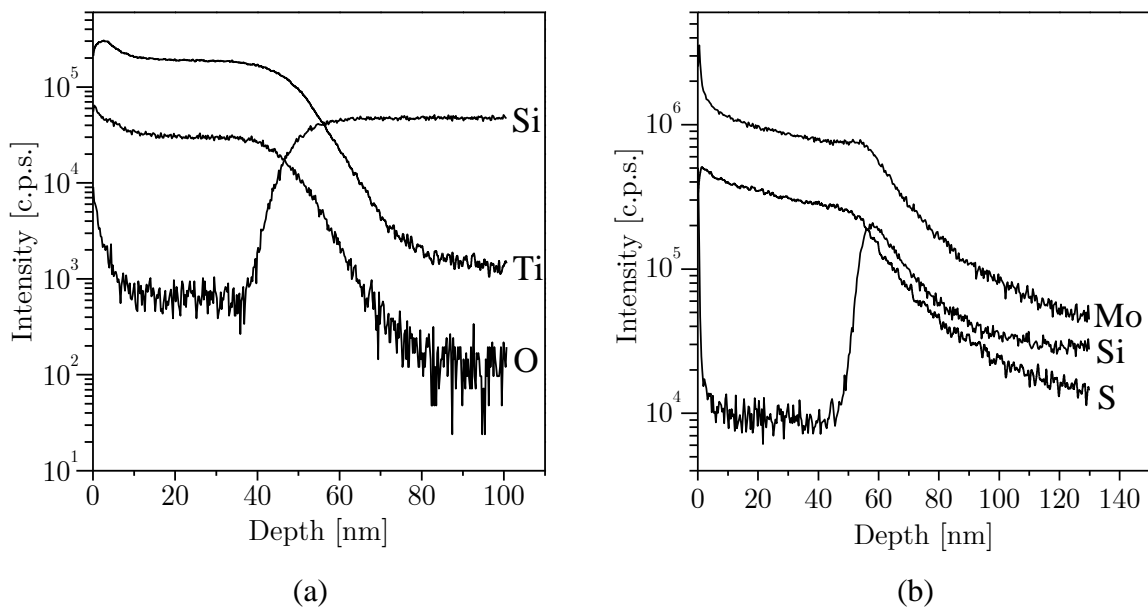


Figure 3.7 Examples of SIMS spectra for thin-films obtained via ALD (TiO_2 - a), and PLD (MoS_2 - b) [128].

As shown in Figure 3.7 for a sample obtained by using ALD (i.e., the TiO_2 film as shown in Figure 3.7a) and a sample obtained by employing PLD (i.e., the MoS_2 film as shown in Figure 3.7b), the obtained results allow hence confirming that the elemental distribution of the thin film constituents along the depths of the used samples is quite constant, revealing once more their good homogeneity. What is more, these results allow establishing that the thickness of the

used thin films is, respectively, 20 nm for Al₂O₃, 50 nm for TiO₂, 100 nm for Al, 65 nm for MoS₂ and 100 nm for SS sample, while the respective constituents permeate the Si substrate also deeper [128].

3.5. Experimental Measurement of the Nanoscale Friction Force

The measurement of the friction force is done on the thus synthesized samples in the 50 sampling points determined by employing the above-described DoE procedure, are then conducted by employing the contact mode of the SPM instrument, as shown principally in Figure 3.8a. In this measurement configuration the tip at the apex of a micro-cantilever (hereafter the respective assembly is designated as “probe”), is in perpetual contact with the surface of the sample as governed by the control parameters of probe’s piezo actuator. A laser is used to acquire the information about cantilever’s deflection in the normal (bending) direction as well as in the lateral (torsional) direction, i.e., by providing a signal onto a position-sensitive photo detector (PSPD) with four channels (A-D). In the raster scanning mode typical of the Lateral Force Microscopy (LFM) measurements, normal deflection of the probe is hence detected by the PSPD system separately from the lateral motion. LFM is hence used particularly for friction force spectroscopy, enabling means to minimise the cross-talk between the PSPD signals and thus to obtain, in terms of the signal magnitude, the clearest determination of the friction force [17].

As shown in Figure 3.8b, the signals obtained onto the PSPD dependant on the torsional deflection of the probe, while the cantilever travels back and forth on a predesignated distance over the sample, are induced by surface topology features and friction. The resulting voltages are converted to values of the lateral (transversal) force exerted on the sample by calibrating the mechanical behaviour of the probe itself, as it will be explained in detail below.

Dry (unlubricated) contacts considered in this work are hence characterised by using LFM measurements on 500 x 500 nm² surfaces of the analysed samples in air, thus approaching the habitual technological conditions. All the samples are then scanned in the determined 50 measurement points along 256 scan lines with varying influencing parameters (F_N , v and θ), while, for uncertainty and error analysis, in each point the measurements are repeated five times for each 500 nm² measured area with a $\pm 100 \mu\text{m}$ distance from each other.

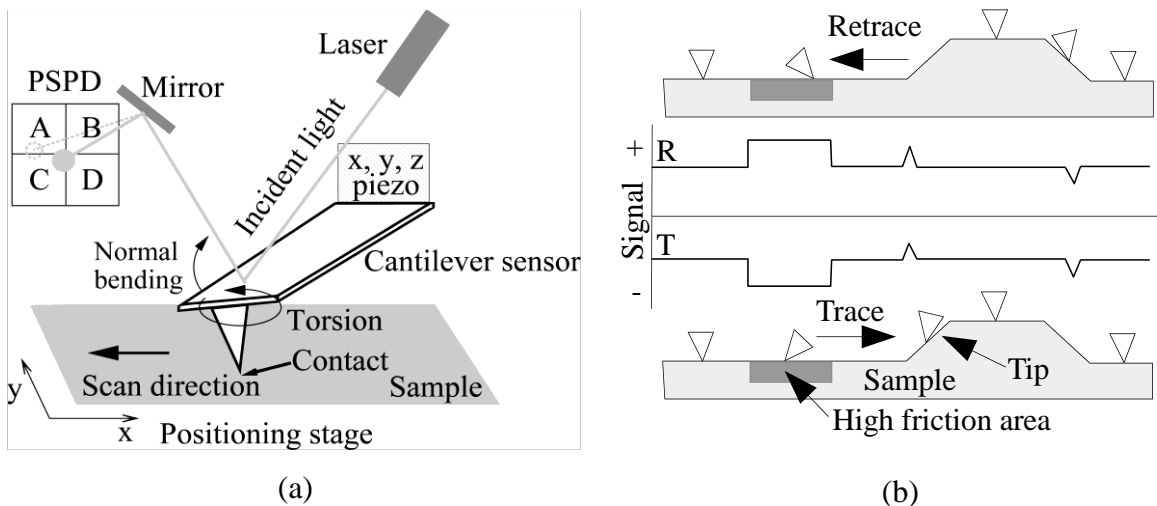


Figure 3.8 Scheme of the SPM (LFM) measurement configuration (a) [128], and schematics of the obtained friction signals when the tip of the probe traverses across the surface with topology and friction variations (b - adapted from [17]).

3.5.1. Calibration of the Probes

The probes used in this thesis are Bruker's SNL-10 high-resolution probes of type D (for the smaller values of the considered normal forces F_N) or of type A (for the largest considered F_N values), both with a Si tip mounted on a triangular Si_3N_4 cantilever [31]. To obtain quantifiable data from the performed LFM measurements, a careful calibration of the stiffness of the probe in both the lateral and in the normal direction is needed. In fact, the calibration of the normal (flexural) stiffness of the cantilever is important for obtaining a precise value of the normal forces exerted on the samples. The calibration of cantilever's lateral (torsional) stiffness is, in turn, important for interpreting the LFM signals and thus attaining a meaningful and accurate data analysis of the performed scans, i.e., in order to obtain the effective values of the friction force [17], [128].

The calibration is principally dependant of the actual dimensions of the cantilevers bearing the aforementioned tip, whereas this assembly constitutes the probe. Considering that these dimensions are in micrometre (μm) range, and their production process inherently prevents the achievement of uniform dimensions in the whole large production batches, the calibration constitutes a hard and tedious task. What is more, in order to extend the range of considered loads, the cantilevers used in this study are of triangular geometry, which is quite seldom for LFM measurements, and induces additional difficulties in determining the lateral stiffness of the probes. The issues of calibrating the triangular cantilevers is successfully overcome by a thorough experimental study of cantilevers' geometries by employing the field-emission

scanning electron microscope (FE-SEM) images, and using multiple calibration techniques available in the current state-of-the art.

Ten probe samples are therefore scanned first on a FE-SEM allowing to obtain their dimension as shown in Figure 3.9. Statistics on the dispersion of the respective values of the specific dimensions, due to the production process of the probes, measured according to the scheme shown in Figure 3.10, can therefore be successfully attained (Table 3.1).

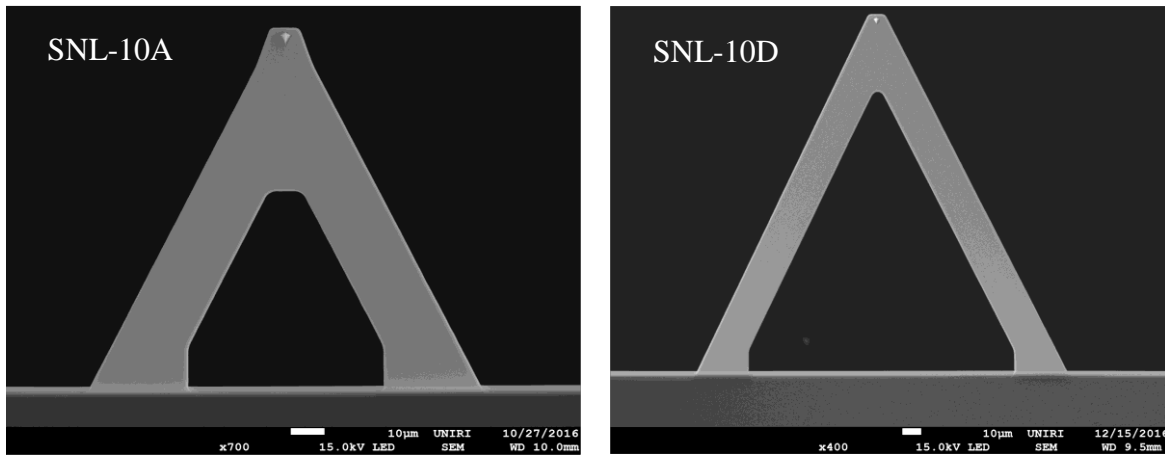


Figure 3.9 SEM micrographs obtained with a magnification of, respectively, 700 and 400 times showing the planar views of the used Bruker SNL-10 probes (the shown scale-bar is 10 μm).

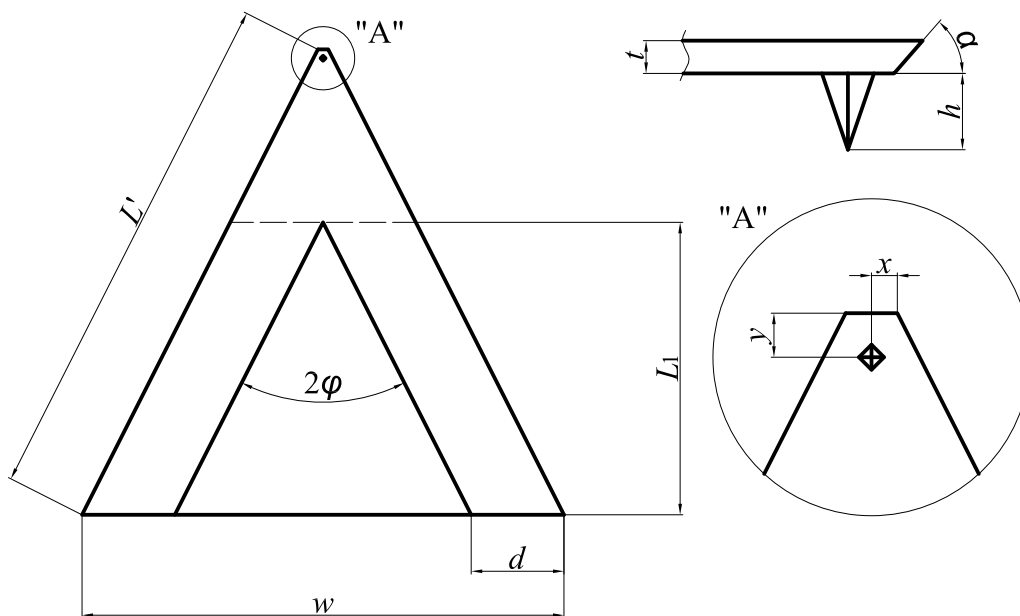


Figure 3.10 Considered geometrical parameters of the used Bruker SNL-10 probes [128].

The validation of the bending stiffness k_b of the microcantilevers with respect to their nominal value (for the SNL-10D probes that hereafter will be referred to as the samples used to explain the adopted procedure, the nominal bending stiffness is $k_b = 0.06 \text{ N/m}$) is performed

via the thermal tune method (TTM), i.e., by measuring in the time-domain the power spectral density of cantilevers' motion in response to dynamic excitations [12]. After measuring the cantilever's oscillations in air, and acquiring data for 30 seconds, the obtained power spectral densities (PSD) are fitted with a Lorentzian model:

$$A(f) = A_0 + \frac{C_1}{(f - f_0)^2 + C_2} \quad (3.4)$$

where $A(f)$ is the amplitude of the oscillations as a function of frequency f , A_0 is the baseline amplitude, f_0 is the centre frequency at the resonant peak, while C_1 and C_2 are Lorentzian fit parameters. The measured PSD and their respective Lorentzian fits for the herein used cantilevers is shown in Figure 3.11 where it is clear that the D-type cantilevers have a significantly lower stiffness than the A-type ones. This method provides, thus, simple *in situ* means of obtaining the normal stiffness of the probes and it does not require any contact of the cantilevers' tips with a surface, thus assuring the preservation of the initial sharpness of the tips. The obtained bending stiffness of the SNL – 10D probe is reported in Table 3.2.

Table 3.1 Measured dimensions of the Bruker SNL – 10 SPM probes with the respective dispersions.

	SNL-10A		SNL-10D	
	Avg.	$\pm \sigma$	Avg.	$\pm \sigma$
α [°]	60.37	4.86	60.29	5.46
d [μm]	29.64	0.48	22.9	0.51
h [μm]	4.87	0.12	4.71	0.14
φ [°]	27.1	0.44	26.25	0.81
L' [μm]	122.5	0.34	214.17	0.77
L_1 [μm]	59.43	0.63	150.58	0.5
t [μm]	0.62	0.07	0.55	0.03
w [μm]	117.77	1.23	201.59	1.1
x [μm]	5.23	0.07	5.08	0.17
y [μm]	3.72	0.14	3.58	0.11

The lateral calibration of the probes presents the most important aspects of quantitative friction force microscopy. Methods of calibrating the lateral stiffness can be divided into the

following main categories [59], [93], [119]:

- ※ calibration using a calibration sample,
- ※ calibration by adding a known mass to the cantilever,
- ※ calibration by using a reference probe with a known stiffness, and
- ※ calibration by determining the stiffness of the probe using numerical methods.

Each of these methods have certain shortcomings in the respective repeatability and accuracy, especially considering the small dimensions of the probes with the corresponding deviations evidenced in Table 3.1.

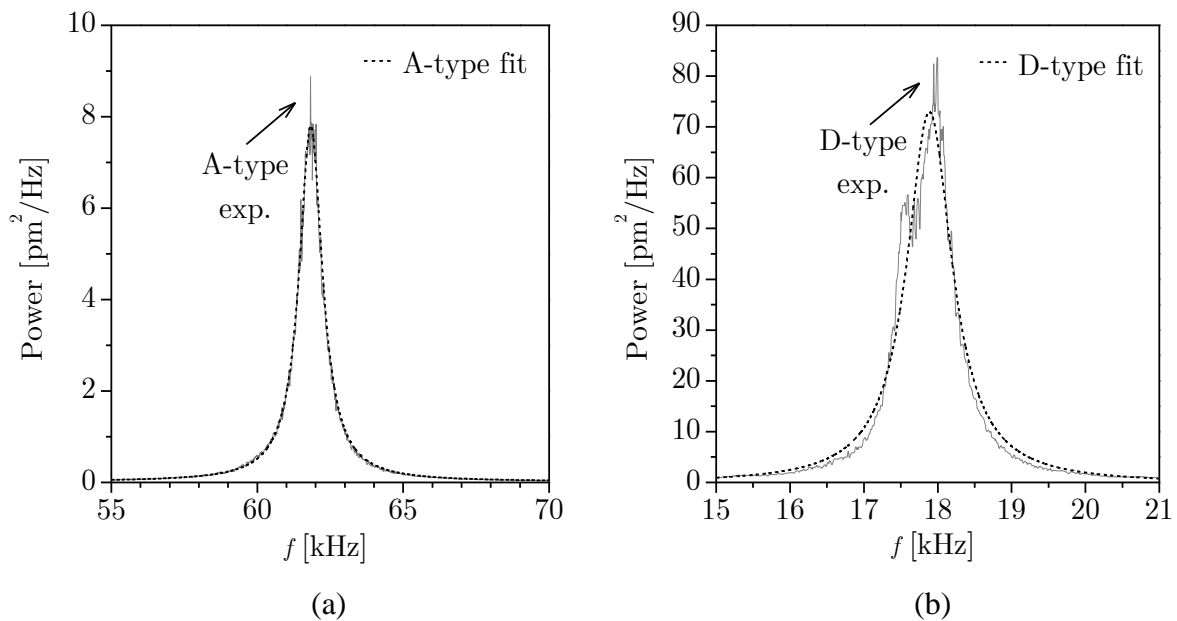


Figure 3.11 Power spectral density (PSD) of cantilevers' response in ambient conditions and the respective Lorentzian fits for A type (a), and D-type probes (b).

A combination of different calibration methods is used in this work, i.e., the calibration is performed by using a calibration sample TGF11, where the input stiffness needed for the respective calculations are based on results attained by employing the analytical method of parallel beam approximations (PBA), and via finite element (FE) calculations performed in Ansys[®]. The dimensions of the probes used in the PBA and FE calculations are, in turn, those obtained from the previously obtained SEM images.

The determination of the factor correlating the lateral voltage signal on the PSPD to forces related to the torsional stiffness k_t , i.e., to forces inducing probes' torsion, is hence conducted by employing calibrated TGF11 arrays of trapezoidal gratings in a monocrystalline Si substrate along the (111) crystallographic planes (Figure 3.12) [114].

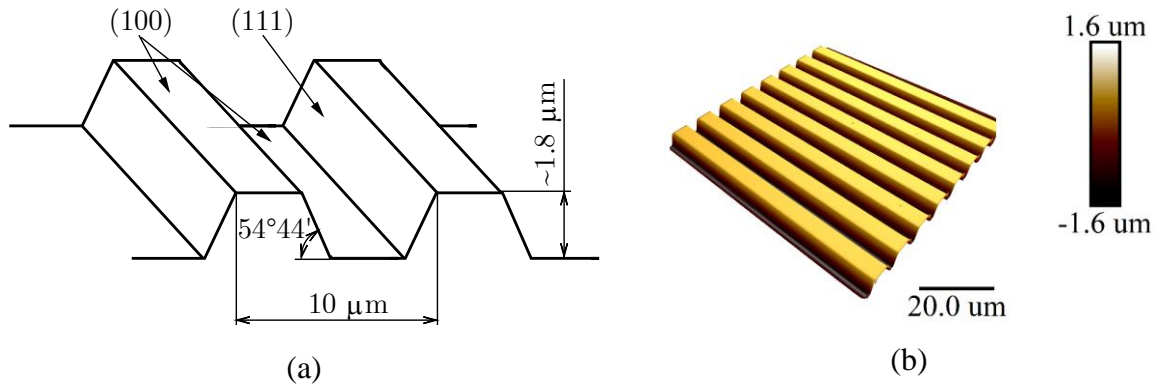


Figure 3.12 Scheme (a) [128], and factual topology of the TGF11 calibration grating (b)

In Figure 3.13 are then schematically represented the forces acting on the tip of the probes while they are scanned along the TGF11 sample (u and d indices stand for upward and downward movement, respectively), i.e., the normal load F_N , the traction (transversal) load F_T , the adhesive forces F_A (see also Section 3.5.2), the friction force F_f and the reactive normal force F_n . The reactive forces F_A , F_f and F_n induce also a torsional torque M on the cantilever bearing the tip. Considering the resulting force and torque equilibria about the contact point between the tip and the surface as explained in [164], as well as the torsional stiffness of the probes attained via the calculations, a relation between the PSPD voltage reading induced by the torsion of the probe, and the friction force F_f can finally be obtained.

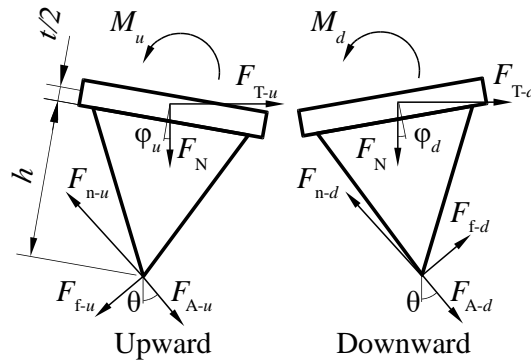


Figure 3.13 Balance of forces acting on probe's tip during the measurements [128].

The respective calculations are then conducted considering 25 permutations of variable normal and transversal loads in the range from 10 to 100 nN. The sensitivity analysis of the FEM results, i.e., the study of the influence of the geometric parameters on the transversal deformation of the probes shows that, as expected, the thickness of the probes has the highest influence on the resulting deformations. In the herein considered case the described procedure on the TGF11 sample allowed, hence, determining that for the Bruker SNL – 10D probes the

correlation factor α linking F_f to the SPM voltages resulting from the LFM measurements is $\alpha = 0.035 \mu\text{N/V}$. The thus obtained values of the flexural stiffness k_b and of the torsional stiffness k_t for the SNL-10D cantilever, are reported in Table 3.2, allows evidencing that the uncertainty of the values of the dimensions of the probe as obtained from the SEM measurements, has a marked (up to roughly $\pm 15\%$) influence on the determined stiffness values.

Table 3.2 Determined bending and torsional stiffness of the Bruker SNL – 10D probes [128].

	TTM	PBA	FE
k_b [$\text{N}\cdot\text{m}^{-1}$]	0.086	$0.056 \pm 12\%$	$0.098 \pm 8\%$
k_t [$\text{Nm}\cdot\text{rad}^{-1}$]		$79.37 \pm 16\%$	$92.59 \pm 11\%$

3.5.2. Measurement of the Adhesion Forces

Since the measurements performed in this work are conducted in air (habitual technological conditions), the friction force F_f is dependent, as evidenced above in relation to Figure 3.13, on the adhesion F_A between the probe and the samples, that is superimposed to the normal loads F_N inducing the friction forces, on surface roughness, but also on the contact area of the probe with the sample [38], [141], [181]. The samples are therefore analysed on the SPM device by employing conventional contact-mode atomic force microscopy (AFM) to obtain the respective surface roughness and determine the adhesion forces.

The adhesive forces are hence determined here from the force vs. approaching distance curves that show these interactions between probe's tip and the surface of the sample (Figure 3.14). In fact, there are five distinct characteristic regions on these curves [18], [128]:

- ※ during phase 1 the tip approaches the surface of the sample,
- ※ in point 2 the tip is adhesively attracted to the surface and makes contact with it,
- ※ a further lowering of the probe in region 3 induces a rising of the force exerted through the cantilever onto the sample up to a predetermined maximal value,
- ※ the retraction of the tip, with the consequent lowering of the force exerted on the sample, is then initiated but, due to adhesion, the tip stays in contact with the sample until 4,
- ※ when the pull-out force becomes greater than the adhesion force, the tip suddenly springs back to zero force deflection (point 5), while the difference of the forces in point 4 and 5 is the value of the sought adhesive force F_A .

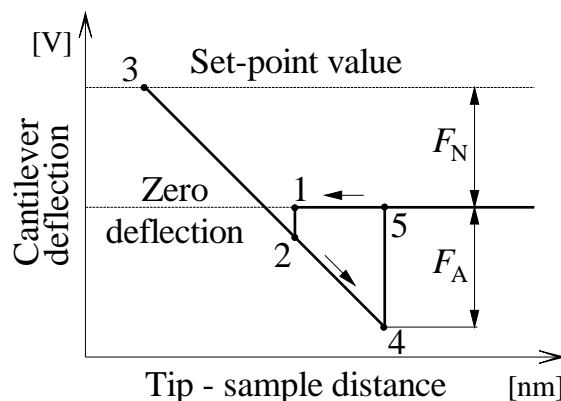


Figure 3.14 Schematic representation of a typical force-distance curve [17], [128].

The adhesive force values are hence determined for all the samples used in the herein performed study, as well as in all the respective measurement points. In this framework, adhesion obviously depends a lot on the state of the surface layer, which, in turn, changes with temperature [6], [10], [17], [92]. A through study of the dependence of F_A on temperature, on the same TGF11 grating used above for the calibration of the stiffness of the probes, is hence performed, while the temperature of the samples is monitored by employing a K-type thermocouple connected to the Arduino controller and logged to the SPM PC, used also to monitor the stabilisation of surface temperature before the LFM measurements. F_A values are thus attained from the conventionally used force vs. tip distance curves of Figure 3.14. It is important to stress here especially the fact that the total force acting on the sample is hence the sum of F_N and F_A (the relevance of this statement will be thoroughly addressed in later chapters). By using the Peak Force Quantitative Nanomechanical Mapping (PF-QNM[®]) measurement mode of the used Bruker's SPM device, the variability of adhesion with temperature is thus determined, while for each measurement point, i.e., for each temperature value, the lateral calibration procedure explained in the above Section 3.5.1 is repeated, resulting in the change of the respective correlation factor (α ($\mu\text{N/V}$)) for each of the 50 sample points determined via the DoE-CVT approach. The thus obtained results on the calibration TGF11 grating, depicted in Figure 3.15, allow establishing a marked variation of F_A with temperature. The respective results in terms of the variation of the correlation factors are, in turn, shown in Figure 3.16 where the variability of the correlation factors is shown in the whole experimental design space, alongside with statistics on the obtained factors on Figure 3.16a which presents a distribution of variability of coefficient α alongside a box-and-whisker plot (denoting distribution's descriptive statistics). It is evident here that a variation of the temperature in the range from 20 °C to 80 °C induces a variation of the correlation factor α

from 0.0068 up to 0.071 $\mu\text{N}/\text{V}$, i.e., a whole order of magnitude.

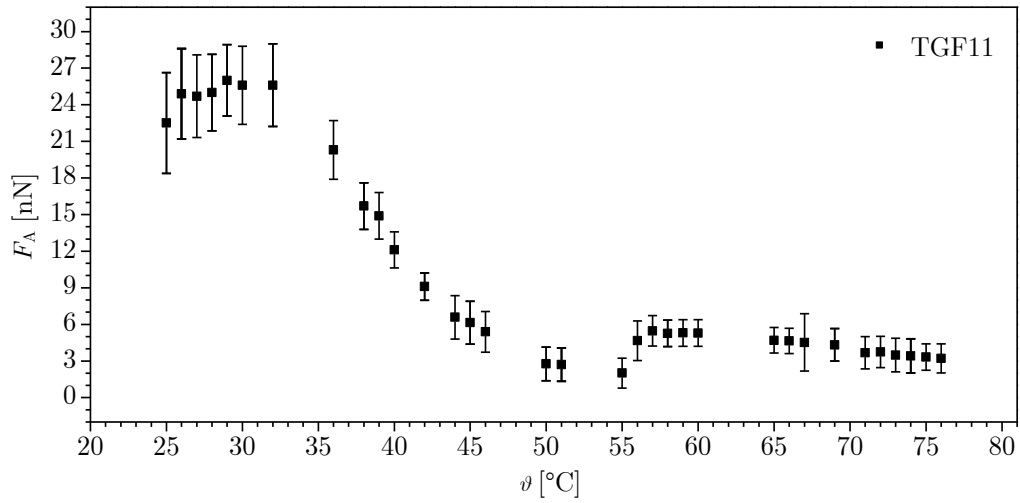


Figure 3.15 Measured values of the adhesion force F_A on the TGF11 calibration grating vs. temperature ϑ [128].

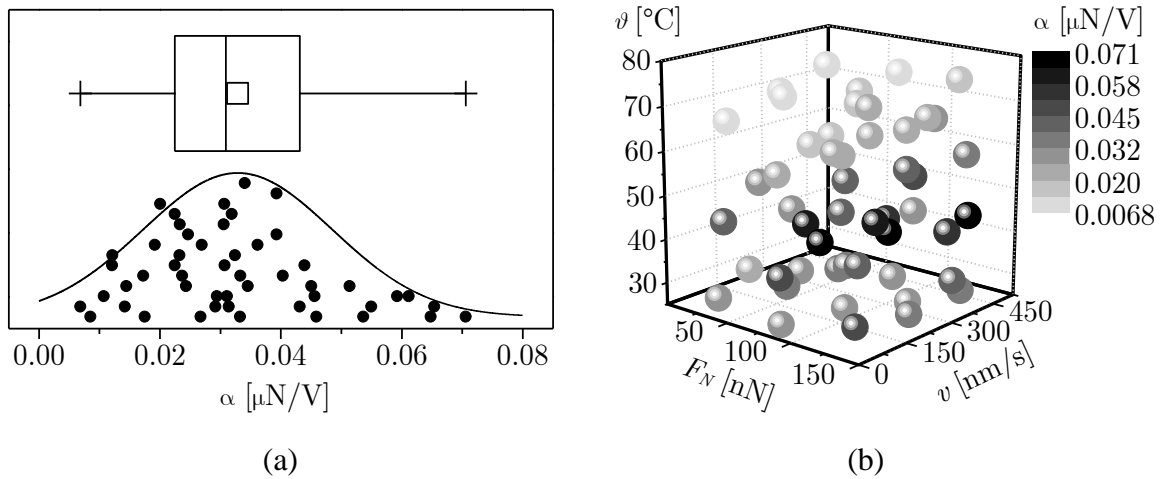


Figure 3.16 Statistics on the corrected correlation factors α (a), and colour-coded values of α in the experimental design space defined by the CVT points (b).

The experimentally obtained variability of the F_A with temperature for all the considered thin-film samples is, in turn, shown in Figure 3.17 where, for clarity reasons, the error bars are omitted. (the respective complete data sets are given in Appendix B). The depicted data allow evidencing that in all cases the adhesion force variability shows similar trends as for the calibration sample TGF11.

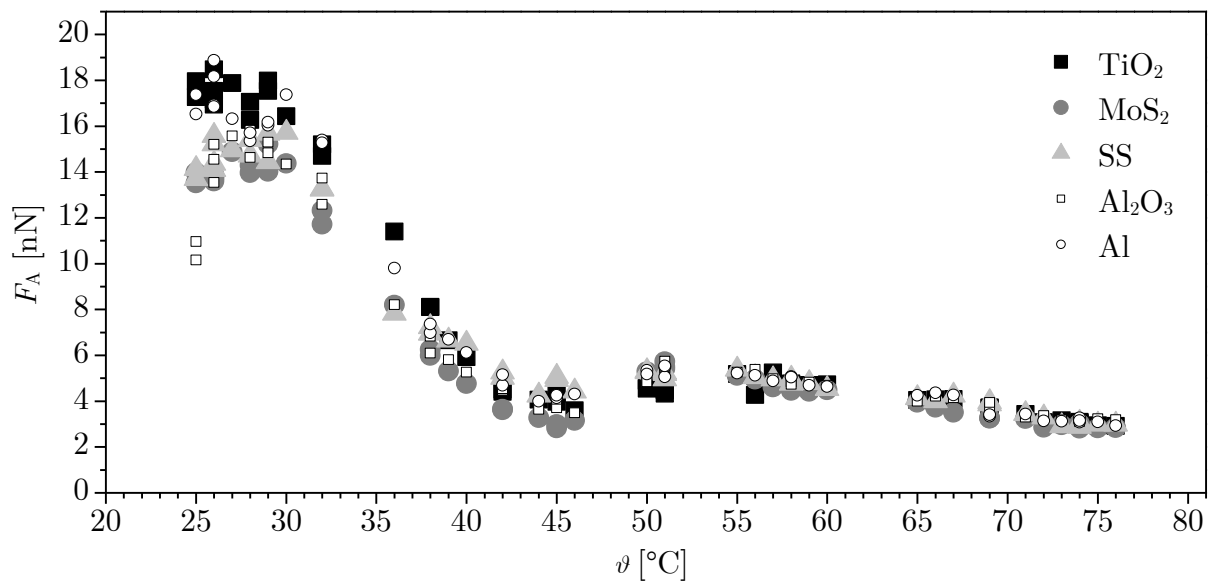


Figure 3.17 Mean adhesion force F_A variability vs. temperature for the considered thin-film samples in the DoE determined experimental points [128].

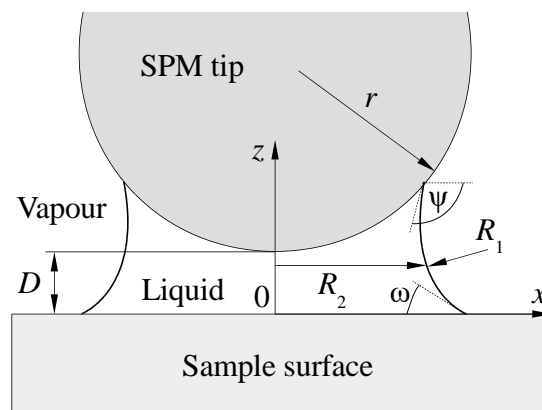


Figure 3.18 Geometry of a capillary condensation water bridge – meniscus.

It is important to note here also that, in nanoscale contacts in air, the capillary condensation of water vapour present in air occurs at the single-asperity contacts of two solid bodies, building a water neck surrounding the contact itself (Figure 3.18) [75], [85]. At thermodynamic equilibrium, the total curvature of the meniscus is hence determined by the amount of water condensed at the contact. The size of the meniscus depends also on the wetting properties of the two bodies in contact. This effects, inducing the interactions of the tips of the probe with the sample are, in fact, those visible in the above SPM measurements of adhesion [26], [38], [42], [181] (see in this regard also Chapter 5 below). Humidity is thus also monitored separately and controlled during the measurements, with average obtained values of the relative humidity of 50 % (± 1 %) and of air temperature, monitored by using the Bruker Thermal Applications

Controller (TAC), of 21 °C (± 0.1 °C). Relative humidity and temperature inside the SPM apparatus enclosure are additionally monitored and logged via a humidity and temperature sensor Texas Instruments HDC1080 (RH accuracy $\pm 2\%$, temp. accuracy ± 0.2 °C) coupled to an Arduino controller.

3.5.3. Temperature Effects on the Variability of the Normal Force

With respect to the flexural stiffness k_b , it is to be noted here that, since temperature is considered as one of the studied influencing parameters, the rise of the temperature of the set-up induces inevitable thermal dilatations of the samples [52], [92], of the piezoelectric actuators used to move the probes, as well as of the probes themselves (Figure 3.19). These thermal effects induce, therefore, a necessity to change the set-point, i.e., to vary the necessary elongation of the vertical actuator needed to maintain a determined (required) value of the normal force F_N , maintaining thus a constant flexural deflection reading on the photodetector of the SPM device during the LFM measurements. Based on a thorough study of this issue [128], where the temperature of the samples is monitored again by employing a K-type thermocouple connected to the Arduino controller, it is hence determined that for lower temperature values the set-points are positive, they have a tendency towards 0 at temperatures of roughly around 40 °C and then, for higher temperatures, the set-points tend to assume negative values (cf. Figure 3.19). These variations have thus been considered in setting-up each measurement. On the other hand, by employing the Bruker Thermal Applications Controller (TAC) as a part of the AFM system, the set sample temperature values (variable across the set of experiments, but constant in each of them) is maintained stable long enough to achieve consistent and steady-state experimental conditions [128].

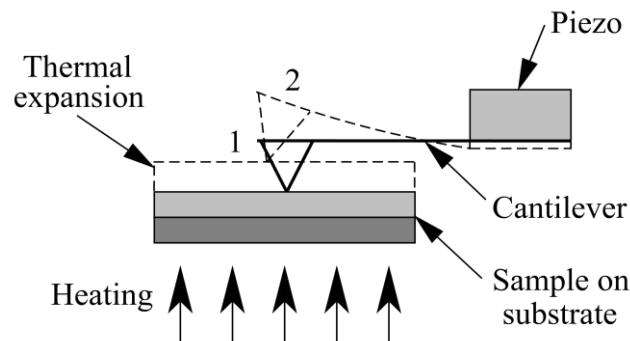


Figure 3.19 Influence of thermal expansion on the necessity to correct the set-point, i.e., maintain the required value of the normal force F_N [128].

The calibration of the flexural and torsional stiffness of the used probes, the measurement of

the variation of the adhesive forces and of the needed set-point with temperature, and of the respective correlation factors for determining the friction force from the measured LFM voltage signals, described above in Sections 3.5.1. and 3.5.2., is thus successfully accomplished, which allows the quantitative measurements of the frictional forces F_f to be performed. Prior to these, considerations of the influence of tip wear on the measurements have also to be made.

3.6. Tip Wear and its Influence on Adhesion

Special attention is dedicated in this work also to the study of the wear of the tip of the probe itself, which has a marked influence on adhesion. In fact, as a consequence of nanoscale wear due to asperity contacts and atomic attrition between the probes and the samples, the geometry of the apex of probes' tips changes [14], [41], [97], [185], inducing a negative influence on the resolution of the SPM imaging of the samples [39], [180], and a significant change of the adhesive forces F_A [16], [33], [137].

Generally, the geometry of probes' tips can be determined by using methods that involve manufacturer's specifications (factory-calibrated tips), SEM or other imaging techniques, and/or by employing tip SPM scans on specially devised titanium (Ti) tip characterizing samples coupled to deconvolution algorithms [30], [158].

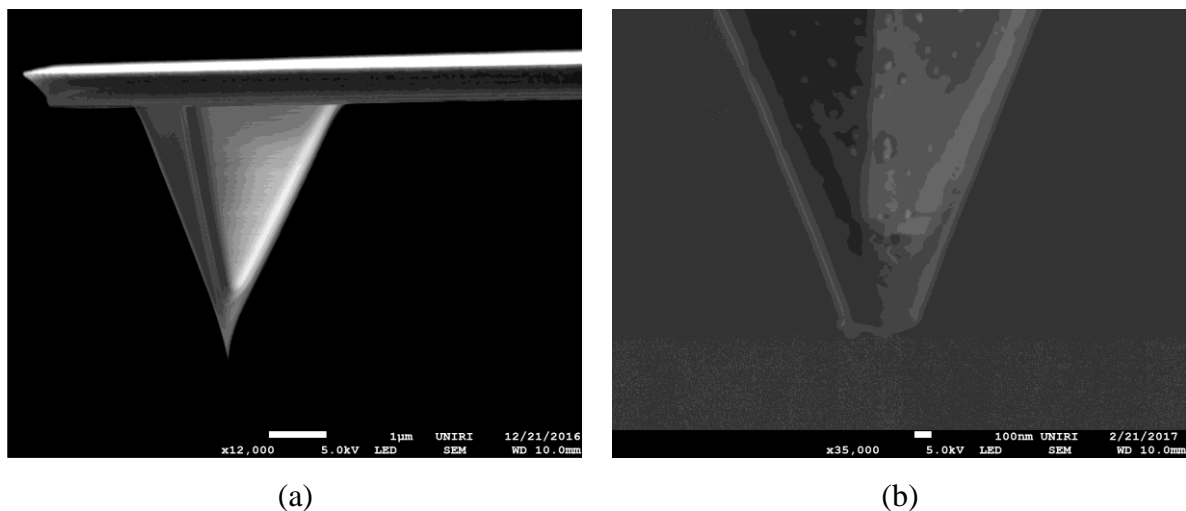


Figure 3.20 SEM micrographs of a fresh SPM tip (a) and of a tip's apex which was used for 200 LFM measurements (b) [128].

The nominal specifications that the manufacturers provide in terms of tips' geometry have to be taken with a degree of caution, because of the variability in the production batches (cf. also Table 3.1), and because tips' wear itself. In this thesis the methods of using SEM images

and tip characterization samples are thus adopted [128]. SEM micrographs of a new tip apex and of the same tip after more than 200 LFM scans, obtained again by using the FE-SEM device, are hence shown in Figure 3.20, allowing to clearly expose the marked wear of the tip. The images are used to measure the radius r of tips' apex by best-fitting a circle through the image of the tip. In the particular example of Figure 3.20, the obtained radius of the new and of the worn tip are, respectively, 32 and 95 nm [128].

Based, in turn, on SPM scans on a standard Bruker's titanium characterizing sample [30], whose surface is specifically adapted to the aim of deducing the tip conditions, the so-called "tip evaluation" tool in the Nanoscope software, coupled to an in-house developed MATLAB[®] code, is then used to generate a model of the tip. The tip evaluation procedure [45], [97], [168] involves in this case analysis of the local peaks in a topographic image, and the respective slopes in all directions, refining a three-dimensional (3D) tip model – thus allowing to deduce the minimal tip sharpness. An estimate of maximal tip's width in cross-sections at two distinct distances (ETD 1 and EDT 2) from its apex can thus be obtained, allowing to determine also the value of an "aspect ratio", defined as the ratio of the major and minor semi-axes of tip's cross section in ETD 1 and ETD 2. Inputting this data into the MATLAB[®] deconvolution algorithm [168], the estimated truncated cone-shaped geometry of the probe is obtained [128]. From the latter, probe's major tip axis in section ETD 1, in the vicinity of probe's apex, is finally found [128]. In the herein considered case, this estimated dimension d_{est} of the virginal tip's apex is therefore approximated with a value of 28.0 nm, whereas that of the worn tip increases to 75.8 nm (Table 3.3) [128].

Table 3.3 Results of the determination of tip's apex radius [128].

Parameter	Fresh tip	Worn tip
ETD 1	31.9 nm	54.1 nm
ETD 1, Aspect Ratio	0.91	0.67
ETD 2	72.9 nm	138.8 nm
ETD 2, Aspect Ratio	0.76	1.00
d_{est}	28.0 nm	75.8 nm

Measurements of the dependence of adhesion on wear are hence conducted by using a fresh tip on an Al₂O₃ sample that has high abrasive properties. Contact-mode scans on 500 x 500 nm² surfaces, with 512 scan lines (i.e., double with respect to the number of scans used in the actual LFM measurements), are hence performed at the maximal considered scan speed of

$v = 500 \text{ nm/s}$, while maintaining $\vartheta = 20^\circ\text{C}$ - $256,000 \text{ nm}$ are thus covered in a single scan while 100 scans are made in total, so that the cumulative scan distance is 25.6 mm [128]. For the maximal considered F_N value $F_N = 150 \text{ nN}$, in Figure 3.21 are hence shown the dependences of the values of the estimated major tip axis d_{est} , of the contact pressure p_c , and of the adhesive forces F_A , attained from the conventionally used force vs. tip distance curves after each Al_2O_3 sample scan, versus the scan distance d_{scan} . The exerted contact pressure variability was calculated for each point to prove that during the measurements the contact itself is in the elastic regime, i.e., that there are no plastic deformations of the sample. This is also confirmed via separate detailed scans employing the soft tapping mode [17] (used forces are of the order of pN) that allowed attaining 3D topology scan results showing no surface deformations. It could hence be concluded that the exerted maximal contact pressure p_c of 590 MPa on the sample with the tip in its sharpest state is far below the Al_2O_3 thin films' yield strength of $5177 \pm 644 \text{ MPa}$ [115] [128].

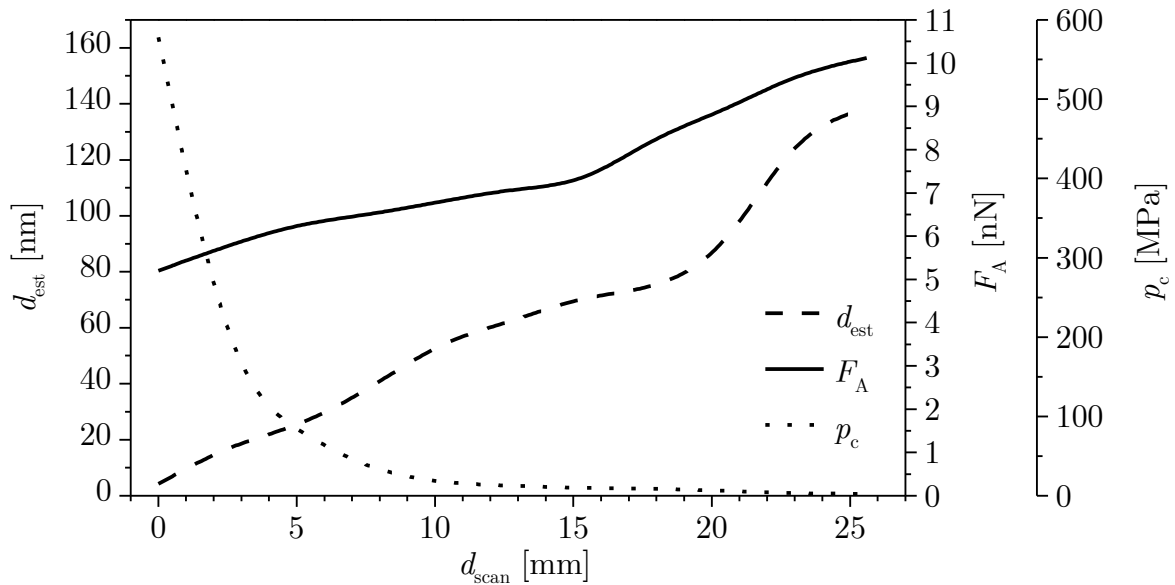


Figure 3.21 Wear of the tip on an Al_2O_3 sample for $F_N = 150 \text{ nN}$: tip dimension d_{est} (left axis), adhesion F_A (right axis) and resulting contact pressure p_c (far right axis) [128].

The values of adhesion will, obviously, increase with increasing tip wear, In terms of the resulting effect of adhesion on the uncertainty of the measurements, the results shown in Figure 3.21 allow establishing that, the planned 200 LFM measurements with 256 scan lines in each of them would have a comparable effect to that of the uncertainty introduced by the dispersion of the stiffness of the probes as determined in Section 3.5.1. Bearing therefore in mind the necessity to have reliable measurements, but at the same time also the need to minimise the

usage of fresh tips and the respective costs, a sufficiently large safety margin is introduced. A new tip is thus used in the subsequent measurements of the friction force F_f for no more than 50 LFM measurements cycles, which corresponds to a travel distance limited to 6 mm. As evident in Figure 3.21 this induces a change of F_A limited to 1.5 nN (i.e. 1 % of the used F_N); the introduced variability of the applied force is consequently also limited to roughly 1 %, i.e., it is markedly smaller than the uncertainty introduced by the variability of the stiffness of the used probes [128]. This important conclusion allows, hence, enhancing the accuracy of the subsequently performed F_f measurements.

In Chapter 3 not only the experimental points are determined via elaborated DoE procedures, but also all the calibration and measurement conditions characterisation values are successfully determined, allowing to evidence the limits of uncertainty inherent in the planned LFM measurements but also creating the preconditions for consequent and structured experimental determination of the values of the friction force F_f in the nanometric domain, that will be described in Chapter 4.

4. Results of Experimental Measurements and their First-order Analysis

All of the procedures described in Chapter 3 allow the actual LFM measurements on the prepared samples to be performed (cf. some examples of the obtained topologies shown in Figure 4.1).² Preliminary measurements on the considered thin-film are made first in conventional SPM contact-mode measurement configuration, i.e., by measuring the topography of the samples. From the thus obtained results, it is evident (Table 4.2) that the used samples are characterised by small values of the arithmetic average surface roughness R_a , the RMS roughness R_q and the maximum height R_z , whereas the dispersion of these values in the performed repetitive measurements is rather small [128].

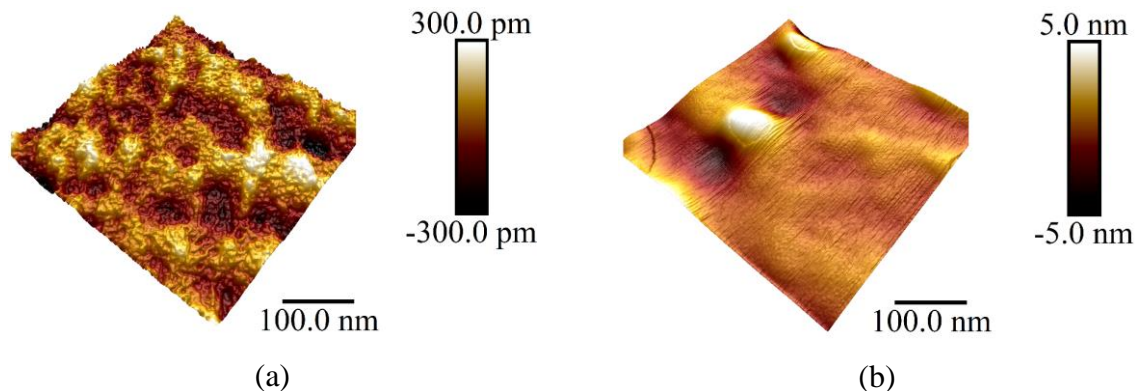


Figure 4.1 Sample surface topologies obtained via LFM measurements on the TiO_2 thin-film (a) and on the MoS_2 sample (b).

LFM measurements are then finally performed with the aim of attaining data relative to the friction forces F_f in the nanometric domain and their variation in the multidimensional space given by the considered influencing parameters and their ranges of variability. The measurements are carried out in the DoE-CVT determined measurement points (cf. again Appendix A) the order of ascending temperature, with a temperature stabilization period, after the required temperature is achieved, of 30 minutes.

² Part of the work described in this chapter is again based, partly directly derived and cited from a recent publication of the author of the thesis and his collaborators in a peer-reviewed scientific paper [128], which was produced and published as part of the obligations foreseen in the curriculum of the doctoral study of the Faculty of Engineering of the University of Rijeka, Croatia.

Table 4.1 Surface roughness of the analysed thin-film samples [128].

	R_a [nm]	$\pm \sigma$ [nm]	R_q [nm]	$\pm \sigma$ [nm]	R_z [nm]	$\pm \sigma$ [nm]
MoS ₂	8.04	1.3	10.18	1.8	15.0	2.3
Al ₂ O ₃	12.4	2.6	14.6	2.9	16.05	3.2
TiO ₂	6.3	1.7	8.8	2.3	9.8	2.8
Al	4.2	1.35	7.1	2.45	7.9	2.3
SS	8.58	0.86	10.5	1.32	14.3	1.7

In Figure 4.2 and Figure 4.3 are thus depicted the F_f values obtained for the considered thin-film samples synthesized by using, respectively, the ALD and PLD technologies,. The points in the figures represent the mean F_f values in repetitive measurements, scaled according to the given colour-coding of the shown legends, while the respective complete measurement datasets are reported in Appendix B. In the left part of the figures are herein depicted the conventional values of F_f generally reported in literature, i.e., those when the average correlation factor α linking F_f to the SPM voltages, resulting from the LFM measurements and neglecting the variation of the adhesive force F_A with temperature, is considered. In the right part of the figures are, in turn, depicted the dependencies of F_f on the considered influencing parameters when the true total force acting on the samples (i.e., $F_N + F_A$), and influencing the torsion of the probes, is considered. In the latter case, the shown F_f values in each sample point account also for the F_A dependency on temperature \mathcal{G} , i.e., the variability of the correlation factors as determined in the above Section 3.5 [128].

From the data reported in Figure 4.2 and Figure 4.3 it can be inferred that the scatter of the obtained F_f values attained by considering a constant $\mu\text{N/V}$ LFM correlation factor do not allow appreciating the real peculiarities of the physical dependence of nanometric friction on its main influencing parameters. What is more, it would seem that, in general, in this case F_f is largest for the highest considered temperatures. When, however, the influence of the variability of F_A on \mathcal{G} and the resulting change of the correlation factor is considered, the similitude of the F_f value trends for all the considered thin films becomes clearer. In fact, in this case the highest F_f values start clustering for temperatures \mathcal{G} at around 40 °C (cf. the above treatise in Section 3.5.2), for the highest considered applied loads $F_N + F_A$ and, tendentially, for lower to mid-range considered velocities v [128].

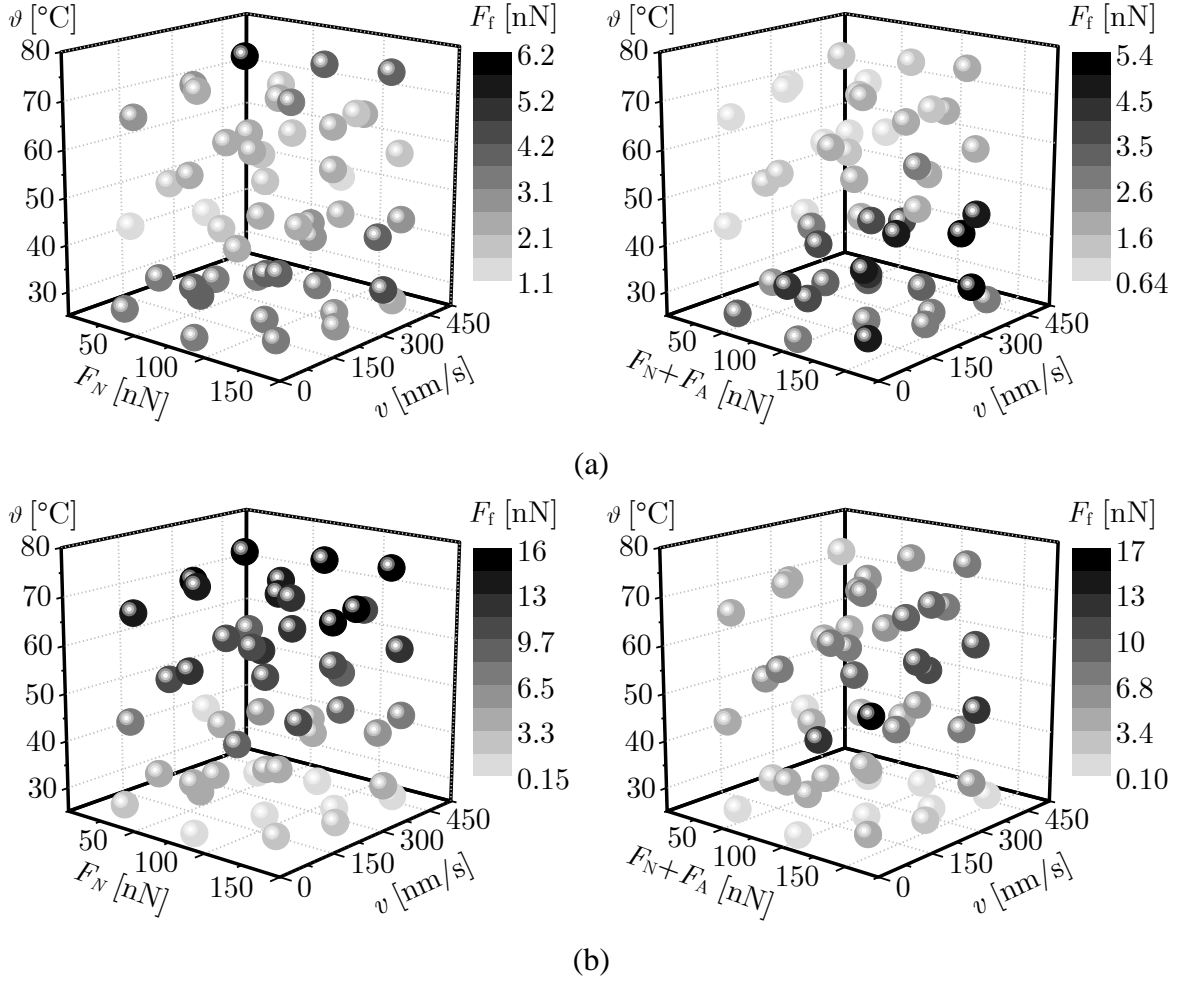


Figure 4.2 Colour-coded distribution of experimentally determined nanometric F_f values on 50 measurement points for the Al_2O_3 (a) and TiO_2 (b) samples obtained via ALD vs. the considered influencing parameters. Left and right columns present F_f values obtained without the calibration factor correction, and with calibration factor correction, respectively [128].

It is to be noted also that in all considered cases the depicted mean F_f values are characterised by a high stochastic dispersion (up to $\pm 15\%$), which, considering also the number of influencing parameters, complicates the development of a mathematical model that would allow correlating the influencing parameters to the respective F_f values. In fact, polynomial fitting of the obtained results via the often-used multidimensional interpolation algorithms yields a poor fit with the best coefficients of determination limited to about $R^2 = 0.1$ [128].

To gain insight into the sensitivity of the F_f values on the considered influencing parameters, statistical analysis is hence used as benchmark and as guidelines for the subsequently planned advanced numerical analyses [128]. Correlation matrices obtained by using Pearson's product-moment correlation (PPMC) [106] on the large set of acquired F_f data are hence summarised in Table 4.2 and Table 4.3.

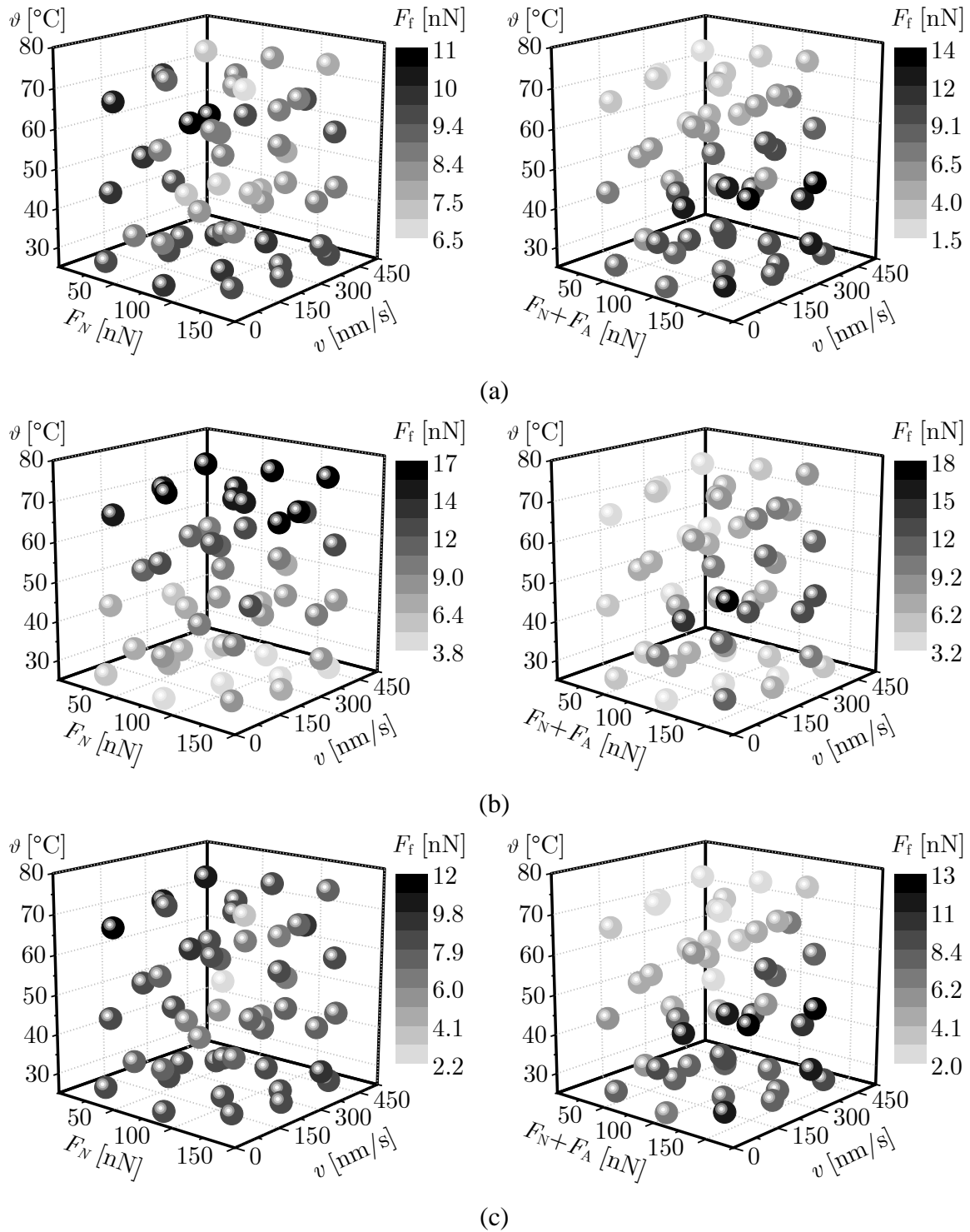


Figure 4.3 Colour-coded distribution of experimentally determined nanometric F_f values on 50 measurement points for the Al (a), MoS₂ (b) and SS (c) samples obtained via PLD vs. the influencing parameters. Left and right columns present F_f values obtained without the calibration factor correction, and with calibration factor correction, respectively [128].

Generally, the PPMCs are calculated as:

$$\rho_{xy} = \frac{\sum_{i=1}^n (x_i - \bar{x})(y_i - \bar{y})}{\sqrt{\sum_{i=1}^n (x_i - \bar{x})^2} \sqrt{\sum_{i=1}^n (y_i - \bar{y})^2}} \quad (4.1)$$

where x_i and y_i are the pairwise variables to be correlated, while \bar{x} and \bar{y} are their respective mean values in the whole set of observations n . In this equation the numerator represents the covariance of the two variables, while the denominator is a multiple of square roots of the variance of each variable. In PPMC a correlation coefficient of 1 or -1 represents then a perfect (linear) correlation of positive (proportional) or negative (inversely proportional) dependence of the dependent variable on the considered influencing parameter, with higher absolute values indicating a stronger dependence. A zero (or near-zero) value indicates, in turn, that there is no correlation.

In Table 4.2 and Table 4.3 both the correlations considering the exerted normal force F_N alone, as well as those considering the total force $F_N + F_A$ acting on the samples, in both cases with adhesion-corrected calibration factors, are shown. It can thus be seen that, for all the considered thin-film sample materials, the influence of F_N on the nanoscale friction force F_f has a positive correlation in the range from, respectively, ca. 0.4 for Al and Al₂O₃, to ca. 0.5 for TiO₂, ca. 0.6 for the MoS₂ samples and ca. 0.35 for the SS samples. When the total force $F_N + F_A$ acting on the samples is considered, the respective correlation coefficients change, however, to roughly 0.45 for Al and Al₂O₃, 0.4 for TiO₂, 0.6 for MoS₂ and 0.4 for SS [128].

Although the general trends observed in relation to Figure 4.2 and Figure 4.3 are thus confirmed, i.e., F_f clearly rises with increasing $F_N + F_A$ values, it is interesting to note especially the peculiar effect of the adhesion force F_A for the different considered sample materials. In fact (cf. also the respective rows related to F_A in Table 4.2 and Table 4.3), in the case of Al, Al₂O₃ and SS samples, F_A has a relatively high positive influence on F_f , i.e., a rise of F_A induces an increase of the total contact load and hence a rise of the friction force F_f . On the other hand, however, in the case of the TiO₂ and MoS₂ samples, there is a negative influence of F_A on F_f , with the respective correlation factors of -0.62 and -0.27, which implies diminishing F_f values for increasing F_A values. This fact not only confirms once more the postulated complex nature of adhesion, induced by multivariate phenomena due to atomic interactions and surface energies, but it could also, perhaps, indicate an occurrence of a possible lubricating effect on the surfaces of the TiO₂ and MoS₂ samples that induces the observed partial decrease of F_f with

increasing F_A . In any case it seems that, for the nanoscale contact of the Si tip with the TiO_2 and MoS_2 samples, adhesion manifests itself as a lubricating effect. What is more, as extensively elaborated above, adhesion is also closely related to temperature [128].

Table 4.2 Matrices of correlation coefficients for the influencing parameters on the nanometric F_f values in the DoE-CVT measurement points for ALD synthesized samples [128].

	ν	F_N	\mathcal{G}	F_f	F_A	F_{N+F_A}
Al_2O_3	ν	1				
	F_N	0.032	1			
	\mathcal{G}	0.028	0.079	1		
	F_f	0.0023	0.38	-0.64	1	
	F_A	-0.068	-0.035	-0.83	0.48	1
	F_{N+F_A}	0.025	/	-0.015	0.44	/
TiO_2	ν	1				
	F_N	0.032	1			
	\mathcal{G}	0.028	0.079	1		
	F_f	0.014	0.48	0.47	1	
	F_A	-0.068	-0.046	-0.85	-0.62	1
	F_{N+F_A}	0.022	/	-0.048	0.386	/

When, in turn, the correlation of nanoscale friction F_f with temperature \mathcal{G} is observed, relatively high negative correlation values of -0.71, -0.64 and -0.57 are attained for the Al, Al_2O_3 and SS samples respectively, i.e., once more a physio-chemical similitude of these films is confirmed, which, in this case, results in a decrease of F_f for rising temperatures. Referring then to the above Figure 4.2 and Figure 4.3, this would imply also that a rising temperature prompts a relative decrease of F_A (i.e., of the respective total load $F_N + F_A$ acting on the samples), thus causing the lowering influence on F_f as well. In the case of the TiO_2 sample, however, a positive (0.47) correlation of F_f with \mathcal{G} is obtained instead. This could be due to exactly an opposite effect with respect to that hypothesized for Al and Al_2O_3 , i.e., that in this case the rise of \mathcal{G} , inducing a relative decrease of F_A , combined with the earlier-discussed negative correlation of F_A on F_f , induces a resulting increase of F_f (i.e., a decrease of the favourable lubricating effect). The MoS_2 sample shows, finally, a negligible (0.06) correlation between F_f and temperature \mathcal{G} [128].

Table 4.3 Matrices of correlation coefficients for the influencing parameters on the nanometric F_f values in the DoE-CVT measurement points for PLD synthesized samples [128]

	ν	F_N	\mathcal{G}	F_f	F_A	F_N+F_A
Al	ν	1				
	F_N	0.032	1			
	\mathcal{G}	0.028	0.079	1		
	F_f	0.014	0.40	-0.71	1	
	F_A	-0.053	-0.05	-0.86	0.44	1
	F_N+F_A	0.025	/	-0.043	0.46	/
MoS ₂	ν	1				
	F_N	0.032	1			
	\mathcal{G}	0.028	0.079	1		
	F_f	-0.056	0.62	0.061	1	
	F_A	-0.071	-0.056	-0.84	-0.27	1
	F_N+F_A	0.024	/	-0.017	0.59	/
SS	ν	1				
	F_N	0.032	1			
	\mathcal{G}	0.028	0.079	1		
	F_f	0.018	0.36	-0.57	1	
	F_A	-0.060	-0.048	-0.87	0.26	1
	F_N+F_A	0.025	/	-0.026	0.39	/

When, referring once more to, the influence of sliding velocity ν on nanoscale friction F_f is finally considered, it becomes evident that, for all the considered thin-films, and contrary to the known effects on the macro- and meso-scales, at the nanoscale, and in the considered velocity regime, there is only a negligible correlation of F_f with ν , with the respective correlation coefficients being in the 10^{-3} to 10^{-2} range. Since in recent literature [122], [178] it is reported that, at the nanoscale, the influence of ν on F_f is highly dependent on the magnitude of sliding velocity, it is evident that, in the herein considered velocity range (up to 500 nm/s), the effect of ν on F_f , especially when related to the effects induced by the other considered influencing parameters (variable loads (F_N or, respectively, $F_N + F_A$) or temperatures \mathcal{G}), is indeed negligible [128].

All the considered effects are summarised for an easier overview in Table 4.4, where for all

the analysed samples the trends of the effects of all the studied influencing parameters on the value of the nanoscale friction force F_f are given. The + and - signs indicate here, respectively, an increase or a decrease of the F_f values depending on the variation of the corresponding influencing parameter, while a “0” sign indicates no meaningful correlation. The value of the respective correlation factors is, in turn, shown in parentheses [128].

Table 4.4 Summary of the effects of the influencing parameters on the F_f value for the analysed thin-film samples in the DoE-CVT measurement points [128].

	F_N	F_A	F_N+F_A	ν	ρ
Al ₂ O ₃	+	+	+	0	-
	(0.38)	(0.48)	(0.44)	(0.0023)	(-0.64)
TiO ₂	+	-	+	0	+
	(0.48)	(-0.62)	(0.39)	(0.014)	(0.47)
Al	+	+	+	0	-
	(0.40)	(0.44)	(0.46)	(0.014)	(-0.71)
MoS ₂	+	-	+	0	0
	(0.62)	(-0.27)	(0.59)	(-0.056)	(0.061)
SS	+	+	+	0	-
	(0.36)	(0.26)	(0.39)	(0.018)	(-0.57)

As stated above, however, the correlations shown in the Table 4.2 and Table 4.3, despite providing important insights, are just first-order linear statistical approximations of the generalised trends of the influence of the studied dependence of nanoscale friction in the multidimensional space defined by the considered process parameters. The full potential of the structured methodology proposed in the thesis will be appreciated only when the obtained experimental data are analysed via more elaborated recently developed nonlinear numerical tools enabling a concurrent consideration of contributions of a large number of parameters, i.e., those allowing to determine the complete set of correlation factors that enable establishing the respective functional dependencies. This is the subject of study described in the following two chapters.

5. Development of a Predictive Model of Nanoscale Friction

The results obtained experimentally, and thoroughly described in Chapter 4, are analysed in this part of the work, as depicted in Figure 5.1, by using state-of-the-art machine learning (ML) and genetic programming (GP) numerical methods to obtain the predictive models linking the process variables to the value of nanometric friction. In this frame not only the nanotribological characteristics of the considered thin-film samples, but the respective effects due to adhesion forces are, once more, thoroughly discussed. These insights provide a foundation for an in-depth understanding of the nanotribological behaviour of each of the analysed samples in the considered range of values of the influencing parameters and provide means for the quantitative and qualitative characterization of the influence of each of these influences.

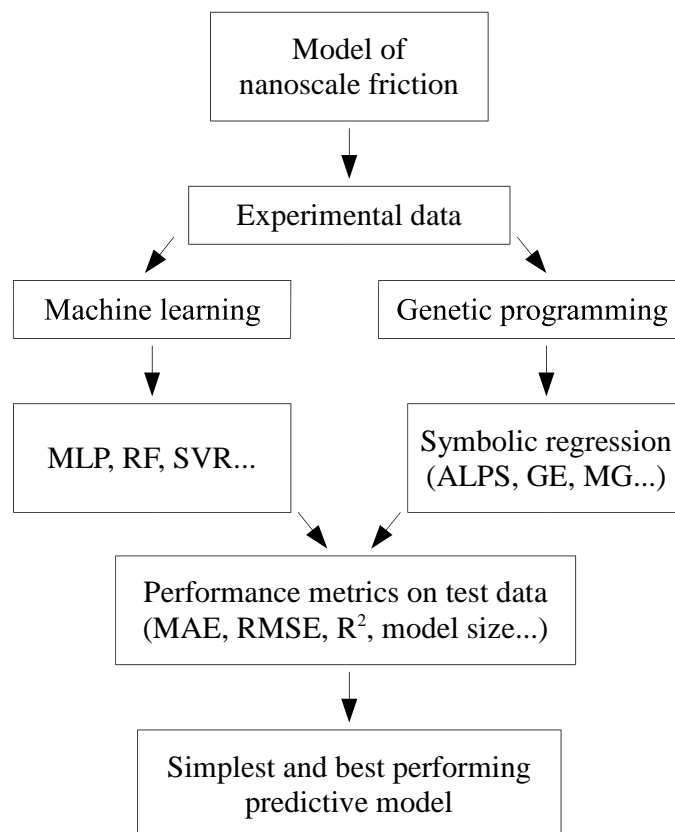


Figure 5.1 Numerical procedure for the development of a predictive model of nanoscale friction.

In order to fully characterize the concurrent effects of observed variable parameters on nanoscale friction and discover further the independent and synergetic effects of each variable,

it is important to achieve a mathematical form of a relationship between the dependent variable (F_f) and multiple independent variables (v , F_N and \mathcal{G}). The process of estimating this relationship in the mathematical form (a regression model) is commonly known as a regression analysis [49], denoting a group of mathematical methods, which provide not only a mathematical description of the analysed data but also (more importantly) the prediction of dependent variable with arbitrary input values of independent variables [49].

Preliminary analyses of obtained experimental data using common regression methods, i.e., linear, nonlinear, multivariate regression, etc., yielded poor results in describing the obtained experimental data, and even weaker predictive performance. This is due to a complex nature of the phenomena itself, but also, due to a relatively sparse amount of data available from each measurement (50 data points), whose availability is hindered by extremely complex and time-consuming experimental methodology. Contemporary methods, employed in the computer science branch, namely, data science, consisting of data mining, machine learning (ML) and artificial intelligence (AI), are often used in complex and/or large data analysis [188]. The process of data mining is used to extract useful (insightful) information from a bulk of observed data, thus, the result of data mining is not data, but discovery of patterns and general knowledge which is impossible for a human analyst to achieve due to complex relationships or the sheer amount of data [65]. This approach requires interdisciplinary use of machine learning and/or artificial intelligence algorithms in order to provide the sought insights. Methods used in this work comprise of multiple machine learning algorithms, and artificial intelligence methods in the form of genetic programming (GP) algorithms. Generally, machine learning algorithms for regression problems provide a so-called black-box solution which gives predictive results but, unfortunately, does not give any functional mathematical form of the underlying relationships in the data [65], [84], [188]. These methods are used in the context of data mining for obtaining important insights into the analysed variable space through visualization analyses, providing knowledge for further studies. Used machine learning algorithms in this work are additive regression, stacking and bagging classifiers, lazy algorithms, multi-layer perceptron, support vector machines, decision trees and forest ensembles [21], [84], [189]. All of them were used to develop models by data preparation, training the algorithms with the data, and optimizing each of their hyper-parameters, in order to develop the models, whose best obtained results are presented in the following chapters.

Furthermore, besides conventional machine learning methods, artificial intelligence methods are also employed in the form of genetic programming [139]. This group of methods provides

an evolutionary approach to development of computer programs or mathematical expressions which are, in comparison to ML-derived black-box models, directly usable and understandable by humans in mathematical or algorithmic form. This is the most valuable tool in the current state-of-the-art of predictive methods [95] which has been thoroughly proven by most complex problems in a wide variety of research and development [87], which will be thoroughly addressed later in this chapter. The employed type of genetic programming in this work is symbolic regression (SR) [21], [22], this method provides means for development of mathematical expressions [147] (regression models) which describe the data they were trained on with the best obtainable predictive performance, which is defined by different performance metrics.

A proper assessment and validation of the derived model(s) is also addressed. For this purpose, the results of the numerical analyses are assessed via a comparative statistical validation of each of the used algorithms, and separately for the employed machine learning regression and symbolic regression methods. The best performing model's predictive performance is, finally, thoroughly scrutinized.

5.1. Test Dataset – Experimental Measurements

Separately performed experimental measurements, are intended to provide a testing dataset for the developed models. These measurements present an un-seen dataset whose results the developed model needs to predict in the best possible way. This dataset provides a benchmark for all the developed models, enabling a thorough testing for their predictive performance. Each model's predictive performance was scrutinized on predictions of F_f from the input variables of this testing dataset. Given the fact that these measurements are performed on samples that were not dried prior to the measurements – yielding, hence, realistic habitual conditions, they provide, moreover, a more difficult predictive challenge for the used advanced numerical models, presenting a realistic scenario in which the model must provide good predictions. These measurements were conducted using the described methodology from the earlier chapters, including the described calibration factor corrections.

Conventionally in ML methods, the whole available dataset is divided into subdivisions comprising of the main training data, validation data, and testing data [84]. Main training data provides input information for the learning (training) process and requires the largest available amount of data (theoretically if an algorithm could be trained on all possible outcomes, it would have perfect predictive performance), validation data is required for optimization of algorithms'

hyper parameters by testing the learned model on this set after each training iteration, and finally, the testing dataset which is completely left out of any interaction with the algorithm during the training phase, and is only used as an independent, realistic presentation of the real world case scenario for testing the developed model's performance [65], [84]. Generally, the ratios between these subdivisions is used as 2/3 of the whole dataset for training, and 1/3 for validation and testing datasets [189]. Thus, the adopted size of the test dataset is chosen to be 15 measurement points with 5 repetitions for each of the 5 analysed thin film samples, representing roughly 1/3 of the main, CVT based dataset, bearing in mind the experimental complexities and the time-consuming nature of the experimental procedure.

The random number generator (Monte Carlo - MC) [57] is used as implemented in GoSumD [2] for a simple random sampling in the boundaries of the considered variable influencing parameters F_N , ν and \mathcal{G} . The MC based measurement points are provided in Appendix C. A simple random sample is a subset of a statistical population in which each member of the subset has an equal probability of being chosen [90]. Test dataset measurements are thus conducted by using the described experimental methodology with the adhesion-corrected calibration factor α that takes into account the variability of F_A as determined on the TGF11 calibration sample (cf. Figure 3.12a).

To test the experimental and modelling prediction hypotheses, the measurements are made on different batches of equivalent samples obtained by the described synthesizing processes and are meant to present as much as possible a realistic state of the surfaces of the used samples in air, i.e., without subjecting them to a drying process before the measurements as was done in the previously described experiments. As depicted in Figure 5.2a, the temperature variability of adhesion force F_A on the calibration sample TGF11 is again evident, and comparable to results obtained earlier, thus confirming the described need for calibration factor correction. More interestingly, in Figure 5.2b, are depicted adhesion force F_A measurements for all samples, where for clarity reasons the error bars are omitted (the complete acquired dataset is available in Appendix D, the effects of different starting conditions (not dried samples), are hence clearly visible for each of the thin-film samples in considerably less similar absolute values of the F_A when compared to the CVT F_A measurements. It can be appreciated here also that the F_A values are the highest (up to of 90 nN) for the TiO_2 and Al_2O_3 samples. Compare in this regard the values on Figure 5.2b with those reported in Figure 3.17, where the measured F_A values on all the used samples are in the ~ 19 nN range. In fact, while MoS_2 shows similar maximal adhesion force values of ~ 20 nN as observed in the CVT-based experiments, on the

SS sample are also obtained higher F_A values than in the previous measurements.

The occurrence of higher F_A values in the lower temperature range (i.e., that close to ambient temperature) is most probably due to the water-vapour layer adsorbed on the surfaces of the samples. On the other hand, the attained variation of the measured F_A values is then the result of the different surface wetting properties. In fact, in the CVT-based measurements, before the SPM experiments the samples are dried for a prolonged amount of time, hence stabilizing the adsorbed water-vapour layer on the surfaces of the samples to a lower value, and consequently all the samples showed similar F_A values in the whole temperature range. This observation is in accordance also with the previously evidenced fact that the adhesive forces in the nanoscale range are strongly dependent on the adsorbed vapour layer formed between the tip and the sample (cf. Section 3.5.2).

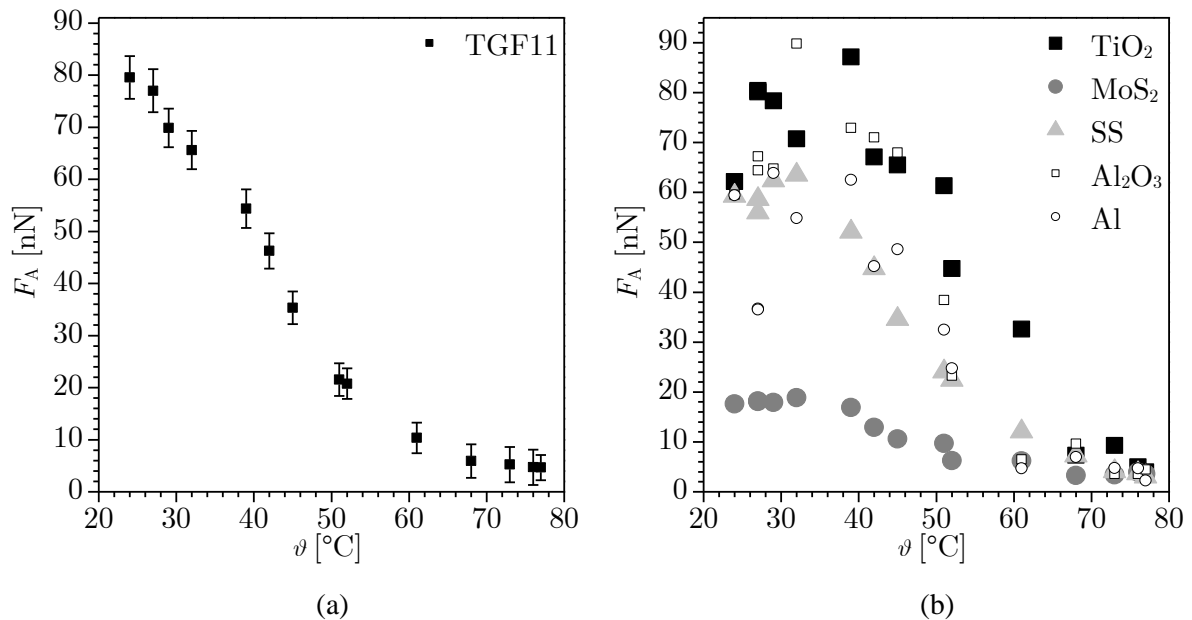


Figure 5.2 Measured F_A values for test dataset of experimental points on the TGF11 calibration sample (a), and on all the analysed thin-film samples (b).

In any case, it can be concluded that, although starting at different values, the trends of variability of the adhesion force with temperature is similar in both sets of measurements (CVT-based and those considered in this MC-based test dataset). What is more, the adhesion force measured on all the used samples in the herein considered experiments tends to stabilize for the highest temperatures at a value of around 4 nN, equivalent value of which is consistent with the previous (CVT-based) experimental results, and supports the theory that the adsorbed water-vapour menisci on the surfaces of the samples are minimized with higher temperatures.

The measured values of nanometric friction force F_f for all the thin-film samples in the MC-

based test dataset are shown, incorporating again, adhesion variability, in Figure 5.3 (the complete set of acquired data is available once more in Appendix D). The corresponding first-order correlation values for the same test dataset measurements is, in turn, given in Table 5.1.

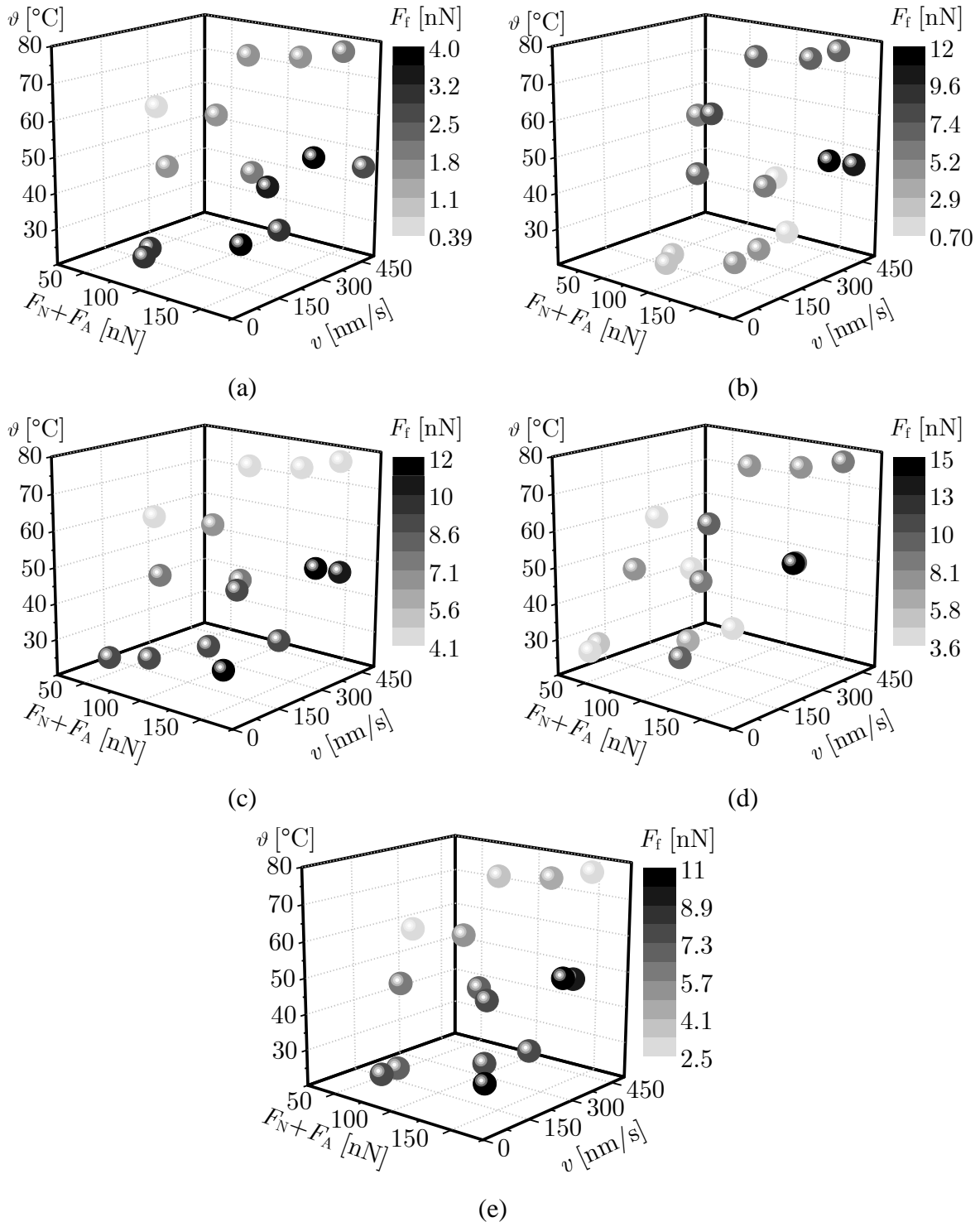


Figure 5.3 Colour-coded distribution of experimentally determined nanometric F_f values for the test dataset measurement points for the Al_2O_3 (a), TiO_2 (b), Al (c), MoS_2 (d) and SS (e) samples vs. the considered process parameters.

In the shown Figure 5.3a are hence depicted the values of F_f for the Al_2O_3 sample, with similar trends as in the case of the CVT measurements. The highest F_f values are concentrated again for temperatures in the 40 to 50 °C range and for the highest F_N+F_A total load. It is, in fact, evident that, due to higher adhesion in the lower temperature ranges, for all the samples the points are shifted towards right (higher total loads). Higher velocities induce, in turn, again, a diminishing effect on friction. The respective correlation coefficients for Al_2O_3 reported in Table 5.1 allow evidencing interesting results for all the considered effects. In fact, the influence of velocity has an impact of -0.12, when compared to that in the CVT case of 0.0023. The effect of the total load is higher with the correlation value of 0.57 (the higher effect of F_A is evident – see Figure 5.2b), while, when compared to previous measurements, the correlation coefficient of temperature has an almost identic value of -0.69.

Table 5.1 Matrices of correlation coefficients for the influencing parameters on the nanometric F_f values on the MC test dataset points for ALD samples.

	v	F_N	ϑ	F_f	F_A	F_N+F_A
Al_2O_3	v	1				
	F_N	0.24	1			
	ϑ	0.31	0.68	1		
	F_f	-0.12	-0.03	-0.69	1	
	F_A	-0.20	-0.59	-0.90	0.69	1
	F_N+F_A	0.11	/	0.05	0.57	/
TiO_2	v	1				
	F_N	0.24	1			
	ϑ	0.31	0.68	1		
	F_f	0.24	0.80	0.63	1	
	F_A	-0.28	-0.60	-0.94	-0.53	1
	F_N+F_A	0.09	/	0.05	0.64	/

The results for the TiO_2 sample, shown in Figure 5.3b, show again higher values of F_f in the high-load, mid temperature regime, but lower relative values for the lower temperatures, which is consistent with the results obtained for this sample in the previous measurements. The correlations show in this case a higher positive impact of velocity, temperature and the total load (almost double the value with respect to that in the CVT-based case, which is probably due to higher adhesion than in the CVT measurements).

The Al sample results (Figure 5.3c), show also similar trends with a prominent adhesion shift of points, while the correlation factors, compared to those of the CVT-based analyses, show a higher negative impact of velocity (-0.24), a very similar effect of temperature (-0.75), and a significantly smaller influence of the total load, with a correlation coefficient of 0.29 (vs. the previously established 0.46), which is hypothesized to be due to a lubricative effect.

Table 5.2 Matrices of correlation coefficients for the influencing parameters on the nanometric F_f values on the MC test dataset points for PLD samples.

		v	F_N	\mathcal{G}	F_f	F_A	F_N+F_A
Al	v	1					
	F_N	0.24	1				
	\mathcal{G}	0.31	0.68	1			
	F_f	-0.24	-0.15	-0.75	1		
	F_A	-0.12	-0.62	-0.88	0.72	1	
	F_N+F_A	0.23	/	0.28	0.29	/	1
MoS ₂	v	1					
	F_N	0.24	1				
	\mathcal{G}	0.31	0.68	1			
	F_f	0.07	0.80	0.35	1		
	F_A	-0.29	-0.65	-0.95	-0.42	1	
	F_N+F_A	0.22	/	0.61	0.81	/	1
SS	v	1					
	F_N	0.24	1				
	\mathcal{G}	0.31	0.68	1			
	F_f	-0.16	-0.13	-0.71	1		
	F_A	-0.29	-0.68	-0.98	0.70	1	
	F_N+F_A	0.11	/	0.20	0.33	/	1

The MoS₂ sample's F_f results shown in Figure 5.3d show the smallest adhesion induced shift in the total load axis direction, due to the lowest manifested F_A values (Figure 5.2b). As before, the influence of v is almost negligible (0.07), the effect of the total load is augmented to 0.81, but still in the positive range, while the influence of temperature shifts to 0.35 (vs. the correlation coefficient value of 0.061 in the CVT-measurements). Finally, the SS sample also

demonstrates a similar behaviour (Figure 5.3e) and, in terms of the resulting correlations, results, if compared to CVT-based data, in a slightly more negative effect of velocity, a very similar correlation factor value for the total load (0.33 vs. 0.39), and a slightly bigger negative influence of temperature (-0.71 vs. -0.57).

The correlation coefficient results, summarized in Table 5.3, allow evidencing the effect of the variable adhesion forces on nanoscale friction, and, interestingly, despite the evidenced differences, show also distinct regularities in the overall trends for the same thin-film samples.

Table 5.3 Summary of the effects of the influencing parameters on the F_f value for the used thin-film samples in the MC-based test dataset.

	F_N	F_A	F_N+F_A	v	\mathcal{G}
Al ₂ O ₃	0	+	+	0	-
	(-0.03)	(0.69)	(0.57)	(0.12)	(-0.69)
TiO ₂	+	-	+	+	+
	(0.80)	(-0.53)	(0.64)	(0.24)	(0.63)
Al	0	+	+	-	-
	(-0.15)	(0.72)	(0.29)	(-0.24)	(-0.75)
MoS ₂	+	-	+	0	+
	(0.80)	(-0.42)	(0.81)	(0.07)	(0.35)
SS	0	+	+	0	-
	(-0.13)	(0.70)	(0.33)	(-0.16)	(0.71)

5.2. Data Preparation

Based on the analysis of large sets of training data, machine learning (ML) methods are a class of numerical algorithms that allow revealing patterns, thus “learning” how to map the respective inputs to outputs also on new sets of data applied to the same system, thus “predicting” its behaviour [65], [84]. The relative weights pertaining to the parameters of the model are initialized to small random values, and, in response to estimates of errors on the training dataset, updated via an optimization algorithm [65], [188]. Given the use of small weight values and the employment of the values of the errors between the predictions and the expected values in the optimization process, the scale of inputs and outputs used to “train” the model are an essential factor for the quality of the resulting method, since the scale of used dataset(s) comprises type of data used (numeric discrete in this case) and their order of

magnitude, i.e., the order of sliding velocity parameter v is in the order of magnitude 10^2 (5 to 500), and, i.e., the value of nanoscale friction force F_f is in the order of magnitude 10^1 , which requires the whole dataset (inputs and outputs) to be scaled. In fact, unscaled input variables can result in a slow or unstable learning process, whereas in regression problems unscaled target variables can result in “exploding” gradients causing the learning process to fail [84], [188]. Especially when features of data have different ranges, which is the case for all three variable process parameters in the herein performed study, data preparation preceding the training of the model involves, thus, using techniques to rescale the input and output variables, such as are the normalization and standardization techniques. Normalization usually means scaling a variable to have a value between 0 and 1, whereas standardization transforms the data so as to have a zero mean and a standard deviation of 1 [65].

Depending on the used ML method, the data in this study is therefore standardized or normalized. Data normalization is hence calculated as [65], [106]:

$$x_{norm} = \frac{x - x_{min}}{x_{max} - x_{min}} \quad (5.1)$$

where x_{norm} is the normalized value of the variable x , while x_{min} and x_{max} are the respective minimum and maximum of the values of x .

Data standardization (or z-score) is, in turn, expressed as [65], [106]:

$$z_i = \frac{x_i - \bar{x}}{\sigma} \quad (5.2)$$

where x_i is the datapoint, \bar{x} is the mean value of the samples, and σ represents the standard deviation.

Experimental data obtained in the 50 points determined via the DoE-based CVT method for each of the considered thin-film samples are thus used next in the training process based on the herein considered ML algorithms, which results in models developed for each sample via each considered algorithm. To explore then the possibility to obtain a general model apt at describing (and predicting) the frictional properties of all analysed materials, all the used algorithms are also trained with the complete set of experimental data, i.e., the data in the 250 measurements used for the five considered thin-film materials. This approach not only provides the opportunity to obtain a generalized insight into the observed physical phenomena, but it is also based on a set of data for the algorithms to learn from, therefore inherently providing better performing models. In training on data pooled for different materials, it is important to describe each material type, which is a (nominal) input variable inserted as a numeric class which can

be input into the machine learning process [65], which is done in the herein considered case, as shown in Table 5.4, by using binary encoding (also called *on-hot* or *one-of-K* scheme) [49], [104], [188] for each of the resulting material classes. This adds to the used ML models additional five variables (dimensions).

Table 5.4 Used encoding classes for the used thin-film sample materials in the pooled data models.

	x_4	x_5	x_6	x_7	x_8
Al	1	0	0	0	0
Al ₂ O ₃	0	1	0	0	0
MoS ₂	0	0	1	0	0
TiO ₂	0	0	0	1	0
SS	0	0	0	0	1

5.3. Data Normality

The experimental data used for training the ML models must also be assessed in terms of the respective normality characteristics defined by skewness and kurtosis parameters [84], [105], [106], [110]. In fact, normally distributed data are desirable for obtaining good predictive performances. Symmetric normal distribution has the property of containing the mean, median, and mode values of the distribution at the peak of the ‘bell curve’. Skewness is a measure of the asymmetry of the distribution, when compared to the normal distribution, the skew can be positive or negative indicating to which direction the distribution is skewed, positive – the distribution is elongated in the positive direction of the values, and negative skew presents the opposite, the positive and negative ends of the distribution curve are also called tails. Also, the shape of the distribution can be described by the kurtosis values, this value presents the curvature of the peak of the ‘bell-curve’ and length of the tails (heaviness), by using positive kurtosis values for describing a leptokurtic distribution, i.e., higher peak of the curve and closer tails w.r.t. the normal distribution, zero value for the mesokurtic or completely normal distribution, and negative or platykurtic for lowered (blunter) peak of the distribution with heavier (wider) tails w.r.t. the normal distribution. Normality of data is analysed by calculating their statistical properties in terms of skewness and kurtosis, parameters that are reported for all measured data in the Appendices B and D. Skewness or, as it is sometimes referred to, Pearson's moment coefficient of skewness of a random variable x , having an average value of \bar{x} , is the

third standardized central moment or, simply, the moment coefficient of skewness γ_1 of a probability model [5], [106], [110] and [105]:

$$\gamma_1 = \frac{n \sum_{i=1}^n x_i - \bar{x}^3}{(n-1)(n-2)\sigma^3} \quad (5.3)$$

where n denotes number of samples while x_i is the value of the sample and \bar{x} the mean of the distribution. Skewness of a normal distribution is zero, and any symmetric set of data should have a skewness near zero.

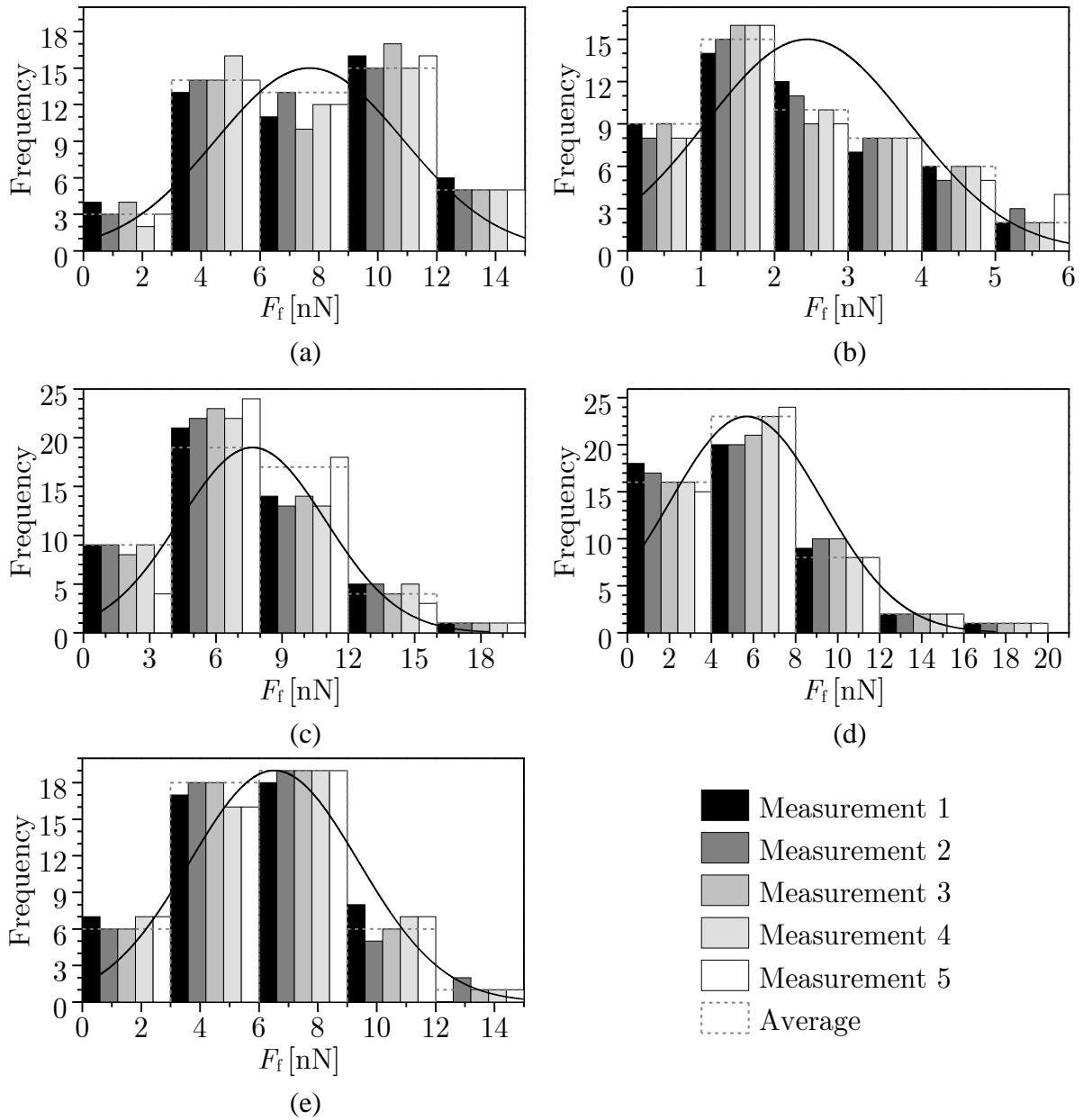


Figure 5.4 Histograms and normal distribution fits for all F_f measurements at CVT-based experimental points on Al (a), Al_2O_3 (b), MoS_2 (c), TiO_2 (d) and SS (e) samples.

On the other hand, kurtosis is a measure of the combined sizes of the two tails, i.e., the amount of probability in the tails [106]. In general, its value is compared to the kurtosis of the normal distribution, which is equal to 3. If the distribution of the data is such that the kurtosis value is < 3 , then the dataset has heavier tails than a normal distribution while, if kurtosis is > 3 , the opposite is true [105]. The expression used for computing the kurtosis γ_2 is [105], [106]:

$$\gamma_2 = \frac{\sum_{i=1}^n (x_i - \bar{x})^4 / n}{\sigma^4} - 3 \quad (5.4)$$

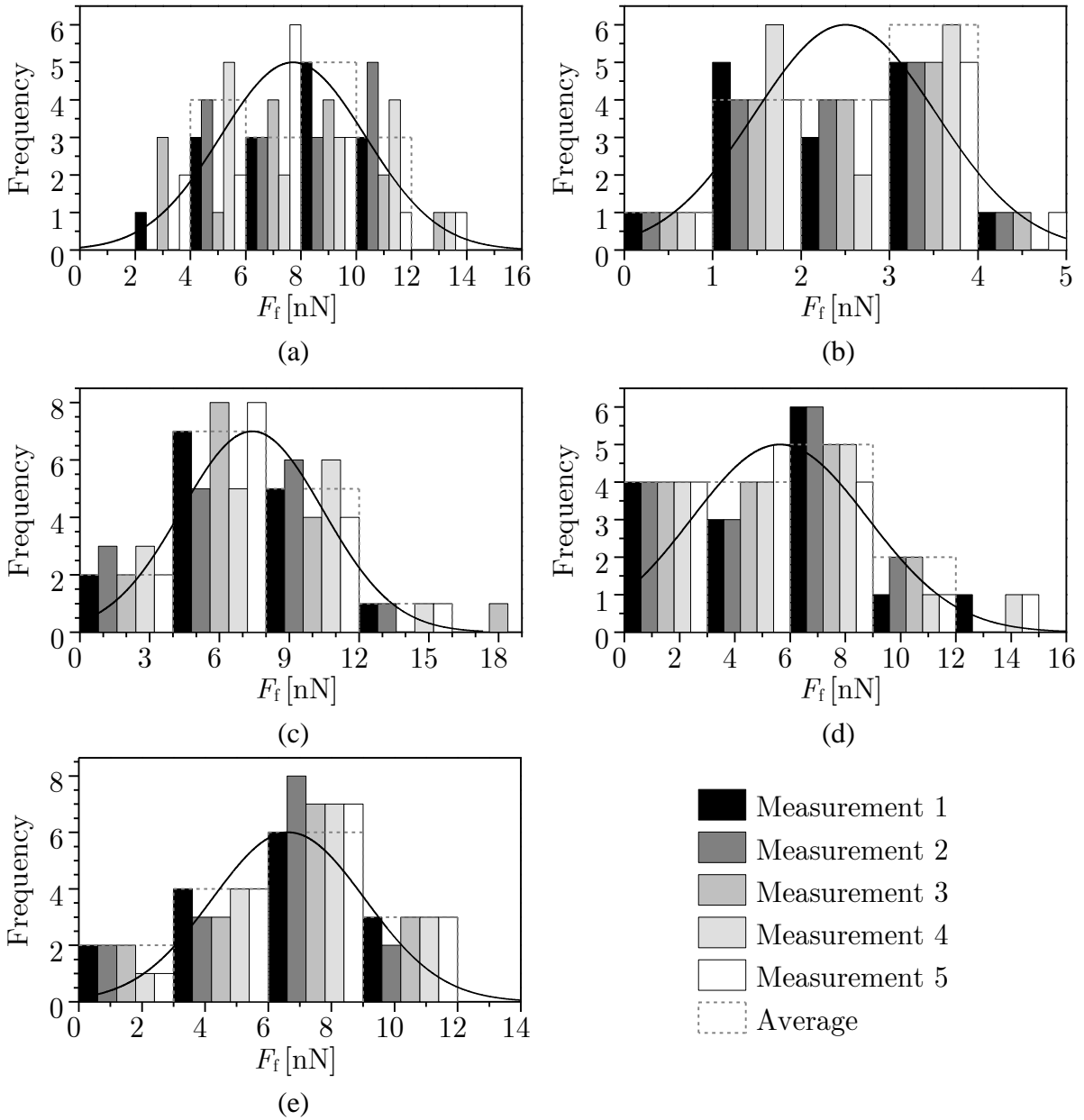


Figure 5.5 Histograms and normal distribution fits for all F_f test dataset measurements at MC-based experimental points on Al (a), Al_2O_3 (b), MoS_2 (c), TiO_2 (d) and SS (e) samples.

This definition of kurtosis is hence used so that the standard normal distribution has a kurtosis of zero. In Figure 5.4 and Figure 5.5 are depicted histograms of all 5 measurements and the average value, with associated normal distribution fits of measured F_f data for the training (CVT) and testing (MC) datasets, respectively. The fitted normal distribution curves visually describe the respective skewness and kurtosis levels for each measurement.

In the CVT data presentation in Figure 5.4, the Al sample shows most close to normal distribution which, while the TiO₂ sample exhibits high amount of positive skewness. MOS₂ and SS samples show similar distributions of slight positive skewness, and Al₂O₃ shows slightly higher positive skewness with a platykurtic nature. In Figure 5.5 are presented histograms and distribution fits for the test (MC) dataset, showing again, the best normality characteristics of the Al sample, while the TiO₂ sample again shows relatively high positive skewness. Other samples' distribution exhibit low positive skewness when compared to the TiO₂ sample.

Complete values of kurtosis and skewness are provided for all measurement points in the Appendix B for the CVT dataset, and in Appendix D for the MC dataset.

Additional tests of normality are also used in this work on all the datasets collected experimentally on the used thin-film samples, namely the Anderson-Darling (AD) test [106], which compares the empirical cumulative distribution function of the sampled data with that expected for a normal distribution. The resulting p -value, i.e., a parameter which is the result of the statistical AD hypothesis test, obtained for a dataset after is thus compared to the selected significance level of 0.05. The p -values obtained for all the herein considered samples confirm hence the null-hypothesis of the test, i.e., the data can be considered normal. For the purpose of detecting eventual outliers, i.e., a datapoint which differs significantly from the other measurements, the Grubbs test [106] is also conducted by calculating the largest absolute deviation of each point from the sample mean, showing no outliers at the 0.05 significance level.

5.4. Metrics – Model Selection Criteria

The decision about selecting the best model is not as straight-forward as it could appear, since the best fitness and predictive performance of a determined model cannot be assessed based on a single metric alone, but only via a careful analysis of model's outputs (including the plotting of the results graphically), residuals, and distribution of predictions [49]. This implies a considerable effort, especially since in the case considered in this thesis (or other similar problems) the multidimensionality of the considered phenomena presents a visualization

problem that requires a large number of low-dimensional plots for all the intricacies of the model solutions to be fully appreciated.

What is more, all the statistics relative to the errors incurring in the outputs of the considered models compare true values to their estimates, but, although allowing to evidence "how far away" the estimated values are from the true value, they all do it in a slightly different way.

One of the most frequent error estimates is the mean absolute error (MAE), which measures the average magnitude of the errors in a set of forecasts, without considering their direction. It measures the accuracy for continuous variables. Expressed in words, MAE is the average of the absolute values of the differences between the forecast and the corresponding observation over the verification sample. MAE is also a linear score, which means that in the average all the individual differences are weighted equally [49], [65]:

$$\text{MAE} = \frac{1}{n} \sum_{i=1}^n |y_i - x_i| \quad (5.5)$$

where y_i is the predicted and x_i the true (experimental) value in a dataset constituted by n members.

The root mean square error (RMSE) is, in turn, a quadratic scoring rule that measures the average magnitude of the error [49], [65]. RMSE represents the standard deviation of the residuals (prediction errors) that represent a measure of how far the data points are from the regression line. In other words, RMSE is a measure of how spread out these residuals are [49], [65]. Expressing the equation used to calculate the RMSE in words, RMSE is the squared difference between the forecast and the corresponding observed values, averaged over the sample. The root of the mean square error indicates the accuracy of the probability estimates that are generated by the model [49], [65]:

$$\text{RMSE} = \sqrt{\frac{1}{n} \sum_{i=1}^n (y_i - x_i)^2} \quad (5.6)$$

Since the errors are squared before they are averaged, RMSE gives a relatively high weight to large errors, and it is thus most useful when large errors are particularly undesirable [49], [65].

MAE and RMSE can be used together to diagnose the variation in the errors in a set of forecasts. In that, RMSE value will always be larger or equal to MAE. The greater the difference between them, the greater the variance in the individual errors in the sample. If, in turn, RMSE equals MAE, then all the errors are of the same magnitude.

R-squared (R^2) is a further statistical measure of a regression model that represents the

proportion of the variance of a dependent variable in relation to an independent variable or variables [49], [65]. Whereas the previously used correlation expresses the strength of the relationship between an independent and a dependent variable, R-squared is the measure to what extent the variance of one variable relates to the variance of the second variable. The respective coefficient of determination is then used to express how much the variability of one factor can be caused by its relationship to another factor. It relies heavily to trend analysis and it is represented as a value between 0 and 1; the closer the value is to 1, the better the fit, or relationship, between the two factors [49], [65]. The coefficient of determination is calculated as [49], [65]:

$$R^2 = 1 - \frac{\sum_{i=1}^n (y_i - x_i)^2}{\sum_{i=1}^n (x_i - \bar{x}_i)^2} \quad (5.7)$$

where \bar{x}_i is the mean of the true values x_i , while the y_i is the predicted value.

In symbolic regression models based on genetic programming (GP-SR), the performance metrics in terms of the here described MAE, RMSE, and R^2 metrics are not enough to assess the quality of the model [95]. Namely, the GP-SR models are symbolic mathematical expressions, and as such their form must be assessed also in terms of complexity [95], [139]. There are, hence, multiple combinations of metrics to be satisfied. The dominant numeric metric for the prediction assessment is chosen to be here the R^2 value, since this parameter best describes the form of the solution in the variable space, so higher R^2 values present the model solutions which best follow the trend of the values, so that the final decision on selecting the best GP-SR model is based on finding the model with a best combination of minimal expression complexity and maximal R^2 . This is accomplished by employing the Pareto frontier method [86], [101], by which a set of multiple solutions is chosen to be quasi-optimal since the optimality is selected on the basis of multiple conditions, optimality of the model is based on the criterion of finding the models characterised by the minima of the combination of the considered multiple process parameters (i.e., Pareto frontier), of the smallest $1-R^2$ values and of the model complexity.

5.5. k-fold Cross-validation

Learning the parameters of a predictive model and testing the resulting function describing the correlation between the input and output parameters on the same dataset is a methodological

mistake: a model that would just repeat the labels of the samples that it has just seen would have a perfect score, but it would fail to predict anything useful on yet-unseen data. This situation is called overfitting [84], [188]. To avoid it, when performing a machine learning experiment it is therefore common practice to hold out part of the available (input) data [65], [84] for validation of best performing hyper-parameters. This is achieved (Figure 5.6) by cross-validation method, i.e., the usage of a limited sample in order to estimate how the model is expected to perform when used to make predictions on data not used during the training, is hence primarily used in applied machine learning to assess the level of confidence (the “skill”) of a model on unseen data [65], [84].

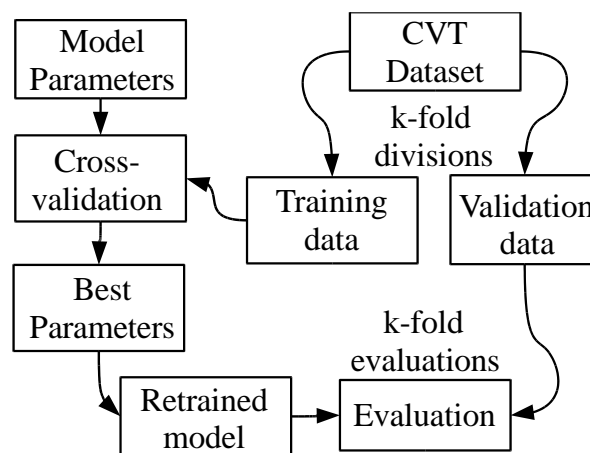


Figure 5.6 Schematic of cross-validation method used to optimize the hyper-parameters of machine learning models on training dataset.

Cross-validation is therefore a technique used to evaluate predictive models by partitioning the original sample (CVT dataset) into a training set to train the model, and a validation set to evaluate the optimal parameters [189]. In a form of this procedure, known as k-fold cross-validation [65], [84], the original sample is thus randomly partitioned into k equal size subsamples. Of the k subsamples, a single subsample is retained as the validation dataset for testing the model, while the remaining k-1 subsamples are used as training data. The cross-validation process is then repeated k times (k-folds), with each of the k subsamples used exactly once as the validation data. The hence obtained k results can then be averaged (or otherwise combined) to produce a single estimate (metric) of the quality of the model. The advantage of this method is that all observations (all measured data, all input data) are used for both training and validation, and each observation is used for validation exactly once [65], [84]. The choice of a value for k is usually 5 or 10, but there is no formal rule. As k gets larger, the difference in size between the training set and the resampling subsets gets smaller. As this difference

decreases, the bias of the technique becomes smaller. A value $k = 10$ is very common in the field of applied ML and it is often recommended [65], [84].

All the models used in this study are thus subjected to 10×10 cross-validation, i.e., 10 repetitions of 10-fold cross-validations on the complete DoE-CVT-based training datasets. This approach involves randomly dividing the set of observations (measurements in the 50 points as determined via the DoE-CVT approach) into k groups, or folds, of approximately equal size. The first fold is then treated as a validation set, and the method is trained on the remaining $k - 1$ folds. The general procedure is as follows [65]:

- ※ shuffle the dataset randomly;
- ※ split the dataset into k groups;
- ※ for each unique group:
 - take the group as a hold-out or test data set;
 - take the remaining groups as training datasets;
 - fit the model on the training sets and evaluate it on the test set;
 - retain the evaluation score and discard the model;
- ※ summarize the skill of the model using the sample of model evaluation scores.

After defining in Section 5.2 the preparation procedures needed to use the experimentally acquired data on the considered thin-film samples in the considered numerical evaluation tools, in Section 5.3 have thus been defined the evaluation metrics parameters that will be used to comparatively assess and validate the quality of the used predictive models. This provides the basis to implement next the considered ML and GP numerical methods to determine functional correlations between the value of nanoscale friction and the corresponding influencing parameters.

5.6. Machine Learning Regression Methods

Based on the considerations of Sections 5.2 and 5.3, and using experimental data measured in the points determined via the DoE-CVT approach, ML is applied here to obtain the dependency of the friction force F_f in the nanodomain in dependence on the process parameters F_N , v , and \mathcal{G} . Presented models are developed using the TensorFlow [108], Scikit-learn [127] and GoSumD [2] implementations.

There is a common principle that underlies all supervised ML algorithms for predictive modelling, supervised ML algorithms are, in contrast to un-supervised methods, trained on a dataset which comprises of both inputs and corresponding outputs for each datapoint, while the

un-supervised ML methods rely only on the input data and are mainly used for clustering and association (i.e., image recognition) [84]. Supervised ML algorithms are described as learning a target function (f) that best maps the input variables (x) to an output variable (y). This is called predictive modelling or predictive analytics and the goal is to make the most accurate predictions possible [49], [84]. In this process the correlation function's form is unknown, i.e., there is no predefined form to fit the parameters. It is thus imperative to “mine” through the data by employing multiple methods of predictive modelling [65] and deduce conclusion that will lead to further understanding of the herein considered complex physical phenomenon. As multiple ML algorithms were used in the used data mining process, only the ones which show satisfying predictive performance are shortly described below, as are their performance metrics achieved on the unseen test datasets. The considered group of ML models, described in the following sub-sections, is generally consisting of conventional ML algorithms that result in a black-box model, i.e., the obtained solutions are not usable in practical applications in a mathematical form, but, nonetheless, these tools are powerful predictive algorithms presenting the state-of-the-art of applied ML.

5.6.1. Multilayer Perceptron

A multilayer perceptron (MLP) is a deep artificial neural network, meaning it is consisted of more than two layers of perceptrons, which are algorithms used for supervised learning of functions, i.e., binary classifiers, which provide outputs in the form of decision whether or not an input belongs to a certain class. They are, in turn, composed of an input layer receiving the signal, an output layer that evaluates or predicts the input and, in between those two, an arbitrary number of hidden layers that are the true computational engine of the MLP algorithm. MLPs with one hidden layer can approximate any continuous function [175].

In the forward pass, the signal flow moves then from the input layer through the hidden layers to the output layer, and the decision of the output layer, i.e., the prediction, is measured against the ground truth labels [175] which present the actual data the model needs to predict. In the backward pass, using backpropagation and the chain rule of calculus for calculation of the derivative of the two or more-function compositions, partial derivatives of the error function are back-propagated through the MLP taking into account the various weights and biases defined as internal parameters which provide feedback for the training process. That differentiation results in gradients, or a landscape of errors, along which the parameters may be adjusted as they move the MLP one step closer to the error minima [175]. This can be done

with any gradient-based optimisation algorithm, such as the stochastic gradient descent [175], which is used in this work. The used activation function [175] defining the output of the neuron is, in turn, a sigmoid function, i.e., a logistic function (an ‘S’-shaped curve) [175] with five hidden layers used.

5.6.2. *Random Decision Trees and Forests*

Random Forest (RF) is one of the most popular and most powerful ML algorithms³. It is a type of ensemble ML algorithm called bootstrap aggregation or bagging. The bootstrap is a powerful statistical method for estimating a quantity from a data sample, such as mean values [151], [184]. In bagging, the same approach is used, but instead of estimating entire statistical models, the most commonly generated decision trees is estimated for the given data [151], [184]. RF are based on combining multiple decision trees into a single stronger predictor. Each tree is trained independently with a randomly selected subset of the considered instances (i.e., experimental data). The resulting prediction is an average of multiple predictions. RFs try to reduce the respective variance by not allowing decision trees to grow large, making them harder to overfit [151], [184].

Trees are an important type of algorithm for predictive modelling ML, the most common representation of the decision tree model being the binary tree. Each node represents therein a single input variable (x) and a split point, i.e., a split in the tree structure with the goal of achieving more optimal (closer to the real result) value of the resulting value of that variable (assuming the variable is numeric). The leaf nodes of the tree contain the output variable (y) which is used to make the prediction. Predictions are hence made by “walking” the splits of the tree until getting to a leaf node and obtaining as output the class value at that leaf node [151], [184].

Trees are fast to learn and very fast in making predictions. They are also often accurate for a broad range of problems and do not require any special preparation of data [151], [184]. Decision trees have a high variance and can yield more accurate predictions when used in an ensemble that is used in the form of an RF algorithm [151], [184].

As already pointed out above, multiple samples of the herein obtained experimental training

³ According to the latest Machine Learning Methods Poll “Top Data Science and Machine Learning Methods Used in 2018, 2019” available at:
<https://www.kdnuggets.com/2019/04/top-data-science-machine-learning-methods-2018-2019.html>
(accessed on November 2019)

data are used in the ML models that are, hence, constructed for each data sample. In order to make predictions for new data, each model makes thus a prediction, and the predictions are averaged to give a better estimate of the true output value. RF is a tweak on this approach where decision trees are created so that, rather than selecting optimal split points after validation, suboptimal splits are made by introducing randomness [151], [184], thus providing more diversity in solutions. The difference of the models created for each sample of the data is, therefore, more pronounced than it would otherwise be, but they are still accurate in their unique and different ways. Combining their predictions, results, however, in a better estimate of the true value [151], [184].

5.6.3. Support Vector Regression

Support vector machines (SVM) are perhaps one of the most popular class of ML algorithms. Generally, in SVM a hyperplane is selected to best separate the points in the input variable space, by their class, either class 0 or class 1, which enables the creation of a hyperplane [64], [103]. In 2D this separation is easily visualized, but the same approach works also for multidimensional data. The SVM (or SVR, for support vector regression) learning algorithm seeks for the coefficients that result in the best separation of the classes by the hyperplane. The distance between the hyperplane and the closest data points is then referred to as the margin. The best or optimal hyperplane that can separate the two classes, is the one that has the largest margin. Only these cases are relevant in defining the hyperplane and in the construction of the classifier, i.e., a function which describes a set of instances that have common features [84]. These class of points are thus called the support vectors, since they “support” or define the hyperplane [64], [103].

The ν -SVR method is used in the thesis as implemented in the commercially available GoSumD software [2]. This type of SVR involves the ν parameter which is used to limit the number of support vectors in the solution with respect to the total number of samples in the dataset [103]. The input variables are scaled in it by normalization, whereas the radial basis function (RBF) kernel is used, where the RBF’s value depends only on the distance between the input and a fixed point, i.e., a support vector, and its parameters are optimally chosen by employing the BOBYQA optimization algorithm (Bound Optimization BY Quadratic Approximation) [136]. SVM/SVR algorithms of the on-line LIBSVM library [37], containing the often-used SVR/SVM algorithms, are finally applied.

By using the analytical representation of the model obtained via the SVM–regression method

(SVR), the output value can then be predicted from the expression [103], [148]:

$$f(x) = \sum_{i=1}^l \alpha_i K(x, x_i) + b \quad (5.8)$$

where x is the input vector, x_i is the i -th support vector, α_i are the coefficients of the used kernel function, l is the number of support vectors and coefficients, K is the kernel function (RBF), and b is a free parameter used for scaling the results.

5.7. Comparison of Machine Learning Models

After successful numerical trials involving many combinations of ML algorithms, including SVR, decision trees and forest ensembles, additive regression, stacking and bagging classifiers, lazy algorithms, and MLPs, their performances can be assessed based on the metrics defined in the above Section 5.3. All models are thus subjected to a 10-fold cross-validation, and only the models that achieved an R^2 value above 0.5 are presented.

5.7.1. 1D Considerations

All the reported predictive performance results are related to the best individual in the ensemble of cross-validated individuals. The values of the hence attained results on testing datasets are presented in Table 5.5 for the best-performing algorithms, where R^2 is selected to be the most dominant (but not exclusive) metric, with values of R^2 above 0.7 considered as good predictive performances (bolded).

All used ML algorithms are compared to the response surface model (RSM) employed as a base model for validating the obtained improvements in predictive performances. In fact, the achieved metrics values for the RSM model in Table 5.5 show poor predictive performances for all combinations of input data, i.e., for the data of each considered thin-film sample material separately, as well as for the pooled data including all analysed materials. The resulting R^2 values are thus in the range from 0.032 for the TiO_2 sample, to a maximal achieved R^2 value of 0.343 for the pooled data.

The RF algorithm shows better results, with the best achieved R^2 value of 0.73 for the Al sample, and the worst predictive result of 0.53 for the Al_2O_3 sample. All metrics of this algorithm show low error variance, i.e., a small difference between RMSE and MAE. The RF method yields also excellent predictive performances on the pooled dataset with an R^2 value of 0.81, which makes this method a candidate for further analyses. What is more, due to the nature of the ensemble of random decision trees, this method is inherently good at predicting the highly

nonlinear variability of the expected outputs.

The MLP algorithm shows even better predictive performances, with achieved $R^2 > 0.7$ for three out of the five considered thin-film sample materials, namely 0.77 for Al, 0.71 for MoS₂, and 0.78 for SS, with a low variance of RMSE and MAE. The performance on the pooled dataset is, interestingly, again the best one, with the resulting R^2 value of 0.88.

Table 5.5 Comparative presentation of predictive performances on the test datasets for the used ML models vs. the response surface methodology.

Algorithm	Sample	RMSE	MAE	R^2
RSM	Al	6.21	6.02	0.062
	Al ₂ O ₃	5.95	5.32	0.13
	MoS ₂	9.68	9.11	0.13
	TiO ₂	7.98	7.32	0.032
	SS	6.96	6.21	0.092
	Pooled	3.82	3.56	0.34
	RF	Al	0.75	0.63
Al ₂ O ₃		1.50	1.20	0.53
MoS ₂		2.12	1.71	0.68
TiO ₂		2.16	1.74	0.63
SS		1.59	1.28	0.55
Pooled		1.06	0.99	0.81
MLP		Al	0.85	0.72
	Al ₂ O ₃	1.64	1.36	0.63
	MoS ₂	2.02	1.60	0.71
	TiO ₂	2.17	1.75	0.68
	SS	1.87	1.54	0.78
	Pooled	0.99	0.77	0.88
	SVR	Al	1.46	1.23
Al ₂ O ₃		1.32	1.11	0.51
MoS ₂		1.34	1.15	0.75
TiO ₂		3.26	2.76	0.66
SS		3.05	2.48	0.72
Pooled		1.46	1.27	0.87

The SVR algorithm shows somewhat generally weaker performances in terms of the highest achieved overall R^2 values for all samples, with achieved R^2 value of 0.72 on the SS sample, also the MoS_2 sample shows better prediction R^2 metric of 0.75 w.r.t. the MLP method, while the pooled data case again results in the highest achieved performance of $R^2 = 0.87$. In SVR the variance of the RMSE-MAE metrics is the lowest.

As it can thus be seen in Table 5.5, all algorithms, including the RSM model, show the best predictive performances when trained by using the pooled dataset; this is due to the largest available set of training data, which provides to the model more information in terms of response variance and, thus, enhances predictivity. Models trained on pooled data show, therefore, excellent results of the fit to the training data, which is always better than the prediction on unseen test data, which, in turn, provides an insight into the performances over each individual material's data in the pool.

In Figure 5.7 is provided the graphical presentation of the training performances of the used ML methods on the pooled datasets. The complete dataset is segregated here in classes for each of the considered thin-film materials. The obtained R^2 values (given in Figure 5.7 in parentheses) are obtained for the complete pooled dataset, whereas the training fit quality for each material can be well observed. Namely, the training performance on the Al_2O_3 dataset is the poorest, which can be explained by this dataset's low kurtosis values (< 3) as well as the platykurtic nature of this dataset, which influences the training process.

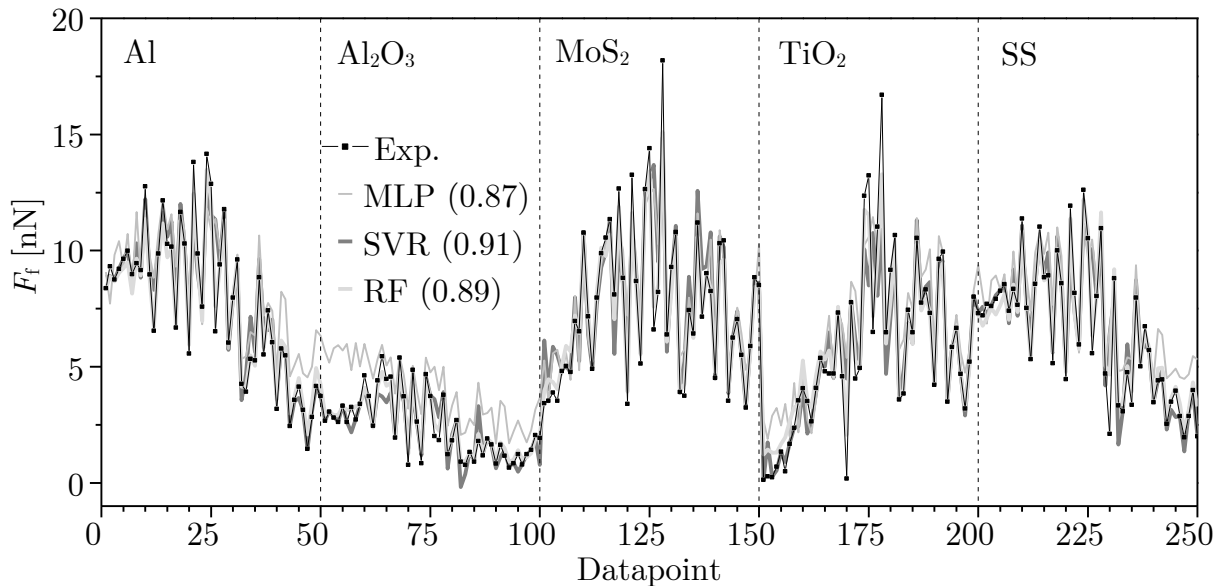


Figure 5.7 Performance of best developed ML – based models (MLP – Multi Layer Perceptron, SVR – Support Vector Regression and RF – Random Forest) on training (pooled) dataset for all samples. Values in parenthesis present achieved R^2 values for each model.

In fact, in order to fully appreciate the predictive performances of pooled data-trained models, their predictive performances must be considered over separate testing datasets for each of the used sample materials. These metrics are hence shown in Table 5.6 for the three best-performing ML algorithms – RF, MLP, and SVR. The shown individual performances of pooled data-trained models show good predictive results, where almost all algorithms result in an R^2 value > 0.7 . The RF algorithm shows a relatively poor performance for the Al_2O_3 and TiO_2 samples, while it exhibits high R^2 values of up to 0.81 for the other considered thin-film samples. The MLP algorithm shows overall the best performances of all used ML methods, and all the samples are predicted here with R^2 in the vicinity of 0.8, i.e., ranging from 0.74 for the TiO_2 sample, to 0.85 for the Al_2O_3 and SS samples. The SVR algorithm predictions result in the highest scoring, with an R^2 value of 0.9 achieved for the Al, MoS_2 and SS samples, while the Al_2O_3 prediction results in a disappointing R^2 value of 0.54.

Overall, when compared to the RSM base model, the performances of the ML methods show significant improvements in prediction capacity.

Table 5.6 Predictive performances of the considered ML models trained on pooled data for each thin-film sample material.

Algorithm	Sample	RMSE	MAE	R^2
RF	Al	1.30	0.604	0.80
	Al_2O_3	0.845	0.652	0.63
	MoS_2	1.59	0.597	0.81
	TiO_2	2.31	1.03	0.56
	SS	1.21	0.554	0.81
MLP	Al	1.87	1.51	0.81
	Al_2O_3	2.24	1.98	0.85
	MoS_2	1.50	0.737	0.79
	TiO_2	2.57	1.90	0.74
	SS	1.78	1.53	0.85
SVR	Al	1.51	0.983	0.90
	Al_2O_3	1.28	0.697	0.54
	MoS_2	1.16	0.613	0.90
	TiO_2	2.40	1.38	0.73
	SS	1.39	0.927	0.90

In order to deduce their trustworthiness in predicting the nanoscale friction force F_f in dependence on the considered process parameters F_N , v , and \mathcal{G} , all the analysed ML models are also further scrutinized graphically, in the form of prediction fits vs. experimental test data, for each used thin-film material. In Figure 5.8. are thus depicted the resulting plots in the MC test data points ordered according to ascending temperatures, with the respective fits for the predictions of the RF, MLP and SVR algorithms, for the thin-film samples synthesized by using the ALD technique.

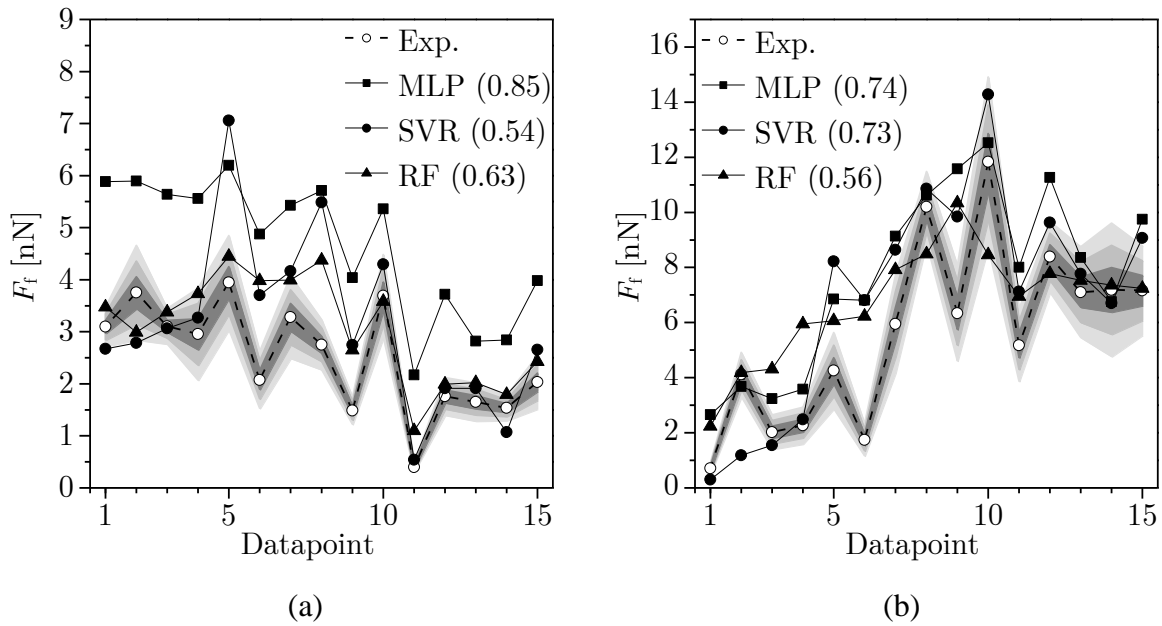


Figure 5.8 Predictive performances of the considered ML models on the MC test dataset for the ALD synthesized samples: Al_2O_3 (a) and TiO_2 (b).

The measured points are shown in Figure 5.8 with shaded uncertainty levels in three shades of grey which present the $\pm \sigma$ variance of data ($\pm 1\sigma$ as the darkest, $\pm 2\sigma$ medium and $\pm 3\sigma$ as the lightest shade of grey). The represented values correspond, in fact, to the three-sigma statistical conventional heuristic, which states that, from the cumulative distribution function of the normal distribution, these three shown confidence levels represent 68.27 %, 95.45 % and 99.73 % of data, thus containing, with empirical near-certainty, all data [106]. What is more, for each considered ML algorithm and the observed material data, in Figure 5.8 is noted in parentheses the respective R^2 value.

The values for Al_2O_3 , as shown in Figure 5.8a, and the immediately obvious respective poor MLP fit, even though the achieved R^2 is large, allows evidencing one of the pitfalls of data mining in general. In fact, MLP shows here a good form of the fit function, but it is significantly away from the six-sigma extent of the measurements. The SVR results also in a poor fit, but the

respective trend is much closer to the six-sigma area of the experimental data, even though in this case the R^2 value is low, which actually means that the trends of the response are not followed closely. This is also the case for the RF model, with slightly better correlation, but also with the obvious lack of fit, especially in the mid-range of the data.

In Figure 5.8b, depicting equivalent data for the TiO₂ thin-film sample, the fits are again generally out of the six-sigma extent (even though the correlations are high for the SVR and MLP methods), but the trends are more closely followed by the models. This is true especially for the MLP model, but also for the RF model in the higher-ordered datapoints.

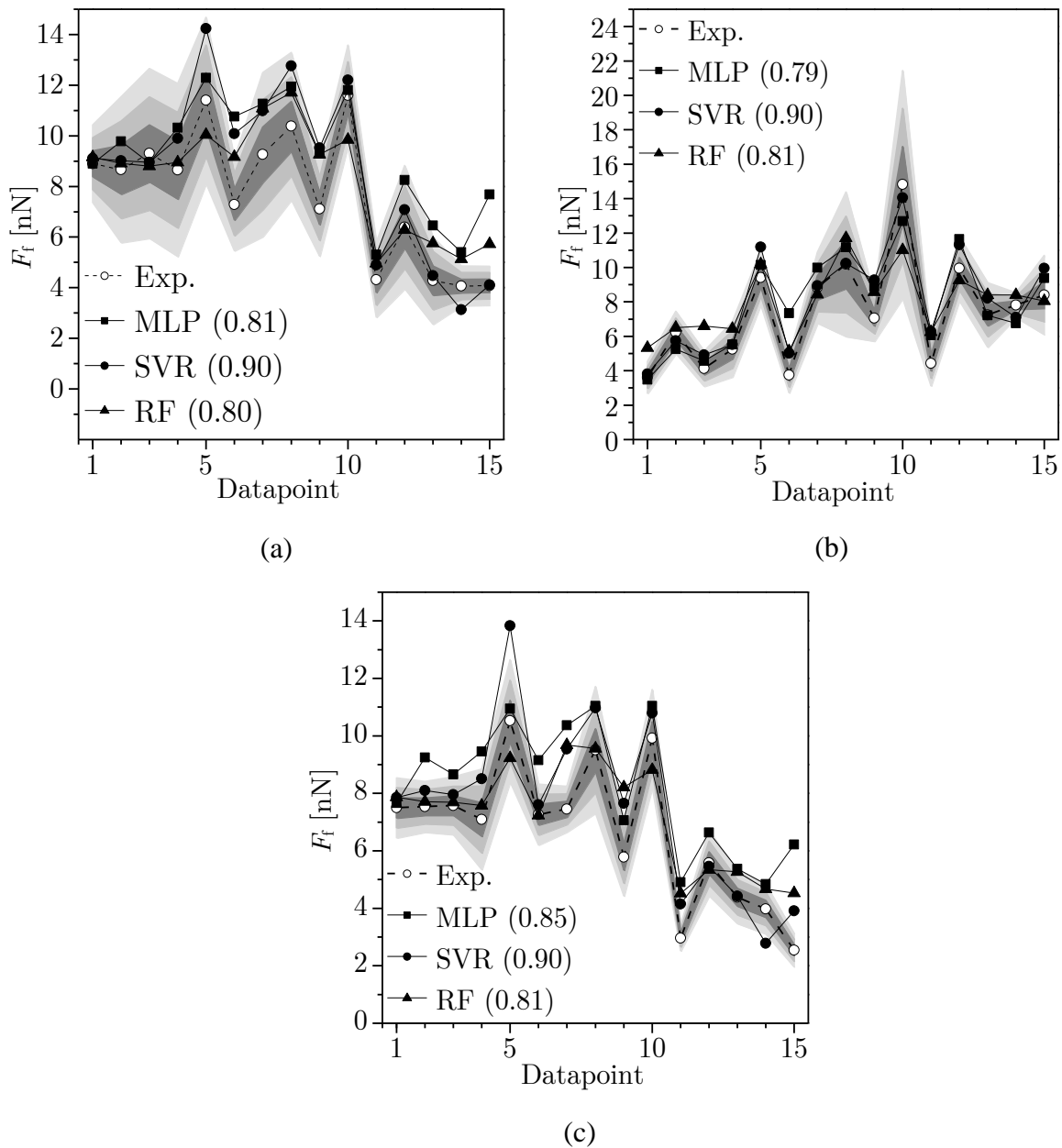


Figure 5.9 Predictive performances of the considered ML models on the MC test dataset for the PLD synthesized samples: Al (a), MoS₂ (b) and SS (c).

In Figure 5.9a, reporting the equivalent results for the thin-film samples obtained by using the PLD synthesis method, the uncertainty bounds of the Al sample are, in turn, much wider than those of the other analysed materials and, in conjunction with the good normality characteristics of this dataset, the fit is good for all algorithms. In the case of the MoS₂ and SS samples shown in Figure 5.9b and Figure 5.9c, respectively, narrow six-sigma areas and generally good fits can be observed for all the used ML models. This is especially true for the MoS₂ sample, while for the SS sample some difficulties can be observed in the low and higher order datapoints when the MLP and SVR models are used.

5.7.2. 2D Considerations

As pointed out previously, one or two single-parameter metrics cannot provide the needed confidence for the assessment of the used numerical models. Thus, the relation between the multiple correlated influential parameters must be represented and considered through the visualization of model functions with at least two variable parameters, i.e., by using surfaces. All the combinations of the used algorithms, even the ones with poor performance metrics, are therefore thoroughly analysed. The main influential characteristics of these are hence presented in the following for each model and each used thin-film material. Due to a large number of possible combinations of variable parameters' representations vs. F_f , the graphs depicted below are showing representative results for a single constant value of each variable parameter chosen arbitrarily for brevity of representation, since many other combinations were visualized during the data analysis which showed no major deviations from the ones depicted. The variable of normal force is shown in context of total normal load defined as $F_L = F_N + F_A$, i.e., as a sum of exerted normal force F_N (experimental parameter) and the adhesion force F_A which is a property of the respective analysed material, which as such acts concurrently with the applied normal force yielding the total exerted normal load F_L as described in the experimental section of this thesis.

In Figure 5.10 and afterwards are thus presented surface plots of the nanoscale friction force F_f values obtained by using the RF model when two of the process parameters are varied while the third one is kept constant, i.e., the normal load is $F_L = 100$ nN, sliding velocity is $v = 250$ nm/s, and temperature is $\vartheta = 40$ °C. The hence obtained results for the Al₂O₃ and TiO₂ samples, obtained via the ALD process, are shown in in Figure 5.10. It can be seen here that the RF ML algorithm predicts a highly nonlinear influence of temperature with a marked peak around ~ 40 °C, which was also noticed in the above Section 3.5.2 and Chapter 4. In relation to the two

considered materials, opposite temperature effects can, in turn, be observed, namely a strong positive trend for Al_2O_3 and a quasi-parabolic negative effect for TiO_2 sample. The influence of velocity shows a quasi-linear trend vs. temperature, but a highly negative effect when related to a variable total load F_L . The total normal load effect shows, finally, a weakening quasi-linear relationship for both materials with respect to variable temperature, but an almost completely flat trend when related to the variable sliding velocity.

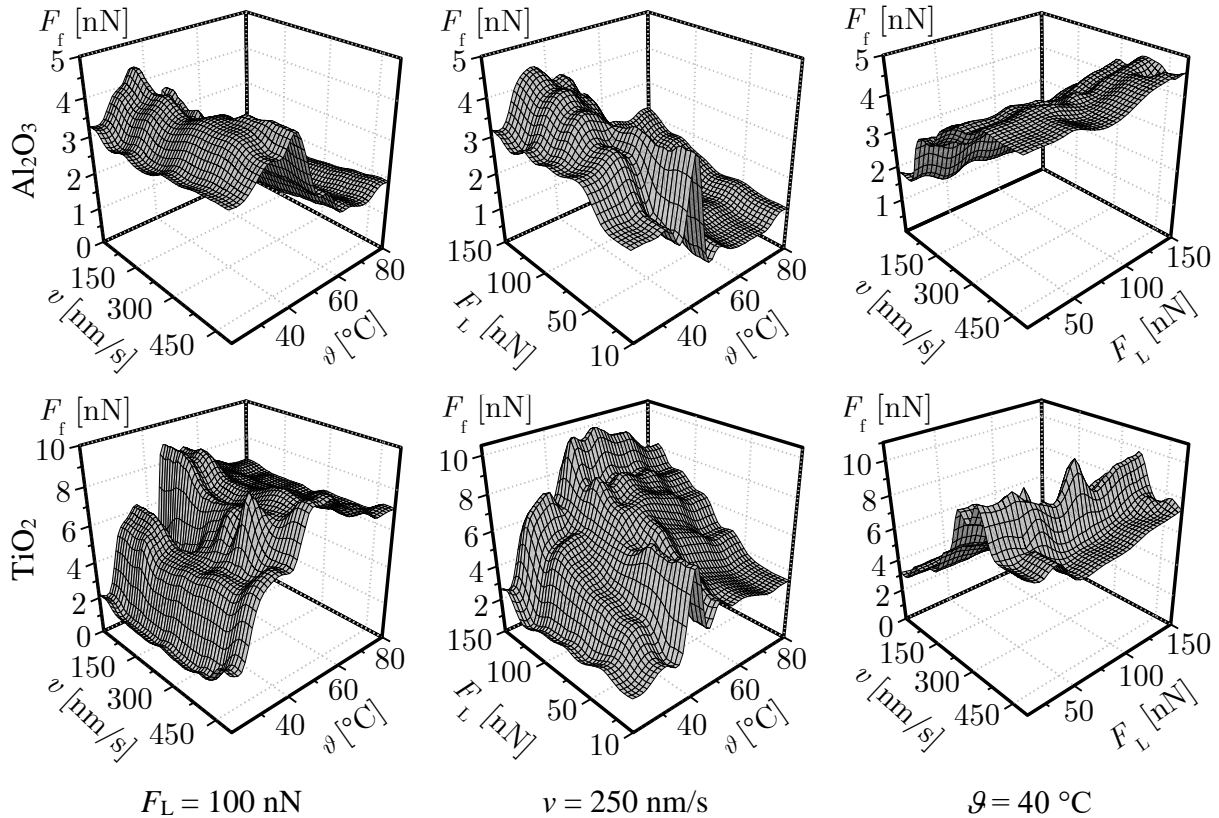


Figure 5.10 Surface plots of the RF ML solutions of the F_f values for constant variables in columns (left to right): total load ($F_L = F_N + F_A$), sliding velocity (v) and temperature (θ), for the ALD samples: Al_2O_3 (top row) and TiO_2 (bottom row).

In Figure 5.11, equivalently as in the previous case, are shown the RF model solutions for the PLD-synthesized samples. The depicted trends of the effects of velocity and temperature on the nanoscale friction force F_f are similar for the Al and SS samples, showing, for a constant F_L value, a strong positive nonlinear correlation for temperature, and a weak quasi-linear effect for velocity. The similarity of the F_L vs. θ trends for $v = \text{const.}$ is clear for all the three considered samples, showing again a highly nonlinear effect of temperature at ~ 40 $^{\circ}\text{C}$, while the v vs. F_L influences at $\theta = \text{const.}$ show similarities in terms of the strong weakening effect

of velocity and a weak quasi-linear effect of F_L . The RF model results in any case in non-smooth predictions, which is inherent in the decision tree models themselves.

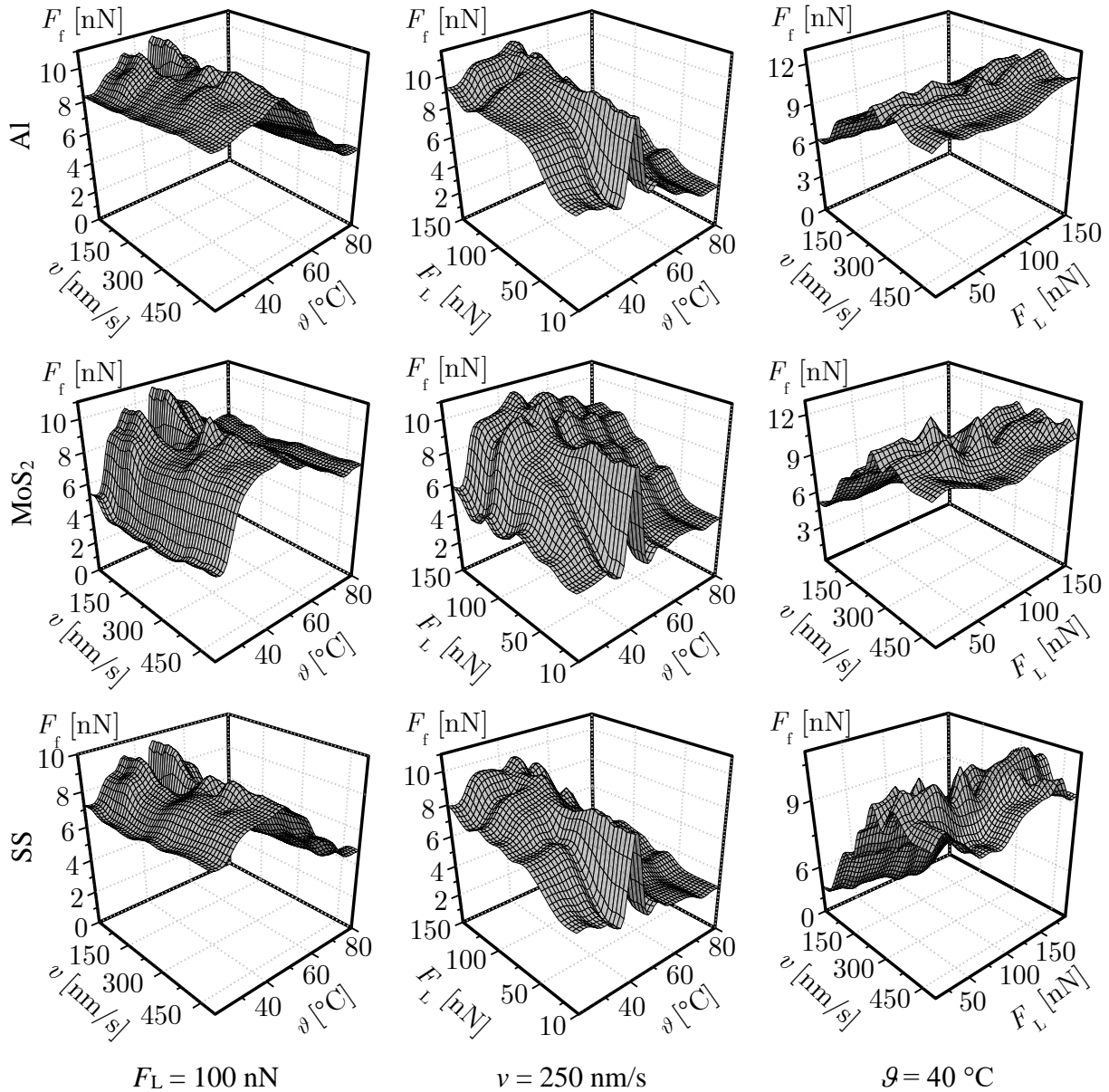


Figure 5.11 Surface plots of the RF ML solutions of the F_f values for constant variables in columns (left to right): total load ($F_L = F_N + F_A$), sliding velocity (v) and temperature (g), for the PLD samples in rows (top to bottom): Al, MoS₂ and SS.

It is important to note here especially that the trends of the F_f values, depicted in the Figures 5.8 and 5.9, show that there is indeed a similarity between the tribological behaviour of the analysed samples, which will probably be made even more evident considering the results given below.

In Figure 5.12 are then depicted, in an analogous fashion as before, the values of the

nanoscale friction force F_f obtained for the ALD – synthesized samples by using the MLP model, maintaining again one of the process parameters constant, while the other two are varied. Smoother predictive solutions are attained in this case. The effects of sliding velocity vs. temperature for $F_L = \text{const.}$ shows, thus, a smooth nonlinear effect of temperature, but also a smooth quasi-linear effect of sliding velocity. This weak linear influence of v is also evident in the v vs. F_L graphs for $\mathcal{G} = \text{const.}$ (right column). The influence of F_L in this right column is, in turn, almost-linear with a positive correlation. For Al_2O_3 sample, the effect of normal load and temperature shows slightly tilted smooth quasi-linear effect of F_L , and a diminishing effect of temperature at around 60°C , while the TiO_2 sample, for equal conditions shows highly non-linear effect of temperature, again with an interesting peak at around 50°C .

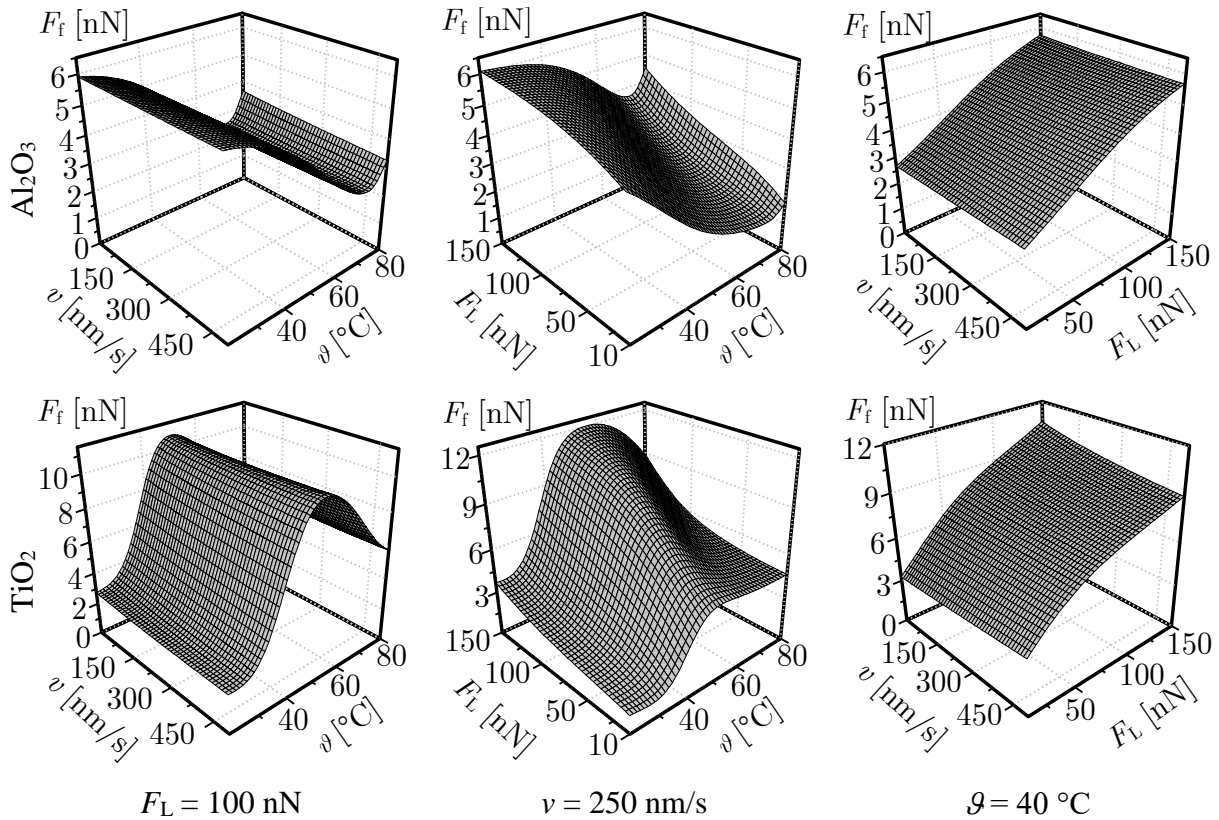


Figure 5.12 Surface plots of the MLP solutions of the F_f values for constant variables in columns (left to right): total load ($F_L = F_N + F_A$), sliding velocity (v) and temperature (\mathcal{G}), for the ALD samples Al_2O_3 (top row) and TiO_2 (bottom row).

In Figure 5.13 are depicted the F_f values obtained via the MLP method for the PLD – synthesized samples. Beautiful overall similarities of the influential effects on F_f can be observed for all the samples. It can be deduced that the effect of temperature, observed in conjunction with a variable velocity (left column) and the total normal load (mid-column) alike,

is again nonlinear with a parabolic-like curvature. The right-most column, depicting the influences of F_L and v , shows a truly remarkable similarity of the continuous positive effect of the load F_L on F_f , and a weak quasi-linear strengthening effect of sliding velocity.

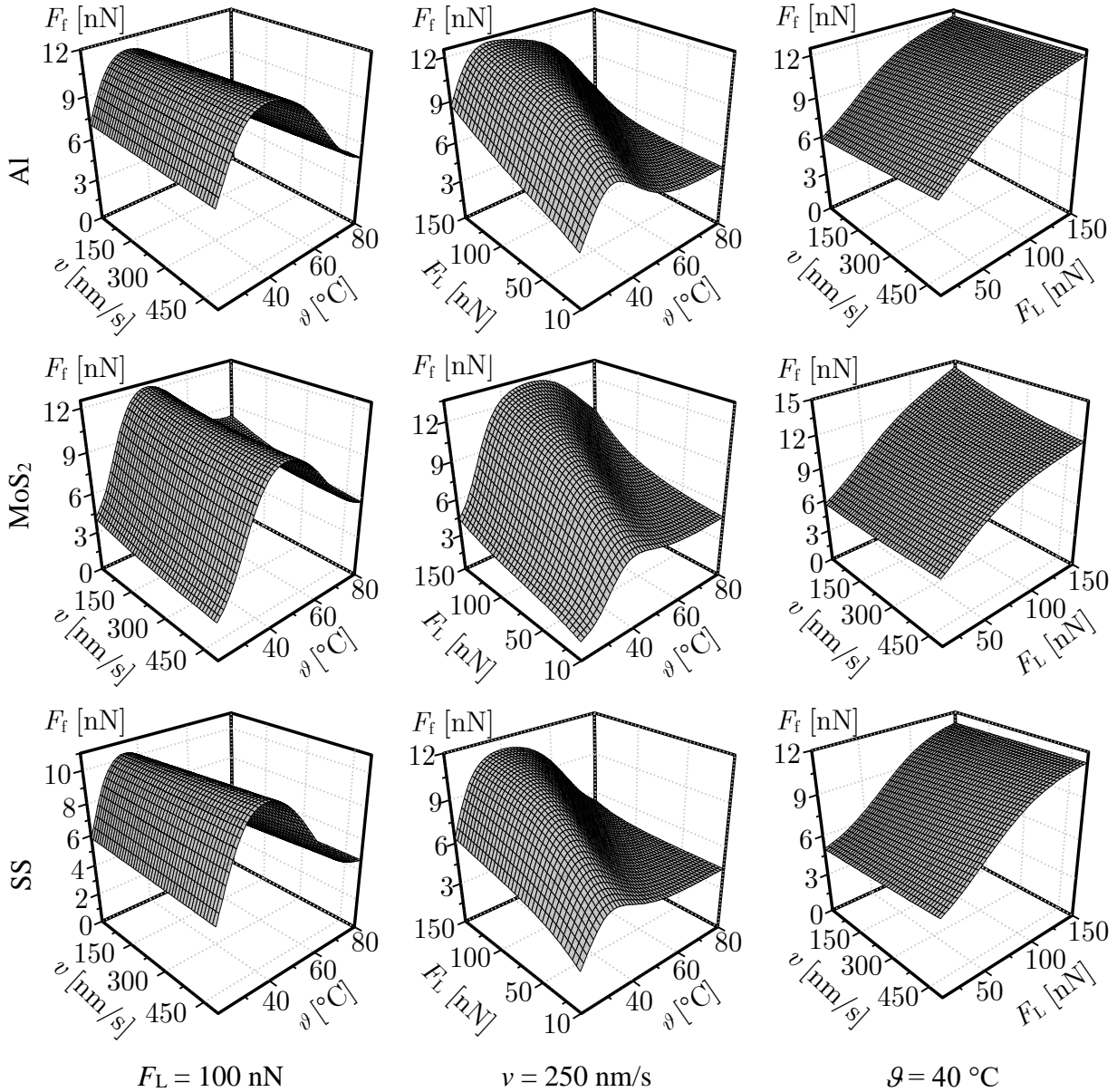


Figure 5.13 Surface plots of the MLP solutions of the F_f values for constant variables in columns (left to right): total load ($F_L = F_N + F_A$), sliding velocity (v) and temperature (θ), for the PLD samples in rows (top to bottom): Al, MoS₂ and SS.

SVR ML solutions for the ALD-obtained samples are finally shown in Figure 5.14, again allowing to evidence clearly the influences of the considered process parameters on the frictional behaviour of all the sample materials in the nanodomain. When compared to the results attained via the RF, and, especially, the MLP algorithms, the results obtained by

employing the SVR method show very curved surfaces, which is an inherent property of the used radial basis kernel function. Once more the most striking resemblance among the two thin-film sample materials is visible in the right-most column showing the effects of F_L and v , a nanofriction feature that is clearly becoming very common and prominent for the all the considered thin-film materials. As in the previous cases, the highly non-linear influence of temperature is obvious. On the other hand, when compared to the current knowledge in the field, the non-linear effect of F_L for the Al_2O_3 at constant v seems to be overemphasized, which could be a consequence of the evidenced low R^2 value achieved for Al_2O_3 by using the SVR model (cf. Figure 5.8). In the case of TiO_2 , the influence of F_L is, in turn, much smoother but still giving rise to an augmenting effect on F_f , which is in accordance with the observed experimental correlations. The effect of sliding velocity is, finally, weak, negative, and quasi-linear in all cases, which is consistent with the low correlation factors found in the above experimental observations.

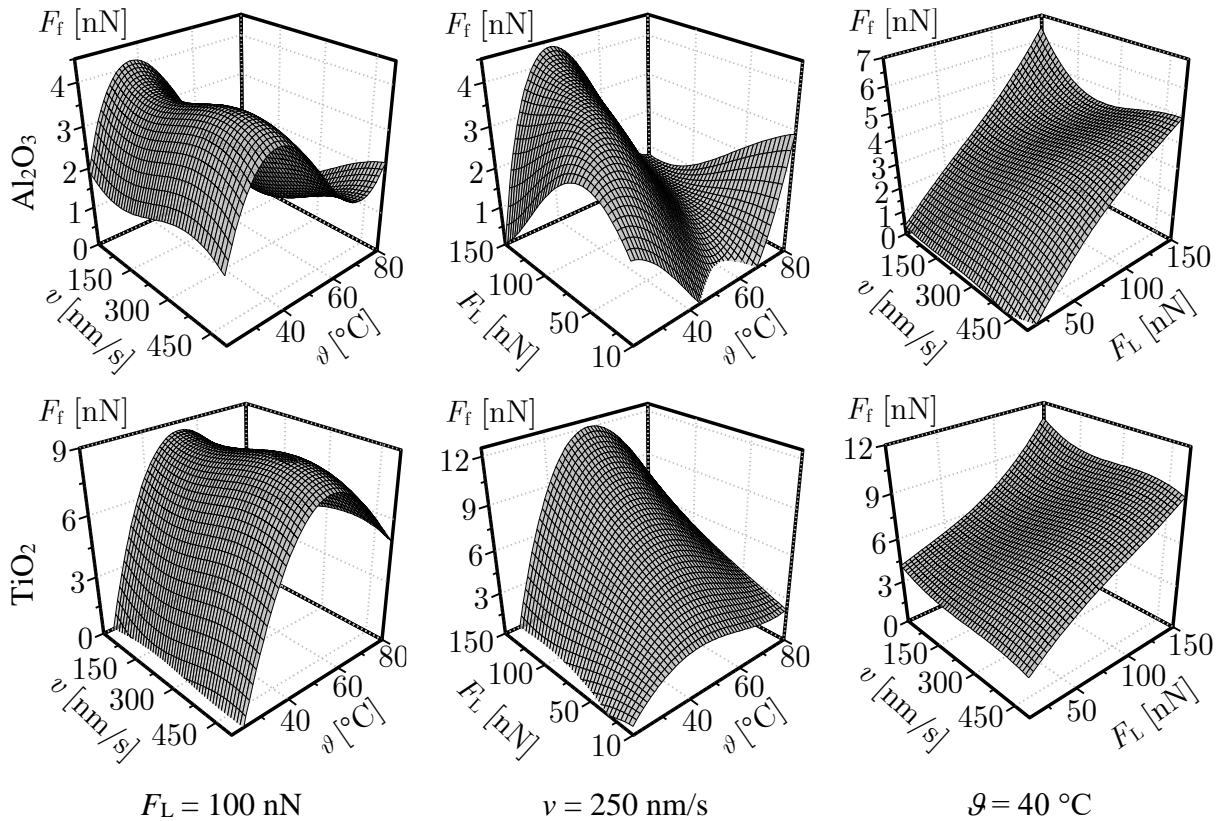


Figure 5.14 Surface plots of the SVR ML solutions of the F_f values for constant variables in columns (left to right): total load ($F_L = F_N + F_A$), sliding velocity (v) and temperature (θ), for the ALD samples: Al_2O_3 (top row) and TiO_2 (bottom row).

In Figure 5.15 are depicted the SVR ML solutions for the remaining (PLD) samples. The

striking similarities, not only between the sample materials themselves, but also in comparison to the MLP solutions, can be appreciated already by a quick visual inspection. The data-mining process seems, *ergo*, to be converging towards a potential unified solution. The right-most column shows again a quasi-linear relationship of velocity and total load vs. the resulting friction force, albeit one negative, and the other one positive.

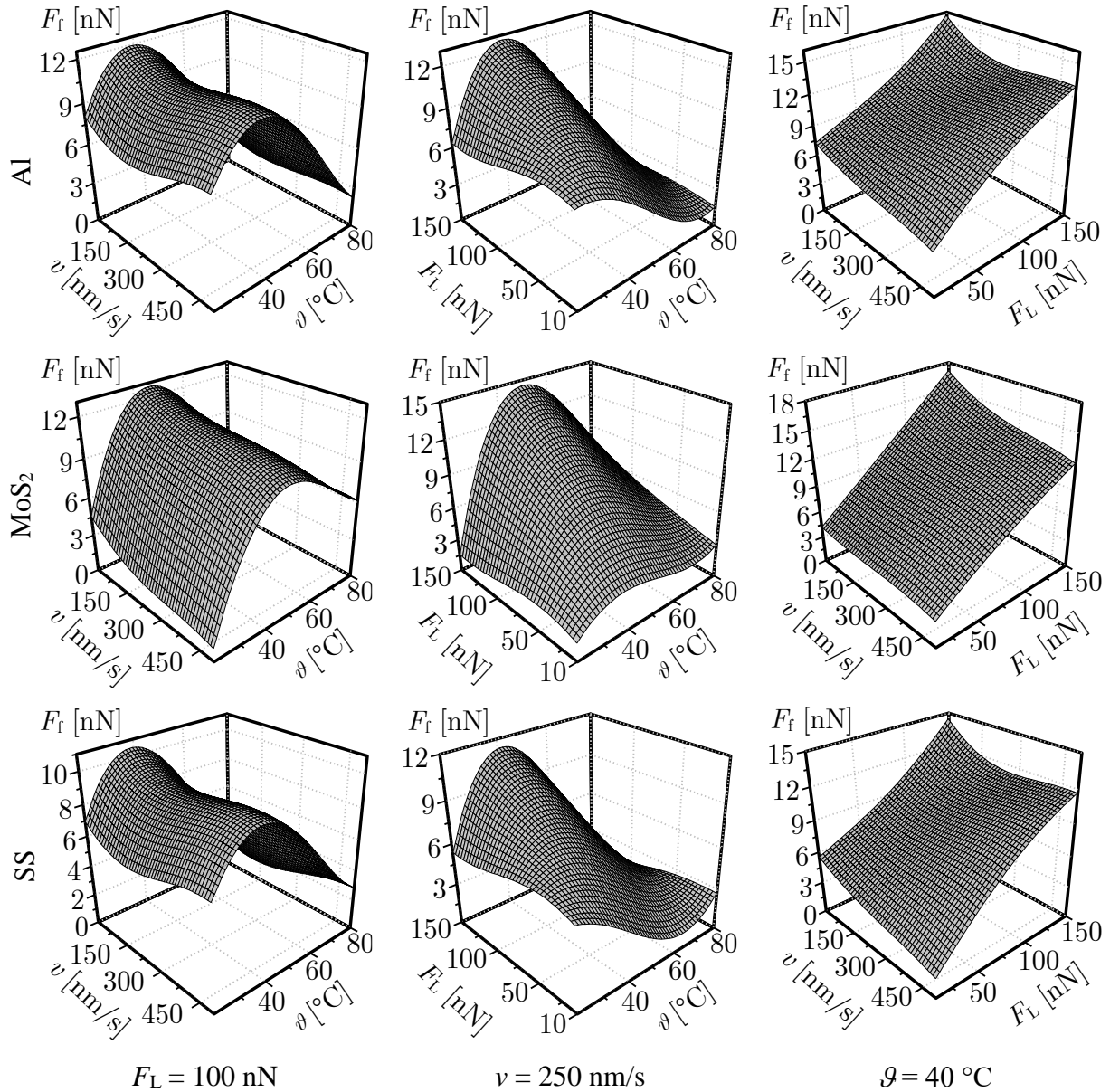


Figure 5.15 Surface plots of the SVR ML solutions of the F_f values for constant variables in columns (left to right): total load ($F_L = F_N + F_A$), sliding velocity (v) and temperature (g), for the PLD samples in rows (top to bottom): Al, MoS₂ and SS.

When the SVR “curvy” predictions are taken into account, the friction force seems, in turn, slightly over-estimated at the extremes of the observed variables’ domains. The effect of F_L vs.

temperature shows again a nonlinear trend, with similar curvatures to those predicted by the MLP algorithm. In the case with variable temperature and constant total load, the effect of velocity is, finally, once more predicted to be quasi-linear, which is also a common feature of the SVR model for all the considered thin-film samples.

The analysis of the frictional behaviour in the nanometric domain performed by using the black-box ML models shows, thus, that it is possible to provide effective predictions of the influence of the multiple process parameter on the value of the friction force with satisfactory levels of accuracy, i.e. with R^2 values ranging from of minimum 0.54 for the SVR algorithm on an Al_2O_3 sample, to 0.9 for the SVR prediction on an Al sample. What is more, the other best-performing algorithms, namely the RF and the MLP ML models also show high predictive performances, especially when MLP is used. It can also be concluded from the respective predictive performance of each model that the smoother solutions are preferable, i.e., the models exhibiting smoother solutions result with a better predictive performance.

5.8. Genetic Programming – Symbolic Regression

From the above analysis of black-box ML models it can be concluded that there is, indeed, an indication that a general and common mathematical form apt at predicting the value of nanoscale friction force depending on variable multiple influencing parameters could exist. The ML models used so far, despite their high capabilities as predictive tools, cannot be used in practice for in-depth analyses, numerical modelling, etc., since in the considered class of problems they entail a large number of coefficients, i.e., 250 support vectors for the SVR, or a large number of sigmoid function's parameters for the MLP. Thus, in this part of the thesis, with the goal of attaining at least the similar level of predictive performances, a symbolic mathematical expression, based on evolutionary algorithms, will be developed and described. A symbolic mathematical expression provides an analytic form of correlation of observed multidimensional experimental data with respect to variable parameters, which is the main goal of this research, and presents a big step towards identification of physical laws that underlie the observed physical phenomena of nanoscale friction. The developed mathematical expression is with respect to previously developed black-box models directly understandable and usable by humans because of its simple mathematical formulation and low number of involved parameters which also provides means for streamlined integration into, modification, and comparison with existing friction models and numerical schemes, as well as direct calculation usage for nanoscale friction prediction, adaptive control purposes and further analytical

analyses.

Evolutionary algorithms are typically used to provide good approximate solutions to problems that cannot be easily solved using other techniques. Many optimisation problems fall into this category. In fact, in this case it may be too computationally-intensive to find an exact solution to the considered problem, but sometimes a near-optimal solution is sufficient. Due to their random nature, evolutionary algorithms never guarantee to find an optimal solution for any problem, but they will often find a very good solution, if one exists. This is exactly suited for the herein considered purpose of determining a functional dependence of multiple variable parameters on the nanoscale friction force, since any kind of the expressional form of the respective dependence is not known a priori [65], [139], [147].

Evolutionary algorithms (EA), such as, i.e., genetic programming (GP) algorithms, are therefore often used to tackle problems that humans do not really know how to solve. It has been shown that EA, free of any human preconceptions or biases, can, in fact, generate surprising solutions that are comparable to, or better than, the best human-generated efforts. It is merely necessary that an obtained good solution is recognised even if it is not known how to create it [139], [147]. In contrast to conventional evolutionary algorithms, genetic programming symbolic regression evolves a genome whose outputs are symbolic expressions, such as mathematical functions and variables, rather than predicted numerical values.

Genetic programming is much more powerful than genetic algorithms, since the output of the genetic algorithms is a quantity, while the output of GP is another computer program or a symbolic expression [88], [89]. Several GPs suitable to be used for the problem at hand in this thesis will hence be described and used in the following sections, and all of the models are developed in HeuristicLab [173].

Standard GP method (i.e., Koza style – by the author) [88], the evolution of the expressions occurs over a number of generations (iterations) and each new generation of individuals is created from the existing population by direct copying as well as performing operations on individuals analogous to the alterations to the DNA sequences. This is accomplished by evaluating each individual in the current population to determine its fit vs. the actual variable's value, and performing selection and recombination of individuals, with a bias towards those that are more fit [88]. At the beginning of each run of this process, a population of symbolic expressions is randomly generated. This is accomplished by using a simple tree building algorithm that randomly selects nodes from a set of primitive functions, i.e., additions, subtractions, divisions, exponentiation, etc. of the input variables, as well as randomly

generated constants. The nodes are then randomly assembled into tree-structured symbolic expressions, with subject-defined trees sizes, i.e., model depth and length, [88], [89].

After evolving the population for 50 generations, a number that is selected after preliminary runs as the best compromise between the computational intensity and results, via a process of copying, mutation and recombination, the tree expression with the best fitness is usually selected as the best solution to the problem. For each expression, a sub-tree is randomly selected next. The sub-trees are then exchanged to create new expressions to go into the next generation. On the other hand, a mutation operation is used relatively infrequently compared to this crossover operation, and its purpose is to maintain genetic diversity over the course of the run and to prevent premature convergence to unsatisfactory solutions [95], [139].

5.8.1. Grammatical Evolution GP

Grammatical Evolution (GE) is a type of GP that applies genetic operators to an integer string, subsequently mapped to a program (or similar) using a grammar formalism, which presents a set of syntaxes of most currently used programming languages, which allows a genetic evolution of solutions not only consisting of standard mathematical terminals (operations and variables), but also loops, logical operators, etc. [143]. One of the benefits of GE is that this mapping simplifies the application of the search process to different programming languages and other structures. In fact, in type-free, conventional Koza-style GP, the function set must meet the requirement of closure: all functions must be capable of accepting as their arguments the output of all other functions in the function set. Usually this is implemented by dealing with a single data-type such as double-precision floating point. While modern GP frameworks support typing, such type-systems have limitations that GE does not suffer from. In fact, GE offers a resolution to this issue by evolving solutions according to a user-specified grammar that can consist of complex operations or even blocks of functional dependencies, rather than simple mathematical operations [121], [143]. In the thesis a wide array of mathematical operators is hence used as grammar, including trigonometric functions, log, ln, exp, etc. The search space can therefore be restricted, and domain knowledge of the problem can be incorporated. The phenotype, however, is the same as in Koza-style GP, i.e., a tree-like structure that is evaluated recursively [121], [143].

5.8.2. Offspring Selection GP

As stated in the original paper defining this type of GP [1]: “In terms of a goal-oriented paradigm, selection is the driving force of GAs. In contrast to crossover and mutation, selection

is completely generic, i.e., independent of the actually employed problem and its representation. Offspring selection (OS) is usually implemented as a selection for reproduction (parent selection). This self-adaptive selection mechanism is closely related to the general selection model of population genetics [1], [91]. As the problem- and representation-specific implementation of reproduction in GAs (crossover) is often critical in terms of the preservation of essential genetic information, for improving the global solution quality and robustness in terms of parameter settings and the operators of GAs. Offspring selection has proven to be very suited in various fields of applications and produces results competitive to human-produced results [87]” Success of this method is confirmed in fields such as quantum computing [154], antennas [100], mechanical systems [70], cancer research [177], etc. This model uses then the same parameters as the standard Koza-style method [1].

5.8.3. Age-Layered Population Structure GP

A common problem in running an EA is that, after a determined number of evaluations, the population converges to a local optimum and no improvements are made, no matter how much longer the EA is run. The existing genetic material in the population has converged so that the variation operators cannot produce new individuals which will move the population into a better part of the fitness landscape. Many attempts at creating a more robust EA have been tried, and this is still an ongoing area of research [139]. To reduce the problem of premature convergence, the Age-Layered Population Structure (ALPS) was designed. This metric of age measures how long the genetic material has been evolving in the population. ALPS modifies a typical EA by segregating individuals by their age into different age-layers, and by regularly introducing new, randomly generated individuals in the youngest layer, thus refreshing the population, resulting in an algorithm that is never completely converged. By using age to restrict competition and breeding, younger individuals are able to develop without being dominated by older ones [69], [95].

5.8.4. Multi-gene GP

A promising variant of GP, namely multi-gene genetic programming (MGGP), which is consisted of multiple genes, where each of them is actually a standard GP symbolic expression as described earlier [95], [139]. The complete MGGP model is derived as a linear combination of each used gene, thus generating a pseudo-linear model which can describe non-linear effects. MGGP model are developed using the GPTIPS2 framework [149] involving 50 genes, which was determined to be optimal in terms of processing time, resulting models complexity and

predictive performance. The capabilities of MGGP have been shown by applying it to the formulation of various complex problems such as mechanical properties of nanomaterials [166], characterisation of 3D printed components [165], and others [94], [117], [123], [167]. The validity of MGGP is confirmed by applying the derived models to the parts of the experimental results that are not included in the training process, i.e., the unseen test datasets, which is thoroughly presented below.

5.9. Comparison of Symbolic Regression Models

The mathematical expressions developed by employing the previously described symbolic regression methods are comparatively analysed next. For a thorough predictive performance assessment, the developed models' performance metrics are, once more, obtained by testing the models on unseen testing data. All shown models performance parameters are obtained here after training them with a 10-fold cross-validation on the DoE-CVT obtained experimental data, where 30 % of the data is used as a validation set for parameter optimization.

In Table 5.7 are hence provided the performance metrics results for all the models developed by training the considered GP models on a single material dataset and on pooled data. With respect to the ML models analysed in Section 5.6, in this case the performance metrics also contains information about the resulting model's length and depth, both of which provide information about the symbolic expression's complexity, and are preferred to be the smallest possible.

By inspecting the data reported in Table 5.7 it can thus be seen that the performance of the ALPS GP models is relatively poor for all the analysed thin-film samples. Only in the case of the MoS₂ sample and the pooled dataset the model shows higher R² values of 0.74 and 0.68 respectively, but also a high variance of MAE and RMSE.

Standard Koza-style GP (KS GP) predictions are quite poor, with maximal predictive correlations (R² values) of 0.6 (for, again, the MoS₂ sample – which is probably due to the distribution of the data for training). High-complexity models are generated, while the error variance is low. The grammatical evolution approach (GE GP) generates the simplest models, but unfortunately with poor predictive performance, i.e., maximal R² values of 0.62. Offspring selection algorithms (OS GP), even though fast in execution, provide again low predictive performance models in all datasets. On the other hand, the multi-gene approach (MG GP) provides by far the most impressive predictive correlations of 0.82 for the Al sample, 0.9 for MoS₂, 0.83 for SS, and an R² value of 0.82 for the pooled data trained model.

Table 5.7 Comparative presentation of predictive performances on the test datasets for the considered GP-based models.

Algorithm	Sample	RMSE	MAE	R ²	Length	Depth
ALPS GP	Al	5.36	4.13	0.162	101	18
	Al ₂ O ₃	2.66	1.51	0.401	153	27
	MoS ₂	1.48	1.08	0.746	39	13
	TiO ₂	3.59	2.91	0.590	48	11
	SS	5.08	2.50	0.084	68	12
	Pooled	2.00	1.48	0.678	197	34
KS GP	Al	5.43	5.26	0.567	153	19
	Al ₂ O ₃	0.648	0.544	0.501	124	15
	MoS ₂	3.68	2.75	0.601	134	21
	TiO ₂	9.32	8.28	0.349	151	18
	SS	4.66	3.83	0.322	149	22
	Pooled	5.30	4.64	0.372	78	15
GE GP	Al	5.16	4.93	0.405	21	12
	Al ₂ O ₃	1.28	1.20	0.466	38	11
	MoS ₂	7.77	6.89	0.619	33	11
	TiO ₂	8.17	6.64	0.349	37	14
	SS	3.37	2.78	0.408	40	12
	Pooled	4.62	3.33	0.053	38	13
OS GP	Al	7.82	4.04	0.167	203	23
	Al ₂ O ₃	1.60	1.19	0.014	54	15
	MoS ₂	5.60	4.68	0.005	154	22
	TiO ₂	18.4	14.9	0.020	151	23
	SS	2.56	2.06	0.195	154	19
	Pooled	4.32	3.70	0.366	53	14
MG GP	Al	1.08	0.948	0.818	81	4
	Al ₂ O ₃	0.693	0.636	0.511	40	3
	MoS ₂	0.933	0.805	0.900	97	3
	TiO ₂	2.10	1.67	0.535	39	4
	SS	0.976	0.815	0.826	89	3
	Pooled	1.48	1.06	0.824	84	4

The minimal achieved predictive performance are, in turn, obtained for the Al_2O_3 and TiO_2 samples due, as noted earlier, to their distribution properties (cf. Figure 5.4 and Figure 5.5). It can be noted again here also that the models trained with the pooled datasets performed the best, which is a common property of all machine learning methods – the more data the better the predictions.

6. Results and Discussion

According to the previously presented performance metrics of various models, it can be concluded that the MG GP model trained with pooled data has shown the best predictive performance (c.f. Table 5.5), with high achieved R^2 values by relatively compact model expression's length and depth. Thus, the model developed by using the MG GP method by employing the pooled CVT dataset for training is considered as the best performing model and is thoroughly analysed and presented.

The best performing model, developed by using MG GP, is assessed next on the testing dataset of each analysed thin-film sample material individually. In Table 6.1 are thus presented the resulting performance metrics parameters of the selected best MG GP model trained on the pooled data. The reported R^2 values allow evidencing a high predictive performance in the range from 0.72 for TiO_2 to 0.91 for the Al sample, which is comparable to the best ML model – the SVR. The segregated performance test of the MG GP model shows also a relatively low variance of RMSE and a low MAE error for all the considered thin-film samples.

Table 6.1 Predictive performance of selected MG GP model trained on pooled data for each thin-film sample material.

Sample	RMSE	MAE	R^2
Al	1.04	0.774	0.909
Al_2O_3	0.552	0.450	0.760
MoS_2	2.43	2.06	0.736
TiO_2	2.19	1.51	0.725
SS	1.20	0.938	0.848

MG GP models are herein selected as best individuals from a population of 5000 models from each training run, which corresponds to a 10 times repeated 10-fold cross validation for 50 genes used in the multi-gene model. With the goal of minimizing the developed model's complexity and the respective $1-R^2$ metrics value, the selection of model is performed here by defining a Pareto frontier, as shown in Figure 6.1. The best selected model, i.e., that whose performance metrics are shown in Table 5.7, satisfying the minimal values on the Pareto frontier, is highlighted here. The respective model is then a mathematical expression involving eight variables, the three main variable parameters (i.e., the considered variable process

parameters F_L , \mathcal{G} and ν) and five material class variables (dummy-variables) defining each material as a binary class.

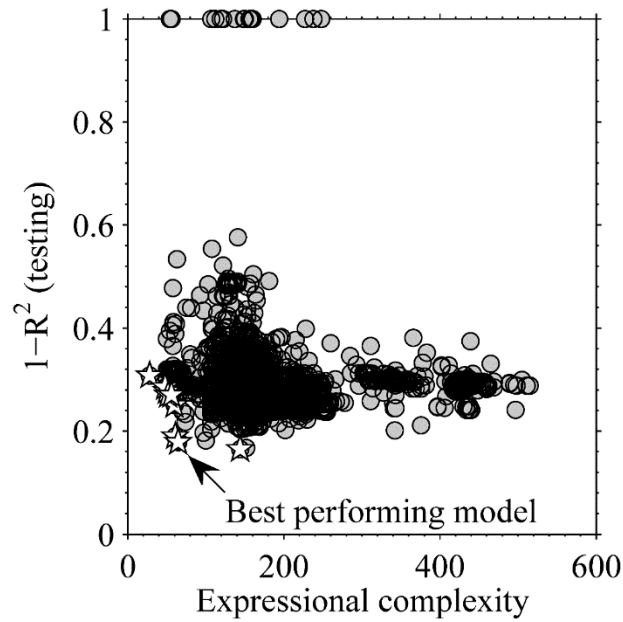


Figure 6.1 Selected symbolic regression MG GP model on a Pareto frontier of expressional complexity vs. the $1-R^2$ performance value on a test dataset.

The resulting optimum-case mathematical expression, with predictive performance metrics as shown in Table 6.1, can be represented in the form of equation (5.9) linking the value of the nanometric friction force F_f to the considered process variables and parameters related to the type of the considered thin-film material, showing its relative complexities, but also, when compared to conventional ML models, providing an invaluable simpler and more user-friendly predictive tool to be used in practical applications outlined in the introductory parts of the thesis:

$$\begin{aligned}
 F_f = & 0.04559 \cdot F_L - 0.0008751 \cdot \nu - 0.1808 \cdot \mathcal{G} + 2.824 \cdot x_4 + 4.512 \cdot x_5 - \\
 & -15.67 \cdot x_6 - 21.07 \cdot x_7 + 1.544 \cdot x_8 - 0.3031 \cdot \mathcal{G} \cdot x_5 + \\
 & +0.02764 \cdot (\mathcal{G} + x_4 + x_5 + x_8)^3 + 0.02599 \cdot (\mathcal{G} + x_6 + x_7 + 3.994)^3 - \\
 & -0.03376 \cdot F_L \cdot x_5^2 + 0.07963 \cdot \mathcal{G} \cdot x_7^2 + 0.0005558 \cdot (\mathcal{G} + 2 \cdot x_5 + 3.944)^3 - \\
 & -0.4198 \cdot \mathcal{G}^2 - 0.05406 \cdot \mathcal{G}^3 + 0.4198 \cdot x_4^3 - 0.0001781 \cdot F_L \cdot \mathcal{G} \cdot x_4 - 15.92
 \end{aligned} \tag{5.9}$$

The developed expression (5.9) is actually a regression model, and it has to be scrutinized further in order to be confirmed as a trustworthy model for the prediction of the nanometric friction force. It is important to investigate first, as shown in Figure 6.2, the actual scatter of the predicted vs. the actual (experimental) data. The good fit of a model must ideally be approaching the R^2 value of 1, which is depicted in Figure 6.2 as a straight 45° line, on which all the experimental observations would lie if there would be no deviations of the measurements

and the model would perfectly predict the considered physical phenomenon. Actually, as stated by George E. P. Box [28]: “*All models are wrong, but some are useful*”, as all models are imperfect, the developed model shows a relatively small scatter of the predictions of the training data shown in Figure 6.2a, and testing data in Figure 6.2b. More important here is the testing data prediction because it represents true predictive performance of the developed model since the test data is unseen, i.e., not used for training and thus no bias exists. The fit of predicted test values and experimental data shows a good linear trend of predictions vs. experimental data, while the accumulation of points is tight around the $R^2=1$ line.

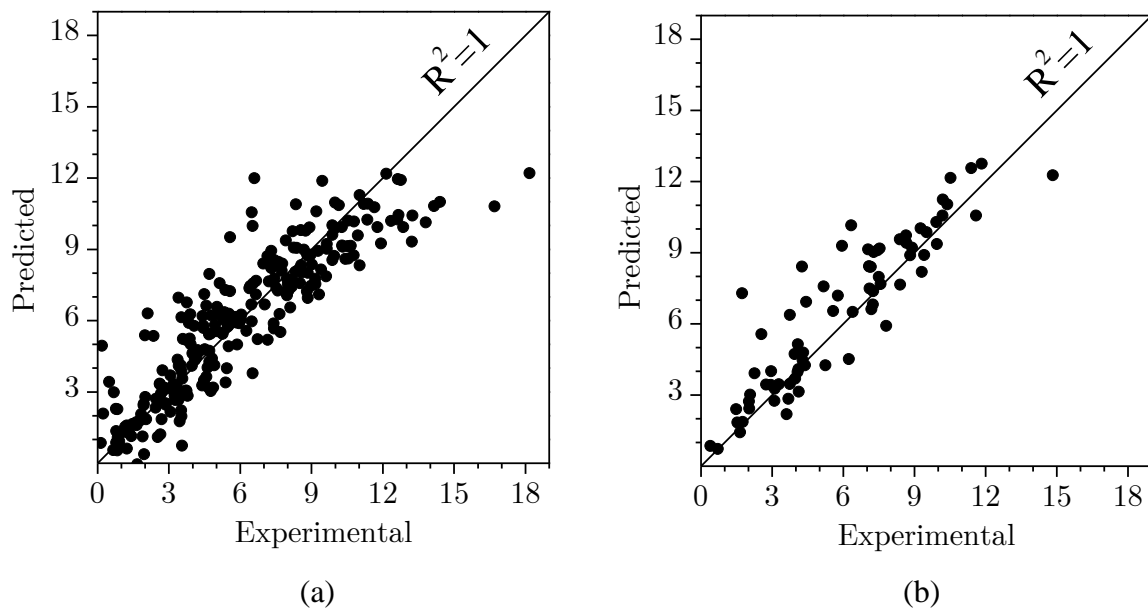


Figure 6.2 Fit of the predicted values vs. experimental data for the main (training) dataset (a), and the test dataset (b) of the model described by equation (5.9).

In order to be able to successfully predict future measured data, the developed model must also reflect the stochastic properties (as any good predictive model). This is statistically tested by analysing the residual plots such as those shown in Figure 6.3. Residual plots depict the scatters of the residuals, i.e., the difference between the predicted and the actual (experimental) value [49]. The goal is to observe stochastic, random distributions of these points. If there are any regularities, in the form of a curve or a linear relationship, the model would not be fit for use, since this kind of predictive residuals indicate a heavy bias in the model. As shown in Figure 6.3a, where the lot of residuals for the training data is depicted, and in Figure 6.3b, showing the plot of residuals for the testing data, good stochastic and random properties are achieved. When the distribution of the residuals for both data sets is considered (Figure 6.3c) the Gaussian distribution of the residuals is confirmed, demonstrating good normality.

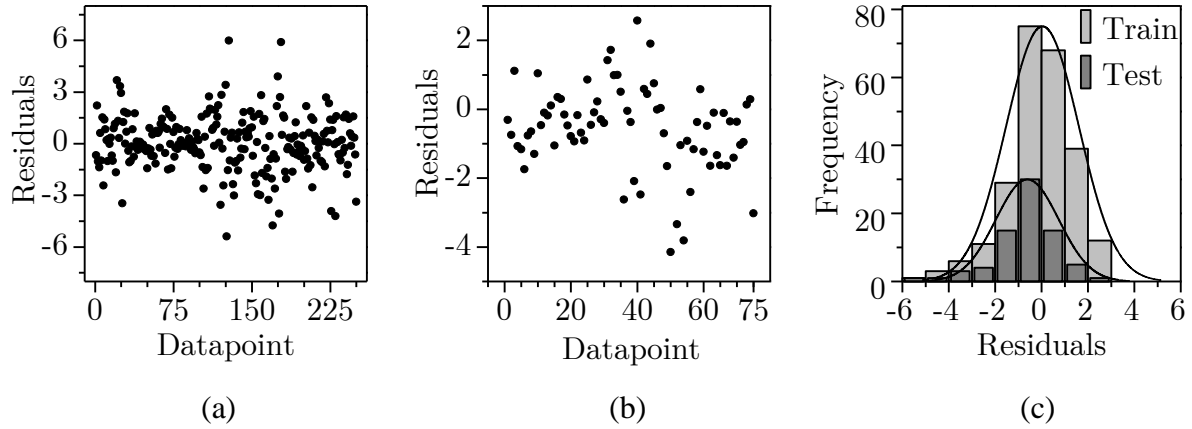


Figure 6.3 Plot of residuals of the best performing model on the main (training) dataset (a) and the test dataset (b). The distribution of residuals shows good normality for both datasets (c).

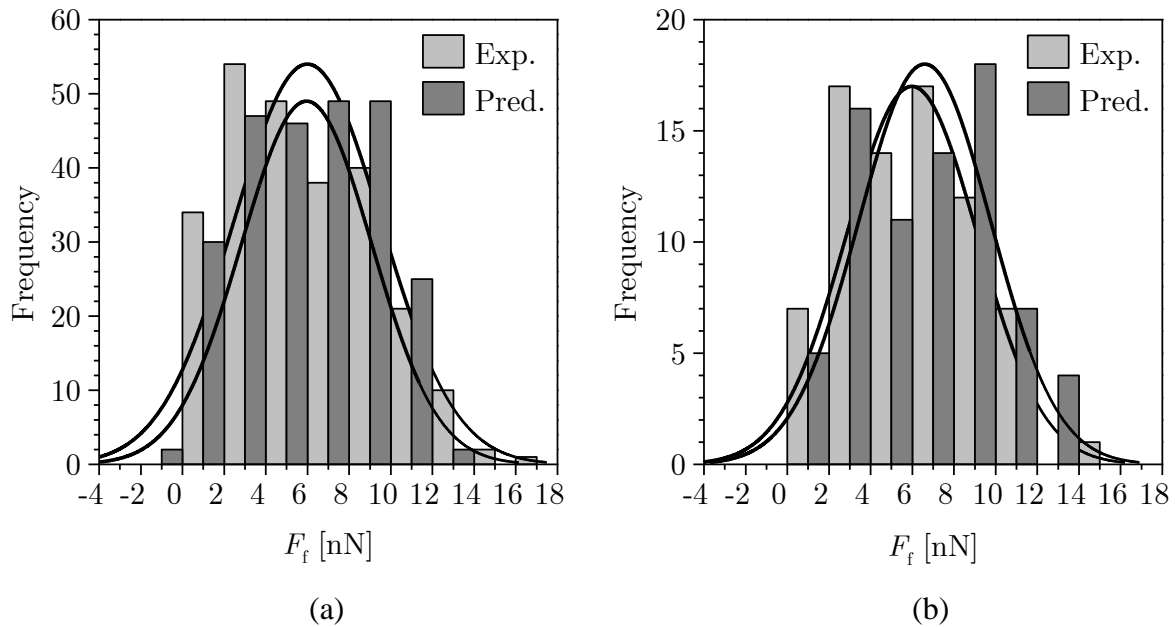


Figure 6.4 Distributions of predicted and experimental data for the main (training) dataset (a), and the test dataset (b).

The performances of the developed model can be assessed also by analysing the distribution of the predicted values and comparing it to the experimentally obtained data distribution. Overlaid distributions of predicted and experimental data are hence shown in Figure 6.4 for both pooled training and testing datasets (the depicted histogram bins are 1 nN wide). The distributions show an equal mean value for the training set, which confirms an extremely good fit. On the other hand, the more important test dataset fit shows also a good fit, although in this case there is a minor shift of the mean of the distribution of the predictions, which is caused by slightly overestimated prediction values.

As in the case of the methodology used previously (cf. the above Section 5.6), the fit of the

model to each of the analysed materials in the MC test datapoints, i.e., its ability to predict the un-seen real-world experimental data of nanoscale friction force F_f in dependence on the considered process parameters F_N , v , and \mathcal{G} , will be considered next to confirm the predictive performance w.r.t. the respective uncertainty of the data. In Figure 6.5a and b are thus depicted the predictions and the experimental data for the ALD synthesized Al_2O_3 and TiO_2 samples. It can hence be clearly seen that the prediction for the Al_2O_3 sample predominantly lie within the six-sigma extent of the experimental data, with only a slight deviation in some of the intermediate points. In the case of the TiO_2 sample, although the fit on the first two data points is perfect, in general the predictions show relatively high deviations from the experimental points, which was already noted earlier for almost all the considered models, and is due to the nature of this sample's data distribution.

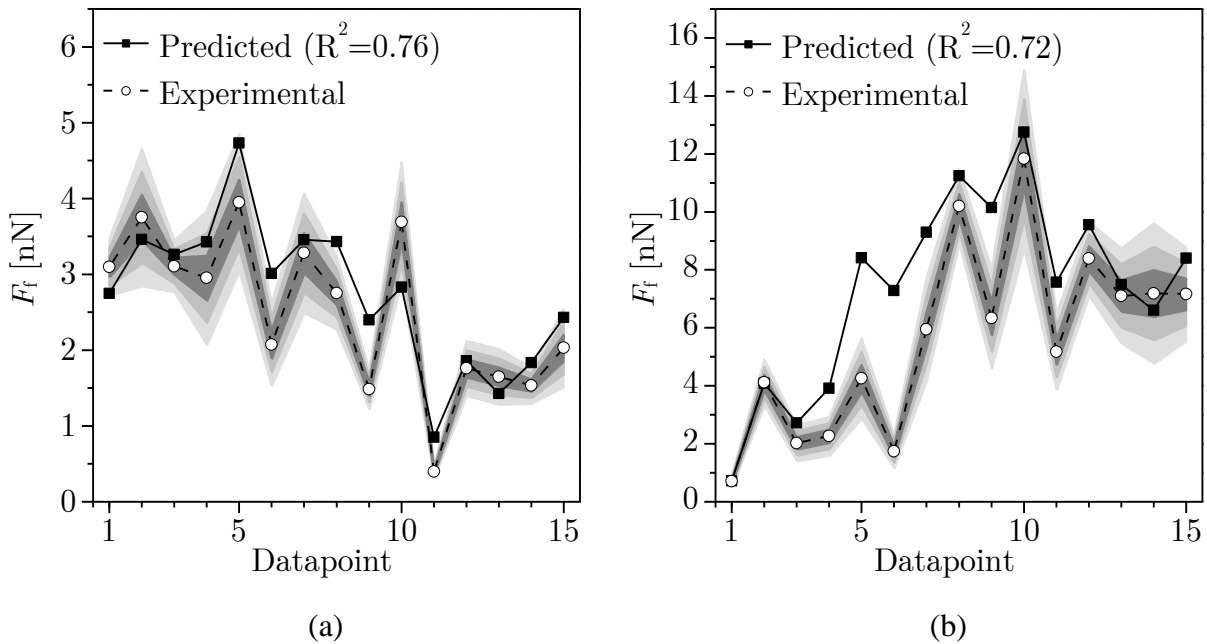


Figure 6.5 Predictive performances of the best developed MG GP model on the MC test dataset for the ALD synthesized samples: Al_2O_3 (a) and TiO_2 (b).

The fits of the model represented by equation (5.9) on the experimental test (MC) data for the PLD synthesized Al, MoS_2 and SS thin-film samples is, in turn, shown in Figure 6.6a, b and c, respectively. These plots show a remarkable fit quality for the considered samples. The Al sample is hence fitted within a two-sigma range in almost all experimental points. The MoS_2 sample's data are fitted also extremely well, bearing especially in mind some issues related to this material reported earlier when using several of the considered predictive models. The SS sample results in a slightly bigger deviation in the predictions, but still the majority of the

predicted points follow closely the trends of the experimental data.

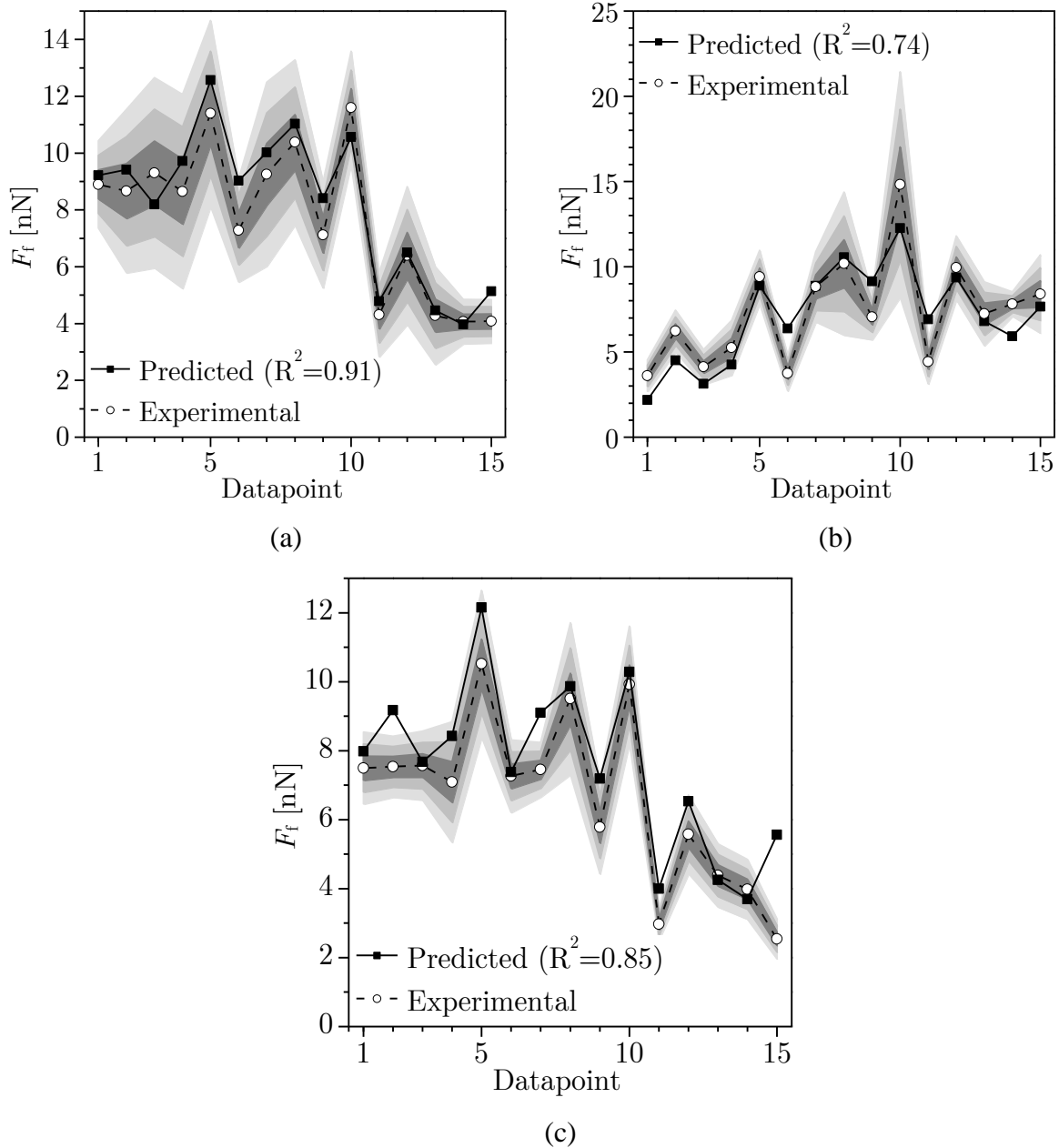


Figure 6.6 Predictive performances of the best developed MG GP model on MC test dataset for the PLD synthesized samples: Al (a), MoS₂ (b) and SS (c).

In Figure 6.7 are shown next the surface plots of the nanoscale friction force F_f values obtained by applying the model of equation (5.9) when two of the process parameters are varied while the third one is kept constant, i.e., when the normal load is $F_L = 100$ nN, sliding velocity is $v = 250$ nm/s, and temperature is $\vartheta = 40$ °C. The plots show a similarity with respect to the solutions obtained by employing the MLP and SVR models, but it is clear that the obtained solutions in this case are much simpler and smoother. For all the ALD synthesized samples the

influence of sliding velocity on friction is smooth, with a negative linear effect vs. temperature. The influence of temperature, as observed in the previously considered ML models, for both materials is again non-linear and stays quite stable with a variable sliding velocity or normal load. Finally, in the right-most column, the effects of sliding velocity and normal load show striking linear dependences as well as a general similarity to previously obtained solutions.

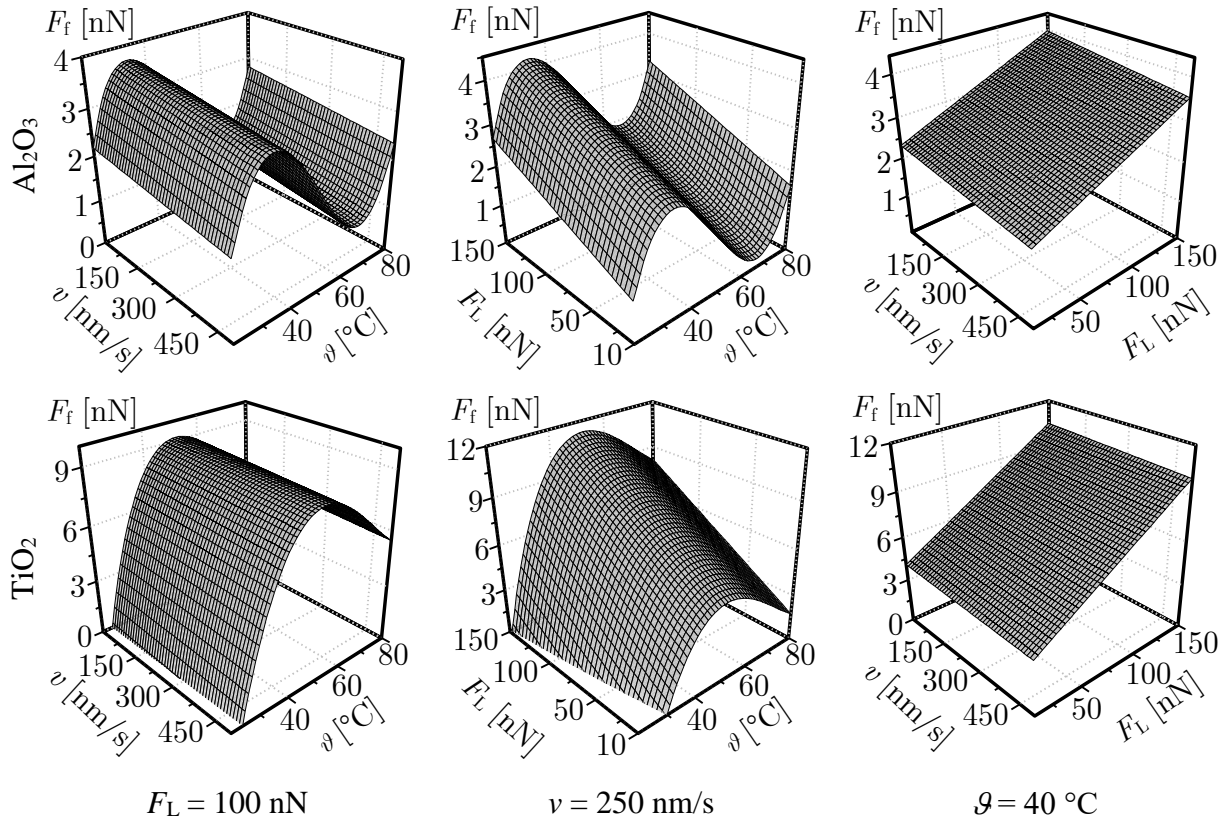


Figure 6.7 Surface plots of the results obtained via the obtained MG GP model for constant variables in columns (left to right): total load ($F_L = F_N + F_A$), sliding velocity (v) and temperature (θ), for the ALD samples: Al_2O_3 (top row) and TiO_2 (bottom row).

These similarities, permeated throughout the analysis based on the proposed MG GP model of nanoscale friction, are also evident in Figure 6.8 for the PLD-synthesized samples. This thus leads to a strong indication that the excellent fitness of the model is a general trend. For all the samples in Figure 6.8 it is then also evident that the velocity dependence is linear, as is the influence of normal load, while the effect of temperature is again nonlinear. What is more, an interesting similarity with almost identical trends in the case of the TiO_2 and MoS_2 samples becomes evident, as do those for the Al and SS samples.

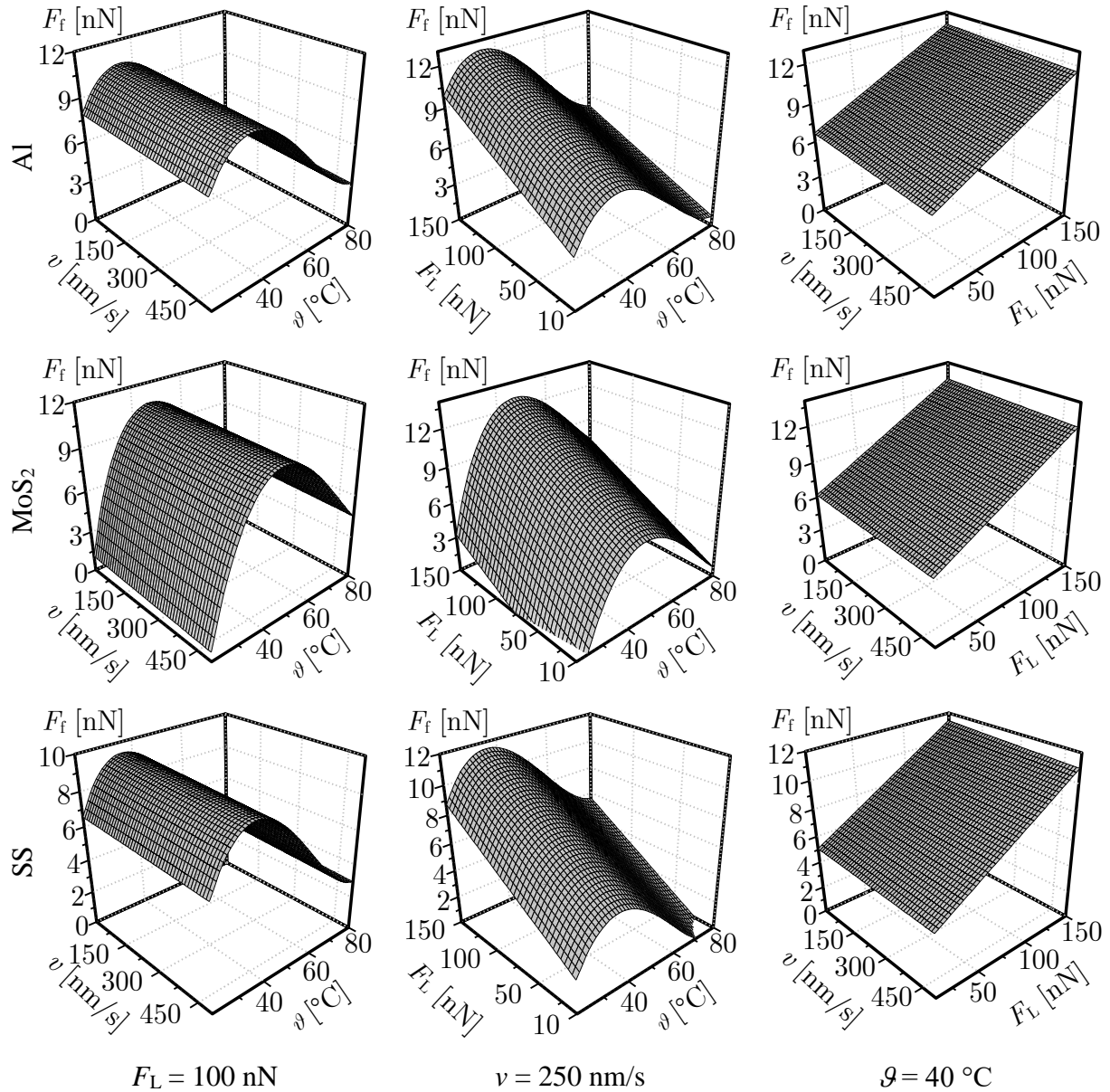


Figure 6.8 Surface plots of the results obtained via the obtained MG GP model for constant variables in columns (left to right): total load ($F_L = F_N + F_A$), sliding velocity (v) and temperature (ϑ), for the PLD samples in rows (top to bottom): Al, MoS₂ and SS.

The results obtained by employing the developed MG GP model show, therefore, undisputable and striking evidence of a similarity of the influence of the considered multiple variable process parameters on nanoscale friction, which was not only a hard idea to grasp in the earlier stages of this research, i.e., in experimental measurement phase, but also a result never systematically attained in the available literature. After all the performed tests and evaluations, it can thus be concluded with a relatively high degree of certainty that, at least for all the tested thin-film materials, the developed model faithfully reproduces the experimental results, but also (and most importantly) provides a robust predictive tool (and even a

mathematical formulation!) for the dependence of the value of the nanoscale friction force on the observed variable influencing parameters! In the previous section it is shown that the proposed MG GP mathematical formulation allows predicting with high accuracy and fidelity the value of nanoscale friction for a range of thin-films, and the influence of the most important process parameters on this value. The hence obtained functional dependencies will be thoroughly described and discussed in this part of the thesis, thus providing invaluable insights into the tribological behaviour of thin-films in the nanometric domain.

The expression of the form given by equation (5.9) is thus further algebraically simplified in terms of the class variables, i.e., by substituting each respective binary (*one-hot*) coding parameter characteristic for each of the used thin-film sample material with values 0 and 1, yielding simple equations that provide not only means for a complete characterization of the influence of the process parameters on friction in the nanometric domain, but also a robust predictive performance of the nanoscale friction force.

The finally developed predictive models of nanoscale friction and its dependence on the total normal load $F_L = F_N + F_A$, on sliding velocity v , and on temperature \mathcal{G} , are therefore:

- for the Al sample:

$$F_f = 0.04559 \cdot F_L - 0.0008751 \cdot v + 1.141 \cdot \mathcal{G} - 0.0001781 \cdot F_L \cdot \mathcal{G} - 0.02279 \cdot \mathcal{G}^2 + 0.0001258 \cdot \mathcal{G}^3 - 11.02 \quad (6.1)$$

- for the Al₂O₃ sample:

$$F_f = 0.01183 \cdot F_L - 0.0008751 \cdot v + 0.8707 \cdot \mathcal{G} - 0.0194 \cdot \mathcal{G}^2 + 0.0001258 \cdot \mathcal{G}^3 - 9.67 \quad (6.2)$$

- for the MoS₂ sample:

$$F_f = 0.04559 \cdot F_L - 0.0008751 \cdot v + 1.751 \cdot \mathcal{G} - 0.02774 \cdot \mathcal{G}^2 + 0.0001258 \cdot \mathcal{G}^3 - 28.41 \quad (6.3)$$

- for the TiO₂ sample:

$$F_f = 0.04559 \cdot F_L - 0.0008751 \cdot v + 1.831 \cdot \mathcal{G} - 0.02774 \cdot \mathcal{G}^2 + 0.0001258 \cdot \mathcal{G}^3 - 33.81 \quad (6.4)$$

- for the X39CrMo17-1 (SS) sample:

$$F_f = 0.04559 \cdot F_L - 0.0008751 \cdot v + 1.141 \cdot \mathcal{G} - 0.02274 \cdot \mathcal{G}^2 + 0.00013 \cdot \mathcal{G}^3 - 12.72 \quad (6.5)$$

The solutions of these expressions are shown graphically in Figure 6.9, allowing a visual representation of the dependence of the nanometric friction force F_f for all the thin-film materials on the total normal load F_L with variable temperatures \mathcal{G} and sliding velocities v . It can hence be concluded that all samples show fundamental similarities with a linear load dependence, as predicted also by contact mechanics models with adhesion effects, such as the DMT [46].

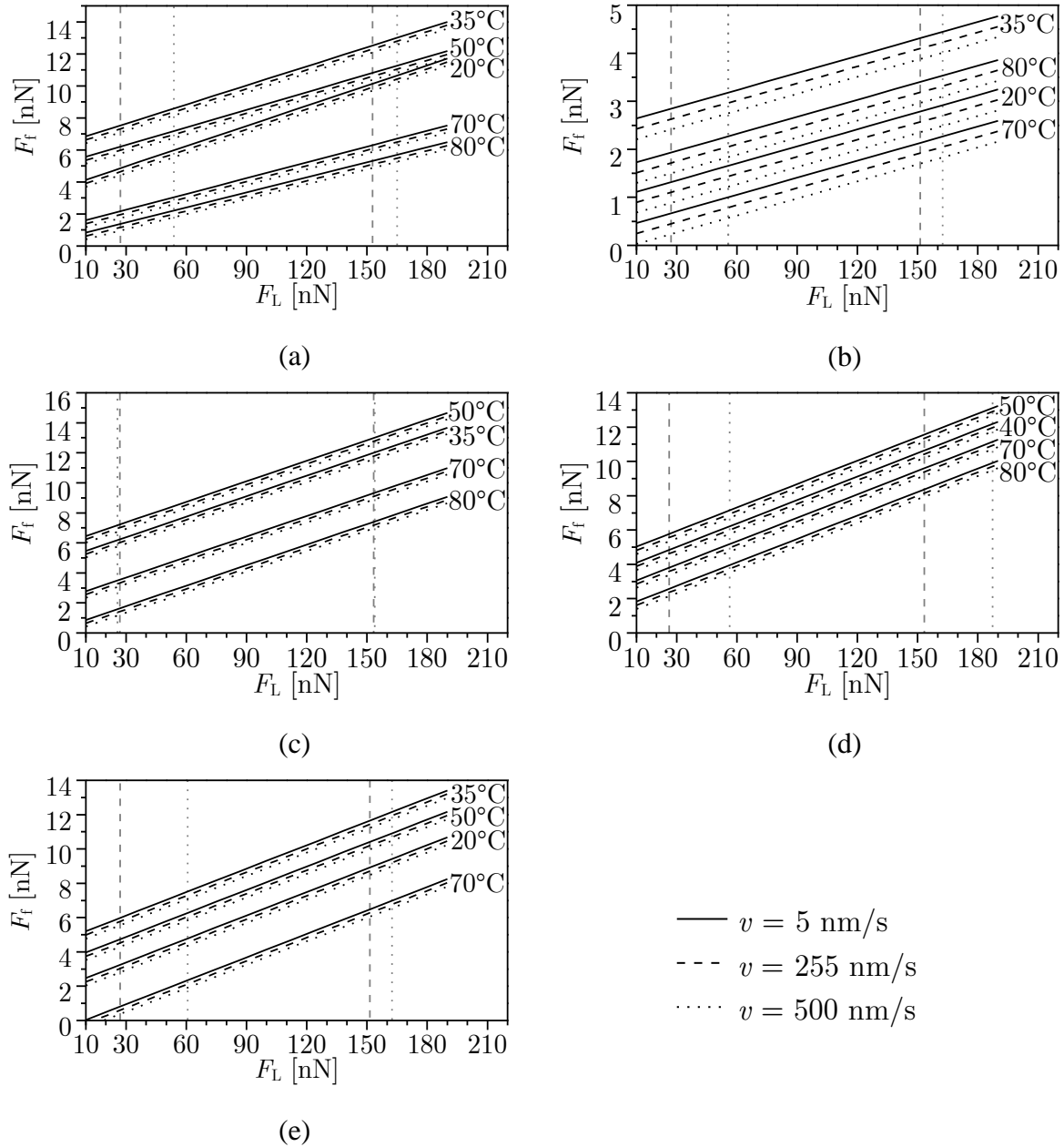


Figure 6.9 Plots of the values of the nanoscale friction force F_f vs. the total normal load ($F_L = F_N + F_A$) for different values of the v and \mathcal{G} for: Al (a), Al_2O_3 (b), MoS_2 (c), TiO_2 (d) and SS (e) as obtained from the proposed models.

The obtained linear dependencies allow evidencing the slight weakening effect of sliding velocity, which was also experimentally proven in previous literature [44], [56], [76], [122], [157]. This effect of diminishing friction with increasing sliding velocities is commonly attributed to the lubricative effect of the water-vapour layer adhered on the surface of the samples. Regarding the value of the sliding velocity effect, it can also be noted that, contrary to the small weakening on F_f for most of the samples, for Al_2O_3 a broader scatter between the parallel lines is obtained, i.e., a more pronounced negative dependence is present here.

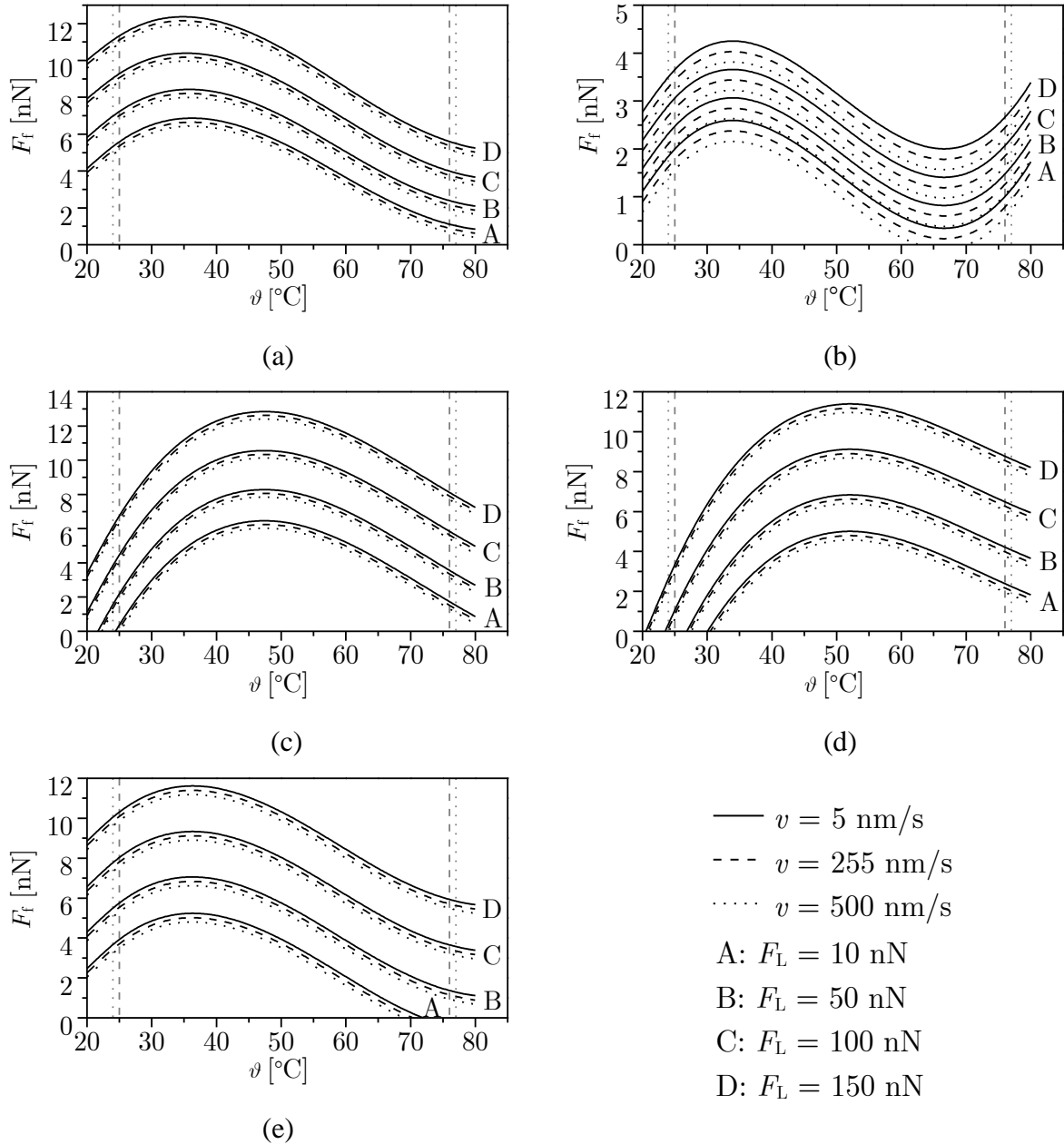


Figure 6.10 Plots of the values of the nanoscale friction force F_f vs. temperature ϑ for different values of v and $F_L = F_N + F_A$ for: Al (a), Al_2O_3 (b), MoS_2 (c), TiO_2 (d) and SS (e) as obtained from the proposed models.

The intricate interdependence of adhesion and friction is emphasised even more with these findings. In fact, the depicted lines show a change of slope and of the y-intercept with changing temperature, which is a direct consequence of the dominant effect of adhesion. What is more, this effect is superimposed to the effect of the normal force itself, since, as discussed in the above Section 3.5.2, at the nanometric scale the influence of the water meniscus force is significant inducing an increase of the total contact forces.

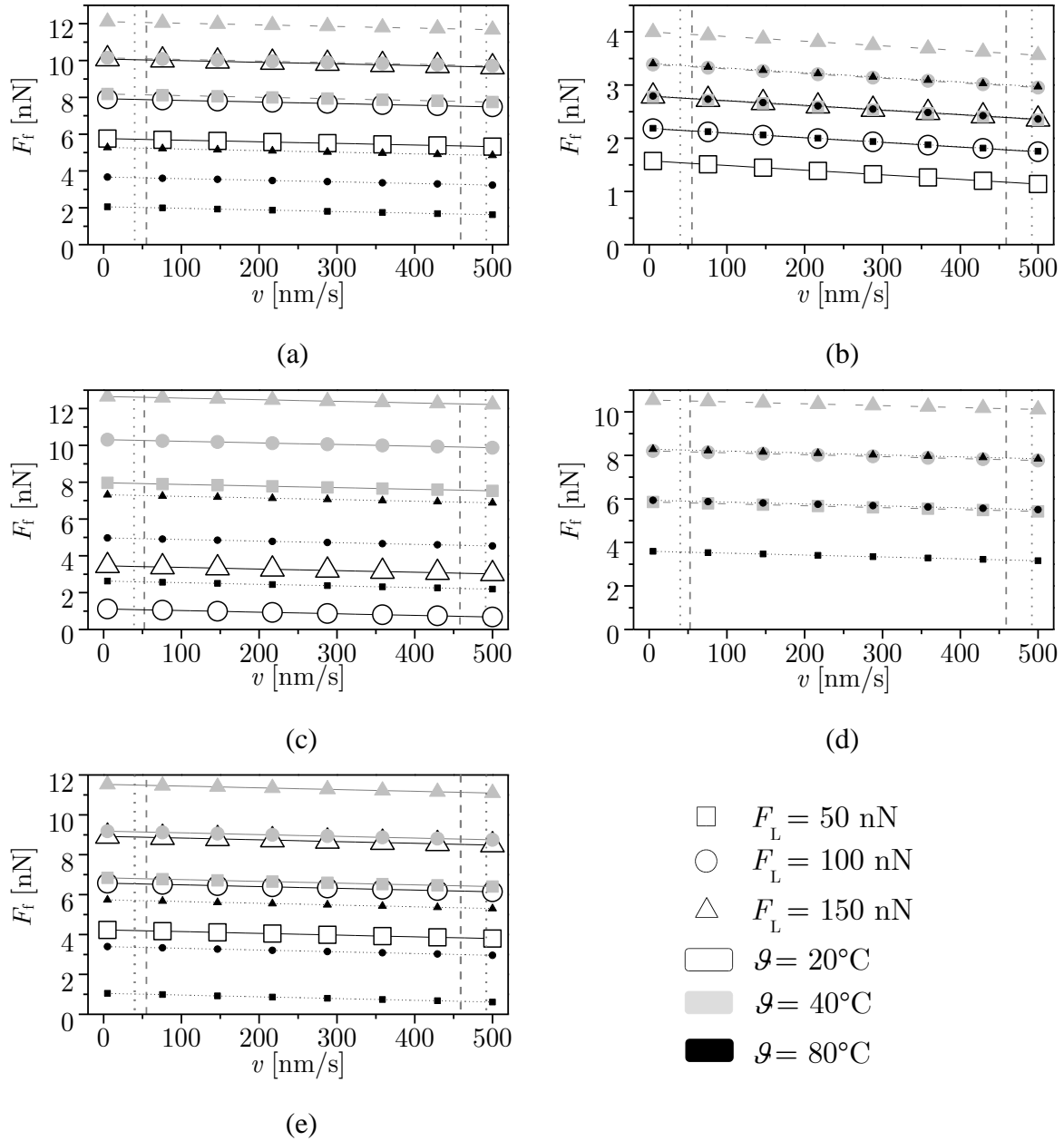


Figure 6.11 Plots of the values of the nanoscale friction force F_f vs. sliding velocity v for different values of \mathcal{G} and of $F_L = F_N + F_A$ for: Al (a), Al_2O_3 (b), MoS_2 (c), TiO_2 (d) and SS (e) as obtained from the proposed models.

Since, on the other hand, the variability of temperature induces a change of the amount of adsorbed water, i.e., the state of the meniscus, the adhesive forces also change and so does consequently the total normal load.

The variability of the influence of temperature is also evident in the graphs of Figure 6.10, as can be noticed from the distance between the depicted friction lines. A larger distance caused by a change of temperature indicates then a clearly more accentuated temperature effect, which is mostly visible on the graphs of the Al and Al_2O_3 thin-film samples.

The influence of sliding velocity v on the value of the nanoscale friction force F_f is, finally, depicted for all the considered thin-film samples in Figure 6.11. These graphs result in a bit more difficult visualization, since there are two strong overlapping effects in the two remaining dimensions. It is, nevertheless, obvious that the influence of velocity is predominantly small and, as amply evidenced before, weakening, while the stronger nonlinear influence of temperature \mathcal{G} changes the absolute value of the velocity effect, but not the trends or the strength of this effect. The influence of the total normal load F_L is also evident as a linear shift of the F_f vs. v line groups, which result in increasing the value of the nanoscale friction force.

All the graphs of Figure 6.9, Figure 6.10 and Figure 6.11 show thus the values of the nanoscale friction force F_f obtained by using the functional dependencies of the equations (6.1) to (6.5) for the considered class of thin-film sample materials and all the analysed variable process parameters. These graphs can be used as a graphical tool for determining the expected value of F_f . On the diagrams are shown also vertical dashed and dotted boundary lines indicating, respectively, the limits of the considered variables in the main (DoE-CVT) and test (MC) datasets, which, considering that the models used to derive the graphs are trained and tested only between these boundaries, provides a sort of a safety margin of their validity.

7. Conclusions and Outlook

A thorough description of a structured methodology to the experimental determination of nanometric friction performed under the concurrent influence of several influencing parameters, namely of the normal forces, of sliding velocity and of temperature, is done in the first phases of this work.⁴ An advanced approach to the design of experimental measurements is hence suggested and successfully implemented. The numerous issues involved in this challenging task are systematically studied: the synthesis and characterisation of conventional and novel thin film samples such as X39CrMo17-1, the importance of the calibration of the used probes and of the variability of adhesion on this calibration, as well as the importance of wear and adhesion of the probes themselves [128].

The results of the thus developed systematic approach provide important insights into the general trends of the dependence of nanoscale friction on the multiple process parameters as well as an indication of the respective correlations. An intricate concurrent dependence of nanoscale friction on the variable parameters is hence obtained.

The DoE-CVT based experimental measurements described in the above Chapter 4 allowed proving the marked significance of adhesion, especially in measurements with variable temperatures, making thus necessary the introduction of corrections in the determined calibration constants. Experimental data were then used to attain first-order trends, i.e., the determination of correlation matrices for each of the considered influential parameter, allowing to determine that the influence of sliding velocity on nanoscale friction is minimal, the effect of temperature is noticeable, especially in terms of adhesion variability, while the influence of the exerted normal force has a highly positive impacts on friction for all the used thin-film samples.

Separately performed experimental measurements, based on MC routines and intended to provide a testing dataset for the developed models, showed similar results as the above main measurements. Given the fact that these are performed on samples that were not dried prior to the measurements – yielding, hence, realistic habitual conditions, they provide, moreover, a more difficult predictive challenge for the used advanced numerical models. The test datasets

⁴ As pointed out in the corresponding parts of the thesis (Chapters 3 and 4), this part of the work was thoroughly described in a recent publication of the author of the thesis and his collaborators in a peer-reviewed scientific paper [128], which was produced and published as part of the obligations foreseen in the curriculum of the doctoral study of the Faculty of Engineering of the University of Rijeka, Croatia.

confirmed thus the low impact of sliding velocity, a high positive impact of the total normal load, and a high impact of temperature on nanometric friction.

These considerations allowed broadening next the insights on the impact of the multiple variable parameters on nanometric friction performed by data mining incorporating multiple machine learning methods on the obtained experimental datasets.

The data mining process allowed thus providing novel and invaluable insights into the functional dependencies of each variable's impact on the friction force at the nanoscale, showing similarities and common trends to all the analysed thin-film samples, providing a strong indication that a common basis for the analysed physical phenomenon exists and can be mathematically described. The search for this common expression is done by employing genetic programming – symbolic regression that allow attaining a single and rather simple mathematical expression resulting in very high predictive performances. The developed expression is considered as the main contribution and result of the research in the thesis.

This study thus finally contributed by attaining correlation functions linking the considered process variables to the value of nanometric friction, thus providing not only an even deeper insight into the studied phenomena made of complex interactions, but also provide invaluable, novel and unprecedented contributions in the field of nanotribology. What is more, the abundance of experimental results given in the appendices, the assessment of these via testing on state-of-the-art numerical modelling methods, the resulting systematic evaluation of the predictive performances of these numerical methods, and, finally, the original proposed model with notably high predictive performances and of simple implementation, apt to be used for practical applications, are all important scientific contributions of the thesis.

All this constitutes the preconditions and provides the means for a further in-depth understanding and practical improvements in the field of nanotribology, and a novel insight into this fundamental force of nature. This should allow eventually extending the formulation of existing friction models to the nanometric domain, hence constituting the foundation for the development of extended friction models and resulting advanced control typologies, thus contributing to increasing the precision of the moving components and of positioning of structural elements and systems to the actual nanometric range.

The results of the described research provide also means to “bridge the gap” from nanoscale tribology to micro-, meso- and, on the upper spectrum of dimensionality, the macroscale systems with friction, enabling therefore also the development and modification of the current best control algorithms (as e.g., [5], [176]), but also with important potential applications to

finite and boundary element simulation schemes involving frictional phenomena (in the current state-of-the-art given e.g., in [19], [36], [74], [96], [120], [179]), multi-asperity contact models (such as in e.g., [29], [144], [146], [169]), fractal surface models (e.g., [35], [124], [125], [183]), comparison and validation of continuum methods (contact mechanics) (e.g., [78], [79], [113]), multiscale methods (such as the [9], [98], [171]), and other practical applications.

On the lower end of the dimensionality spectrum, the measurements and models given in the thesis provide an important validation tool for the molecular, atomic, and quantum effects of nanoscale friction. The herein given results provide thus means for assessing and validating the results obtained by using molecular dynamics models involving the atomic structures of the surfaces in contact. In fact, the possibility to compare the results obtained in the thesis to molecular modelling calculations performed at the Molecular Simulations Engineering (MOSE) laboratory of the University of Trieste, Italy [161] is already under way.

List of References

- [1] Affenzeller, M. and Wagner, S., ‘Offspring Selection: A New Self-Adaptive Selection Scheme for Genetic Algorithms’, in *Adaptive and Natural Computing Algorithms*, Vienna, 2005, pp. 218–221.
- [2] AIMdyn – System Analytics, Engineering Consulting and Software Development. GoSUMD Software, [Online]. Available: <https://aimdyn.com/gosumd>. [Accessed: 15-May-2018].
- [3] Akamine, S., Barrett, R. C., and Quate, C. F., ‘Improved atomic force microscope images using microcantilevers with sharp tips’, *Applied Physics Letters*, vol. 57, no. 3, pp. 316–318, Jul. 1990.
- [4] Alam, F. M., McNaught, K. R., and Ringrose, T. J., ‘A comparison of experimental designs in the development of a neural network simulation metamodel’, *Simulation Modelling Practice and Theory*, vol. 12, no. 7–8, pp. 559–578, Nov. 2004.
- [5] Al-Bender, F., Lampaert, V., and Swevers, J., ‘Modeling of dry sliding friction dynamics: From heuristic models to physically motivated models and back’, *Chaos*, vol. 14, no. 2, pp. 446–460, May 2004.
- [6] Altfeder, I. and Krim, J., ‘Temperature dependence of nanoscale friction for Fe on YBCO’, *Journal of Applied Physics*, vol. 111, no. 9, p. 094916, May 2012.
- [7] Amthor, A., Zschaek, S., and Ament, C., ‘High Precision Position Control Using an Adaptive Friction Compensation Approach’, *IEEE Transactions on Automatic Control*, vol. 55, no. 1, pp. 274–278, Jan. 2010.
- [8] Baljon, A. R. C. and Robbins, M. O., ‘Adhesion and Friction of Thin Films’, *MRS Bulletin*, vol. 22, no. 1, pp. 22–26, Jan. 1997.
- [9] Barber, J. R., ‘Multiscale Surfaces and Amontons’ Law of Friction’, *Tribol Lett*, vol. 49, no. 3, pp. 539–543, Mar. 2013.
- [10] Barel, I., Urbakh, M., Jansen, L., and Schirmeisen, A., ‘Temperature Dependence of Friction at the Nanoscale: When the Unexpected Turns Normal’, *Tribol Lett*, vol. 39, no. 3, pp. 311–319, Sep. 2010.
- [11] Bazrafshan, M., de Rooij, M. B., and Schipper, D. J., ‘Adhesive force model at a rough interface in the presence of thin water films: the role of relative humidity’, *International Journal of Mechanical Sciences*.
- [12] Belikov, S., Alexander, J., Wall, C., Yermolenko, I., Magonov, S., and Malovichko, I.,

- ‘Thermal tune method for AFM oscillatory resonant imaging in air and liquid’, in *2014 American Control Conference*, 2014, pp. 1009–1014.
- [13] Bhushan, B., ‘Nanotribology, nanomechanics and nanomaterials characterization’, *Philosophical Transactions of the Royal Society A: Mathematical, Physical and Engineering Sciences*, vol. 366, no. 1869, pp. 1351–1381, Apr. 2008.
- [14] Bhushan, B., *Introduction to tribology*, Second edition. Chichester, West Sussex, United Kingdom: John Wiley & Sons Inc, 2013.
- [15] Bhushan, B., ‘Nanotribology and Nanomechanics of MEMS/NEMS and BioMEMS/BioNEMS Materials and Devices’, *Microelectron. Eng.*, vol. 84, no. 3, pp. 387–412, Mar. 2007.
- [16] Bhushan, B., ‘Adhesion and stiction: Mechanisms, measurement techniques, and methods for reduction’, *Journal of Vacuum Science & Technology B: Microelectronics and Nanometer Structures*, vol. 21, no. 6, p. 2262, 2003.
- [17] Bhushan, B., Ed., *Springer Handbook of Nanotechnology*. Springer Berlin Heidelberg, 2010.
- [18] Bhushan, B., Ed., *Nanotribology and Nanomechanics I*. Berlin, Heidelberg: Springer Berlin Heidelberg, 2011.
- [19] Bhushan, B. and Agrawal, G. B., ‘Stress analysis of nanostructures using a finite element method’, *Nanotechnology*, vol. 13, no. 4, p. 515, 2002.
- [20] Bhushan, B. and Sundararajan, S., ‘Micro/nanoscale friction and wear mechanisms of thin films using atomic force and friction force microscopy’, *Acta Mater.*, vol. 46, 1998.
- [21] Billard, L. and Diday, E., *Symbolic Data Analysis: Conceptual Statistics and Data Mining*. John Wiley & Sons, 2012.
- [22] Billard, L. and Diday, E., ‘Symbolic Regression Analysis’, in *Classification, Clustering, and Data Analysis*, Berlin, Heidelberg, 2002, pp. 281–288.
- [23] Binnig, G., Quate, C. F., and Gerber, Ch., ‘Atomic force microscope’, *Physical Review Letters*, vol. 56, no. 9, pp. 930–933, 1986.
- [24] Binnig, G. and Rohrer, H., ‘Scanning tunneling microscopy’, *Surface Science*, vol. 152–153, pp. 17–26, Apr. 1985.
- [25] Binnig, G., Rohrer, H., Gerber, Ch., and Weibel, E., ‘Surface Studies by Scanning Tunneling Microscopy’, *Phys. Rev. Lett.*, vol. 49, no. 1, pp. 57–61, Jul. 1982.
- [26] Birleanu, C., Pustan, M., Rusu, F., Dudescu, C., Muller, R., and Baracu, A., ‘Relative humidity influence on adhesion effect in MEMS flexible structures’, *Microsyst Technol.*

- pp. 1–11, Mar. 2018.
- [27] Bowden, F. P. and Tabor, D., ‘The Friction and Lubrication of Solids’, *American Journal of Physics*, vol. 19, no. 7, pp. 428–429, Oct. 1951.
- [28] Box, G. E. P., ‘Science and Statistics’, *Journal of the American Statistical Association*, vol. 71, no. 356, pp. 791–799, Dec. 1976.
- [29] Brodnik Zugelj, B. and Kalin, M., ‘Submicron-scale experimental analyses of the multi-asperity contact behaviour of various steels, an aluminium alloy and a polymer’, *Tribology International*, vol. 141, p. 105955, Jan. 2020.
- [30] Bruker. AFM Probes – RS titanium roughness sample, [Online]. Available: <https://www.brukerafmprobes.com/a-3552-rs.aspx>. [Accessed: 16-May-2018].
- [31] Bruker. Silicon Nitride AFM Probes SNL-10, [Online]. Available: <https://www.brukerafmprobes.com/p-3693-snl-10.aspx>. [Accessed: 15-May-2018].
- [32] B.Sc, G. A. T., ‘CVI. A molecular theory of friction’, *The London, Edinburgh, and Dublin Philosophical Magazine and Journal of Science*, vol. 7, no. 46, pp. 905–939, Jun. 1929.
- [33] Buckley, D. H., *Surface effects in adhesion, friction, wear, and lubrication*. Amsterdam ; New York : New York: Elsevier Scientific Pub. Co. ; Distributors for the U.S. and Canada, Elsevier North-Holland, 1981.
- [34] Busuttill, K., Geoghegan, M., Hunter, C. A., and Leggett, G. J., ‘Contact Mechanics of Nanometer-Scale Molecular Contacts: Correlation between Adhesion, Friction, and Hydrogen Bond Thermodynamics’, *J. Am. Chem. Soc.*, vol. 133, no. 22, pp. 8625–8632, Jun. 2011.
- [35] Buzio, R., Boragno, C., Biscarini, F., Mongeot, F. B. D., and Valbusa, U., ‘The contact mechanics of fractal surfaces’, *Nature Materials*, vol. 2, no. 4, pp. 233–236, Apr. 2003.
- [36] Carpick, R. W. and Plesha, M. E., ‘Development and integration of single-asperity nanotribology experiments & nanoscale interface finite element modeling for prediction and control of friction and damage in micro- and nano-mechanical systems’, Mar. 2007.
- [37] Chang, C.-C. and Lin, C.-J., ‘LIBSVM: A library for support vector machines’, *ACM Transactions on Intelligent Systems and Technology*, vol. 2, no. 3, pp. 1–27, Apr. 2011.
- [38] Chen, L., Xiao, C., Yu, B., Kim, S. H., and Qian, L., ‘What governs friction of silicon oxide in humid environment – contact area between solids, water meniscus around the contact, or water layer structure?’, *Langmuir*, Aug. 2017.
- [39] Choi, J. L. and Gethin, D. T., ‘Simulation of atomic force microscopy operation via three-dimensional finite element modelling’, *Nanotechnology*, vol. 20, no. 6, p. 065702, Feb.

2009.

- [40] Chu, E.-D., Wang, P.-H., Hong, Y.-Z., Woon, W.-Y., and Chiu, H.-C., ‘Frictional characteristics of nano-confined water mediated hole-doped single-layer graphene on silica surface’, *Nanotechnology*, vol. 30, no. 4, p. 045706, 2019.
- [41] Chung, K.-H., ‘Wear characteristics of atomic force microscopy tips: A reivew’, *International Journal of Precision Engineering and Manufacturing*, vol. 15, no. 10, pp. 2219–2230, Oct. 2014.
- [42] Çolak, A., Wormeester, H., Zandvliet, H. J. W., and Poelsema, B., ‘Surface adhesion and its dependence on surface roughness and humidity measured with a flat tip’, *Applied Surface Science*, vol. 258, no. 18, pp. 6938–6942, Jul. 2012.
- [43] Cox, D. R. and Reid, N., *The theory of the design of experiments*. Boca Raton: Chapman & Hall/CRC, 2000.
- [44] Dagdeviren, O. E., ‘Exploring load, velocity, and surface disorder dependence of friction with one-dimensional and two-dimensional models’, *Nanotechnology*, vol. 29, no. 31, p. 315704, 2018.
- [45] Dahlen, G., Osborn, M., Okulan, N., Foreman, W., Chand, A., and Foucher, J., ‘Tip characterization and surface reconstruction of complex structures with critical dimension atomic force microscopy’, *Journal of Vacuum Science & Technology B: Microelectronics and Nanometer Structures*, vol. 23, no. 6, p. 2297, 2005.
- [46] Derjaguin, B. V., Muller, V. M., and Toporov, Yu. P., ‘Effect of contact deformations on the adhesion of particles’, *Journal of Colloid and Interface Science*, vol. 53, no. 2, pp. 314–326, Nov. 1975.
- [47] Devasia, S., Eleftheriou, E., and Moheimani, S. O. R., ‘A Survey of Control Issues in Nanopositioning’, *IEEE Transactions on Control Systems Technology*, vol. 15, no. 5, pp. 802–823, Sep. 2007.
- [48] Dowson, D., *History of tribology*. London; New york, Longman., 1978.
- [49] Draper, N. R. and Smith, H., *Applied Regression Analysis, 3rd Edition | Wiley*, Third Edition. John Wiley & Sons, Ltd, 1998.
- [50] Du, Q., Faber, V., and Gunzburger, M., ‘Centroidal Voronoi Tessellations: Applications and Algorithms’, *SIAM Rev.*, vol. 41, no. 4, pp. 637–676, Jan. 1999.
- [51] Enachescu, M., van den Oetelaar, R. J. A., Carpick, R. W., Ogletree, D. F., Flipse, C. F. J., and Salmeron, M., ‘Observation of proportionality between friction and contact area at the nanometer scale’, *Tribology Letters*, vol. 7, no. 2, p. 73, Sep. 1999.

- [52] Fang, W. and Lo, C.-Y., ‘On the thermal expansion coefficients of thin films’, *Sensors and Actuators A: Physical*, vol. 84, no. 3, pp. 310–314, Sep. 2000.
- [53] Fu, L., Hu, X. Y., and Adams, N. A., ‘A physics-motivated Centroidal Voronoi Particle domain decomposition method’, *Journal of Computational Physics*, vol. 335, pp. 718–735, Apr. 2017.
- [54] Fujisawa, S., Sugawara, Y., Ito, S., Mishima, S., Okada, T., and Morita, S., ‘The two-dimensional stick-slip phenomenon with atomic resolution’, *Nanotechnology*, vol. 4, no. 3, p. 138, 1993.
- [55] Galan, U. and Sodano, H. A., ‘Molecular dynamics prediction of interfacial strength and validation through atomic force microscopy’, *Applied Physics Letters*, vol. 101, no. 15, p. 151603, Oct. 2012.
- [56] Gangloff, D., Bylinskii, A., Counts, I., Jhe, W., and Vuletić, V., ‘Velocity tuning of friction with two trapped atoms’, *Nature Physics*, vol. 11, no. 11, pp. 915–919, Sep. 2015.
- [57] Gentle, J. E., *Random Number Generation and Monte Carlo Methods*. New York: Springer-Verlag, 1998.
- [58] Ghodssi, R. and Lin, P., Eds., *MEMS Materials and Processes Handbook*. Springer US, 2011.
- [59] Gibson, C. T., Smith, D. A., and Roberts, C. J., ‘Calibration of silicon atomic force microscope cantilevers’, *Nanotechnology*, vol. 16, no. 2, pp. 234–238, Feb. 2005.
- [60] Gotsmann, B. and Lantz, M. A., ‘Atomistic Wear in a Single Asperity Sliding Contact’, *Physical Review Letters*, vol. 101, no. 12, Sep. 2008.
- [61] Greenwood, J. A., ‘Constriction resistance and the real area of contact’, *British Journal of Applied Physics*, pp. 1621–1633, 1966.
- [62] Greenwood, J. A. and Williamson, J. B. P., ‘Contact of Nominally Flat Surfaces’, *Proceedings of the Royal Society A: Mathematical, Physical and Engineering Sciences*, vol. 295, no. 1442, pp. 300–319, Dec. 1966.
- [63] Guo, Y., Qu, Z., Braiman, Y., Zhang, Z., and Barhen, J., ‘Nanotribology and nanoscale friction’, *IEEE Control Systems Magazine*, vol. 28, no. 6, pp. 92–100, Dec. 2008.
- [64] Hamel, L., *Knowledge discovery with support vector machines*. Hoboken, N.J: John Wiley & Sons, 2009.
- [65] Hastie, T., Tibshirani, R., and Friedman, J., *The Elements of Statistical Learning: Data Mining, Inference, and Prediction, Second Edition*, 2nd ed. New York: Springer-Verlag, 2009.

- [66] Hinkelmann, K. and Kempthorne, O., *Design and analysis of experiments. Vol. 1: Introduction to experimental design*, 2. ed. Hoboken, NJ: Wiley-Interscience, 2008.
- [67] Holmberg, K., Andersson, P., and Erdemir, A., ‘Global energy consumption due to friction in passenger cars’, *Tribology International*, vol. 47, pp. 221–234, Mar. 2012.
- [68] Holmberg, K. and Erdemir, A., ‘The impact of tribology on energy use and CO2 emission globally and in combustion engine and electric cars’, *Tribology International*, Mar. 2019.
- [69] Hornby, G. S., ‘ALPS: The Age-layered Population Structure for Reducing the Problem of Premature Convergence’, in *Proceedings of the 8th Annual Conference on Genetic and Evolutionary Computation*, New York, NY, USA, 2006, pp. 815–822.
- [70] Hu, J., Goodman, E. D., Li, S., and Rosenberg, R., ‘Automated synthesis of mechanical vibration absorbers using genetic programming’, *AI EDAM*, vol. 22, no. 3, pp. 207–217, Aug. 2008.
- [71] Hughes, A. E. and Sexton, B. A., ‘Curve fitting XPS spectra’, *Journal of Electron Spectroscopy and Related Phenomena*, vol. 46, no. 1, pp. 31–42, Jan. 1988.
- [72] Hulikal, S., Lapusta, N., and Bhattacharya, K., ‘Static and sliding contact of rough surfaces: effect of asperity-scale properties and long-range elastic interactions’, *Journal of the Mechanics and Physics of Solids*.
- [73] Hutchings, I. M., ‘Leonardo da Vinci’s studies of friction’, *Wear*, vol. 360–361, pp. 51–66, Aug. 2016.
- [74] Hyun, S., Pei, L., Molinari, J.-F., and Robbins, M. O., ‘Finite-element analysis of contact between elastic self-affine surfaces’, *Phys Rev E Stat Nonlin Soft Matter Phys*, vol. 70, no. 2 Pt 2, p. 026117, Aug. 2004.
- [75] Jang, J., Yang, M., and Schatz, G., ‘Microscopic origin of the humidity dependence of the adhesion force in atomic force microscopy’, *The Journal of Chemical Physics*, vol. 126, no. 17, p. 174705, May 2007.
- [76] Jing, D., Pan, Y., Li, D., Zhao, X., and Bhushan, B., ‘Effect of Surface Charge on the Nanofriction and Its Velocity Dependence in an Electrolyte Based on Lateral Force Microscopy’, *Langmuir*, vol. 33, no. 8, pp. 1792–1798, Feb. 2017.
- [77] Johnson, K. L., ‘Contact Mechanics by K. L. Johnson’, *Cambridge Core*, May-1985. [Online]. Available: [/core/books/contact-mechanics/E3707F77C2EBCE727C3911AFBD2E4AC2](https://doi.org/10.1017/core/books/contact-mechanics/E3707F77C2EBCE727C3911AFBD2E4AC2). [Accessed: 12-Mar-2019].
- [78] Johnson, K. L., ‘Continuum Mechanics Modeling of Adhesion and Friction’, *Langmuir*, vol. 12, no. 19, pp. 4510–4513, Jan. 1996.

- [79] Johnson, K. L., ‘A Continuum Mechanics Model of Adhesion and Friction in a Single Asperity Contact’, in *Micro/Nanotribology and Its Applications*, Bhushan, B., Ed. Dordrecht: Springer Netherlands, 1997, pp. 151–168.
- [80] Johnson, K. L., Kendall, K., Roberts, A. D., and Tabor, D., ‘Surface energy and the contact of elastic solids’, *Proceedings of the Royal Society of London. A. Mathematical and Physical Sciences*, vol. 324, no. 1558, pp. 301–313, Sep. 1971.
- [81] Jost H. P., ‘Lubrication (Tribology) Education and Research, A Report on the Present Position and Industry’s Needs’, *London: Her Majesty’s Stationary Office, Department of Education and Science*, 1966.
- [82] Kamenar, E. and Zelenika, S., ‘Nanometric positioning accuracy in the presence of presliding and sliding friction: Modelling, identification and compensation’, *Mechanics Based Design of Structures and Machines*, vol. 45, no. 1, pp. 111–126, Jan. 2017.
- [83] Kamenar, E. and Zelenika, S., ‘Issues in validation of pre-sliding friction models for ultra-high precision positioning’, *Proceedings of the Institution of Mechanical Engineers, Part C: Journal of Mechanical Engineering Science*, p. 0954406218758797, Feb. 2018.
- [84] Kecman, V., *Learning and soft computing: support vector machines, neural networks, and fuzzy logic models*. Cambridge, Mass: MIT Press, 2001.
- [85] Kim, D.-I., Grobelny, J., Pradeep, N., and Cook, R. F., ‘Origin of Adhesion in Humid Air’, *Langmuir*, vol. 24, no. 5, pp. 1873–1877, Mar. 2008.
- [86] Knowles, J., Corne, D., and Deb, K., Eds., *Multiobjective Problem Solving from Nature: From Concepts to Applications*. Berlin Heidelberg: Springer-Verlag, 2008.
- [87] Koza, J. R., ‘Human-competitive results produced by genetic programming’, *Genet Program Evolvable Mach*, vol. 11, no. 3, pp. 251–284, Sep. 2010.
- [88] Koza, J. R., *Genetic Programming: On the Programming of Computers by Means of Natural Selection*. Cambridge, MA, USA: MIT Press, 1992.
- [89] Koza, J. R., ‘Genetic programming as a means for programming computers by natural selection’, *Stat Comput*, vol. 4, no. 2, pp. 87–112, Jun. 1994.
- [90] Kroese, D. P., Taimre, T., and Botev, Z. I., ‘Uniform Random Number Generation’, in *Handbook of Monte Carlo Methods*, John Wiley & Sons, Ltd, 2011, pp. 1–23.
- [91] Kronberger, G., Winkler, S., Affenzeller, M., and Wagner, S., ‘On Crossover Success Rate in Genetic Programming with Offspring Selection’, in *Genetic Programming*, Berlin, Heidelberg, 2009, pp. 232–243.
- [92] Krylov, S. Y. and Frenken, J. W. M., ‘The crucial role of temperature in atomic scale

- friction’, *Journal of Physics: Condensed Matter*, vol. 20, no. 35, p. 354003, Sep. 2008.
- [93] Labuda, A., Cao, C., Walsh, T., Meinhold, J., Proksch, R., Sun, Y., and Filleter, T., ‘Static and dynamic calibration of torsional spring constants of cantilevers’, *Review of Scientific Instruments*, vol. 89, no. 9, p. 093701, Sep. 2018.
- [94] Langdon, W. B. and Buxton, B. F., ‘Genetic Programming for Mining DNA Chip data from Cancer Patients’, *Genetic Programming and Evolvable Machines*, vol. 5, no. 3, pp. 251–257, Sep. 2004.
- [95] Langdon, W. B. and Poli, R., *Foundations of Genetic Programming*. Berlin Heidelberg: Springer-Verlag, 2002.
- [96] Li, Q. and Popov, V. L., ‘Boundary element method for normal non-adhesive and adhesive contacts of power-law graded elastic materials’, *Computational Mechanics*, Aug. 2017.
- [97] Liu, J., Notbohm, J. K., Carpick, R. W., and Turner, K. T., ‘Method for Characterizing Nanoscale Wear of Atomic Force Microscope Tips’, *ACS Nano*, vol. 4, no. 7, pp. 3763–3772, Jul. 2010.
- [98] Liu, W. K., Karpov, E. G., and Park, H. S., *Nano mechanics and materials: theory, multiscale methods and applications*. Chichester, England ; Hoboken, NJ: John Wiley, 2006.
- [99] Liu, Y. F., Li, J., Zhang, Z. M., Hu, X. H., and Zhang, W. J., ‘Experimental comparison of five friction models on the same test-bed of the micro stick-slip motion system’, *Mechanical Sciences*, vol. 6, no. 1, pp. 15–28, Mar. 2015.
- [100] Lohn, J. D., Hornby, G. S., and Linden, D. S., ‘An Evolved Antenna for Deployment on Nasa’s Space Technology 5 Mission’, in *Genetic Programming Theory and Practice II*, O’Reilly, U.-M., Yu, T., Riolo, R., and Worzel, B., Eds. Boston, MA: Springer US, 2005, pp. 301–315.
- [101] Lotov, A., Bushenkov, V. A., and Kamenev, G. K., *Interactive Decision Maps: Approximation and Visualization of Pareto Frontier*. Springer US, 2004.
- [102] Love, G., Nicholson, W. A. P., and Armigliato, A., Eds., *Modern Developments and Applications in Microbeam Analysis*. Wien: Springer-Verlag, 1998.
- [103] Ma, Y. and Guo, G., Eds., *Support Vector Machines Applications*. Springer International Publishing, 2014.
- [104] Madansky, A., ‘Categorical Variables in Regression’, in *Prescriptions for Working Statisticians*, Madansky, A., Ed. New York, NY: Springer, 1988, pp. 214–251.
- [105] Madansky, A., ‘Testing for Normality’, in *Prescriptions for Working Statisticians*,

- Madansky, A., Ed. New York, NY: Springer, 1988, pp. 14–55.
- [106] Mandel, J., *The Statistical Analysis of Experimental Data*. Courier Corporation, 2012.
- [107] Manini, N., Mistura, G., Paolicelli, G., Tosatti, E., and Vanossi, A., ‘Current trends in the physics of nanoscale friction’, *Advances in Physics: X*, vol. 2, no. 3, pp. 569–590, May 2017.
- [108] Martín Abadi, Ashish Agarwal, Paul Barham, Eugene Brevdo, Zhifeng Chen, Craig Citro, Greg S. Corrado, Andy Davis, Jeffrey Dean, Matthieu Devin, Sanjay Ghemawat, Ian Goodfellow, Andrew Harp, Geoffrey Irving, Michael Isard, Jia, Y., Rafal Jozefowicz, Lukasz Kaiser, Manjunath Kudlur, Josh Levenberg, Dan Mané, Rajat Monga, Sherry Moore, Derek Murray, Chris Olah, Mike Schuster, Jonathon Shlens, Benoit Steiner, Ilya Sutskever, Kunal Talwar, Paul Tucker, Vincent Vanhoucke, Vijay Vasudevan, Fernanda Viégas, Oriol Vinyals, Pete Warden, Martin Wattenberg, Martin Wicke, Yuan Yu, and Xiaoqiang Zheng, *TensorFlow: Large-Scale Machine Learning on Heterogeneous Systems*. 2015.
- [109] Mate, C. M., McClelland, G. M., Erlandsson, R., and Chiang, S., ‘Atomic-scale friction of a tungsten tip on a graphite surface’, 1987. *Phys. Rev. Lett.*, vol. 59.
- [110] Mead, R., Gilmour, S. G., and Mead, A., *Statistical principles for the design of experiments*. Cambridge: Cambridge University Press, 2012.
- [111] Mekid, S., ‘Precision design aspects for friction actuation with error compensation’, *J Mech Sci Technol*, vol. 23, no. 11, pp. 2873–2884, Nov. 2009.
- [112] Meljanac, D., Juraić, K., Plodinec, M., Siketić, Z., Gracin, D., Krstulović, N., Salamon, K., Skenderović, H., Kregar, Z., Rakić, I. Š., and Bernstorff, S., ‘Influence of RF excitation during pulsed laser deposition in oxygen atmosphere on the structural properties and luminescence of nanocrystalline ZnO:Al thin films’, *Journal of Vacuum Science & Technology A*, vol. 34, no. 2, p. 021514, Feb. 2016.
- [113] Mergel, J. C., Sahli, R., Scheibert, J., and Sauer, R. A., ‘Continuum contact models for coupled adhesion and friction’, *The Journal of Adhesion*, vol. 95, no. 12, pp. 1101–1133, Oct. 2019.
- [114] MIKROMASCH. Test Structures – TGF11 Series, [Online]. Available: www.spmtips.com/test-structures-TGF11-series.html. [Accessed: 15-May-2018].
- [115] Miller, D. C., Foster, R. R., Jen, S.-H., Bertrand, J. A., Cunningham, S. J., Morris, A. S., Lee, Y.-C., George, S. M., and Dunn, M. L., ‘Thermo-mechanical properties of alumina films created using the atomic layer deposition technique’, *Sensors and Actuators A:*

- Physical*, vol. 164, no. 1, pp. 58–67, Nov. 2010.
- [116] Milne, Z. B., Bernal, R. A., and Carpick, R. W., ‘Sliding History-Dependent Adhesion of Nanoscale Silicon Contacts Revealed by in situ Transmission Electron Microscopy’, *Langmuir*, Aug. 2019.
- [117] Mohammadi Bayazidi, A., Wang, G.-G., Bolandi, H., Alavi, A. H., and Gandomi, A. H., ‘Multigene Genetic Programming for Estimation of Elastic Modulus of Concrete’, *Mathematical Problems in Engineering*, 2014. [Online]. Available: <https://www.hindawi.com/journals/mpe/2014/474289/>. [Accessed: 27-Nov-2019].
- [118] Moulder, J. F., *Handbook of X-ray Photoelectron Spectroscopy: A Reference Book of Standard Spectra for Identification and Interpretation of XPS Data*. Physical Electronics Division, Perkin-Elmer Corporation, 1992.
- [119] Munz, M., ‘Force calibration in lateral force microscopy: a review of the experimental methods’, *Journal of Physics D: Applied Physics*, vol. 43, no. 6, p. 063001, Feb. 2010.
- [120] Nguyen, V. T. and Hwu, C., ‘Boundary element method for two-dimensional frictional contact problems of anisotropic elastic solids’, *Engineering Analysis with Boundary Elements*, vol. 108, pp. 49–59, Nov. 2019.
- [121] O’Neill, M. and Ryan, C., *Grammatical Evolution: Evolutionary Automatic Programming in an Arbitrary Language*. Springer US, 2003.
- [122] Ouyang, W., Ramakrishna, S. N., Rossi, A., Urbakh, M., Spencer, N. D., and Arcifa, A., ‘Load and Velocity Dependence of Friction Mediated by Dynamics of Interfacial Contacts’, *Phys. Rev. Lett.*, vol. 123, no. 11, p. 116102, Sep. 2019.
- [123] Pan, I., Pandey, D. S., and Das, S., ‘Global solar irradiation prediction using a multi-gene genetic programming approach’, *Journal of Renewable and Sustainable Energy*, vol. 5, no. 6, p. 063129, Nov. 2013.
- [124] Pan, W., Li, X., Wang, L., Mu, J., and Yang, Z., ‘A loading fractal prediction model developed for dry-friction rough joint surfaces considering elastic–plastic contact’, *Acta Mech*, vol. 229, no. 5, pp. 2149–2162, May 2018.
- [125] Panagouli, O. K. and Iordanidou, K., ‘Dependence of friction coefficient on the resolution and fractal dimension of metallic fracture surfaces’, *International Journal of Solids and Structures*, vol. 50, no. 20, pp. 3106–3118, Oct. 2013.
- [126] Payne, B. P., Biesinger, M. C., and McIntyre, N. S., ‘X-ray photoelectron spectroscopy studies of reactions on chromium metal and chromium oxide surfaces’, *Journal of Electron Spectroscopy and Related Phenomena*, vol. 184, no. 1, pp. 29–37, Feb. 2011.

- [127] Pedregosa, F., Varoquaux, G., Gramfort, A., Michel, V., Thirion, B., Grisel, O., Blondel, M., Prettenhofer, P., Weiss, R., Dubourg, V., Vanderplas, J., Passos, A., Cournapeau, D., Brucher, M., Perrot, M., and Duchesnay, E., ‘Scikit-learn: Machine Learning in Python’, *Journal of Machine Learning Research*, vol. 12, pp. 2825–2830, 2011.
- [128] Perčić, M., Zelenika, S., Mezić, I., Peter, R., and Krstulović, N., ‘An experimental methodology for the concurrent characterization of multiple parameters influencing nanoscale friction’, *Friction*, Apr. 2019.
- [129] Perčić, M., Zelenika, S., Mezić, I., Peter, R., and Krstulović, N., ‘Experimental approach to establishing a model of nanoscale friction’, *Proceedings of the 18th EUSPEN International Conference*, p. 63, Jun. 2018.
- [130] Persson, J., *Sliding Friction: Physical Principles and Applications*. Springer, Heidelberg, 2000.
- [131] Piatkowski, T., ‘GMS friction model approximation’, *Mechanism and Machine Theory*, vol. 75, pp. 1–11, May 2014.
- [132] Piatkowski, T., ‘Dahl and LuGre dynamic friction models — The analysis of selected properties’, *Mechanism and Machine Theory*, vol. 73, pp. 91–100, Mar. 2014.
- [133] Popov, V. L., ‘Is tribology approaching its Golden Age? Grand Challenges in Engineering Education and Tribological Research’, *Front. Mech. Eng.*, vol. 4, 2018.
- [134] Popov, V. L., *Contact Mechanics and Friction: Physical Principles and Applications*. Berlin Heidelberg: Springer-Verlag, 2010.
- [135] Popov, V. L., ‘Numerical Simulation Methods in Friction Physics’, in *Contact Mechanics and Friction*, Berlin, Heidelberg: Springer Berlin Heidelberg, 2010, pp. 301–322.
- [136] Powell, M. J. D., ‘The BOBYQA algorithm for bound constrained optimization without derivatives’, p. 39.
- [137] Rabinovich, Y. I., Adler, J. J., Ata, A., Singh, R. K., and Moudgil, B. M., ‘Adhesion between Nanoscale Rough Surfaces’, *Journal of Colloid and Interface Science*, vol. 232, no. 1, pp. 17–24, Dec. 2000.
- [138] Rabinowicz, E., *Friction and wear of materials*. Number 2nd Edition, 1995.
- [139] Riolo, R. and Worzel, B., Eds., *Genetic Programming Theory and Practice*. Springer US, 2003.
- [140] Romero, V. J., Burkardt, J. V., Gunzburger, M. D., and Peterson, J. S., ‘Comparison of pure and “Latinized” centroidal Voronoi tessellation against various other statistical sampling methods’, *Reliability Engineering & System Safety*, vol. 91, no. 10, pp. 1266–

1280, Oct. 2006.

- [141] Rota, A., Serpini, E., Gazzadi, G. C., and Valeri, S., ‘AFM-based tribological study of nanopatterned surfaces: the influence of contact area instabilities’, *Journal of Physics: Condensed Matter*, vol. 28, no. 13, p. 134008, Apr. 2016.
- [142] Ruan, J.-A. and Bhushan, B., ‘Frictional behavior of highly oriented pyrolytic graphite’, *Journal of Applied Physics*, vol. 76, no. 12, pp. 8117–8120, Dec. 1994.
- [143] Ryan, C., O’Neill, M., and Collins, J. J., Eds., *Handbook of Grammatical Evolution*. Springer International Publishing, 2018.
- [144] Sadeghi, A., ‘Superlubricity controlled by the multiatomic nature of nanocontacts’, *Phys. Rev. B*, vol. 98, no. 7, p. 075407, Aug. 2018.
- [145] Sankar, K. M., Kakkar, D., Dubey, S., Garimella, S. V., Goyat, M., Joshi, S., and Pandey, J. K., ‘Theoretical and computational studies on nanofriction: A review’, *Proceedings of the Institution of Mechanical Engineers, Part J: Journal of Engineering Tribology*, p. 1350650119863993, Jul. 2019.
- [146] Santhapuram, R. R. and Nair, A. K., ‘Frictional properties of multi-asperity surfaces at the nanoscale’, *Computational Materials Science*, vol. 136, pp. 253–263, Aug. 2017.
- [147] Schmidt, M. and Lipson, H., ‘Distilling Free-Form Natural Laws from Experimental Data’, *Science*, vol. 324, no. 5923, pp. 81–85, Apr. 2009.
- [148] Schölkopf, B. and Smola, A. J., *Learning with kernels: support vector machines, regularization, optimization, and beyond*, Reprint. Cambridge, Mass.: MIT Press, 2002.
- [149] Searson, D. P., ‘GPTIPS 2: an open-source software platform for symbolic data mining’, *arXiv:1412.4690 [cs]*, May 2015.
- [150] Sebastian, A. and Salapaka, S. M., ‘Design methodologies for robust nano-positioning’, *IEEE Transactions on Control Systems Technology*, vol. 13, no. 6, pp. 868–876, 2005.
- [151] Sheppard, C., *Tree-based Machine Learning Algorithms: Decision Trees, Random Forests, and Boosting*. CreateSpace Independent Publishing Platform, 2017.
- [152] Simonovic, K. and Kalin, M., ‘Methodology of a statistical and DOE approach to the prediction of performance in tribology – A DLC boundary-lubrication case study’, *Tribology International*, vol. 101, pp. 10–24, Sep. 2016.
- [153] Singer, I. L. and Pollack, H. M., *Fundamentals of Friction: Macroscopic and Microscopic Processes*. Dordrecht, Netherlands: Kluwer, 1992.
- [154] Spector, L., *Automatic Quantum Computer Programming: A Genetic Programming Approach*. Springer US, 2004.

- [155] Sung, I.-H., Lee, H.-S., and Kim, D.-E., ‘Effect of surface topography on the frictional behavior at the micro/nano-scale’, *Wear*, vol. 254, no. 10, pp. 1019–1031, Jul. 2003.
- [156] Tambe, N. S. and Bhushan, B., ‘Scale dependence of micro/nano-friction and adhesion of MEMS/NEMS materials, coatings and lubricants’, *Nanotechnology*, vol. 15, no. 11, pp. 1561–1570, Nov. 2004.
- [157] Tambe, N. S. and Bhushan, B., ‘Friction model for the velocity dependence of nanoscale friction’, *Nanotechnology*, vol. 16, no. 10, pp. 2309–2324, Oct. 2005.
- [158] Tranchida, D., Piccarolo, S., and Deblieck, R. A. C., ‘Some experimental issues of AFM tip blind estimation: the effect of noise and resolution’, *Meas. Sci. Technol.*, vol. 17, no. 10, p. 2630, 2006.
- [159] University of Rijeka, Croatia. Centre for Micro- and Nanosciences and Technologies, [Online]. Available: <http://cmnzt.uniri.hr/>. [Accessed: 17-May-2018].
- [160] University of Rijeka, Croatia. Equipment of the Centre for Micro- and Nanosciences and Technologies, [Online]. Available: http://cmnzt.uniri.hr/wp-content/uploads/2018/04/Katalog-CMNZT_ENG.pdf. [Accessed: 17-May-2018].
- [161] University of Trieste, Italy. Laboratorio MOSE., [Online]. Available: <http://www.mose.units.it/default.aspx>. [Accessed: 21-May-2018].
- [162] Vanossi, A., Dietzel, D., Schirmeisen, A., Meyer, E., Pawlak, R., Glatzel, T., Kisiel, M., Kawai, S., and Manini, N., ‘Recent highlights in nanoscale and mesoscale friction’, *Beilstein J Nanotechnol*, vol. 9, pp. 1995–2014, Jul. 2018.
- [163] Vanossi, A., Dietzel, D., Schirmeisen, A., Meyer, E., Pawlak, R., Glatzel, T., Kisiel, M., Kawai, S., and Manini, N., ‘Recent highlights in nanoscale and mesoscale friction’, *Beilstein Journal of Nanotechnology*, vol. 9, no. 1, pp. 1995–2014, Jul. 2018.
- [164] Varenberg, M., Etsion, I., and Halperin, G., ‘An improved wedge calibration method for lateral force in atomic force microscopy’, *Review of Scientific Instruments*, vol. 74, no. 7, pp. 3362–3367, Jul. 2003.
- [165] Vijayaraghavan, V., Garg, A., Lam, J. S. L., Panda, B., and Mahapatra, S. S., ‘Process characterisation of 3D-printed FDM components using improved evolutionary computational approach’, *Int J Adv Manuf Technol*, vol. 78, no. 5, pp. 781–793, May 2015.
- [166] Vijayaraghavan, V., Garg, A., Wong, C. H., and Tai, K., ‘Estimation of mechanical properties of nanomaterials using artificial intelligence methods’, *Appl. Phys. A*, vol. 116, no. 3, pp. 1099–1107, Sep. 2014.
- [167] Vijayaraghavan, V., Garg, A., Wong, C. H., Tai, K., and Singru, P. M., ‘An integrated

- computational approach for determining the elastic properties of boron nitride nanotubes’, *Int J Mech Mater Des*, vol. 11, no. 1, pp. 1–14, Mar. 2015.
- [168] Villarrubia, J. S., ‘Algorithms for Scanned Probe Microscope Image Simulation, Surface Reconstruction, and Tip Estimation’, *J Res Natl Inst Stand Technol*, vol. 102, no. 4, pp. 425–454, Aug. 1997.
- [169] Violano, G. and Afferrante, L., ‘Contact of rough surfaces: Modeling adhesion in advanced multiasperity models’, *Proceedings of the Institution of Mechanical Engineers, Part J: Journal of Engineering Tribology*, p. 1350650119838669, Mar. 2019.
- [170] Voevodin, A. A., Zabinski, J. S., and Jones, J. G., ‘Pulsed Laser Deposition of Tribological Coatings’, in *Pulsed Laser Deposition of Thin Films*, John Wiley & Sons, Ltd, 2006, pp. 585–609.
- [171] Waddad, Y., Magnier, V., Dufrénoy, P., and De Saxcé, G., ‘Multiscale thermomechanical modeling of frictional contact problems considering wear – Application to a pin-on-disc system’, *Wear*, vol. 426–427, pp. 1399–1409, Apr. 2019.
- [172] Wagner, C., Riggs, W., Davis, L., Moulder, J., and Muilenberg, G., *Handbook of X-ray Photoelectron Spectroscopy*. Eden Prairie, Michigan, USA: Perkin – Elmer Corp., 1979.
- [173] Wagner, S., Kronberger, G., Beham, A., Kommenda, M., Scheibenpflug, A., Pitzer, E., Vonolfen, S., Kofler, M., Winkler, S., Dorfer, V., and Affenzeller, M., ‘Advanced Methods and Applications in Computational Intelligence’, vol. 6, Klempous, R., Nikodem, J., Jacak, W., and Chaczko, Z., Eds. Springer, 2014, pp. 197–261.
- [174] Wang, Q. J. and Chung, Y.-W., Eds., *Encyclopedia of Tribology*. Springer US, 2013.
- [175] Waszczyszyn, Z., ‘Fundamentals of Artificial Neural Networks’, in *Neural Networks in the Analysis and Design of Structures*, Vienna, 1999, pp. 1–51.
- [176] Worden, K., Wong, C. X., Parlitz, U., Hornstein, A., Engster, D., Tjahjowidodo, T., Al-Bender, F., Rizos, D. D., and Fassois, S. D., ‘Identification of pre-sliding and sliding friction dynamics: Grey box and black-box models’, *Mechanical Systems and Signal Processing*, vol. 21, no. 1, pp. 514–534, Jan. 2007.
- [177] Worzel, W. P., Yu, J., Almal, A. A., and Chinnaiyan, A. M., ‘Applications of Genetic Programming in Cancer Research’, *Int J Biochem Cell Biol*, vol. 41, no. 2, pp. 405–413, Feb. 2009.
- [178] Xiang, H. and Komvopoulos, K., ‘The effect of impact velocity on interfacial adhesion of contact-mode surface micromachines’, *Appl. Phys. Lett.*, vol. 101, no. 5, p. 053506, Jul. 2012.

- [179] Xu, Y. and Jackson, R. L., ‘Boundary element method (BEM) applied to the rough surface contact vs. BEM in computational mechanics’, *Friction*, vol. 7, no. 4, pp. 359–371, Aug. 2019.
- [180] Yacoot, A. and Koenders, L., ‘Aspects of scanning force microscope probes and their effects on dimensional measurement’, *Journal of Physics D: Applied Physics*, vol. 41, no. 10, p. 103001, May 2008.
- [181] Yang, L., Hu, J., Xiao, H., and Quan, W., ‘Analysis of humidity-dependent adhesion between a probe tip and a surface’, *Particuology*, vol. 33, pp. 91–97, Aug. 2017.
- [182] Yoon, J. Y. and Trumper, D. L., ‘Friction modeling, identification, and compensation based on friction hysteresis and Dahl resonance’, *Mechatronics*, vol. 24, no. 6, pp. 734–741, Sep. 2014.
- [183] You, J.-M. and Chen, T.-N., ‘A static friction model for the contact of fractal surfaces’, *Proceedings of the Institution of Mechanical Engineers, Part J: Journal of Engineering Tribology*, vol. 224, no. 5, pp. 513–518, 2010.
- [184] Zhang, C. and Ma, Y., Eds., *Ensemble Machine Learning: Methods and Applications*. New York: Springer-Verlag, 2012.
- [185] Zhang, P., Chen, C., Xiao, C., Chen, L., and Qian, L., ‘Comparison of wear methods at nanoscale: line scanning and area scanning’, *Wear*, vol. 400–401, pp. 137–143, Apr. 2018.
- [186] ‘Influence of tribology on global energy consumption, costs and emissions | SpringerLink’. [Online]. Available: <https://link.springer.com/article/10.1007/s40544-017-0183-5>. [Accessed: 13-Jul-2019].
- [187] ‘Institute of Physics - Laboratory for Plasma Processing’. [Online]. Available: <http://calt.ifs.hr/laboratories/plasma-technologies/laboratory-for-laser-plasma/>. [Accessed: 21-Nov-2018].
- [188] ‘Machine Learning Overview’, in *The Data Science Handbook*, John Wiley & Sons, Ltd, 2017, pp. 87–91.
- [189] ‘Data Mining: Practical Machine Learning Tools and Techniques - 3rd Edition’. [Online]. Available: <https://www.elsevier.com/books/data-mining-practical-machine-learning-tools-and-techniques/witten/978-0-12-374856-0>. [Accessed: 12-Apr-2019].

List of Symbols

Latinic symbols

variable	definition, unit
$A(f)$	amplitude as function of frequency of cantilever, nm
a, b	lower and upper bounds of values of considered influencing parameter
A_0	baseline amplitude of the cantilever's thermal excitations, nm
A_R	real area of contact, m^2
b	free parameter of the SVR predicted output function
C_1, C_2	Lorentzian fit parameters
d	width of the probe's leg, μm
D	distance between cantilever tips' apex and the samples' surface, nm
d_{est}	estimated dimension of tip's apex radius, nm
d_{scan}	scan distance, nm
E	indentation Young's modulus, GPa
E^*	effective Young's modulus, Gpa
f	frequency, Hz
f_0	centre frequency at resonant peak, Hz
$f(k)$	probability mass function
$F(k)$	cumulative distribution function
F_A	adhesion force, nN
F_f	friction force, nN
F_N	normal force, nN
F_{n-d}	normal reaction force acting on cantilever tip during downward sliding, nN
F_{n-u}	normal reaction force acting on cantilever tip during upward sliding, nN
F_P	pull-out force, nN
F_{T-d}	torsional force acting on cantilever during downward sliding, nN
F_{T-u}	torsional force acting on cantilever during upward sliding, nN
h	height of the tip of the probe, μm
K	kernel function (RBF)
k	discrete probability distribution

k_b	bending (flexural) stiffness, N.m-1
k_t	torsional stiffness, Nm.rad-1
L'	probe's length, μm
L_1	vertical length of the slot in the probe, μm
l	number of support vectors
M_d	torsional moment acting on the cantilever during downward sliding, μNm
M_u	torsional moment acting on the cantilever during upward sliding, μNm
n	number of homogeneously spaced values in the Voronoi subdivision of the experimental space
p_c	contact pressure, Mpa
r	radius of the apex of the tip of the probe, μm
R^*	effective contact radius, m
R_1	water meniscus' radius of curvature in the vertical plane, nm
R_2	water meniscus' radius of curvature in the horizontal plane, nm
R^2	coefficient of determination
R_a	arithmetic mean height roughness, nm
R_i	radii of the spheres in contact, m
R_q	root mean square deviation, nm
R_z	maximum height of profile, nm
t	thickness of probe's cantilever, μm
v	sliding velocity, nm/s
x, y	position of the tip of the probe with respect to the free end of the respective cantilever, μm
x_4	Al sample binary coding
x_5	Al_2O_3 sample binary coding
x_6	MoS_2 sample binary coding
x_7	TiO_2 sample binary coding
x_8	SS sample binary coding
x_{max}	maximum value of the variable x
x_{min}	minimum value of the variable x
x_{norm}	normalized value of the variable x
\bar{x}	mean of the variable x
y_i	predicted value

z_i	standardized data point
w	overall width of the probe, μm

Greek symbols

variable	definition, unit
α	lateral force correlation factor, $\mu\text{N/V}$
α_i	coefficients of the used RBF kernel function
γ_1	skewness
γ_2	kurtosis
θ	angle of the TGF11 samples' crystallographic planes, $^\circ$
ϑ	temperature, $^\circ\text{C}$
λ	effective surface energy, J/m^2
μ	coefficient of friction, -
ν	Poisson ratio
ρ	Pearson's product-moment correlation
σ	standard deviation
ϕ	angle defining the inclination of the legs of the probe, $^\circ$
φ_d	angle of cantilever tip during downward sliding, $^\circ$
φ_u	angle of cantilever tip during upward sliding, $^\circ$
ψ	water contact angle on SPM tip, $^\circ$
ω	water contact angle on sample surface, $^\circ$

List of Abbreviations

abbreviation	definition
AFM	atomic force microscope
AI	artificial intelligence
ALD	atomic layer deposition
ALPS	age layered population structure
CVD	chemical vapour deposition
CVT	centroidal Voronoi tessellation
DLP	digital light processor
DoE	design of experiments
FEM	finite element method
FE-SEM	field-emission scanning electron microscope
FFM	friction force microscopy
GE	grammatical evolution
GMS	generalised Maxwell slip
GP	genetic programming
IC	integrated circuit
LFM	lateral force microscopy
MAE	mean absolute error
MC	monte carlo
MD	molecular dynamics
MEMS	micro-electromechanical systems
MG	multi gene
ML	machine learning
MLP	multi layer perceptron
NEMS	nano-electromechanical systems
OES	optical emission spectroscopy
PBA	parallel beam approximation
PF-QNM	peak force quantitative nanomechanical mapping
PLD	pulsed laser deposition
PPMC	Pearson product moment correlation

PSD	power spectral density
PSPD	position sensitive photo detector
RBF	radial basis function
RF	random forest
RGA	residual gas analyser
RMS	root mean square
RMSE	root mean square error
RSM	response surface method
SIMS	secondary ion mass spectroscopy
SLG	single layer graphene
SPM	scanning probe microscope
SR	symbolic regression
STM	scanning tunneling microscopy
SVM	support vector machine
SVR	support vector regression
TAC	thermal applications controller
TTM	thermal tune method
XPS	x-ray photoelectron spectroscopy

List of Figures

Figure 2.1 Friction between two surfaces is governed by the behaviour in a single asperity contact.	9
Figure 3.1 Bruker Dimension Icon Scanning Probe Microscope at the NANORI lab [160]...	18
Figure 3.2 Proposed experimental methodology for obtaining concurrently the dependence of nanoscale friction on several influencing parameters by using LFM [128].....	19
Figure 3.3 Scheme of the ALD process (a) and the used Beneq ALD device (b) [128].....	21
Figure 3.4 Scheme of the PLD process (a) and the factual PLD set-up used in the work (b) [128].	22
Figure 3.5 Used Specs X-ray Photoelectron Spectroscopy (XPS) equipped with a hemispherical energy analyser PHOIBOS 100 MCD-5 [159].....	24
Figure 3.6 Used Hiden Secondary Ion Mass Spectrometer (SIMS) at the NANORI [159]. ...	25
Figure 3.7 Examples of SIMS spectra for thin-films obtained via ALD (TiO ₂ - a), and PLD (MoS ₂ - b) [128].	25
Figure 3.8 Scheme of the SPM (LFM) measurement configuration (a) [128], and schematics of the obtained friction signals when the tip of the probe traverses across the surface with topology and friction variations (b - adapted from [17]).	27
Figure 3.9 SEM micrographs obtained with a magnification of, respectively, 700 and 400 times showing the planar views of the used Bruker SNL-10 probes (the shown scale-bar is 10 μm).....	28
Figure 3.10 Considered geometrical parameters of the used Bruker SNL-10 probes [128]....	28
Figure 3.11 Power spectral density (PSD) of cantilevers' response in ambient conditions and the respective Lorentzian fits for A type (a), and D-type probes (b).	30
Figure 3.12 Scheme (a) [128], and factual topology of the TGF11 calibration grating (b).....	31
Figure 3.13 Balance of forces acting on probe's tip during the measurements [128].....	31
Figure 3.14 Schematic representation of a typical force-distance curve [17], [128].	33
Figure 3.15 Measured values of the adhesion force F_A on the TGF11 calibration grating vs.	

temperature \mathcal{G} . [128].....	34
Figure 3.16 Statistics on the corrected correlation factors α (a), and colour-coded values of α in the experimental design space defined by the CVT points (b).	34
Figure 3.17 Mean adhesion force F_A variability vs. temperature for the considered thin-film samples in the DoE determined experimental points. [128]	35
Figure 3.18 Geometry of a capillary condensation water bridge – meniscus.	35
Figure 3.19 Influence of thermal expansion on the necessity to correct the set-point, i.e., maintain the required value of the normal force F_N [128].	36
Figure 3.20 SEM micrographs of a fresh SPM tip (a) and of a tip’s apex which was used for 200 LFM measurements (b) [128].....	37
Figure 3.21 Wear of the tip on an Al_2O_3 sample for $F_N = 150$ nN: tip dimension d_{est} (left axis), adhesion F_A (right axis) and resulting contact pressure p_c (far right axis) [128]. .	39
Figure 4.1 Sample surface topologies obtained via LFM measurements on the TiO_2 thin-film (a) and on the MoS_2 sample (b).....	41
Figure 4.2 Colour-coded distribution of experimentally determined nanometric F_f values on 50 measurement points for the Al_2O_3 (a) and TiO_2 (b) samples obtained via ALD vs. the considered influencing parameters. Left and right columns present F_f values obtained without the calibration factor correction, and with calibration factor correction, respectively [128].....	43
Figure 4.3 Colour-coded distribution of experimentally determined nanometric F_f values on 50 measurement points for the Al (a), MoS_2 (b) and SS (c) samples obtained via PLD vs. the influencing parameters. Left and right columns present F_f values obtained without the calibration factor correction, and with calibration factor correction, respectively [128].	44
Figure 5.1 Numerical procedure for the development of a predictive model of nanoscale friction.	49
Figure 5.2 Measured F_A values for test dataset of experimental points on the TGF11 calibration sample (a), and on all the analysed thin-film samples (b).....	53
Figure 5.3 Colour-coded distribution of experimentally determined nanometric F_f values for	

the test dataset measurement points for the Al ₂ O ₃ (a), TiO ₂ (b), Al (c), MoS ₂ (d) and SS (e) samples vs. the considered process parameters.....	54
Figure 5.4 Histograms and normal distribution fits for all F_f measurements at CVT-based experimental points on Al (a), Al ₂ O ₃ (b), MoS ₂ (c), TiO ₂ (d) and SS (e) samples.	60
Figure 5.5 Histograms and normal distribution fits for all F_f test dataset measurements at MC-based experimental points on Al (a), Al ₂ O ₃ (b), MoS ₂ (c), TiO ₂ (d) and SS (e) samples.	61
Figure 5.6 Schematic of cross-validation method used to optimize the hyper-parameters of machine learning models on training dataset.	65
Figure 5.7 Performance of best developed ML – based models (MLP – Multi Layer Perceptron, SVR – Support Vector Regression and RF – Random Forest) on training (pooled) dataset for all samples. Values in parenthesis present achieved R^2 values for each model.....	72
Figure 5.8 Predictive performances of the considered ML models on the MC test dataset for the ALD synthesized samples: Al ₂ O ₃ (a) and TiO ₂ (b).....	74
Figure 5.9 Predictive performances of the considered ML models on the MC test dataset for the PLD synthesized samples: Al (a), MoS ₂ (b) and SS (c).....	75
Figure 5.10 Surface plots of the RF ML solutions of the F_f values for constant variables in columns (left to right): total load ($F_L = F_N + F_A$), sliding velocity (v) and temperature (\mathcal{G}), for the ALD samples: Al ₂ O ₃ (top row) and TiO ₂ (bottom row).....	77
Figure 5.11 Surface plots of the RF ML solutions of the F_f values for constant variables in columns (left to right): total load ($F_L = F_N + F_A$), sliding velocity (v) and temperature (\mathcal{G}), for the PLD samples in rows (top to bottom): Al, MoS ₂ and SS.	78
Figure 5.12 Surface plots of the MLP solutions of the F_f values for constant variables in columns (left to right): total load ($F_L = F_N + F_A$), sliding velocity (v) and temperature (\mathcal{G}), for the ALD samples Al ₂ O ₃ (top row) and TiO ₂ (bottom row).....	79
Figure 5.13 Surface plots of the MLP solutions of the F_f values for constant variables in columns (left to right): total load ($F_L = F_N + F_A$), sliding velocity (v) and temperature (\mathcal{G}), for the PLD samples in rows (top to bottom): Al, MoS ₂ and SS.	80

Figure 5.14 Surface plots of the SVR ML solutions of the F_f values for constant variables in columns (left to right): total load ($F_L = F_N + F_A$), sliding velocity (v) and temperature (\mathcal{G}), for the ALD samples: Al_2O_3 (top row) and TiO_2 (bottom row)..... 81

Figure 5.15 Surface plots of the SVR ML solutions of the F_f values for constant variables in columns (left to right): total load ($F_L = F_N + F_A$), sliding velocity (v) and temperature (\mathcal{G}), for the PLD samples in rows (top to bottom): Al, MoS_2 and SS. 82

Figure 6.1 Selected symbolic regression MG GP model on a Pareto frontier of expressional complexity vs. the $1-R^2$ performance value on a test dataset. 92

Figure 6.2 Fit of the predicted values vs. experimental data for the main (training) dataset (a), and the test dataset (b) of the model described by equation (5.9). 93

Figure 6.3 Plot of residuals of the best performing model on the main (training) dataset (a) and the test dataset (b). The distribution of residuals shows good normality for both datasets (c)..... 94

Figure 6.4 Distributions of predicted and experimental data for the main (training) dataset (a), and the test dataset (b). 94

Figure 6.5 Predictive performances of the best developed MG GP model on the MC test dataset for the ALD synthesized samples: Al_2O_3 (a) and TiO_2 (b). 95

Figure 6.6 Predictive performances of the best developed MG GP model on MC test dataset for the PLD synthesized samples: Al (a), MoS_2 (b) and SS (c). 96

Figure 6.7 Surface plots of the results obtained via the obtained MG GP model for constant variables in columns (left to right): total load ($F_L = F_N + F_A$), sliding velocity (v) and temperature (\mathcal{G}), for the ALD samples: Al_2O_3 (top row) and TiO_2 (bottom row). 97

Figure 6.8 Surface plots of the results obtained via the obtained MG GP model for constant variables in columns (left to right): total load ($F_L = F_N + F_A$), sliding velocity (v) and temperature (\mathcal{G}), for the PLD samples in rows (top to bottom): Al, MoS_2 and SS. 98

Figure 6.9 Plots of the values of the nanoscale friction force F_f vs. the total normal load ($F_L = F_N + F_A$) for different values of the v and \mathcal{G} for: Al (a), Al_2O_3 (b), MoS_2 (c), TiO_2 (d) and SS (e) as obtained from the proposed models. 100

Figure 6.10 Plots of the values of the nanoscale friction force F_f vs. temperature \mathcal{G} for different

values of v and $F_L = F_N + F_A$ for: Al (a), Al_2O_3 (b), MoS_2 (c), TiO_2 (d) and SS (e) as obtained from the proposed models. 101

Figure 6.11 Plots of the values of the nanoscale friction force F_f vs. sliding velocity v for different values of \mathcal{G} and of $F_L = F_N + F_A$ for: Al (a), Al_2O_3 (b), MoS_2 (c), TiO_2 (d) and SS (e) as obtained from the proposed models. 102

List of Tables

Table 3.1 Measured dimensions of the Bruker SNL – 10 SPM probes with the respective dispersions.	29
Table 3.2 Determined bending and torsional stiffness of the Bruker SNL – 10D probes. [128]	32
Table 3.3 Results of the determination of tip’s apex radius [128].	38
Table 4.1 Surface roughness of the analysed thin-film samples [128].	42
Table 4.2 Matrices of correlation coefficients for the influencing parameters on the nanometric F_f values in the DoE-CVT measurement points for ALD synthesized samples [128].	46
Table 4.3 Matrices of correlation coefficients for the influencing parameters on the nanometric F_f values in the DoE-CVT measurement points for PLD synthesized samples [128]	47
Table 4.4 Summary of the effects of the influencing parameters on the F_f value for the analysed thin-film samples in the DoE-CVT measurement points [128].	48
Table 5.1 Matrices of correlation coefficients for the influencing parameters on the nanometric F_f values on the MC test dataset points for ALD samples.	55
Table 5.2 Matrices of correlation coefficients for the influencing parameters on the nanometric F_f values on the MC test dataset points for PLD samples.	56
Table 5.3 Summary of the effects of the influencing parameters on the F_f value for the used thin-film samples in the MC-based test dataset.	57
Table 5.4 Used encoding classes for the used thin-film sample materials in the pooled data models.	59
Table 5.5 Comparative presentation of predictive performances on the test datasets for the used ML models vs. the response surface methodology.	71
Table 5.6 Predictive performances of the considered ML models trained on pooled data for each thin-film sample material.	73

Table 5.7 Comparative presentation of predictive performances on the test datasets for the considered GP-based models..... 88

Table 6.1 Predictive performance of selected MG GP model trained on pooled data for each thin-film sample material. 91

Appendices

Appendix A

CVT-based Measurement points

Table A.1 Distribution of measurement points in the considered multidimensional experimental space (F_N , v and \mathcal{G}) as determined by applying CVT-sampling.

Meas. point no.	v [nm/s]	\mathcal{G} [°C]	F_N [nN]	Meas. point no.	v [nm/s]	\mathcal{G} [°C]	F_N [nN]
1	65	25	76	26	253	50	131
2	412	25	36	27	459	50	86
3	206	26	91	28	117	51	134
4	321	26	113	29	179	51	29
5	428	26	77	30	311	51	66
6	451	26	125	31	356	55	103
7	58	27	27	32	443	56	22
8	220	28	136	33	325	57	34
9	283	28	36	34	71	58	72
10	74	29	130	35	440	58	55
11	168	29	54	36	419	59	134
12	176	30	21	37	215	60	86
13	290	32	72	38	442	65	105
14	358	32	138	39	56	66	118
15	55	36	78	40	79	67	30
16	174	38	108	41	200	69	137
17	438	38	32	42	310	69	128
18	452	39	114	43	234	71	33
19	418	40	74	44	310	72	77
20	291	42	27	45	188	73	104
21	297	42	103	46	104	74	69
22	182	44	66	47	401	74	29
23	59	45	32	48	442	74	77
24	425	45	135	49	431	75	125
25	61	46	107	50	81	76	137

Appendix B

CVT-based F_f and F_A Measurements

This appendix contains the measured and processed experimental data obtained at CVT-based measurement points. The tables presented further contain F_f and F_A experimental measurements for each material in each CVT-based measurement point (CVT column) for all repetitions (Meas. 1 to Meas. 5 columns), and calculated values of mean (\bar{F} column), median (\tilde{F} column), standard deviation (σ column), relative standard deviation (RSD column) [106], skewness (γ_1 column) and kurtosis (γ_2 column), calculated according to expressions 5.3 and 5.4 respectively. Data presented in this appendix is used for training all models.

Table B.1 Experimentally obtained values of the nanoscale friction force F_f [nN] for the Al sample at the CVT-based experimental points.

CVT	Meas. 1	Meas. 2	Meas. 3	Meas. 4	Meas. 5	\bar{F}_f [nN]	\tilde{F}_f [nN]	σ_{F_f} [nN]	RSD $_{F_f}$ [%]	γ_1	γ_2
1	8.28	8.53	8.44	8.18	8.48	8.38	8.44	0.15	1.76	-0.67	-1.64
2	9.27	9.41	9.46	9.27	9.19	9.32	9.27	0.11	1.22	0.31	-2.00
3	8.60	8.69	9.04	8.71	8.74	8.75	8.71	0.17	1.91	1.70	3.49
4	9.01	9.33	9.41	9.25	9.05	9.21	9.25	0.17	1.88	-0.14	-2.50
5	9.44	9.51	9.63	9.80	9.81	9.64	9.63	0.17	1.71	-0.02	-2.59
6	9.83	10.09	10.05	9.74	10.25	9.99	10.05	0.21	2.06	-0.08	-1.48
7	8.97	8.92	9.37	8.85	8.84	8.99	8.92	0.22	2.41	1.94	3.90
8	9.25	9.50	9.57	9.22	9.73	9.46	9.50	0.22	2.29	0.05	-1.94
9	9.13	9.05	9.22	9.13	9.28	9.16	9.13	0.09	0.96	0.22	-0.49
10	13.15	12.78	12.59	12.31	12.97	12.76	12.78	0.33	2.56	-0.31	-0.64
11	9.05	8.90	8.95	8.93	9.00	8.97	8.95	0.06	0.65	0.57	-0.69
12	6.50	6.56	6.52	6.62	6.52	6.54	6.52	0.05	0.72	1.02	0.55
13	10.06	9.71	9.87	9.89	9.85	9.88	9.87	0.13	1.28	0.22	1.81
14	12.24	12.20	12.07	12.18	12.07	12.15	12.18	0.08	0.65	-0.20	-2.59
15	10.32	10.61	9.90	10.30	10.30	10.28	10.30	0.25	2.48	-0.57	2.15
16	10.25	10.17	9.88	10.15	10.34	10.16	10.17	0.17	1.68	-1.22	2.08
17	6.68	6.66	6.80	6.57	6.69	6.68	6.68	0.08	1.27	0.27	1.70
18	11.39	11.48	11.79	11.95	11.67	11.66	11.67	0.23	1.96	0.13	-1.45
19	10.19	10.09	10.44	10.42	10.35	10.30	10.35	0.15	1.48	-0.60	-1.99

CVT	Meas. 1	Meas. 2	Meas. 3	Meas. 4	Meas. 5	\bar{F}_f [nN]	\tilde{F}_f [nN]	σ_{F_f} [nN]	RSD _{F_f} [%]	γ_1	γ_2
20	5.50	5.55	5.57	5.62	5.63	5.57	5.57	0.05	0.94	-0.40	-1.03
21	13.46	13.55	13.90	13.79	14.37	13.81	13.79	0.36	2.60	1.01	0.88
22	9.89	9.70	9.72	10.07	10.00	9.88	9.89	0.17	1.67	0.03	-2.53
23	7.46	7.54	7.59	7.64	7.69	7.58	7.59	0.09	1.19	-0.31	-0.64
24	13.84	14.21	14.52	13.87	14.35	14.16	14.21	0.30	2.10	-0.02	-2.33
25	12.54	12.96	12.82	12.73	13.27	12.86	12.82	0.27	2.11	0.62	0.67
26	6.67	6.28	6.74	6.58	6.33	6.52	6.58	0.20	3.13	-0.34	-2.68
27	9.80	9.07	9.30	9.42	9.42	9.40	9.42	0.27	2.83	0.54	1.48
28	12.37	11.34	11.91	11.67	11.59	11.78	11.67	0.39	3.30	0.87	0.80
29	5.89	6.01	6.06	6.10	6.12	6.04	6.06	0.09	1.52	-1.14	0.88
30	6.85	8.10	8.32	8.49	8.10	7.97	8.10	0.65	8.13	-1.89	3.86
31	9.80	9.46	9.93	9.50	9.42	9.62	9.50	0.23	2.39	0.73	-2.19
32	4.10	4.23	4.30	4.32	4.36	4.26	4.30	0.10	2.43	-1.32	1.45
33	3.78	3.91	3.96	3.97	3.98	3.92	3.96	0.08	2.10	-1.60	2.28
34	5.42	5.49	5.15	5.31	5.30	5.33	5.31	0.13	2.44	-0.33	-0.02
35	4.89	5.42	5.38	5.29	5.34	5.26	5.34	0.21	4.03	-1.97	4.06
36	9.21	8.65	8.68	8.48	9.23	8.85	8.68	0.35	3.91	0.37	-2.88
37	5.79	5.27	5.54	5.39	5.65	5.53	5.54	0.21	3.72	0.00	-1.38
38	7.45	7.82	7.25	7.71	6.87	7.42	7.45	0.38	5.11	-0.64	-0.47
39	6.39	6.01	5.62	5.86	6.37	6.05	6.01	0.33	5.47	-0.14	-1.92

CVT	Meas. 1	Meas. 2	Meas. 3	Meas. 4	Meas. 5	\bar{F}_f [nN]	\tilde{F}_f [nN]	σ_{F_f} [nN]	RSD $_{F_f}$ [%]	γ_1	γ_2
40	2.62	3.18	3.27	3.37	3.48	3.18	3.27	0.33	10.50	-1.61	2.95
41	6.28	5.33	5.66	5.78	5.89	5.79	5.78	0.34	5.95	0.24	0.98
42	5.95	5.00	5.35	5.54	5.62	5.49	5.54	0.35	6.37	-0.24	0.57
43	1.89	2.69	2.48	2.55	2.61	2.45	2.55	0.32	13.10	-1.91	3.89
44	3.44	3.47	3.56	3.66	3.74	3.57	3.56	0.13	3.56	0.33	-1.92
45	4.35	3.98	3.97	4.06	4.34	4.14	4.06	0.19	4.61	0.48	-3.19
46	3.18	3.38	2.99	3.03	3.15	3.15	3.15	0.15	4.84	0.89	0.68
47	1.97	1.26	1.25	1.26	1.60	1.47	1.26	0.32	21.60	1.30	0.56
48	2.70	2.86	2.82	3.03	2.75	2.83	2.82	0.13	4.47	1.10	1.41
49	4.40	4.42	4.02	3.94	4.04	4.16	4.04	0.23	5.49	0.50	-3.12
50	3.35	3.87	3.44	3.73	4.30	3.74	3.73	0.38	10.10	0.73	0.00

Table B.2 Experimentally obtained values of the nanoscale friction force F_f [nN] for the Al_2O_3 sample at the CVT-based experimental points.

CVT	Meas. 1	Meas. 2	Meas. 3	Meas. 4	Meas. 5	\bar{F}_f [nN]	\tilde{F}_f [nN]	s_{F_f} [nN]	RSD $_{F_f}$ [%]	γ_1	γ_2
1	2.61	2.61	2.67	2.71	2.74	2.67	2.67	0.06	2.21	0.15	-2.41
2	2.91	3.08	3.04	3.14	3.14	3.06	3.08	0.09	3.06	-1.22	1.33
3	2.61	2.77	2.83	2.86	2.98	2.81	2.83	0.14	4.81	-0.42	0.97
4	2.39	2.56	2.70	2.71	2.71	2.62	2.70	0.14	5.38	-1.34	0.81
5	3.23	3.23	3.40	3.36	3.38	3.32	3.36	0.08	2.55	-0.52	-3.20

CVT	Meas. 1	Meas. 2	Meas. 3	Meas. 4	Meas. 5	\bar{F}_f [nN]	\tilde{F}_f [nN]	s_{F_f} [nN]	RSD $_{F_f}$ [%]	γ_1	γ_2
6	2.57	2.39	2.59	2.68	2.86	2.62	2.59	0.17	6.51	0.21	0.93
7	3.17	3.25	3.27	3.38	3.28	3.27	3.27	0.07	2.29	0.31	1.61
8	2.56	2.64	2.68	2.78	3.00	2.73	2.68	0.17	6.27	1.14	1.31
9	3.43	3.38	3.29	3.44	3.46	3.40	3.43	0.07	1.98	-1.25	0.95
10	4.53	4.34	4.68	4.79	4.79	4.63	4.68	0.19	4.13	-0.86	-0.48
11	3.67	3.60	3.79	3.79	3.85	3.74	3.79	0.10	2.71	-0.50	-1.42
12	2.36	2.53	2.44	2.56	2.44	2.46	2.44	0.08	3.25	-0.11	-1.29
13	4.54	4.43	4.28	4.44	4.35	4.41	4.43	0.10	2.25	-0.05	-0.19
14	5.21	5.01	5.69	5.54	5.74	5.44	5.54	0.32	5.83	-0.60	-1.95
15	4.57	4.27	4.48	4.65	4.42	4.48	4.48	0.14	3.23	-0.43	-0.08
16	4.42	4.40	4.32	4.68	5.06	4.58	4.42	0.30	6.58	1.33	1.09
17	1.88	1.92	1.98	1.85	2.10	1.95	1.92	0.10	5.06	1.19	1.05
18	5.00	5.74	5.43	5.31	5.48	5.39	5.43	0.27	4.96	-0.37	1.11
19	3.67	3.55	3.60	3.83	3.99	3.73	3.67	0.18	4.79	0.81	-0.80
20	0.77	0.82	0.75	0.79	0.75	0.77	0.77	0.03	3.77	0.95	-0.04
21	4.66	5.38	4.63	4.72	4.92	4.86	4.72	0.31	6.35	1.61	2.33
22	2.72	2.97	2.53	2.32	2.62	2.63	2.62	0.24	9.12	0.24	0.66
23	0.96	0.85	0.83	0.78	0.79	0.84	0.83	0.07	8.77	1.51	2.36
24	4.44	4.35	4.63	4.55	5.40	4.67	4.55	0.42	8.93	1.90	3.81
25	3.81	3.75	3.84	3.67	3.61	3.74	3.75	0.09	2.54	-0.38	-1.91

CVT	Meas. 1	Meas. 2	Meas. 3	Meas. 4	Meas. 5	\bar{F}_f [nN]	\tilde{F}_f [nN]	s_{F_f} [nN]	RSD $_{F_f}$ [%]	γ_1	γ_2
26	2.13	1.97	2.11	1.86	1.99	2.01	1.99	0.11	5.49	-0.23	-1.20
27	1.90	1.78	1.98	1.74	1.79	1.83	1.79	0.10	5.42	0.74	-1.33
28	3.82	3.58	3.80	3.74	4.01	3.79	3.80	0.16	4.15	0.16	1.34
29	1.26	1.26	1.23	1.23	1.20	1.23	1.23	0.03	2.10	-0.51	-0.61
30	1.94	1.94	1.81	1.70	1.73	1.82	1.81	0.12	6.31	0.09	-2.83
31	2.59	2.72	2.78	2.60	2.78	2.69	2.72	0.09	3.48	-0.37	-2.97
32	0.90	0.93	0.93	0.89	0.89	0.91	0.90	0.02	2.48	0.41	-2.84
33	0.82	0.77	0.77	0.81	0.73	0.78	0.77	0.04	4.49	-0.43	-0.43
34	1.38	1.42	1.17	1.23	1.41	1.32	1.38	0.12	8.79	-0.71	-2.18
35	0.52	1.11	0.86	1.00	1.03	0.90	1.00	0.23	25.70	-1.48	2.11
36	1.53	1.56	1.84	2.25	1.81	1.80	1.81	0.29	16.20	1.05	1.01
37	1.22	1.14	1.09	1.27	1.15	1.17	1.15	0.07	6.02	0.42	-1.50
38	1.90	2.05	1.89	1.74	1.93	1.90	1.90	0.11	5.67	-0.29	1.71
39	1.89	1.58	1.49	1.61	1.65	1.65	1.61	0.15	9.15	1.44	2.73
40	0.83	0.83	0.89	0.83	0.79	0.83	0.83	0.04	4.44	0.55	2.10
41	2.24	1.63	1.26	1.42	1.64	1.64	1.63	0.37	22.80	1.27	2.15
42	1.22	1.13	1.02	1.35	1.10	1.16	1.13	0.12	10.70	0.72	0.19
43	0.70	0.69	0.69	0.61	0.59	0.66	0.69	0.05	7.82	-0.62	-3.08
44	0.96	0.82	0.83	0.90	0.74	0.85	0.83	0.08	9.72	0.16	-0.32
45	1.25	1.38	1.38	1.14	1.03	1.24	1.25	0.16	12.60	-0.44	-1.66

CVT	Meas. 1	Meas. 2	Meas. 3	Meas. 4	Meas. 5	\bar{F}_f [nN]	\tilde{F}_f [nN]	s_{F_f} [nN]	RSD $_{F_f}$ [%]	γ_1	γ_2
46	0.84	0.79	0.80	0.83	0.66	0.78	0.80	0.07	9.34	-1.87	3.73
47	1.25	1.24	1.23	1.22	1.21	1.23	1.23	0.01	1.18	0.16	-1.74
48	1.49	1.48	1.43	1.37	1.31	1.42	1.43	0.08	5.49	-0.58	-1.63
49	2.07	2.44	1.77	1.93	2.04	2.05	2.04	0.25	12.00	0.97	1.73
50	1.82	2.04	1.82	2.11	1.86	1.93	1.86	0.13	6.85	0.69	-2.41

Table B.3 Experimentally obtained values of the nanoscale friction force F_f [nN] for the MoS₂ sample at the CVT-based experimental points.

CVT	Meas. 1	Meas. 2	Meas. 3	Meas. 4	Meas. 5	\bar{F}_f [nN]	\tilde{F}_f [nN]	σ_{F_f} [nN]	RSD $_{F_f}$ [%]	γ_1	γ_2
1	2.85	3.09	3.35	3.67	4.14	3.42	3.35	0.51	14.80	0.54	-0.51
2	3.34	3.54	3.64	3.49	3.65	3.53	3.54	0.13	3.54	-0.83	0.11
3	3.61	3.73	4.02	3.80	4.25	3.88	3.80	0.26	6.60	0.69	-0.71
4	3.54	3.16	3.66	3.36	3.95	3.54	3.54	0.30	8.48	0.28	-0.09
5	4.68	4.94	4.56	4.48	5.39	4.81	4.68	0.37	7.67	1.22	0.91
6	4.83	5.32	4.92	5.18	4.92	5.03	4.92	0.21	4.18	0.72	-1.70
7	4.61	4.65	4.86	5.16	4.56	4.77	4.65	0.25	5.16	1.28	0.84
8	7.41	6.49	6.49	7.02	7.43	6.97	7.02	0.46	6.66	-0.14	-3.01
9	6.63	6.20	6.52	6.44	6.82	6.52	6.52	0.23	3.49	-0.20	0.31
10	12.59	9.66	10.03	10.65	10.95	10.77	10.65	1.14	10.50	1.19	1.60
11	7.70	6.58	6.94	7.07	7.54	7.16	7.07	0.46	6.39	-0.03	-1.56

CVT	Meas. 1	Meas. 2	Meas. 3	Meas. 4	Meas. 5	\bar{F}_f [nN]	\tilde{F}_f [nN]	σ_{F_f} [nN]	RSD $_{F_f}$ [%]	γ_1	γ_2
12	4.96	4.75	4.86	4.82	5.16	4.91	4.86	0.16	3.26	1.13	0.97
13	7.65	7.53	7.51	8.39	8.78	7.97	7.65	0.58	7.27	0.82	-1.83
14	9.42	10.15	10.01	10.30	9.51	9.88	10.01	0.39	3.96	-0.34	-2.72
15	10.37	11.26	9.86	12.13	9.17	10.56	10.37	1.16	11.00	0.32	-0.99
16	11.22	12.49	11.10	11.75	10.21	11.36	11.22	0.84	7.42	-0.01	0.46
17	9.00	7.57	7.96	7.60	8.39	8.10	7.96	0.60	7.42	0.88	-0.39
18	13.33	13.58	13.46	13.36	9.61	12.67	13.36	1.71	13.50	-2.22	4.94
19	8.98	9.36	8.93	8.70	8.11	8.82	8.93	0.46	5.20	-0.81	1.37
20	3.17	3.24	3.06	3.16	4.37	3.40	3.17	0.55	16.10	2.16	4.72
21	13.67	14.45	13.28	13.40	11.47	13.25	13.40	1.10	8.27	-1.25	2.59
22	8.58	8.92	8.42	8.90	8.62	8.69	8.62	0.22	2.52	0.03	-2.10
23	5.07	4.98	4.72	5.17	5.73	5.14	5.07	0.37	7.30	1.07	2.08
24	12.36	12.47	12.17	12.64	13.55	12.64	12.47	0.54	4.28	1.69	3.18
25	14.12	14.57	14.35	14.54	14.46	14.41	14.46	0.18	1.27	-1.16	0.79
26	6.73	7.30	6.66	6.98	5.35	6.60	6.73	0.74	11.30	-1.58	3.07
27	7.15	7.31	6.98	7.31	12.30	8.21	7.31	2.29	27.90	2.22	4.93
28	18.74	18.58	18.69	17.83	17.07	18.18	18.58	0.72	3.97	-1.15	-0.11
29	6.37	6.39	6.42	6.47	6.30	6.39	6.39	0.06	0.96	-0.13	0.38
30	9.57	9.35	9.17	8.97	9.37	9.29	9.35	0.23	2.42	-0.35	-0.07
31	10.77	10.77	11.25	10.12	11.06	10.79	10.77	0.43	3.98	-1.03	1.47

CVT	Meas. 1	Meas. 2	Meas. 3	Meas. 4	Meas. 5	\bar{F}_f [nN]	\tilde{F}_f [nN]	σ_{F_f} [nN]	RSD $_{F_f}$ [%]	γ_1	γ_2
32	3.88	3.94	3.80	3.67	4.25	3.91	3.88	0.22	5.55	1.05	1.73
33	3.67	3.67	3.67	3.70	4.05	3.75	3.67	0.17	4.52	2.21	4.91
34	7.44	7.45	7.46	7.55	7.32	7.44	7.45	0.08	1.09	-0.58	2.01
35	6.37	6.39	6.35	6.38	6.66	6.43	6.38	0.13	2.04	2.17	4.78
36	11.87	11.39	10.78	11.70	10.26	11.20	11.39	0.67	6.00	-0.65	-1.33
37	7.13	7.20	6.65	6.89	7.87	7.15	7.13	0.46	6.39	1.03	1.58
38	9.48	8.84	8.87	8.95	8.95	9.02	8.95	0.26	2.92	2.06	4.39
39	7.88	7.84	7.91	7.52	10.13	8.26	7.88	1.06	12.80	2.11	4.61
40	4.33	5.10	5.05	4.04	4.06	4.51	4.33	0.52	11.60	0.42	-3.11
41	9.22	9.71	11.39	10.42	10.83	10.32	10.42	0.86	8.38	-0.10	-1.37
42	10.25	10.13	11.54	10.86	9.38	10.43	10.25	0.81	7.76	0.19	-0.03
43	3.53	3.52	3.51	3.53	3.58	3.53	3.53	0.03	0.80	1.58	3.23
44	6.71	6.34	6.12	6.14	5.98	6.26	6.14	0.28	4.50	1.26	1.47
45	7.71	6.95	7.04	6.82	6.68	7.04	6.95	0.40	5.67	1.59	2.93
46	5.49	5.51	5.14	5.76	5.65	5.51	5.51	0.24	4.29	-1.09	1.66
47	3.08	3.06	3.06	3.27	3.72	3.24	3.08	0.29	8.83	1.75	2.85
48	6.17	5.94	5.72	5.73	5.86	5.88	5.86	0.18	3.12	1.06	0.73
49	9.58	9.25	9.09	8.17	8.11	8.84	9.09	0.66	7.50	-0.28	-2.72
50	9.95	10.53	9.94	7.06	5.12	8.52	9.94	2.33	27.40	-0.93	-1.15

CVT	Meas. 1	Meas. 2	Meas. 3	Meas. 4	Meas. 5	\bar{F}_f [nN]	\tilde{F}_f [nN]	σ_{F_f} [nN]	RSD $_{F_f}$ [%]	γ_1	γ_2
20	0.23	0.19	0.14	0.20	0.17	0.18	0.19	0.03	17.60	-0.22	-0.34
21	7.91	7.82	7.53	7.88	7.74	7.78	7.82	0.15	1.99	-1.31	1.40
22	4.57	4.43	4.34	4.64	4.50	4.50	4.50	0.12	2.63	-0.21	-0.84
23	4.90	4.92	5.01	4.90	4.99	4.94	4.92	0.05	1.03	0.60	-3.07
24	12.42	12.45	12.34	12.31	12.25	12.36	12.34	0.08	0.66	0.04	-1.80
25	13.88	13.02	13.16	12.96	13.13	13.23	13.13	0.37	2.82	1.98	4.13
26	6.71	6.46	6.38	6.48	6.42	6.49	6.46	0.13	1.98	1.76	3.47
27	10.31	10.93	11.16	11.33	11.43	11.03	11.16	0.45	4.03	-1.32	1.58
28	16.81	16.81	16.84	16.23	16.86	16.71	16.81	0.27	1.60	-2.20	4.86
29	6.75	6.82	6.89	5.95	6.00	6.48	6.75	0.47	7.18	-0.56	-3.22
30	9.43	9.18	9.20	8.85	9.18	9.17	9.18	0.21	2.24	-0.67	2.22
31	11.12	11.07	10.91	10.14	10.06	10.66	10.91	0.52	4.85	-0.52	-3.13
32	3.42	3.39	3.39	3.77	3.98	3.59	3.42	0.27	7.62	0.93	-1.41
33	3.71	3.76	3.79	3.91	4.07	3.85	3.79	0.15	3.79	1.12	0.41
34	7.56	7.62	7.74	7.01	7.33	7.45	7.56	0.29	3.88	-0.99	0.26
35	6.58	6.63	6.69	6.11	6.37	6.48	6.58	0.24	3.69	-1.12	0.20
36	10.57	10.44	10.44	10.44	10.84	10.55	10.44	0.17	1.62	1.75	2.84
37	7.98	8.06	8.14	7.42	7.15	7.75	7.98	0.44	5.66	-0.73	-2.09
38	8.57	8.46	8.44	8.06	8.09	8.32	8.44	0.23	2.78	-0.40	-2.89
39	6.46	6.45	6.39	8.56	8.70	7.31	6.46	1.20	16.40	0.61	-3.29

CVT	Meas. 1	Meas. 2	Meas. 3	Meas. 4	Meas. 5	\bar{F}_f [nN]	\tilde{F}_f [nN]	σ_{F_f} [nN]	RSD $_{F_f}$ [%]	γ_1	γ_2
40	4.19	4.15	4.13	4.34	4.30	4.22	4.19	0.09	2.14	0.52	-2.60
41	9.44	9.47	9.36	9.97	10.00	9.65	9.47	0.31	3.23	0.53	-3.16
42	10.30	10.35	10.28	9.20	9.63	9.95	10.28	0.52	5.18	-0.97	-1.19
43	3.54	3.54	3.60	3.33	3.45	3.49	3.54	0.10	2.99	-0.97	0.32
44	6.02	6.03	5.93	5.61	5.66	5.85	5.93	0.20	3.47	-0.50	-2.98
45	6.76	6.73	6.70	6.62	6.52	6.66	6.70	0.10	1.47	-0.98	-0.02
46	4.31	4.44	4.43	5.05	5.26	4.70	4.44	0.43	9.10	0.68	-2.48
47	3.29	3.30	3.33	3.03	3.07	3.20	3.29	0.14	4.41	-0.59	-2.91
48	5.33	5.30	5.25	5.07	5.13	5.21	5.25	0.11	2.13	-0.49	-2.08
49	8.52	8.51	8.40	7.32	7.30	8.01	8.40	0.64	8.04	-0.58	-3.30
50	8.26	8.32	8.20	6.85	4.85	7.30	8.20	1.50	20.60	-1.49	1.53

Table B.5 Experimentally obtained values of the nanoscale friction force F_f [nN] for the SS sample at the CVT-based experimental points.

CVT	Meas. 1	Meas. 2	Meas. 3	Meas. 4	Meas. 5	\bar{F}_f [nN]	\tilde{F}_f [nN]	σ_{F_f} [nN]	RSD $_{F_f}$ [%]	γ_1	γ_2
1	7.08	7.10	7.21	7.23	7.41	7.21	7.21	0.13	1.83	0.93	0.70
2	7.55	7.66	7.72	7.68	7.89	7.70	7.68	0.12	1.60	0.67	1.55
3	7.40	7.57	7.81	7.55	7.71	7.61	7.57	0.16	2.06	0.03	-0.44
4	7.82	7.97	7.89	7.99	7.96	7.93	7.96	0.07	0.86	-0.97	-0.47
5	8.12	8.06	8.16	8.62	8.37	8.26	8.16	0.23	2.79	1.10	0.12

CVT	Meas. 1	Meas. 2	Meas. 3	Meas. 4	Meas. 5	\bar{F}_f [nN]	\tilde{F}_f [nN]	σ_{F_f} [nN]	RSD $_{F_f}$ [%]	γ_1	γ_2
6	8.37	8.32	8.67	8.78	8.65	8.56	8.65	0.20	2.34	-0.36	-2.55
7	7.28	7.44	7.38	7.57	7.38	7.41	7.38	0.11	1.44	0.69	1.13
8	8.35	8.11	8.32	8.37	8.62	8.35	8.35	0.18	2.16	0.24	1.82
9	7.66	7.73	7.58	7.73	7.61	7.66	7.66	0.07	0.88	-0.15	-2.41
10	11.11	11.37	11.65	11.69	11.09	11.38	11.37	0.29	2.52	0.07	-2.92
11	7.63	7.47	7.47	7.58	7.48	7.53	7.48	0.08	1.01	0.81	-1.96
12	5.16	5.28	5.35	5.40	5.44	5.33	5.35	0.11	2.08	-0.83	0.10
13	8.53	8.53	8.64	8.55	8.59	8.57	8.55	0.05	0.55	1.21	0.58
14	10.84	11.04	11.04	11.10	11.10	11.03	11.04	0.11	0.97	-1.74	3.25
15	8.62	8.69	8.99	8.99	8.99	8.85	8.99	0.18	2.06	-0.68	-2.93
16	8.74	8.76	8.93	9.18	9.01	8.92	8.93	0.18	2.02	0.46	-1.08
17	5.09	5.19	5.01	5.12	5.31	5.14	5.12	0.11	2.18	0.66	0.62
18	10.16	9.61	9.85	10.30	10.11	10.01	10.11	0.27	2.75	-0.71	-0.72
19	8.64	8.31	8.57	8.75	8.66	8.59	8.64	0.17	1.95	-1.38	2.38
20	4.31	4.41	4.48	4.53	4.55	4.46	4.48	0.10	2.18	-0.87	-0.27
21	11.80	12.09	11.89	11.89	11.98	11.93	11.89	0.11	0.93	0.69	0.39
22	7.78	8.30	8.28	8.30	8.21	8.18	8.28	0.22	2.72	-2.08	4.37
23	5.71	5.90	5.99	6.08	6.13	5.96	5.99	0.16	2.74	-0.83	0.11
24	11.98	12.63	12.72	13.00	12.72	12.61	12.72	0.38	3.01	-1.44	3.01
25	10.25	10.39	10.53	10.95	10.55	10.53	10.53	0.26	2.50	1.04	1.68

CVT	Meas. 1	Meas. 2	Meas. 3	Meas. 4	Meas. 5	\bar{F}_f [nN]	\tilde{F}_f [nN]	σ_{F_f} [nN]	RSD $_{F_f}$ [%]	γ_1	γ_2
26	5.40	5.47	5.60	5.74	5.70	5.58	5.60	0.15	2.66	-0.27	-2.28
27	7.86	7.84	8.15	8.15	8.22	8.04	8.15	0.18	2.26	-0.52	-3.12
28	10.76	10.63	10.90	11.33	11.17	10.96	10.90	0.29	2.64	0.31	-1.79
29	4.53	4.65	4.74	4.77	4.81	4.70	4.74	0.11	2.38	-1.01	0.36
30	2.27	2.14	2.09	2.04	1.98	2.10	2.09	0.11	5.28	0.72	0.64
31	9.07	8.59	8.84	8.97	8.60	8.81	8.84	0.22	2.44	-0.01	-2.54
32	3.22	3.31	3.36	3.38	3.40	3.34	3.36	0.07	2.15	-1.10	0.47
33	2.96	3.05	3.09	3.11	3.14	3.07	3.09	0.07	2.29	-1.16	1.21
34	4.69	4.72	4.75	4.88	4.77	4.76	4.75	0.07	1.54	1.20	1.79
35	4.44	4.03	3.05	2.68	2.62	3.36	3.05	0.83	24.50	0.58	-2.38
36	8.05	7.96	7.93	7.85	8.09	7.97	7.96	0.10	1.21	-0.13	-1.42
37	4.82	4.97	5.23	5.03	5.03	5.02	5.03	0.15	2.96	0.25	1.58
38	6.48	6.75	6.78	6.69	7.00	6.74	6.75	0.19	2.80	-0.01	1.39
39	5.80	5.50	5.69	5.68	5.90	5.71	5.69	0.15	2.59	-0.39	0.39
40	3.37	3.45	3.47	3.49	3.53	3.46	3.47	0.06	1.70	-1.00	1.44
41	3.63	4.54	4.69	4.78	4.44	4.42	4.54	0.46	10.40	-1.79	3.44
42	4.74	4.57	4.35	4.46	4.13	4.45	4.46	0.23	5.22	-0.29	0.01
43	2.44	2.54	2.57	2.57	2.58	2.54	2.57	0.06	2.34	-1.87	3.51
44	3.25	3.48	3.49	3.63	3.60	3.49	3.49	0.15	4.21	-1.25	1.73
45	3.49	3.66	4.06	4.32	4.31	3.97	4.06	0.38	9.57	-0.42	-2.46

CVT	Meas. 1	Meas. 2	Meas. 3	Meas. 4	Meas. 5	\bar{F}_f [nN]	\tilde{F}_f [nN]	σ_{F_f} [nN]	RSD $_{F_f}$ [%]	γ_1	γ_2
46	2.71	2.84	2.86	2.98	2.98	2.87	2.86	0.11	3.91	-0.59	-0.45
47	1.99	1.96	1.95	1.94	1.96	1.96	1.96	0.02	0.89	1.61	3.12
48	2.95	2.82	2.83	2.86	2.90	2.87	2.86	0.05	1.77	0.79	-0.61
49	4.32	3.74	3.96	4.16	3.77	3.99	3.96	0.25	6.31	0.40	-1.90
50	2.31	1.62	1.91	1.91	2.26	2.00	1.91	0.28	14.20	-0.20	-1.36

Table B.6 Experimentally obtained values of the adhesion force F_A [nN] for the Al sample at the CVT-based experimental points.

CVT	Meas. 1	Meas. 2	Meas. 3	Meas. 4	Meas. 5	\bar{F}_A [nN]	\tilde{F}_A [nN]	σ_{F_A} [nN]	RSD $_{F_A}$ [%]	γ_1	γ_2
1	17.00	15.98	18.36	15.81	15.47	16.52	15.98	1.17	7.11	1.18	0.55
2	17.00	18.53	15.47	18.02	17.85	17.37	17.85	1.20	6.90	-1.22	1.19
3	17.70	15.58	15.75	16.82	18.76	16.92	16.82	1.34	7.92	0.46	-1.41
4	17.70	19.12	19.65	18.94	18.94	18.87	18.94	0.71	3.79	-1.26	2.71
5	17.70	17.88	18.41	18.41	18.41	18.16	18.41	0.35	1.90	-0.76	-2.48
6	17.70	15.75	16.99	15.93	17.88	16.85	16.99	0.98	5.82	-0.18	-2.87
7	16.90	15.21	17.41	16.06	16.06	16.33	16.06	0.85	5.21	0.02	-0.73
8	16.00	14.08	14.88	16.48	15.36	15.36	15.36	0.94	6.12	-0.27	-0.82
9	16.00	15.68	15.84	15.52	15.52	15.71	15.68	0.21	1.33	0.54	-1.49
10	16.60	17.60	15.27	14.77	15.94	16.04	15.94	1.11	6.93	0.46	-0.70
11	16.60	16.77	14.77	17.60	15.11	16.17	16.60	1.19	7.35	-0.18	-2.14
12	16.90	18.42	17.41	15.72	18.42	17.37	17.41	1.14	6.54	-0.67	-0.51
13	14.80	16.28	15.84	15.98	14.06	15.39	15.84	0.93	6.04	-0.82	-1.23
14	14.80	16.43	16.58	14.80	13.76	15.27	14.80	1.20	7.85	0.02	-2.00
15	9.57	8.52	9.86	10.34	10.72	9.80	9.86	0.84	8.59	-0.83	0.73
16	7.45	6.93	6.56	6.56	7.45	6.99	6.93	0.45	6.41	0.16	-3.02
17	7.45	8.12	7.38	6.78	7.08	7.36	7.38	0.50	6.80	0.73	1.02
18	6.91	7.26	6.15	6.22	6.91	6.69	6.91	0.48	7.21	-0.21	-2.43

CVT	Meas. 1	Meas. 2	Meas. 3	Meas. 4	Meas. 5	\bar{F}_A [nN]	\tilde{F}_A [nN]	σ_{F_A} [nN]	RSD $_{F_A}$ [%]	γ_1	γ_2
19	6.29	5.98	6.10	5.85	6.42	6.13	6.10	0.23	3.74	0.14	-1.63
20	4.91	4.86	4.32	4.67	4.67	4.68	4.67	0.23	4.95	-1.03	1.09
21	4.91	5.50	5.25	4.96	5.16	5.16	5.16	0.24	4.62	0.59	-0.54
22	3.86	4.05	4.17	4.29	3.63	4.00	4.05	0.26	6.50	-0.60	-0.67
23	4.21	3.75	3.75	4.46	4.55	4.14	4.21	0.38	9.22	-0.19	-2.93
24	4.21	3.92	4.04	4.67	4.46	4.26	4.21	0.31	7.24	0.38	-1.49
25	4.19	3.94	4.69	4.36	4.40	4.32	4.36	0.28	6.44	-0.03	0.54
26	5.01	5.36	5.51	5.36	5.51	5.35	5.36	0.20	3.83	-1.52	2.52
27	5.01	5.11	5.36	5.26	5.16	5.18	5.16	0.14	2.61	0.18	-0.68
28	5.30	5.51	5.88	4.93	5.78	5.48	5.51	0.38	6.99	-0.61	-0.62
29	5.30	5.57	4.66	5.09	4.66	5.06	5.09	0.40	7.83	0.17	-2.00
30	5.30	5.67	5.83	5.04	5.83	5.53	5.67	0.35	6.38	-0.77	-1.51
31	5.42	5.31	4.88	5.53	4.99	5.23	5.31	0.28	5.37	-0.36	-2.41
32	5.27	4.80	4.74	4.90	5.90	5.12	4.90	0.48	9.41	1.40	1.37
33	5.12	4.51	5.12	4.86	4.81	4.88	4.86	0.26	5.22	-0.72	-0.08
34	5.00	5.00	5.40	5.15	4.80	5.07	5.00	0.22	4.39	0.61	0.81
35	5.00	4.85	4.65	5.60	5.15	5.05	5.00	0.36	7.11	0.86	0.96
36	4.87	4.53	4.29	5.26	4.53	4.70	4.53	0.38	8.06	0.83	0.09
37	4.70	5.08	4.56	4.18	4.65	4.63	4.65	0.32	6.90	-0.07	1.51
38	4.22	4.05	4.26	4.60	4.14	4.25	4.22	0.21	4.93	1.42	2.48

CVT	Meas. 1	Meas. 2	Meas. 3	Meas. 4	Meas. 5	\bar{F}_A [nN]	\tilde{F}_A [nN]	σ_{F_A} [nN]	RSD $_{F_A}$ [%]	γ_1	γ_2
39	4.39	4.57	4.30	4.52	4.04	4.36	4.39	0.21	4.80	-1.01	0.70
40	4.22	4.68	3.93	3.88	4.64	4.27	4.22	0.38	8.93	0.16	-2.96
41	3.44	3.17	3.51	3.41	3.17	3.34	3.41	0.16	4.84	-0.36	-2.91
42	3.44	3.44	3.61	3.27	3.27	3.41	3.44	0.14	4.23	0.51	-0.61
43	3.30	3.63	3.66	3.14	3.43	3.43	3.43	0.22	6.49	-0.32	-1.65
44	3.11	3.27	3.30	3.11	2.92	3.14	3.11	0.15	4.75	-0.59	-0.24
45	3.20	3.04	2.94	2.85	3.55	3.12	3.04	0.28	8.85	1.15	1.08
46	3.15	3.37	3.02	3.06	2.80	3.08	3.06	0.21	6.68	0.15	1.05
47	3.15	3.06	3.40	3.50	3.28	3.28	3.28	0.18	5.48	0.00	-1.71
48	3.15	3.47	2.80	3.40	2.90	3.14	3.15	0.29	9.36	-0.06	-2.63
49	3.06	2.91	3.24	2.94	3.34	3.10	3.06	0.19	6.07	0.37	-2.33
50	2.97	2.94	2.91	3.09	2.73	2.93	2.94	0.13	4.40	-0.65	1.73

Table B.7 Experimentally obtained values of the adhesion force F_A [nN] for the Al_2O_3 sample at the CVT-based experimental points.

CVT	Meas. 1	Meas. 2	Meas. 3	Meas. 4	Meas. 5	\bar{F}_A [nN]	\tilde{F}_A [nN]	σ_{F_A} [nN]	RSD $_{F_A}$ [%]	γ_1	γ_2
1	10.90	11.23	10.14	11.23	11.34	10.97	11.23	0.49	4.48	-1.70	2.73
2	10.90	10.57	9.81	9.92	9.59	10.16	9.92	0.55	5.44	0.59	-1.93
3	14.40	15.55	16.13	14.11	15.84	15.21	15.55	0.90	5.90	-0.44	-2.68
4	14.40	12.96	12.96	13.97	13.39	13.54	13.39	0.64	4.70	0.55	-1.79

CVT	Meas. 1	Meas. 2	Meas. 3	Meas. 4	Meas. 5	\bar{F}_A [nN]	\tilde{F}_A [nN]	σ_{F_A} [nN]	RSD $_{F_A}$ [%]	γ_1	γ_2
5	14.40	14.26	15.55	14.40	14.11	14.54	14.40	0.58	3.96	1.99	4.21
6	14.40	13.82	13.25	15.26	15.98	14.54	14.40	1.10	7.54	0.25	-1.38
7	15.00	15.60	16.80	14.70	15.75	15.57	15.60	0.81	5.21	0.80	0.60
8	15.30	16.98	16.68	15.45	14.69	15.82	15.45	0.97	6.14	0.25	-2.24
9	15.30	13.77	14.23	15.61	14.23	14.63	14.23	0.78	5.36	0.42	-2.35
10	14.80	16.43	13.32	16.43	15.54	15.30	15.54	1.30	8.50	-0.96	0.17
11	14.80	14.95	14.95	14.50	14.95	14.83	14.95	0.19	1.30	-1.71	2.66
12	14.70	16.17	12.94	13.52	14.41	14.35	14.41	1.24	8.62	0.60	0.27
13	13.20	13.07	14.39	14.12	13.86	13.73	13.86	0.58	4.19	-0.18	-2.50
14	13.20	12.14	12.94	12.01	12.67	12.59	12.67	0.51	4.03	-0.07	-2.28
15	8.52	7.50	7.84	8.09	9.12	8.21	8.09	0.63	7.64	0.58	-0.31
16	6.57	7.23	6.24	7.36	6.77	6.83	6.77	0.46	6.77	-0.08	-1.77
17	6.57	5.85	6.24	5.91	5.91	6.10	5.91	0.31	5.02	1.18	0.08
18	5.85	6.14	6.14	5.56	5.38	5.82	5.85	0.34	5.89	-0.29	-2.33
19	5.03	4.53	5.58	5.53	5.63	5.26	5.53	0.48	9.06	-1.17	-0.03
20	4.42	4.11	4.64	4.82	4.38	4.47	4.42	0.27	6.03	-0.06	-0.36
21	4.42	4.55	4.86	4.60	4.29	4.54	4.55	0.22	4.74	0.57	0.64
22	3.63	3.49	3.85	3.67	3.56	3.64	3.63	0.14	3.76	0.86	1.09
23	3.75	3.98	3.45	3.49	3.86	3.71	3.75	0.23	6.21	-0.11	-2.49
24	3.75	4.16	4.20	4.16	4.13	4.08	4.16	0.19	4.57	-2.12	4.60

CVT	Meas. 1	Meas. 2	Meas. 3	Meas. 4	Meas. 5	\bar{F}_A [nN]	\tilde{F}_A [nN]	σ_{F_A} [nN]	RSD $_{F_A}$ [%]	γ_1	γ_2
25	3.61	3.18	3.65	3.50	3.50	3.49	3.50	0.19	5.31	-1.58	2.80
26	5.08	5.39	4.72	5.28	4.78	5.05	5.08	0.30	5.85	-0.07	-2.67
27	5.08	4.67	4.78	4.67	5.03	4.85	4.78	0.20	4.03	0.46	-2.94
28	5.77	5.14	5.19	5.48	5.71	5.46	5.48	0.29	5.32	-0.10	-2.81
29	5.77	5.83	5.25	5.08	5.19	5.42	5.25	0.35	6.43	0.48	-3.00
30	5.77	5.83	6.00	5.60	5.54	5.75	5.77	0.19	3.22	0.30	-1.02
31	5.41	4.82	5.74	4.82	5.57	5.27	5.41	0.43	8.17	-0.29	-2.87
32	5.20	4.68	5.82	5.51	5.72	5.39	5.51	0.46	8.57	-1.01	0.27
33	5.18	5.44	4.61	4.97	4.66	4.97	4.97	0.35	7.03	0.32	-1.65
34	4.97	5.42	4.42	4.62	4.77	4.84	4.77	0.38	7.84	0.84	0.65
35	4.97	4.37	4.42	5.22	4.67	4.73	4.67	0.36	7.63	0.48	-1.73
36	4.90	4.46	4.66	4.75	5.34	4.82	4.75	0.33	6.88	1.01	1.40
37	4.80	4.66	4.66	4.94	4.42	4.69	4.66	0.20	4.18	-0.27	0.46
38	4.28	3.81	3.90	4.19	3.81	4.00	3.90	0.22	5.59	0.59	-2.75
39	4.26	4.56	3.96	4.09	4.18	4.21	4.18	0.22	5.33	0.96	1.31
40	4.22	4.05	3.97	4.22	4.26	4.14	4.22	0.13	3.09	-0.76	-1.84
41	3.86	3.98	3.40	3.67	3.67	3.71	3.67	0.22	5.94	-0.41	0.03
42	3.86	3.67	3.98	4.17	4.05	3.95	3.98	0.19	4.86	-0.56	0.00
43	3.38	3.11	3.52	3.28	3.21	3.30	3.28	0.16	4.73	0.35	-0.45
44	3.33	3.46	3.40	3.60	3.03	3.36	3.40	0.21	6.26	-1.04	1.75

CVT	Meas. 1	Meas. 2	Meas. 3	Meas. 4	Meas. 5	\bar{F}_A [nN]	\bar{F}_A [nN]	\bar{F}_A [nN]	σ_{F_A} [nN]	RSD $_{F_A}$ [%]	γ_1	γ_2
45	3.21	2.92	3.21	3.24	3.31	3.18	3.18	3.21	0.15	4.68	-1.83	3.82
46	3.14	3.45	3.33	2.76	3.52	3.24	3.24	3.33	0.30	9.35	-1.17	0.88
47	3.14	3.01	3.33	2.80	3.30	3.12	3.12	3.14	0.22	7.03	-0.72	-0.52
48	3.14	3.45	3.27	3.49	2.80	3.23	3.23	3.27	0.28	8.68	-1.01	0.57
49	3.10	3.29	3.35	3.32	3.13	3.24	3.24	3.29	0.11	3.49	-0.48	-2.85
50	3.04	3.28	3.22	2.98	3.41	3.19	3.19	3.22	0.18	5.50	-0.04	-1.80

Table B.8 Experimentally obtained values of the adhesion force F_A [nN] for the MoS₂ sample at the CVT-based experimental points.

CVT	Meas. 1	Meas. 2	Meas. 3	Meas. 4	Meas. 5	\bar{F}_A [nN]	\bar{F}_A [nN]	\bar{F}_A [nN]	σ_{F_A} [nN]	RSD $_{F_A}$ [%]	γ_1	γ_2
1	13.70	12.47	14.52	14.66	14.52	13.97	13.97	14.52	0.92	6.61	-1.47	1.54
2	13.70	13.02	13.70	14.80	12.33	13.51	13.51	13.70	0.92	6.79	0.21	0.38
3	13.60	14.55	13.46	14.14	12.78	13.71	13.71	13.60	0.68	4.93	-0.17	-0.35
4	13.60	14.96	13.06	12.38	14.96	13.79	13.79	13.60	1.15	8.36	-0.01	-2.30
5	13.60	14.69	14.42	12.24	13.06	13.60	13.60	13.60	1.00	7.35	-0.35	-1.29
6	13.60	12.78	15.23	13.46	14.28	13.87	13.87	13.60	0.93	6.69	0.63	0.25
7	14.20	14.77	14.34	15.76	15.34	14.88	14.88	14.77	0.66	4.44	0.43	-1.84
8	14.40	14.11	12.67	14.54	14.11	13.97	13.97	14.11	0.75	5.36	-1.89	3.83
9	14.40	15.84	14.98	12.67	13.54	14.28	14.28	14.40	1.23	8.62	-0.12	-0.86
10	14.60	14.16	16.35	15.04	15.91	15.21	15.21	15.04	0.91	5.97	0.24	-1.96

CVT	Meas. 1	Meas. 2	Meas. 3	Meas. 4	Meas. 5	\bar{F}_A [nN]	\tilde{F}_A [nN]	σ_{F_A} [nN]	RSD $_{F_A}$ [%]	γ_1	γ_2
11	14.60	14.45	14.02	12.99	14.02	14.02	14.02	0.63	4.48	-1.32	2.00
12	14.20	15.19	15.90	13.63	12.92	14.37	14.20	1.19	8.31	0.18	-1.42
13	12.10	11.86	11.86	11.01	11.74	11.71	11.86	0.41	3.53	-1.65	3.33
14	12.10	12.22	11.62	12.10	13.55	12.32	12.10	0.73	5.91	1.63	3.43
15	7.86	7.78	8.41	8.33	8.57	8.19	8.33	0.35	4.26	-0.36	-2.70
16	5.98	5.56	6.16	5.92	6.28	5.98	5.98	0.27	4.58	-0.83	0.81
17	5.98	6.46	6.04	6.04	6.70	6.24	6.04	0.32	5.10	0.89	-1.53
18	5.37	5.32	5.42	5.42	4.99	5.31	5.37	0.18	3.39	-1.91	3.76
19	4.53	4.39	5.03	4.89	4.94	4.76	4.89	0.28	5.83	-0.60	-2.35
20	3.67	3.89	3.38	3.56	3.78	3.66	3.67	0.20	5.43	-0.41	-0.44
21	3.67	4.11	3.23	3.71	3.34	3.61	3.67	0.35	9.60	0.50	-0.33
22	3.22	3.57	3.45	2.87	3.25	3.27	3.25	0.27	8.22	-0.73	0.69
23	2.88	2.71	2.85	2.91	2.79	2.83	2.85	0.08	2.83	-0.93	0.13
24	2.88	2.71	3.17	3.11	3.05	2.98	3.05	0.19	6.31	-0.85	-0.67
25	3.10	2.79	3.38	3.29	3.16	3.14	3.16	0.23	7.17	-1.03	1.27
26	5.15	5.00	5.46	5.56	5.31	5.29	5.31	0.23	4.32	-0.21	-1.46
27	5.15	5.46	5.25	5.36	5.25	5.29	5.25	0.12	2.22	0.40	-0.18
28	5.56	5.23	6.06	5.06	5.06	5.39	5.23	0.43	7.89	1.21	0.58
29	5.56	5.39	6.06	5.84	5.78	5.73	5.78	0.26	4.50	-0.08	-0.73
30	5.56	4.89	6.01	5.95	5.06	5.49	5.56	0.51	9.20	-0.22	-2.70

CVT	Meas. 1	Meas. 2	Meas. 3	Meas. 4	Meas. 5	\bar{F}_A [nN]	\bar{F}_A [nN]	σ_{F_A} [nN]	RSD $_{F_A}$ [%]	γ_1	γ_2
31	5.04	5.59	5.49	4.59	4.84	5.11	5.04	0.43	8.39	0.03	-2.17
32	4.96	4.86	4.41	5.16	5.36	4.95	4.96	0.35	7.17	-0.73	0.80
33	4.77	4.34	5.06	4.39	4.48	4.61	4.48	0.30	6.53	0.96	-0.57
34	4.61	4.75	4.24	4.43	4.29	4.46	4.43	0.21	4.81	0.43	-1.84
35	4.61	4.93	4.38	4.56	4.61	4.62	4.61	0.20	4.32	0.89	2.26
36	4.57	4.30	4.98	4.20	4.07	4.42	4.30	0.36	8.18	1.04	0.44
37	4.44	3.95	4.80	4.66	4.57	4.48	4.57	0.32	7.24	-1.40	2.22
38	3.94	3.66	3.98	4.10	4.02	3.94	3.98	0.16	4.18	-1.54	2.91
39	3.79	3.71	3.34	3.53	4.25	3.72	3.71	0.34	9.18	0.82	1.07
40	3.41	3.79	3.24	3.72	3.38	3.51	3.41	0.23	6.68	0.31	-2.41
41	3.22	3.45	3.45	2.96	3.19	3.25	3.22	0.20	6.22	-0.51	-0.65
42	3.22	3.25	3.54	2.90	3.38	3.26	3.25	0.24	7.31	-0.69	1.17
43	3.05	3.36	3.39	3.42	2.93	3.23	3.36	0.22	6.89	-0.73	-2.31
44	2.92	2.80	2.86	2.77	2.86	2.84	2.86	0.06	2.00	0.08	-0.82
45	2.88	2.77	3.17	2.79	3.17	2.96	2.88	0.20	6.74	0.42	-3.12
46	2.91	2.85	3.00	2.71	3.11	2.92	2.91	0.15	5.25	-0.14	0.00
47	2.91	2.65	2.85	2.91	2.71	2.81	2.85	0.12	4.31	-0.58	-2.46
48	2.91	2.85	2.94	3.11	3.23	3.01	2.94	0.16	5.23	0.72	-1.42
49	2.72	2.75	2.75	3.02	2.88	2.82	2.75	0.13	4.49	1.18	0.08
50	2.72	2.91	2.72	2.97	2.86	2.83	2.86	0.11	3.92	-0.09	-2.55

Table B.9 Experimentally obtained values of the adhesion force F_A [nN] for the TiO₂ sample at the CVT-based experimental points.

CVT	Meas. 1	Meas. 2	Meas. 3	Meas. 4	Meas. 5	\bar{F}_A [nN]	\tilde{F}_A [nN]	σ_{F_A} [nN]	RSD _{F_A} [%]	γ_1	γ_2
1	17.40	19.31	17.57	18.97	16.53	17.96	17.57	1.16	6.44	0.11	-1.93
2	17.40	16.53	18.62	15.83	17.92	17.26	17.40	1.10	6.39	-0.16	-1.24
3	17.50	17.32	15.40	17.15	18.38	17.15	17.32	1.09	6.33	-1.13	2.47
4	17.50	17.32	17.50	19.60	15.75	17.54	17.50	1.37	7.81	0.50	2.08
5	17.50	17.85	18.38	19.25	19.43	18.48	18.38	0.84	4.57	0.07	-2.53
6	17.50	18.02	15.57	17.32	16.27	16.94	17.32	0.99	5.86	-0.56	-1.35
7	17.80	17.09	17.80	17.27	19.40	17.87	17.80	0.91	5.11	1.58	2.80
8	17.30	16.26	17.13	17.82	16.78	17.06	17.13	0.58	3.41	-0.15	0.15
9	17.30	15.74	17.13	15.57	15.57	16.26	15.74	0.87	5.37	0.60	-3.17
10	17.40	18.62	16.70	16.53	18.44	17.54	17.40	0.96	5.50	0.18	-2.87
11	17.40	17.57	17.40	18.27	19.31	17.99	17.57	0.82	4.57	1.39	1.16
12	16.60	15.27	16.93	15.11	18.26	16.43	16.60	1.30	7.89	0.44	-0.87
13	15.00	15.45	16.65	15.75	13.20	15.21	15.45	1.28	8.39	-1.00	1.78
14	15.00	15.75	15.75	13.65	13.35	14.70	15.00	1.14	7.77	-0.36	-2.88
15	11.00	11.00	11.99	11.55	11.44	11.40	11.44	0.42	3.65	0.52	-0.73
16	8.02	8.02	8.58	7.86	8.02	8.10	8.02	0.28	3.43	1.86	3.98
17	8.02	8.18	8.66	7.22	8.50	8.12	8.18	0.56	6.93	-1.19	1.51
18	6.92	7.20	6.09	6.99	6.09	6.66	6.92	0.53	7.93	-0.43	-3.02

CVT	Meas. 1	Meas. 2	Meas. 3	Meas. 4	Meas. 5	\bar{F}_A [nN]	\tilde{F}_A [nN]	σ_{F_A} [nN]	RSD $_{F_A}$ [%]	γ_1	γ_2
19	5.98	5.62	5.26	6.34	6.40	5.92	5.98	0.48	8.14	-0.48	-1.56
20	4.54	4.45	4.40	4.40	4.22	4.40	4.40	0.12	2.63	-0.91	2.00
21	4.54	4.59	4.04	4.63	4.68	4.50	4.59	0.26	5.76	-2.02	4.25
22	3.92	4.39	4.31	3.84	3.84	4.06	3.92	0.27	6.60	0.59	-2.98
23	4.10	4.35	4.51	4.47	4.10	4.31	4.35	0.20	4.57	-0.23	-2.96
24	4.10	3.90	3.61	4.22	4.02	3.97	4.02	0.23	5.91	-0.92	0.88
25	3.68	3.42	3.46	3.42	4.05	3.61	3.46	0.27	7.46	1.51	1.72
26	4.93	4.63	4.49	4.34	4.34	4.55	4.49	0.25	5.44	1.09	0.54
27	4.93	4.83	5.42	4.83	4.39	4.88	4.83	0.37	7.56	0.33	1.82
28	4.44	4.35	4.40	4.53	3.91	4.33	4.40	0.24	5.60	-1.82	3.69
29	4.44	4.04	4.75	4.97	4.17	4.48	4.44	0.39	8.69	0.24	-1.93
30	4.44	4.93	4.17	4.40	4.53	4.49	4.44	0.28	6.15	0.96	1.96
31	5.22	5.32	5.22	5.38	4.75	5.18	5.22	0.25	4.80	-1.82	3.63
32	4.30	4.47	4.34	3.83	4.43	4.27	4.34	0.26	6.06	-1.86	3.69
33	4.97	5.07	5.32	5.52	5.37	5.25	5.32	0.22	4.27	-0.22	-1.82
34	4.84	4.84	4.40	4.55	4.60	4.65	4.60	0.19	4.10	-0.04	-2.00
35	4.84	4.45	5.42	4.89	4.26	4.77	4.84	0.45	9.39	0.50	-0.05
36	4.72	4.77	5.10	4.30	4.67	4.71	4.72	0.29	6.07	-0.24	1.76
37	4.66	4.71	4.52	5.03	4.75	4.74	4.71	0.19	3.97	1.02	2.03
38	4.10	3.73	4.18	3.65	4.59	4.05	4.10	0.38	9.37	0.48	-0.61

CVT	Meas. 1	Meas. 2	Meas. 3	Meas. 4	Meas. 5	\bar{F}_A [nN]	\tilde{F}_A [nN]	σ_{F_A} [nN]	RSD $_{F_A}$ [%]	γ_1	γ_2
39	4.13	4.09	4.46	3.63	4.05	4.07	4.09	0.29	7.23	-0.41	1.90
40	4.06	3.78	4.39	4.22	4.02	4.09	4.06	0.23	5.59	-0.17	0.09
41	3.75	3.49	4.16	3.56	3.64	3.72	3.64	0.27	7.14	1.55	2.52
42	3.75	3.60	3.98	3.68	3.53	3.71	3.68	0.17	4.66	1.03	1.13
43	3.40	3.74	3.67	3.03	3.33	3.43	3.40	0.29	8.34	-0.48	-0.62
44	3.18	2.89	3.34	3.09	2.93	3.09	3.09	0.18	5.97	0.43	-1.21
45	3.17	3.49	3.30	3.01	2.82	3.16	3.17	0.26	8.11	-0.06	-0.63
46	3.10	3.04	2.85	2.95	3.16	3.02	3.04	0.12	4.08	-0.37	-1.11
47	3.10	2.73	2.88	3.32	3.44	3.09	3.10	0.30	9.54	-0.09	-1.93
48	3.10	2.91	2.82	2.95	3.47	3.05	2.95	0.26	8.40	1.47	2.11
49	3.03	2.94	2.67	3.24	2.85	2.95	2.94	0.21	7.25	0.18	0.38
50	2.93	3.02	2.78	2.93	2.93	2.92	2.93	0.08	2.89	-1.01	2.55

 Table B.10 Experimentally obtained values of the adhesion force F_A [nN] for the SS sample at the CVT-based points.

CVT	Meas. 1	Meas. 2	Meas. 3	Meas. 4	Meas. 5	\bar{F}_A [nN]	\tilde{F}_A [nN]	σ_{F_A} [nN]	RSD $_{F_A}$ [%]	γ_1	γ_2
1	14.40	13.54	13.10	12.82	14.69	13.71	13.54	0.81	5.91	0.26	-2.45
2	14.40	15.41	12.96	14.40	13.54	14.14	14.40	0.94	6.62	0.10	-0.38
3	15.10	15.86	13.29	13.89	13.74	14.38	13.89	1.07	7.41	0.68	-1.49
4	15.10	13.74	16.91	15.86	16.31	15.58	15.86	1.22	7.85	-0.82	0.34

CVT	Meas. 1	Meas. 2	Meas. 3	Meas. 4	Meas. 5	\bar{F}_A [nN]	\tilde{F}_A [nN]	σ_{F_A} [nN]	RSD $_{F_A}$ [%]	γ_1	γ_2
5	15.10	15.55	14.04	16.31	15.10	15.22	15.10	0.82	5.41	-0.24	1.09
6	15.10	14.19	13.59	14.35	13.29	14.10	14.19	0.71	5.00	0.39	-0.40
7	14.90	13.56	14.15	15.94	16.24	14.96	14.90	1.14	7.64	-0.06	-2.21
8	14.90	15.05	15.50	15.79	15.79	15.41	15.50	0.42	2.70	-0.34	-2.69
9	14.90	14.30	16.09	15.05	13.26	14.72	14.90	1.04	7.06	-0.21	0.68
10	15.40	14.48	13.71	13.71	14.94	14.45	14.48	0.75	5.19	0.18	-2.12
11	15.40	16.48	16.94	14.32	15.25	15.68	15.40	1.04	6.64	-0.02	-1.22
12	15.50	14.57	15.97	15.65	16.90	15.72	15.65	0.84	5.34	0.09	1.24
13	13.40	12.06	13.40	14.87	12.60	13.27	13.40	1.06	8.02	0.73	0.79
14	13.40	13.53	13.80	12.86	12.60	13.24	13.40	0.50	3.75	-0.38	-1.81
15	8.25	7.92	7.43	7.51	8.00	7.82	7.92	0.35	4.44	-0.07	-2.03
16	7.09	7.37	7.37	6.52	7.87	7.25	7.37	0.49	6.79	-0.47	1.07
17	7.09	7.09	7.16	6.88	6.52	6.95	7.09	0.26	3.75	-1.46	1.67
18	6.61	6.41	6.54	6.81	6.87	6.65	6.61	0.19	2.86	0.04	-1.80
19	6.31	6.37	7.00	6.18	6.69	6.51	6.37	0.33	5.10	0.89	-0.47
20	5.07	4.66	4.66	5.12	5.63	5.03	5.07	0.40	7.92	0.78	0.13
21	5.07	4.77	5.53	5.68	5.27	5.26	5.27	0.36	6.89	-0.35	-1.00
22	4.48	3.94	4.03	4.21	4.61	4.26	4.21	0.29	6.74	0.27	-2.24
23	4.91	4.91	4.81	5.25	5.50	5.08	4.91	0.29	5.71	0.91	-1.03
24	4.91	5.01	4.42	5.06	5.25	4.93	5.01	0.31	6.32	-1.33	2.51

CVT	Meas. 1	Meas. 2	Meas. 3	Meas. 4	Meas. 5	\bar{F}_A [nN]	\tilde{F}_A [nN]	σ_{F_A} [nN]	RSD $_{F_A}$ [%]	γ_1	γ_2
25	4.50	4.77	4.19	4.68	4.05	4.44	4.50	0.31	7.01	-0.31	-2.36
26	5.31	5.15	5.10	5.74	5.10	5.28	5.15	0.27	5.11	1.73	2.84
27	5.31	5.36	5.31	5.10	5.52	5.32	5.31	0.15	2.86	-0.33	1.67
28	5.08	4.62	4.67	5.33	5.08	4.96	5.08	0.30	6.09	-0.06	-2.04
29	5.08	5.49	5.03	5.03	5.64	5.25	5.08	0.29	5.50	0.74	-2.41
30	5.08	4.72	5.13	5.39	5.69	5.20	5.13	0.36	6.93	0.10	0.15
31	5.30	5.30	5.19	5.57	5.57	5.39	5.30	0.17	3.16	0.30	-2.72
32	5.05	4.50	4.50	5.66	5.61	5.06	5.05	0.57	11.20	0.03	-2.98
33	4.93	5.13	4.73	4.59	5.47	4.97	4.93	0.35	6.99	0.60	-0.33
34	4.88	4.78	5.17	4.59	4.44	4.77	4.78	0.28	5.89	0.42	-0.18
35	4.88	4.98	5.37	5.12	4.59	4.99	4.98	0.29	5.81	-0.13	0.38
36	4.81	4.95	4.57	5.24	4.43	4.80	4.81	0.32	6.70	0.32	-0.80
37	4.61	4.52	4.15	4.47	4.93	4.54	4.52	0.28	6.21	0.08	1.40
38	3.99	4.23	4.27	3.99	4.27	4.15	4.23	0.15	3.53	-0.55	-3.27
39	4.18	4.22	4.06	3.76	3.85	4.01	4.06	0.20	5.05	-0.33	-2.49
40	4.11	3.78	4.40	4.48	4.48	4.25	4.40	0.30	7.13	-1.17	0.12
41	3.90	3.74	3.82	4.29	3.59	3.87	3.82	0.26	6.78	1.17	2.03
42	3.90	3.98	4.25	3.74	3.98	3.97	3.98	0.18	4.63	0.69	1.71
43	3.43	3.74	3.22	3.67	3.19	3.45	3.43	0.25	7.26	0.14	-2.77
44	3.16	3.38	3.10	3.51	3.35	3.30	3.35	0.17	5.10	-0.11	-1.75

CVT	Meas. 1	Meas. 2	Meas. 3	Meas. 4	Meas. 5	\bar{F}_A [nN]	\tilde{F}_A [nN]	σ_{F_A} [nN]	RSD $_{F_A}$ [%]	γ_1	γ_2
45	3.09	2.78	2.75	2.97	3.03	2.92	2.97	0.15	5.16	-0.26	-2.66
46	3.08	2.90	2.93	2.83	2.71	2.89	2.90	0.14	4.67	0.19	0.89
47	3.08	2.74	2.83	3.30	3.42	3.07	3.08	0.29	9.44	0.02	-2.32
48	3.08	2.80	2.83	3.23	3.05	3.00	3.05	0.18	6.01	0.09	-1.71
49	3.06	2.97	3.31	2.91	2.69	2.99	2.97	0.22	7.48	0.25	0.92
50	2.94	2.68	3.09	3.29	2.91	2.98	2.94	0.23	7.66	0.09	0.43

Appendix C

MC-based Measurement Points

Table C.1 Distribution of measurement points in the considered multidimensional experimental space given by the varying process parameters v , ϑ and F_N , as determined by applying the MC-based sampling methodology for obtaining the test experimental dataset.

Measurement point no.	v [nm/s]	ϑ [°C]	F_N [nN]
1	429	24	51
2	237	27	59
3	40	27	25
4	57	29	28
5	48	32	101
6	430	39	13
7	297	42	60
8	492	45	98
9	84	51	62
10	317	52	140
11	216	61	49
12	68	68	135
13	476	73	112
14	323	76	104
15	458	77	150

Appendix D

MC-based F_f and F_A Measurements

This appendix contains the measured and processed experimental data obtained at MC-based measurement points. The tables presented further contain F_f and F_A experimental measurements for each material in each MC-based point (MC column) for all repetitions (Meas. 1 to Meas. 5 columns), and calculated values of mean (\bar{F} column), median (\tilde{F} column), standard deviation (σ column), relative standard deviation (RSD column) [106], skewness (γ_1 column) and kurtosis (γ_2 column), calculated according to expressions 5.3 and 5.4 respectively. Data presented in this appendix is used for testing predictive performance of all developed models.

Table D.1 Experimentally obtained values of the nanoscale friction force F_f [nN] for the Al sample at the MC-based experimental points.

MC	Meas. 1	Meas. 2	Meas. 3	Meas. 4	Meas. 5	\bar{F}_f [nN]	\tilde{F}_f [nN]	σ_{F_f} [nN]	RSD F_f [%]	γ_1	γ_2
1	9.43	9.24	8.77	8.96	8.11	8.90	8.96	0.51	5.73	-0.98	0.93
2	8.82	9.71	9.44	7.68	7.68	8.67	8.82	0.96	11.05	-0.16	-2.87
3	8.95	10.20	7.52	10.11	9.76	9.31	9.76	1.12	11.99	-1.33	1.17
4	9.03	8.04	8.04	10.47	7.68	8.65	8.04	1.14	13.15	1.34	1.17
5	11.50	11.96	12.88	10.23	10.46	11.41	11.50	1.09	9.55	0.29	-1.36
6	7.52	6.47	7.45	8.05	6.92	7.28	7.45	0.61	8.31	-0.21	-0.51
7	9.32	10.62	9.88	8.66	7.83	9.26	9.32	1.08	11.64	-0.14	-0.65
8	10.45	11.39	10.65	10.65	8.78	10.38	10.65	0.97	9.32	-1.43	3.01
9	7.13	6.99	7.92	6.20	7.35	7.12	7.13	0.62	8.72	-0.42	1.31
10	11.38	10.81	11.26	12.29	12.29	11.61	11.38	0.66	5.67	0.12	-2.33
11	4.12	4.74	4.33	4.78	3.59	4.31	4.33	0.49	11.40	-0.72	-0.28
12	6.19	7.12	6.19	5.26	7.24	6.40	6.19	0.81	12.62	-0.42	-0.79
13	4.32	4.71	3.80	4.97	3.63	4.29	4.32	0.57	13.36	-0.01	-2.30
14	3.75	4.13	3.86	4.35	4.28	4.07	4.13	0.26	6.37	-0.31	-2.36
15	4.23	4.10	3.68	4.35	4.06	4.08	4.10	0.25	6.24	-1.11	1.78

Table D.2 Experimentally obtained values of the nanoscale friction force F_f [nN] for the Al_2O_3 sample at the MC-based experimental points.

MC	Meas. 1	Meas. 2	Meas. 3	Meas. 4	Meas. 5	\bar{F}_f [nN]	\tilde{F}_f [nN]	σ_{F_f} [nN]	RSD F_f [%]	γ_1	γ_2
1	3.23	2.94	3.20	3.10	3.01	3.10	3.10	0.12	4.00	-0.19	-2.17
2	3.78	3.51	4.23	3.78	3.47	3.75	3.78	0.30	8.04	1.09	1.18
3	3.02	3.05	3.02	3.26	3.20	3.11	3.05	0.11	3.63	0.72	-2.36
4	2.93	3.25	3.25	2.70	2.64	2.95	2.93	0.29	9.96	0.07	-2.92
5	4.05	4.38	3.81	3.93	3.57	3.95	3.93	0.30	7.60	0.35	0.58
6	2.07	2.01	2.36	1.86	2.07	2.08	2.07	0.18	8.71	0.96	2.16
7	3.33	3.23	2.90	3.63	3.33	3.28	3.33	0.26	8.01	-0.37	1.60
8	2.84	2.50	2.73	2.93	2.76	2.75	2.76	0.16	5.82	-0.96	1.43
9	1.60	1.52	1.39	1.50	1.41	1.48	1.50	0.09	5.77	0.22	-1.36
10	3.67	3.38	3.67	3.63	4.11	3.69	3.67	0.26	7.15	0.94	2.42
11	0.40	0.35	0.42	0.42	0.41	0.40	0.41	0.03	6.84	-1.67	2.82
12	1.84	1.84	1.64	1.86	1.62	1.76	1.84	0.12	6.80	-0.60	-3.23
13	1.69	1.57	1.49	1.79	1.72	1.65	1.69	0.12	7.39	-0.46	-1.30
14	1.57	1.66	1.52	1.47	1.47	1.54	1.52	0.08	5.11	1.09	0.54
15	1.97	2.20	2.08	1.77	2.14	2.03	2.08	0.17	8.42	-1.02	0.46

Table D.3 Experimentally obtained values of the nanoscale friction force F_f [nN] for the MoS₂ sample at the MC-based experimental points.

MC	Meas. 1	Meas. 2	Meas. 3	Meas. 4	Meas. 5	\bar{F}_f [nN]	\tilde{F}_f [nN]	σ_{F_f} [nN]	RSD F_f [%]	γ_1	γ_2
1	3.56	3.78	3.10	3.88	3.74	3.61	3.74	0.31	8.56	-1.53	2.35
2	6.04	6.46	6.04	6.83	5.80	6.23	6.04	0.41	6.55	0.75	-0.62
3	4.29	3.65	4.51	3.91	4.25	4.12	4.25	0.34	8.27	-0.53	-1.02
4	4.98	4.49	5.88	5.48	5.43	5.25	5.43	0.53	10.17	-0.56	-0.14
5	9.52	9.05	8.76	9.62	10.09	9.41	9.52	0.52	5.52	0.04	-0.83
6	3.74	4.23	3.78	3.25	3.78	3.76	3.78	0.34	9.17	-0.22	1.99
7	9.10	9.29	9.56	8.19	8.01	8.83	9.10	0.69	7.78	-0.40	-2.71
8	9.89	11.57	8.31	11.57	9.59	10.19	9.89	1.40	13.71	-0.24	-1.45
9	7.63	6.87	7.32	6.49	6.94	7.05	6.94	0.44	6.25	0.14	-0.63
10	15.75	13.38	18.27	13.86	12.91	14.83	13.86	2.20	14.83	1.18	0.46
11	4.53	3.99	4.39	4.17	5.12	4.44	4.39	0.43	9.76	1.03	1.25
12	10.24	10.03	10.54	10.03	8.91	9.95	10.03	0.62	6.23	-1.58	3.15
13	7.13	8.27	6.92	6.63	7.28	7.25	7.13	0.62	8.60	1.41	2.50
14	7.83	7.52	7.91	8.15	7.68	7.82	7.83	0.24	3.04	0.23	-0.14
15	8.26	9.58	7.93	8.67	7.60	8.40	8.26	0.77	9.12	0.91	0.60

Table D.4 Experimentally obtained values of the nanoscale friction force F_f [nN] for the TiO₂ sample at the MC-based experimental points.

MC	Meas. 1	Meas. 2	Meas. 3	Meas. 4	Meas. 5	\bar{F}_f [nN]	\tilde{F}_f [nN]	σ_{F_f} [nN]	RSD F_f [%]	γ_1	γ_2
1	0.74	0.77	0.65	0.64	0.77	0.72	0.74	0.07	9.09	-0.49	-3.02
2	3.87	4.06	4.34	4.45	3.87	4.12	4.06	0.27	6.46	0.36	-2.52
3	2.05	2.24	2.22	1.85	1.78	2.03	2.05	0.21	10.21	-0.20	-2.76
4	2.24	2.44	2.20	1.95	2.51	2.27	2.24	0.22	9.77	-0.50	-0.40
5	4.40	3.83	4.93	4.31	3.83	4.26	4.31	0.46	10.77	0.61	-0.39
6	1.74	1.62	1.93	1.50	1.93	1.74	1.74	0.19	11.01	-0.22	-2.05
7	6.13	6.81	5.21	5.71	5.89	5.95	5.89	0.59	9.86	0.47	0.88
8	9.80	10.10	9.90	10.29	10.88	10.20	10.10	0.43	4.19	1.27	1.49
9	6.18	6.42	6.86	6.79	5.44	6.34	6.42	0.58	9.08	-1.10	0.87
10	12.35	11.12	10.50	13.09	12.10	11.83	12.10	1.03	8.68	-0.22	-1.24
11	5.27	5.64	4.48	5.37	5.11	5.17	5.27	0.43	8.38	-1.17	1.98
12	7.89	8.99	8.60	8.12	8.36	8.39	8.36	0.43	5.09	0.41	-0.44
13	7.30	7.66	6.42	6.64	7.52	7.11	7.30	0.55	7.70	-0.45	-2.54
14	7.22	6.35	8.16	7.80	6.43	7.19	7.22	0.81	11.19	0.07	-2.50
15	6.97	7.25	8.02	6.55	7.04	7.17	7.04	0.54	7.52	1.00	1.90

Table D.5 Experimentally obtained values of nanoscale the friction force F_f [nN] for the SS sample at the MC-based points.

MC	Meas. 1	Meas. 2	Meas. 3	Meas. 4	Meas. 5	\bar{F}_f [nN]	\tilde{F}_f [nN]	σ_{F_f} [nN]	RSD F_f [%]	γ_1	γ_2
1	7.65	8.03	7.19	7.27	7.35	7.50	7.35	0.35	4.62	1.13	0.24
2	7.49	7.27	7.72	7.27	7.94	7.54	7.49	0.29	3.89	0.54	-1.49
3	7.38	7.68	7.16	8.04	7.60	7.57	7.60	0.33	4.39	0.33	0.22
4	7.42	7.79	6.53	7.27	6.45	7.09	7.27	0.58	8.19	-0.13	-2.34
5	10.26	9.95	9.95	11.59	10.88	10.53	10.26	0.71	6.70	1.02	-0.26
6	6.84	7.52	7.32	7.66	6.98	7.26	7.32	0.35	4.82	-0.19	-2.30
7	7.36	7.22	7.51	7.88	7.29	7.45	7.36	0.26	3.52	1.39	1.78
8	9.40	8.37	9.59	10.34	9.87	9.51	9.59	0.73	7.70	-0.95	1.62
9	5.62	6.07	5.06	6.13	6.02	5.78	6.02	0.45	7.76	-1.37	1.07
10	10.25	10.35	9.53	10.35	9.12	9.92	10.25	0.56	5.68	-0.87	-1.64
11	2.93	2.84	2.84	3.20	3.02	2.97	2.93	0.15	4.96	1.09	0.54
12	5.43	5.54	6.13	5.10	5.70	5.58	5.54	0.38	6.79	0.45	0.91
13	4.27	4.49	3.93	4.74	4.49	4.39	4.49	0.30	6.91	-0.69	0.75
14	4.03	3.55	4.03	3.95	4.35	3.98	4.03	0.29	7.24	-0.54	1.91
15	2.56	2.58	2.50	2.27	2.81	2.55	2.56	0.19	7.53	-0.07	1.60

Table D.6 Experimentally obtained values of the adhesion force F_A [nN] for the AI sample at the MC-based experimental points (test dataset).

MC	Meas. 1	Meas. 2	Meas. 3	Meas. 4	Meas. 5	\bar{F}_A [nN]	\tilde{F}_A [nN]	σ_{F_A} [nN]	RSD $_{F_A}$ [%]	γ_1	γ_2
1	60.30	57.28	57.89	56.68	65.12	59.46	57.89	3.45	5.81	1.49	1.84
2	36.50	34.67	39.06	33.58	39.78	36.72	36.50	2.69	7.33	0.04	-2.44
3	36.50	34.67	35.04	38.69	37.59	36.50	36.50	1.69	4.64	0.23	-1.89
4	63.90	68.37	64.54	62.62	60.07	63.90	63.90	3.03	4.74	0.47	1.17
5	56.80	52.82	54.53	57.37	52.82	54.87	54.53	2.15	3.92	0.24	-2.84
6	61.90	65.00	64.38	58.19	63.14	62.52	63.14	2.70	4.32	-1.27	1.49
7	47.20	43.42	43.42	45.31	46.73	45.22	45.31	1.78	3.93	-0.02	-2.84
8	48.40	52.27	48.88	47.92	45.50	48.59	48.40	2.43	5.01	0.57	1.80
9	31.80	34.34	29.89	31.80	34.66	32.50	31.80	1.99	6.13	-0.11	-1.62
10	25.00	26.25	23.25	22.75	26.50	24.75	25.00	1.71	6.89	-0.22	-2.75
11	4.79	4.46	4.36	5.13	4.69	4.69	4.69	0.30	6.44	0.61	-0.18
12	6.89	6.82	6.41	7.51	7.10	6.95	6.89	0.40	5.80	0.17	0.82
13	4.76	4.86	5.00	4.57	4.47	4.73	4.76	0.21	4.48	-0.02	-1.58
14	4.56	4.88	4.83	4.93	4.20	4.68	4.83	0.31	6.52	-1.29	0.74
15	2.30	2.16	2.23	2.35	2.28	2.26	2.28	0.07	3.10	-0.54	0.00

Table D.7 Experimentally obtained values of the adhesion force F_A [nN] for the Al_2O_3 sample at the MC-based experimental points (test dataset).

MC	Meas. 1	Meas. 2	Meas. 3	Meas. 4	Meas. 5	\bar{F}_A [nN]	\tilde{F}_A [nN]	σ_{F_A} [nN]	RSD $_{F_A}$ [%]	γ_1	γ_2
1	59.80	55.02	63.39	55.61	63.99	59.56	59.80	4.20	7.05	-0.07	-2.90
2	66.40	68.39	64.41	61.75	61.09	64.41	64.41	3.08	4.78	0.23	-1.89
3	66.40	65.74	69.72	69.72	64.41	67.20	66.40	2.41	3.59	0.20	-2.59
4	65.70	67.01	61.76	64.39	65.04	64.78	65.04	1.95	3.01	-0.88	1.45
5	87.90	90.54	92.30	87.02	91.42	89.83	90.54	2.28	2.53	-0.36	-2.41
6	74.90	68.91	71.16	77.90	71.90	72.95	71.90	3.50	4.79	0.54	-0.56
7	70.60	73.42	67.78	68.48	74.84	71.02	70.60	3.06	4.31	0.27	-2.34
8	70.80	65.14	69.38	68.68	65.84	67.97	68.68	2.40	3.53	-0.19	-2.23
9	40.00	36.80	39.20	38.80	37.20	38.40	38.80	1.36	3.53	-0.19	-2.23
10	23.00	23.69	24.15	22.77	22.54	23.23	23.00	0.67	2.89	0.61	-1.60
11	6.71	6.31	6.38	6.31	6.84	6.51	6.38	0.25	3.86	0.72	-2.36
12	9.77	9.18	9.77	9.48	10.06	9.65	9.77	0.33	3.46	-0.40	-0.18
13	3.57	3.36	3.64	3.78	3.46	3.56	3.57	0.16	4.61	0.14	-0.51
14	3.55	3.83	3.44	3.59	3.30	3.54	3.55	0.20	5.55	0.53	0.92
15	4.46	4.24	4.37	4.59	4.59	4.45	4.46	0.15	3.43	-0.53	-1.14

Table D.8 Experimentally obtained values of the adhesion force F_A [nN] for the MoS₂ sample at the MC-based experimental points (test dataset).

MC	Meas. 1	Meas. 2	Meas. 3	Meas. 4	Meas. 5	\bar{F}_A [nN]	\tilde{F}_A [nN]	σ_{F_A} [nN]	RSD $_{F_A}$ [%]	γ_1	γ_2
1	17.30	19.38	18.68	16.26	16.43	17.61	17.30	1.38	7.81	0.42	-2.32
2	18.00	19.26	16.74	17.46	19.08	18.11	18.00	1.07	5.91	-0.13	-1.95
3	18.00	17.64	19.98	16.74	18.54	18.18	18.00	1.20	6.61	0.66	0.96
4	18.00	16.74	17.10	19.98	17.82	17.93	17.82	1.26	7.01	1.34	2.10
5	18.70	17.77	20.38	17.58	19.82	18.85	18.70	1.24	6.56	0.26	-2.42
6	16.10	15.78	16.74	17.87	18.03	16.90	16.74	1.02	6.02	0.15	-2.75
7	12.70	12.19	12.95	12.57	14.22	12.93	12.70	0.77	5.99	1.54	2.87
8	10.60	10.07	10.81	10.60	10.92	10.60	10.60	0.33	3.08	-1.28	2.00
9	9.72	10.40	9.04	9.82	9.62	9.72	9.72	0.49	5.00	0.00	1.61
10	6.25	6.00	6.19	6.06	6.88	6.28	6.19	0.35	5.57	1.80	3.49
11	6.31	6.00	6.18	5.93	6.37	6.16	6.18	0.19	3.13	-0.16	-2.50
12	3.30	3.40	3.17	3.40	3.14	3.28	3.30	0.12	3.80	-0.24	-2.84
13	3.30	3.17	3.33	3.53	3.60	3.39	3.33	0.18	5.19	0.11	-1.75
14	3.95	3.67	4.07	3.95	4.11	3.95	3.95	0.17	4.30	-1.32	2.00
15	3.42	3.66	3.49	3.42	3.73	3.54	3.49	0.14	4.02	0.58	-2.46

Table D.9 Experimentally obtained values of the adhesion force F_A [nN] for the TiO₂ sample at the MC-based experimental points (test dataset).

MC	Meas. 1	Meas. 2	Meas. 3	Meas. 4	Meas. 5	\bar{F}_A [nN]	\tilde{F}_A [nN]	σ_{F_A} [nN]	RSD $_{F_A}$ [%]	γ_1	γ_2
1	60.80	64.45	66.88	55.33	63.23	62.14	63.23	4.39	7.07	-0.97	1.03
2	79.00	71.89	79.79	87.69	82.16	80.11	79.79	5.71	7.13	-0.25	1.25
3	79.00	76.63	75.05	87.69	83.74	80.42	79.00	5.22	6.49	0.61	-1.35
4	79.00	75.84	75.05	77.42	84.53	78.37	77.42	3.76	4.80	1.41	1.99
5	67.90	69.26	74.01	74.01	68.58	70.75	69.26	3.01	4.26	0.49	-3.17
6	86.30	81.98	83.71	95.79	88.03	87.16	86.30	5.36	6.14	1.26	1.74
7	69.60	66.12	66.12	66.12	67.51	67.09	66.12	1.53	2.27	1.53	1.75
8	64.60	65.25	69.12	66.54	62.02	65.50	65.25	2.61	3.98	0.12	0.68
9	63.50	60.33	57.78	67.31	57.78	61.34	60.33	4.08	6.65	0.81	-0.73
10	44.80	42.11	45.70	41.22	49.73	44.71	44.80	3.36	7.51	0.74	0.15
11	31.90	31.90	34.77	29.03	35.41	32.60	31.90	2.57	7.87	-0.34	-0.86
12	7.39	7.17	6.80	7.91	7.32	7.32	7.32	0.40	5.49	0.42	1.36
13	9.02	10.10	9.29	8.57	9.38	9.27	9.29	0.56	6.05	0.49	1.12
14	4.93	4.78	4.63	5.08	5.42	4.97	4.93	0.30	6.09	0.76	0.39
15	4.05	3.69	4.21	4.05	3.93	3.99	4.05	0.20	4.91	-0.83	1.21

Table D.10 Experimentally obtained values of the adhesion force F_A [nN] for the SS sample at the MC-based experimental points.

MC	Meas. 1	Meas. 2	Meas. 3	Meas. 4	Meas. 5	\bar{F}_A [nN]	\tilde{F}_A [nN]	σ_{F_A} [nN]	RSD $_{F_A}$ [%]	γ_1	γ_2
1	57.90	59.06	62.53	63.69	53.27	59.29	59.06	4.13	6.96	-0.60	-0.23
2	56.10	61.71	52.73	61.71	61.15	58.68	61.15	4.08	6.95	-0.96	-1.21
3	56.10	53.30	54.98	58.91	56.66	55.99	56.10	2.08	3.71	0.21	0.49
4	61.90	66.85	62.52	57.57	63.14	62.40	62.52	3.32	5.32	-0.27	1.70
5	61.20	66.71	61.81	65.48	62.42	63.53	62.42	2.43	3.82	0.61	-2.34
6	51.20	53.25	48.13	55.30	52.74	52.12	52.74	2.67	5.12	-0.67	0.81
7	44.90	42.21	48.49	44.45	44.00	44.81	44.45	2.30	5.13	1.09	2.31
8	35.10	33.34	34.40	37.91	32.29	34.61	34.40	2.13	6.15	0.93	1.12
9	24.10	24.34	23.62	22.65	25.79	24.10	24.10	1.14	4.74	0.47	1.17
10	22.50	22.27	21.82	23.63	22.05	22.45	22.27	0.70	3.12	1.55	2.68
11	11.70	10.76	12.75	12.29	12.75	12.05	12.29	0.84	6.97	-1.04	0.17
12	6.95	7.09	7.65	7.30	7.44	7.28	7.30	0.28	3.78	0.13	-1.17
13	4.15	3.78	4.36	4.07	4.19	4.11	4.15	0.21	5.20	-0.88	1.63
14	3.67	3.34	3.60	3.93	3.93	3.69	3.67	0.25	6.69	-0.52	-0.75
15	2.91	3.20	3.20	2.77	3.20	3.06	3.20	0.21	6.73	-0.88	-1.75

Curriculum Vitae et Studiorum

Marko Perčić was born in 1982 in Rijeka, Croatia. After finishing the elementary school, he graduated as an engineering technician from the “Tehnička škola za strojarstvo i brodogradnju” high school in Rijeka. He then worked (2000 - 2006) as a technical draftsman and laboratory technician at the “Institut Građevinarstva Hrvatske – IGH d.d.” company. In 2006 he enrolls the mechanical engineering study at the Faculty of Engineering of the University of Rijeka, Croatia, where he graduates *Cum Laude*



in 2012 with a thesis in dealing with numerical modelling via CFD. The results of the work pertaining to the thesis were published as his first scientific paper. In 2012 he resumes working as a design associate, working on 30+ projects concerning thermal system designs, while he concurrently also enrolled the doctoral study programme of the Faculty of Engineering focused on nanofluids and renewable energy. In 2014 he started working part-time also as a teaching assistant at the Department of Mechanical Engineering Design of the Faculty of Engineering in Rijeka, where he finally finds a full-time employment in 2016. Ever since he is working as a teaching assistant on classes involving engineering graphics, 3D modelling, visualization, and laboratory exercises. In 2016 was defined also the topic of the herein presented doctoral thesis, under the supervision of Prof. S. Zelenika. In 2017 he has spent, as an ERASMUS+ scholarship holder, four months at the University of Udine in Italy (*Università degli Studi di Udine – Dipartimento di ingegneria elettrica gestionale e meccanica*). During his doctoral studies he attended also a scientific workshops on Modelling and Simulation of Tribological Problems in Technology (CISM, Udine, Italy), and another one on Atomic Layer Deposition: Fundamentals and Applications (University of Rijeka, Department of Physics).

He is currently actively involved in the activities of the Centre for Micro- and Nanosciences and Technologies (NANORI) of the University of Rijeka. His main scientific interests include experimental measurements, material characterization, mathematical modelling and simulation of physical systems at various scales, data mining and processing, optimization and machine learning. In this frame he is actively cooperating with various inland and foreign research institutions and companies including UC Santa Barbara, Department of Mechanical Engineering, CA, USA, AimDYN Inc., CA, USA, the Department of Physics of the University of Rijeka, the Institute of Physics and the Ruđer Bošković Institute, Zagreb, Croatia, the

Molecular Simulation Engineering Laboratory (MOSE) of the University of Trieste, Italy, and the Laboratory for Tribology and Interface Nanotechnology of the University of Ljubljana, Slovenia. In his professional career he is devoted to bring together fundamental scientific research with engineering applications, as well as promoting scientific collaborations.

He has authored eight papers in peer reviewed scientific journals and held several conference presentations. He has been an active member of numerous organizing committees of international conferences, and a reviewer for several CC and SCI-indexed journals. He was also technical editor of a scientific journal.

He is very active in the popularization and broadening of science via events at the Faculty of Engineering in Rijeka, and as an active participant of the “European Researcher’s Night” events.

He is member of the Croatian Chamber of Mechanical Engineers, and of the Technical Committee TO 537 of the Croatian Standards Institute.

List of Publications

Journal papers

1. M. Perčić, S. Zelenika, I. Mezić, R. Peter, N. Krstulović (2019) An experimental methodology for the concurrent characterization of multiple parameters influencing nanoscale friction, *Friction*, 1-17 (doi.org/10.1007/s40544-019-0289-z).
2. V. Glažar, M. Perčić, G. Marunić, B. Franković (2016) A Comparative Study of Evolutionary and Search Algorithms for Optimization of Heat Exchanger with Microchannel Coil. *Trans. FAMENA* 40/17 75-84.
3. V. Glažar, G. Marunić, M. Perčić, Z. Butković (2015) Application of glyph-based techniques for multivariate engineering visualization. *Eng. Opt.* 48/1 39-52.
4. Z. Čarija, B. Franković, M. Perčić, M. Čavrak (2014) Heat transfer analysis of fin-and-tube heat exchangers with flat and louvered fin geometries. *Int. J. Refrigeration* 45 160-167.
5. M. Perčić, B. Franković (2016) Solar Energy in Coastal Area of Croatia – Today and Tomorrow. *J. Maritime & Transportation Sci.* 52/1 223-229.
6. M. Perčić (2016) Renewable Energy Sources in the Context of Marine Technology – Present and Future Trends. *J. Maritime & Transportation Sci.* 52/1 213-221.
7. I. Jakovljević, M. Perčić (2015) Dependence of changes in pressure of superheated steam for reducing heat drop in the throttling regulation of steam turbines. *Eng. Rev.* 35/2 205-210.

8. M. Perčić, K. Lenić, A. Trp (2013) A three-dimensional numerical analysis of complete crossflow heat exchangers with conjugate heat transfer. *Eng. Rev.* 33/1 23-40.

Conference proceedings papers

1. E. Kamenar, M. Perčić, S. Zelenika, I. Šarić, D. Jardas, P. Gljuščić (2019) LFM characterization of TiO₂ films on a nanoindenter, 36th Danubia-Adria Symposium on Advances in Experimental Mechanics.
2. E. Kamenar, M. Perčić, S. Zelenika (2019) From nanometric to meso-scale characterisation of friction using nanoindentation, 19th EUSPEN International Conference.
3. M. Perčić, S. Zelenika, I. Mezić, R. Peter, N. Krstulović (2018) Experimental approach to establishing a model of nanoscale friction. *Proc. 18th EUSPEN Int. Con. Venezia, IT*, pp. 63-64.
4. M. Perčić, S. Zelenika (2017) Issues in characterizing parameters influencing nanometric friction. *Proc. My First Conf. 2017. Rijeka, HR*, pp. 40-41.
5. M. Perčić, S. Zelenika, E. Kamenar (2017) Issues in validation of friction in the nanometric domain. *Proc. 17th EUSPEN Int. Con. Hannover, DE*, pp. 105-106.
6. A. Jurov, I. Šrut Rakić, I. Delač Marion, T. Filipič, J. Kovač, R. Peter, I. Kavre Piltaver, I. Šarić, M. Perčić, N. Krstulović (2017) APPJ and PAW assisted nanoparticle impregnation and treatment of polymers. *Proc. 7th Cent. Eur. Sym. Plasma Chemistry. Sveti Martin na Muri, HR*, pp. 112-113.
7. V. Glažar, M. Perčić, A. Trp, K. Lenić (2017) A Comparative Study of Evolutionary Algorithms for Optimization of Fin-and-tube Heat Exchangers. *Proc. 9th Int. Exergy, Energy and Environment Sym. Split, HR*, pp. 817-824.
8. V. Katić, S. Zelenika, E. Kamenar, K. Marković, M. Perčić, S. Špalj (2016) Mechanical testing of orthodontic archwires. *Proc. 16th EUSPEN Int. Conf. Nottingham, UK*, pp. 339-340.
9. B. Franković, M. Perčić, P. Blečić (2014) Solar energy in Croatia – current state and future development. *Proc. 24th Int. Cong. Energy and Environment. Opatija, HR*, pp. 39-46.
10. P. Blečić, M. Perčić, B. Franković (2014) Renewable energy in Croatia – The rapid increase in recent years. *Proc. 24th Int. Cong. Energy and Environment. Opatija, HR*, pp. 47-52.

Conference abstracts

1. V. Glažar, M. Perčić, G. Marunić, B. Franković (2015) A Comparative Study of Evolutionary Algorithms for Optimization of Heat Exchanger with Microchannel Coil. Proc. Interklima, Zagreb, HR, p. 18.

Expertise

1. T. Bazina, E. Kamenar, Ž. Vrcan, M. Perčić, S. Zelenika (2019) Izvještaj provedenog mjerenja vibracija transformatora tvrtke Končar D&ST d.d. od strane Laboratorija za precizno inženjerstvo Tehničkog fakulteta Sveučilišta u Rijeci, 36 pages.
2. S. Zelenika, E. Kamenar, P. Gljušić, M. Perčić (2016) Development of an ultra-high precision mechatronics device for the automotive industry. Report on results of a project performed on behalf of the Yazaki Europe Ltd. company, 18 pages.

Razvoj istraživačke infrastrukture na Kampusu Sveučilišta u Rijeci
OBRAZAC ZA IZVJEŠĆIVANJE O KORIŠTENJU ZNANSTVENE OPREME

Projekt Sveučilišta u Rijeci „Razvoj istraživačke infrastrukture na Kampusu Sveučilišta u Rijeci“ financiran je iz Europskog fonda za regionalni razvoj (EFRR) u iznosu od 180.182.048,91 kn.

Vrsta rada:	Doktorski rad
Datum:	5. prosinca 2019.
Institucija/e:	Centar za mikro- i nanoznanosti i tehnologije Sveučilišta u Rijeci
Naziv rada (HRV):	Karakterizacija utjecajnih parametara na trenje u nanometarskom području
Naziv rada (ENG):	Characterization of Influential Parameters on Friction in the Nanometric Domain
Sažetak:	Trenje i trošenje su jedan od najizazovnijih problema u mnogih inženjerskim i proizvodnim tehnologijama. Trenje je nelinearna stohastička pojava s izraženom vremenskom, prostornom i temperaturnom varijabilnošću. U nanometarskom području je proučavanje mehanizama nastanka trenja, parametara koji utječu na trenje te nalaženje odgovarajućeg modela tih pojavnosti još u zametku. Predstavljeno istraživanje daje znanstveni doprinos istraživanju trenja klizanja bez podmazivanja karakterizacijom utjecajnih parametara u nanometarskom području, a posebice ovisnosti ovog fenomena o svojstvima materijala, opterećenju, brzini relativnog gibanja te temperaturi tribološkog para. Eksperimentalno su analizirani tanki filmovi pet različitih materijala. Eksperimentalno mjerenje pretražnim mikroskopom atomskih sila vršeno je na svim uzorcima strukturiranim načinom u eksperimentalnim točkama definiranim triju promjenjivim parametrima: normalna sila, brzina klizanja i temperatura. Razvijenom metodologijom je postignuto prvi puta mjerenje trenja u nanorazini sa promjenjive tri veličine. Određivanje korelacijskih funkcija iz dobivenih eksperimentalnih podataka, tj. prediktivnog modela, je izvršeno komparativnom analizom metoda strojnog učenja te je najbolji razvijeni matematički model metodom simboličke regresije pokazao točnost predikcije sile trenja u odnosu na radne parametre u rasponu od 72 do 91% ovisno o uzorku. Funkcija ove točnosti predikcije za ovako stohastičku pojavu omogućava ne samo uvid u funkcijsku zavisnost varijabli i potpunu karakterizaciju utjecajnih parametara, nego i buduće proširenje postojećih modela trenja, čime bi se njihova praktična primjenjivost proširila i na nanometarsku razinu.
Ključne riječi (HRV):	trenje u nanometarskom području, mikroskopija atomskih sila, nanotribologija tankih filmova, eksperimentalna mjerenja, modeliranje trenja
Ključne riječi (ENG):	nanometric friction, atomic force microscopy, nanotribology of thin films, experimental measurements, friction modelling
Autor rada:	Marko Perčić, mag. ing. mech.
Mentor/i:	Prof. dr. sc. Saša Zelenika
Komentor:	Prof. dr. sc. Igor Mezić



Europska unija
Ulaganje u budućnost



Ministarstvo
znanosti,
obrazovanja
i sporta

